



**Michigan  
Technological  
University**

Michigan Technological University  
**Digital Commons @ Michigan Tech**

---

Dissertations, Master's Theses and Master's Reports

---

2020

# INVESTIGATION OF THE STABILITY OF LIQUID AND AIR FILMS BY SYNCHRONIZED TRI-WAVELENGTH REFLECTION INTERFEROMETRY MICROSCOPE

Yuesheng Gao  
*Michigan Technological University, ygao4@mtu.edu*

Copyright 2020 Yuesheng Gao

---

## Recommended Citation

Gao, Yuesheng, "INVESTIGATION OF THE STABILITY OF LIQUID AND AIR FILMS BY SYNCHRONIZED TRI-WAVELENGTH REFLECTION INTERFEROMETRY MICROSCOPE", Open Access Dissertation, Michigan Technological University, 2020.  
<https://doi.org/10.37099/mtu.dc.etr/1122>

Follow this and additional works at: <https://digitalcommons.mtu.edu/etr>



Part of the [Mining Engineering Commons](#), [Other Chemical Engineering Commons](#), and the [Petroleum Engineering Commons](#)

INVESTIGATION OF THE STABILITY OF LIQUID AND AIR FILMS BY  
SYNCHRONIZED TRI-WAVELENGTH REFLECTION INTERFEROMETRY MICROSCOPE

By

Yuesheng Gao

A DISSERTATION

Submitted in partial fulfillment of the requirements for the degree of

DOCTOR OF PHILOSOPHY

In Chemical Engineering

MICHIGAN TECHNOLOGICAL UNIVERSITY

2020

© 2020 Yuesheng Gao

This dissertation has been approved in partial fulfillment of the requirements for the Degree of DOCTOR OF PHILOSOPHY in Chemical Engineering.

Department of Chemical Engineering

Dissertation Advisor: *Dr. Lei Pan*

Committee Member: *Dr. Jeffrey S. Allen*

Committee Member: *Dr. Caryn Heldt*

Committee Member: *Dr. Michael E. Mullins*

Department Chair: *Dr. Pradeep K. Agrawal*

## **Dedication**

To the best love of my life, Zhen Zhang.



# Table of Contents

List of figures.....	ix
List of tables.....	xv
Preface.....	xvi
Acknowledgements.....	xviii
Abstract.....	xix
1 Introduction and Overview.....	1
1.1 Introduction.....	1
1.2 Overview.....	2
1.3 Reference.....	4
2 Literature Review.....	6
2.1 Liquid films.....	6
2.1.1 Introduction.....	6
2.1.2 Collison.....	7
2.1.2.1 Collision efficiency.....	7
2.1.2.2 Collision forces.....	9
2.1.3 Attachment.....	10
2.1.3.1 Bubble-solid interaction forces.....	10
2.1.3.1.1 Hydrodynamic force.....	10
2.1.3.1.2 van der Waals force.....	12
2.1.3.1.3 Electrical double-layer force.....	13
2.1.3.1.4 Hydrophobic force.....	14
2.1.3.2 Theoretical modes.....	16
2.1.3.2.1 Stefan–Reynolds Model.....	16
2.1.3.2.2 Modified Stefan–Reynolds Model.....	17
2.1.3.2.3 Hydrodynamic model.....	17
2.1.3.3 Experimental approaches.....	18
2.1.3.3.1 Induction timer.....	18
2.1.3.3.2 Three dimensional (3D) imaging.....	19
2.1.3.3.3 Surface forces apparatus (SFA).....	20
2.1.3.3.4 Atomic Force Microscopy (AFM).....	21
2.1.3.3.5 Reflection Interference Contrast Microscope (RICM).....	22
2.1.3.3.6 Combining the force measurement and film thickness measurement.....	23
2.1.3.4 General factors.....	24

2.1.3.5	Other film rupture mechanism .....	28
2.1.4	Stability or detachment .....	29
2.1.4.1	Detachment models.....	29
2.1.4.1.1	Hydrodynamic model.....	29
2.1.4.1.2	Molecular-kinetic model.....	30
2.1.4.1.3	Combined model.....	30
2.1.4.2	Detachment force measurement.....	30
2.1.4.3	Spreading speed .....	32
2.2	Air films .....	32
2.2.1	Introduction.....	32
2.2.2	Experimental approaches .....	34
2.2.3	Theoretical models.....	37
2.2.4	Involved factors .....	38
2.3	Reference.....	41
3	Measurement of Instability of Thin Liquid Films by Synchronized Tri-wavelength Reflection Interferometry Microscope* .....	52
3.1	Introduction .....	52
3.2	Instrumentation.....	54
3.3	Experimental section .....	58
3.4	Results .....	59
3.5	Discussion .....	68
3.6	Summary and conclusions.....	70
3.7	Reference.....	72
4	Understanding the Mechanism of Froth Flotation of Molybdenite Using Oily Collectors from a Perspective of Thinning and Rupture of Thin Liquid Film* .....	77
4.1	Introduction .....	77
4.2	Materials and experiments.....	78
4.2.1	Materials .....	78
4.2.2	Oil emulsion.....	79
4.2.3	Contact Angle Measurements.....	79
4.2.4	Bubble-molybdenite attachment .....	79
4.3	Results and discussion.....	81
4.3.1	Oil Emulsion .....	81
4.3.2	Surface hydrophobicity by contact angle measurement .....	83
4.3.3	Stability of Thin Liquid Films (TLFs).....	85
4.4	Summary and conclusion .....	92
4.5	References .....	93

5	Stability of Thin Liquid Films between Dodecane Drops and Hydrophobic Surfaces*	96
5.1	Introduction	96
5.2	Material and method	97
5.2.1	Materials	97
5.2.2	Contact Angle Measurements	97
5.2.3	Evolution of TLF	98
5.2.4	Modeling	99
5.3	Results and discussions	100
5.3.1	Effect of NaCl concentration on the TLF stability between dodecane drops and talc	100
5.3.1.1	Contact angles of dodecane drops on talc	100
5.3.1.2	TLF thinning process by STRIM	101
5.3.2	Effect of dodecane drop size on the TLF stability between dodecane drops and talc	105
5.3.3	Comprehensive understanding of the effects of the dodecane drop size and NaCl concentration on the TLF stability between dodecane drops and talc	107
5.3.4	On other hydrophobic minerals	109
5.4	Summary and conclusions	112
5.5	Reference	113
6	Interaction Forces between Water Droplets and Solid Surfaces Across Air Films*	115
6.1	Introduction	115
6.2	Results	117
6.2.1	Water vs. Quartz	117
6.2.2	Water vs. Minerals	122
6.3	Discussion	125
6.4	Conclusion and Summary	127
6.5	Materials and Experiments	128
6.5.1	Materials	128
6.5.2	Experimental setup	129
6.5.3	Experimental procedure	131
6.5.4	Force calculation	131
6.6	Reference	133
7	Interaction and Instability of Air Films Between Bituminous Coal Surfaces and Surfactant Droplets*	137
7.1	Introduction	137

7.2	Materials and Experimental.....	138
7.2.1	Materials .....	138
7.2.2	Contact angle measurements.....	139
7.2.3	Instability of Air Film <i>via</i> STRIM.....	140
7.2.4	Force Calculation.....	142
7.3	Results .....	143
7.3.1	Instability of Air Films.....	143
7.3.2	Effect of the non-ionic surfactant .....	145
7.3.3	Effect of anionic surfactants .....	149
7.4	Discussion .....	151
7.5	Conclusion.....	154
7.6	Reference.....	155
8	Summary and Future Work.....	160
8.1	Summary .....	160
8.2	Future work .....	162
A.	Copyright perimission documentation.....	163
A.1	Figure 2.2 permission.....	163
A.2	Figure 2.3 permission.....	165
A.3	Figure 2.4 permission.....	167
A.4	Figure 2.5 permission.....	169
A.5	Figure 2.6 permission.....	171
A.6	Figure 2.7 permission.....	173
A.7	Figure 2.8 permission.....	175
A.8	Figure 2.9 permission.....	177
A.9	Figure 2.10 permission.....	177
A.10	Figure 2.11 permission.....	178
A.11	Figure 2.12 permission.....	178
A.12	Figure 2.13 permission.....	179
A.13	Figure 2.14 permission.....	179
A.14	Figure 2.15 permission.....	180
A.15	Figure 2.16 permission.....	181
A.16	Figure 2.17 permission.....	183
A.17	Figure 2.18 permission.....	184

A.18 Figure 2.19 permission.....	185
A.19 Figure 2.20 permission.....	186
A.20 Chapter 3 permission .....	188
A.21 Chapter 6 permission .....	188
A.22 Chapter 7 permission .....	190

## List of figures

<b>Figure 2.1</b> Bubble-particle attaching process in mineral flotation.....	6
<b>Figure 2.2</b> Possible article-bubble collision case <sup>12</sup> , reprinted with permission. ....	7
<b>Figure 2.3</b> Schematic of the collision of the bubble and particle: a). the particle is smaller than the bubble; b). the bubble is smaller than the particle. $R_c$ is the grazing trajectory radius, $\varphi_{0,max}$ maximum initial angle, and $\varphi_{c,max}$ maximum collision angle <sup>5</sup> , reprinted with permission. ....	7
<b>Figure 2.4</b> A coordinate system between a curved surface and a flat surface <sup>14</sup> , reprinted with permission. ....	11
<b>Figure 2.5</b> An induction timer used by Li et al., <sup>43</sup> reprinted with permission. ....	18
<b>Figure 2.6</b> A high-speed camera recording the rising of an air bubble to a solid surface <sup>44</sup> , reprinted with permission. ....	19
<b>Figure 2.7</b> A 3D imaging set-up of thin liquid film <sup>45</sup> , reprinted with permission. ....	20
<b>Figure 2.8</b> A schematic of SFA <sup>50</sup> , reprinted with permission. ....	21
<b>Figure 2.9</b> Schematic of the AFM to investigate the bubble-particle attachment <sup>54</sup> , reprinted with permission. ....	21
<b>Figure 2.10</b> Schematic and outcome of RICM <sup>57</sup> , reprinted with permission.....	22
<b>Figure 2.11</b> Combined AFM and RICM <sup>20</sup> , reprinted with permission. ....	23
<b>Figure 2.12</b> Schematics of the thin liquid film force apparatus (ITLFFA) <sup>61</sup> , reprinted with permission. ....	24
<b>Figure 2.13</b> Bridge role of picobubbles in solid-bubble attachment <sup>99</sup> , reprinted with permission. ....	29
<b>Figure 2.14</b> Configuration of bubble-particle interaction by AFM <sup>109</sup> , reprinted with permission. ....	31
<b>Figure 2.15</b> Schematic of the adhesion force measurement method <sup>110</sup> , reprinted with permission. ....	31
<b>Figure 2.16</b> Schematic of a vibration technique <sup>112</sup> , reprinted with permission. ....	32
<b>Figure 2.17</b> Outcomes of liquid droplets impacting solid surfaces by CCD <sup>116</sup> , reprinted with permission. ....	35

<b>Figure 2.18</b> Schematic of ultrafast x-ray phase-contrast imaging <sup>146</sup> , reprinted with permission. ....	35
<b>Figure 2.19</b> Schematic of total internal reflection microscopy <sup>149</sup> , reprinted with permission. ....	36
<b>Figure 2.20</b> Schematic of dual-wavelength reflection interference microscopy. (DWF: dual-wavelength filter; SRM: semi reflecting mirror; DM: dichroic mirror; SPF: short pass filter; CCD 1 and CCD 2: CCD cameras) <sup>156</sup> , reprinted with permission. ....	37
<b>Figure 3.1</b> Optical setup of the Synchronized Tri-wavelength Reflection Interferometry Microscope (STRIM). ....	55
<b>Figure 3.2</b> a) a photo and schematic representation of the STRIM instrument developed in this study. b) side-view images of air-water-solid, air-water-air, and air-water-dodecane interaction. ....	56
<b>Figure 3.3</b> Analysis of the interference fringes obtained at three difference wavelengths to obtain the film thickness. a) a timed series of interference fringes at $\lambda = 460$ , 527 and 60 nm; b) changes in pixel intensity at the center of the fringes as a function of time; c) film thickness as a function of the time at three different wavelengths. The smoothed film thickness is shown in black dashed line. The RMS error of the film thickness measurement is below 3 nm. ....	60
<b>Figure 3.4</b> Spatiotemporal thickness profiles of the thin liquid film (TLF) formed between an air bubble of 0.835 mm in radius and a hydrophilic silicon surface in water at an approaching velocity of 0.7 $\mu\text{m/s}$ . ....	61
<b>Figure 3.5</b> Comparison of spatiotemporal thickness profiles of the thin liquid films (TLFs) of water between an air bubble of a) 0.942 mm and b) 0.169 mm in radius and a hydrophobic silicon surface of a water equilibrium contact angle of $90^\circ$ in $10^{-2}$ M NaCl solutions. The time interval between two adjacent profiles is 0.5 s. ....	62
<b>Figure 3.6</b> Results of the critical rupture thicknesses of the TLF between air bubbles and hydrophobic silicon surfaces with water contact angles of $90^\circ$ . ....	64
<b>Figure 3.7</b> Time evolution of spatiotemporal film profiles of TLFs formed between two air bubbles in $10^{-2}$ M NaCl solutions at bubble sizes of a) 0.915 $\mu\text{m}$ and b) 0.217 $\mu\text{m}$ . The time interval between two adjacent profiles is 1 s. ....	65
<b>Figure 3.8</b> Effect of bubble sizes on critical rupture thickness ( $h_c$ ) of the TLFs between two air bubbles. ....	66

<b>Figure 3.9</b> Timed evolution of film profiles of the thin liquid films formed between an 8-mm diameter droplet of dodecane and an air bubble in $10^{-2}$ M NaCl solutions using different sizes of air bubbles. ....	66
<b>Figure 3.10</b> Effect of bubble sizes on critical rupture thickness of the TLF of water between a droplet of dodecane and an air bubble in $10^{-2}$ M NaCl solution.....	68
<b>Figure 4.1</b> A schematic representation of synchronized tri-wavelength reflection interferometry microscope (STRIM) that is used to study thinning and rupture of TLFs during the bubble-molybdenite attachment process.....	80
<b>Figure 4.2</b> Photos and size distribution of dodecane drops in the aqueous emulsions of DI water at a) 0.01%, b) 0.1%, c) 0.5%, and d) 1.0% oil dosage. ....	82
<b>Figure 4.3</b> Photos and size distribution of kerosene drops in the aqueous emulsion of DI water at a) 0.01%, b) 0.1%, c) 0.5%, and d) 1.0% oil dosage. ....	82
<b>Figure 4.4</b> Bright-field microscope images of molybdenite face surface with and without treated with kerosene emulsions at different oil dosages.....	84
<b>Figure 4.5</b> Effect of oil types and oil concentration in the oil emulsions on the equilibrium water contact angle on molybdenite face surfaces using captive bubble method.....	85
<b>Figure 4.6</b> The spatiotemporal evolution of the thin liquid films of DI water when an air bubble approaches a freshly peeled molybdenite face surface. (a) interference fringes obtained at three different wavelengths, (b) spatiotemporal profiles of the thin liquid films (TLFs). ....	86
<b>Figure 4.7</b> The evolution of the TLFs when an air bubble approaches towards a molybdenite face surface treated with 0.1% emulsified dodecane solutions. (a) interference images; (b) spatiotemporal thickness profiles. ....	87
<b>Figure 4.8</b> Kinetics of thinning of the TLFs formed between air bubbles and molybdenite surfaces treated with dodecane and kerosene emulsions solutions.....	88
<b>Figure 4.9</b> Film rupture between air bubbles and molybdenite surfaces treated in oil emulsions at a) 0.1% dodecane and b) 0.5% kerosene dosage. ....	89
<b>Figure 4.10</b> A schematic of two different mechanisms involved in the film rupture. ....	90
<b>Figure 4.11</b> Effect of a) dodecane and d) concentration in oil emulsion on the occurrence of rupture of thin liquid films on molybdenite face surfaces treated in the oil emulsion solutions. ....	91



<b>Figure 5.1</b> Schematic of the synchronized tri-wavelength reflection interferometry microscopy (STRIM) used in this work.....	98
<b>Figure 5.2</b> Contact angles of dodecane drops on talc at different NaCl concentrations .	101
<b>Figure 5.3</b> A stable film in water between a dodecane drop and talc .....	102
<b>Figure 5.4</b> The film ruptures in water between a dodecane drop and talc .....	103
<b>Figure 5.5</b> Effects of NaCl concentrations on critical TLF thicknesses between dodecane drops and talc .....	104
<b>Figure 5.6</b> Effects of NaCl concentrations on thinning kinetics of TLF between dodecane drops and talc .....	105
<b>Figure 5.7</b> Effects of dodecane drop size on critical TLF thicknesses between dodecane drops and talc .....	106
<b>Figure 5.8</b> Effects of dodecane drop size on thinning kinetics of TLF between dodecane drops and talc .....	107
<b>Figure 5.9</b> The stabilities of TLFs between talc and dodecane drops with different sizes at different NaCl concentrations .....	108
<b>Figure 5.10</b> Explanation of the effects of the dodecane drop size and NaCl concentration on the TLF stability between dodecane drops and talc.....	109
<b>Figure 5.11</b> The stabilities of TLFs between molybdenite and dodecane drops with different sizes at different NaCl concentrations.....	110
<b>Figure 5.12</b> The stabilities of TLFs between hydrophobized quartz and dodecane drops with different sizes at different NaCl concentrations .....	110
<b>Figure 5.13</b> Comparison of stability boundaries for molybdenite-dodecane, talc-dodecane, and hydrophobized quartz-dodecane systems.....	111
<b>Figure 5.14</b> Comparison of water contact angles on molybdenite, talc, and hydrophobized quartz.....	112
<b>Figure 6.1</b> Side view (a) and bottom view (b) of the interaction between water droplets and hydrophobic quartz surfaces. ....	117
<b>Figure 6.2</b> a) Spatiotemporal thickness profiles of the air film between a drop of DI water and a flat quartz surface having $\theta_w$ of $96^\circ$ and the difference ( $\Delta h$ ) between experimental data and the polynomial fit.....	118

<b>Figure 6.3</b> Effect of surface hydrophobicity on spatiotemporal profiles of the air films between water droplets and quartz surfaces.....	119
<b>Figure 6.4</b> Effect of hydrophobicity on the kinetics of film thinning (a) and approaching velocity (b).....	120
<b>Figure 6.5</b> Effect of surface hydrophobicity on the Interaction forces between water droplets and silica surfaces across air films.....	122
<b>Figure 6.6</b> Spatiotemporal profiles of water droplets against layered mineral surfaces.	123
<b>Figure 6.7</b> Thinning kinetics of air films between water droplets and mineral substrates. ....	123
<b>Figure 6.8</b> Interaction forces between water droplets and a variety of natural mineral surfaces. ....	125
<b>Figure 6.9</b> Fitting of obtained force curves on quartz plates with $F = c/h$ function. ....	127
<b>Figure 6.10</b> A schematic drawing of an experimental set-up for measuring the spatiotemporal thickness profile of air films between water droplets and flat solid surfaces. ....	130
<b>Figure 7.1</b> a) Surface morphology of a polished bituminous coal surface determined by atomic force microscopy (AFM), b) height profiles on two color-coded lines. ...	139
<b>Figure 7.2</b> A schematics of the synchronized tri-wavelength reflection interferometry microscope (STRIM) used for studying interactions between water droplets and coal surfaces.....	141
<b>Figure 7.3</b> a) Temporal changes in interference fringes of an air film between a DI water droplet and a polished bituminous coal surface at $\lambda = 460$ nm, 526 nm, and 620 nm; b) spatiotemporal thickness profiles of the air films. ....	143
<b>Figure 7.4</b> a) Bottom-view and side-view images of a water droplet spreading on a bituminous coal surface. ....	144
<b>Figure 7.5</b> Spatiotemporal thickness profiles, $h(r,t)$ , of air films between aqueous Triton X-100 droplets and polished bituminous coal surfaces at a) 0.001 mM, b) 0.01 mM, and c) 0.1 mM Triton X-100. ....	146
<b>Figure 7.6</b> Effect of Triton X-100 concentration on the kinetics of thinning of air films between aqueous Triton -100 droplets and polished bituminous coal surfaces...	147

**Figure 7.7** Interaction forces between aqueous Triton X-100 droplets and bituminous coal surfaces across air films at different concentrations of Triton X-100. Solid lines show the fitted force curves with an  $F = c/h$  function.....149

**Figure 7.8** Effects of AOT (a) and SDS (b) on the air film kinetics of approaching.....150

**Figure 7.9** a) critical rupture thickness as a function of surface tension of wetting liquids, b) critical rupture thickness of air films as a function of contact angles of wetting liquids on coal surfaces.....152

**Figure 7.10** A schematic representation of the mechanism for the attractive electric force between water droplets and coal surfaces.....153

## List of tables

<b>Table 2.1</b> The components of the four forces <sup>13</sup> .....	10
<b>Table 3.1</b> Characteristic parameters of film rupture at different bubble radius. ....	67
<b>Table 4.1</b> Various drop sizes and the number of drops in dodecane and kerosene emulsions at different oil dosages.....	83
<b>Table 6.1</b> Characteristics of the rupture of air films formed between water droplet and solid surfaces.....	120
<b>Table 6.2</b> Characteristics of thinning and rupture of air films between water droplets and different mineral surfaces. ....	124
<b>Table 7.1</b> Effect of Triton X-100 concentration on surface tensions of the liquid droplet and the contact angles of polished bituminous coal surfaces. ....	145
<b>Table 7.2</b> Characteristics of the instability of air films between aqueous droplets and bituminous coal surfaces at different concentrations of Triton X-100. ....	148
<b>Table 7.3</b> A list of $R$ , $c$ , and $dF_{\max}/dh$ values at different concentrations of Triton X-100. ....	149
<b>Table 7.4</b> Characteristics of attachments between bituminous coal surfaces and aqueous droplets of AOT and SDS.....	151

## Preface

Chapter 3 is introducing the newly developed Synchronized Tri-wavelength Reflection Interferometry Microscope (STRIM). The details of STRIM system are included in this chapter, especially its configuration. Experiments on liquid films in different contexts, such as the air-solid system, air-oil system, and air-air system, were attempted. It showed that the STRIM system is capable of characterizing the liquid films between different surfaces. And the hydrophobicity of the surfaces holds the key to the stability of the liquid films. Besides, film sizes were found to be closely related to its stability. In this work, Dr. Lei Pan helped build the system, design the experiments, review, and improve the paperwork. I performed the experiments, collected and analyzed the data, and wrote the draft of the paperwork. This chapter has been published in the peer-review journal, *Langmuir* (<https://doi.org/10.1021/acs.langmuir.8b02891>), and was selected as the cover article of the issue.

Chapter 4 is focusing on fundamental research on the flotation of molybdenite using oily collectors. Here, dodecane is chosen as the oily collector. In this work, the interactions between air bubbles and molybdenite with/without the treatment by dodecane emulsion were uncovered. Experimental results show the liquid films on the new molybdenite surfaces are stable at a certain thickness. The molybdenite surfaces were hydrophobized by the adsorption of dodecane drops. Both the contact angle measurement and the liquid film stability measurement confirmed that the dodecane-treated molybdenite surfaces are more hydrophobic, which is the primary reason for the enhanced molybdenite flotation recovery by the oily collectors. Dr. Pan provided experimental materials and protocols, improved the graph and paperwork. I launched the experiments, collected, and analyzed the data, and wrote the draft for the manuscript. This chapter has been submitted to a peer-review journal, *Minerals Engineering*, and its current status is under review.

Chapter 5 is a follow-up research on the adsorption of oil drops on hydrophobic surfaces. In this work, endeavors are made to investigate the effect of surface hydrophobicity and surface forces on the instability of thin liquid film (TLF) of aqueous solutions between dodecane oil droplets and various hydrophobic surfaces. It was found that the thin liquid film was stable between dodecane oil droplets and hydrophobic mineral surfaces in the presence of long-range repulsive electrostatic double-layer force. The equilibrium film thickness decreased with increasing electrolyte concentrations. When the repulsive electrostatic double-layer force was suppressed in the concentrated electrolyte solutions, the TLF ruptured, followed by forming a three-phase contact line. The TLF becomes less stable when the thicknesses were reduced to a range of film destabilization. And the range of film destabilization increased with increasing surface hydrophobicity. In the absence of repulsive, long-range, electrostatic double-layer force, the film rupture tended to occur when the sizes of dodecane drops were small. Understanding the instability of TLFs between oil and solid surfaces involved is essential to achieve the desired system performance for many industrial applications. Dr. Pan designed the experiments and finalized the manuscript. I operated the instruments to obtain data and wrote the draft. This chapter is to be submitted to a peer-review journal.

Chapter 6 is about the air film between water drops and quartz surfaces. The quartz surfaces were rendered hydrophobic by coating a layer of OTS. By adjusting the OTS concentrations, quartz surfaces with different hydrophobicity were successfully obtained. The subsequent investigation of the air films was implemented by driving water drops towards the quartz surfaces. The main conclusion is that the air films were less stable and more readily rupture if the quartz was more hydrophobic. Dr. Pan proposed the experiments and created an interaction model for this system. Dr. Jung contributed to the interaction calculation. I performed the experiments and fit the experimental data with the theoretical model. This chapter has been published in the peer-review journal, *ACS Omega* (<https://doi.org/10.1021/acsomega.9b02646>).

Chapter 7 applies the methodology of characterizing the air film stability to dust control in underground coal mines. The STRIM system was employed to investigate the interactions between coal surfaces and water drops. Also, in practice, the water spray is used to collect coal dust. But wetting agents are usually added into the water to enhance the dust collecting efficiency. Here, Triton X-100 was selected to modify the sprayed water. Results showed that in the presence of Triton X-100, the air films became unstable, and thus the coal particles tended to be easily captured by the liquid drops. Dr. Pan provided the experimental materials, selected the protocols, and polished the manuscript. Dr. Jung revised the paperwork. I performed the experiments, analyzed the data, drew graphs, and wrote the manuscript draft. This chapter has been published in the peer-review journal, *Fuel* (<https://doi.org/10.1016/j.fuel.2020.117839>).

## Acknowledgements

First and foremost, I would like to thank my advisor, Dr. Lei Pan, for relentless guidance and encouragement. He is an excellent supervisor who has a creative mind, critical and logical thinking, and a great passion for research and teaching. Besides, he is very patient and supportive, giving me freedom and room to explore the areas I am interested in. It has been such a great honor to join his group and be his first Ph.D. student. I also want to thank the generous support from the Department of Chemical Engineering of Michigan Tech, the Alpha Foundation for the Improvement of Mine Safety and Health, the American Chemistry Society Petroleum Research Fund, the Vincent Vellella Endowed Scholarship, and the Graduate School of Michigan Tech.

Besides, I want to express my deep gratitude to Dr. Jeffrey S. Allen, Dr. Caryn Heldt, and Dr. Michael E. Mullins. They have been so supportive of serving as my committee members and providing professional guidance to my research and paperwork. Their suggestions and feedback help a lot in improving the quality of my work. And I thank Dr. Chito Kendrick for his assistance at the Microfabrication Facility of Michigan Tech. I want to thank Dr. Timothy Leftwich, Dr. Edward Laitila, Elizabeth Miller, and Aleister Kerr for their instructions to operate the instruments in Applied Chemical and Morphological Analysis Laboratory. I am also grateful to Dr. Agrawal, Dr. Kawatra, Dr. Eisele, Dr. Ong, Dr. Morrison, Dr. Co, Dr. Caneba, Alexis E. Snell, Taana Blom, Jerry A. Norkol, and Steve Wisniewski in the Department of Chemical Engineering of Michigan Tech for their constant help and support.

In addition, I would like to thank all my labmates for their friendship and support, especially Ruiting, Tinu, Mike, John, Sean, Emily, and Zack. In the meantime, I would like to thank Dr. Sunghwan Jung at Cornell University for his expert guidance in building theoretical models, and thank Dr. Jan Miller, Dr. Xuming Wang and Dr. Venkata Atluri at University of Utah for their help. I also appreciate the collaboration in the classic flotations with Dr. Yuehua Hu, Dr. Zhiyong Gao, Dr. Wei Sun, Jianjun, Gaogui, Zheyi, and Cong at Central South University. I thank Dr. Wencai Zhang at Virginia Tech for his direct support. And I would like to express my gratitude to my boss, Mr. Don Kemp, at Minnpar, LLC, for his wise suggestions on my work and future.

Last but not least, I would like to thank my friends, Dr. Chunpei Cai, Dr. Peilin Lan, Dr. Fangyu Liu, Dr. Qingming Feng, Dr. Weiping Liu, Leah Mertes, Tianhao Yan, Emily Kuo, Emily Chien, Jiajia Wu, Zhaolin Hu, Fugui Liu, Xiaolong Chen, Feng Wei, Bin Han, Dr. Zhenyue Yang, Dr. Hongbo Chen, Dr. Xue Mi, Dr. Huaguang Wang, Donghui Wang, Dr. Dongdong Ge, Xiaodong Zhou, Jiawei Li, Junfeng Gao, Ruizhe Si, Yunxiang Ma, Jiaqing Wang, Qinjie Lv, and Shiyang Cai for their company. My deepest thanks are given to my family members: My lover Zhen Zhang, my father Mr. Zongxiao Gao, my mother, Mrs. Guiyun Lian, my uncle Mr. Suimin Gao, my lover's parents Mr. and Mrs. Zhang, my sister Lijun. I will never be able to complete my degree without your constant love.

## Abstract

Liquid films are widely involved in many processes, such as froth flotation, oil extraction, foam/bubble stabilization, etc. In the meantime, air films are commonly seen in diverse fields like dust control, ink print, coating industry, and so on. Stabilities of these liquid/air films are of great importance to improve the processes. As more and more researchers are paying increasing attention to liquid/air films, tremendous efforts have been made to explore the properties of the films. On the one hand, some theoretical models have also been well developed in recent decades. State-of-the-art technologies, such as AFM, SFA, and RICM, have also been employed to visualize the films in either a direct or indirect manner. However, due to the limitations of the techniques, it is still challenging to fully uncover the mechanisms of the film stabilities. A new and powerful methodology to characterize the film properties has been a top priority.

In this work, a novel technique, namely Synchronized Tri-wavelength Reflection Interferometry Microscope (STRIM), was developed in our lab. It allows the accurate measurement of a separation distance within a range of few nanometers to micrometers. Based on the previous RICM, STRIM employs two additional light sources and achieves the determination of the absolute distance. The accuracy of the film thickness measurements was found to be within 1 nm over a range of 0-200 nm and within 3 nm over the range of 200–1000 nm. By recording the thinning process of films, STRIM is able to reconstruct the spatiotemporal profiles, which contain massive information. First, the conditions under which the films are stable or unstable are the urges to figure out for industrial applications. Besides, the films' stabilities are closely related to the interfacial properties, and thus they can be alternative indicators of some essential properties, such as hydrophobicity. Additionally, the interactions and surface forces across the films between involved surfaces can be calculated by the dynamic film thinning kinetics, unraveling the underlying mechanisms for the processes of interest. Furthermore, other approaches, including AFM, contact angle measurement, and flotation, are also referred to in this work and confirm the drawn conclusions. The STRIM can investigate both the liquid and air films with the flexibility of controlling the involved objects like the surfaces with adjustable hydrophobicity and media with designed properties. This newly-developed equipment has the potential to be extensively used within the colloid and interfacial science and engineering areas.



# 1 Introduction and Overview

## 1.1 Introduction

A layer of liquid/air film is formed when a surface is approached towards another surface in a liquid/air medium. The films will end up with either a stable status or rupture, depending on the interactions across the film between two surfaces. Understanding the stability of the films is crucial in diverse fields, such as ore beneficiation<sup>1</sup>, bitumen extraction<sup>2,3</sup>, emulsion and foam<sup>4,5</sup>, theranostic applications<sup>6</sup>.

Numerous endeavors have been made to study the lifetime of thin liquid films (TLFs). It is well accepted that the thinning of TLFs, or the drainage, determines the final status<sup>7</sup>. And the thinning process has been studied both by theoretical models<sup>8</sup> and experimental visualizations<sup>9</sup>. Reynolds contributed a lot to establish the theory of hydrodynamic lubrication for a TLF confined between two moving solid surfaces<sup>10</sup>, and almost all the following developed models are based on his theory. On the technique side, the instruments have been updated for many generations, from the indirect method, like induction timer, to the more advanced tools such as atomic force microscope (AFM). More details have been found while studying the TLFs. First, the properties of the surface significantly affect the stability of the TLFs. For example, films on hydrophobic surfaces tend to rupture, but that on hydrophilic surfaces are usually stable<sup>11</sup>. Besides, films on rough surfaces rupture generally at a considerable distance<sup>12</sup>. Also, the effects of the electrolyte types and concentrations are also essential for the stability of the TLFs. Special zones of electrolyte conditions for the rupture films are recently summarized<sup>13</sup>. These factors can thus be adjusted in practice to control the film stability as required.

Researchers have been working hard to directly observe the evolution of films. However, the visualization maintains a challenge due to the limitation of the camera resolutions. Reflection interference contrast microscopy (RICM) is an excellent candidate to achieve this goal. But it is tricky to determine the absolute distance because a monochromatic wavelength light beam is employed and causes confusion to find the right order. Later, the use of an additional beam makes the determination of the order more accurate in a range of 0-800nm. In some cases, this range is still not enough to fully describe the film evolution. Thus the requirement of more advanced techniques is attracting increasing attention.

Similarly, air films are commonly seen in many applications, such as dust control, ink-jet printing, rapid spray cooling, fire suppression, spray coating and painting, spray plasma, pesticide spraying, etc.<sup>14</sup>. The most common phenomenon in nature would be the rainfall. Unlike the liquid films, the air films always rupture, no matter what objects are involved: when the separation distance reached a specific value, the ruptures would occur spontaneously, and the distance was defined as critical separation distance, which varies from nanometer scale to micrometer scale<sup>15,16</sup>.

Different techniques have been used to investigate the status of air films. CCD cameras are widely employed to record the impacting processes and the outcomes, including deposition, prompt splash, corona splash, receding break-up, partial rebound, and complete rebound<sup>17</sup>. In addition, X-ray phase-contrast imaging, reflection interference microscopy (RIM), and total internal reflection microscopy (TRIM) allow the characterization of air film profiles. The experimental results showed that the properties of the solid surface and the liquid are keys to the stability of air films. For instance, the asperities of solid surfaces can cause the stochastic failure of the interstitial film<sup>18</sup>. Besides, it is also found that microtextures have a profound effect on the macroscopic splash, providing convenient means to control splashes and the directions<sup>19</sup>. On the other hand, the density of the liquid is vital: The heavier the drop, the stronger the impact force<sup>20</sup>. Additionally, the velocity of impact, the drop size, and shape, or the liquid surface tension can influence the mass and energy distribution of the ejected droplets<sup>21</sup>.

However, the determination of the critical rupture separation has not been well addressed in air film studies. And the utilized tools need to be improved to observe the in-site evolution of air films during the impact. Plus, the air films are, in most cases, studied as a scientific topic, and they are not well-related to industrial applications. More efforts are required to further understand the properties of air films.

## 1.2 Overview

The dissertation begins with a general introduction of the background and motivation of this work, stated here as Chapter 1. It is followed by Chapter 2, which is a detailed literature review on both the liquid and air films. For the liquid film part, flotation will be set as an example to give more details on current research processes. And for the air film part, a more general review is provided on updated studies.

Chapters 3 to 5 are studying the liquid film. In Chapter 3, details are given on the newly developed Synchronized Tri-wavelength Reflection Interferometry Microscope (STRIM), especially its configuration. Experiments on liquid films in different contexts, such as the bubble-solid system, bubble-oil system, and bubble-bubble system, were studied. It showed that the STRIM system is capable of characterizing the liquid films between different surfaces. And the hydrophobicity of the surfaces holds the key to the stability of the liquid films. Besides, film curvatures were found to be closely related to the stability. Chapter 4 is fundamental research on the recovery of molybdenite by flotation with oil as the collector. Here, the interactions between air bubbles and molybdenite with/without the treatment by dodecane emulsions were detected. Experimental results show the liquid films on the new molybdenite surfaces were stable at a certain thickness. The molybdenite surfaces were hydrophobized by the adsorption of dodecane drops. Both the contact angle measurement and the liquid film stability measurement confirmed that the dodecane-treated molybdenite surfaces were more hydrophobic. Chapter 5 is a follow-up research on the adsorption of oil drops on hydrophobic surfaces. Prior to the adsorption of dodecane drops on a hydrophobic surface, the liquid films should drain and rupture first. During the drainage of the liquid film, two pressures can be adjusted: capillary

pressure and disjoining pressure. The former was modified by changing the oil drop sizes, while the latter could be adjusted by altering the electrolyte concentrations. Experimental results showed smaller drop sizes and higher electrolyte concentrations benefited the adsorption of oil on hydrophobic surfaces. And for more hydrophobic surfaces, the required drop size for film rupture was greater, and the concentration of electrolyte needed was smaller.

Chapters 6 and 7 are studies of air films. Chapter 6 is about the air film between water drops and quartz surfaces. The quartz surfaces were rendered hydrophobic by coating a layer of OTS or MTS. By adjusting the OTS/MTS concentrations, quartz surfaces with different hydrophobicity were successfully obtained. The subsequent investigation of the air films was implemented by driving water drops towards the quartz surfaces. The main conclusion is that the air films are less stable and more readily rupture if the quartz is more hydrophobic. Chapter 7 is a follow-up study of Chapter 6 about the dust control in coal mines. The STRIM system was employed to characterize the interactions between the coal surface and water drops. Also, in practice, the water spray is used to collect coal dust. But wetting agents are usually used as additives into the sprayed water to enhance the dust collecting efficiency. Here, Triton X-100 was selected to modify the sprayed water. Results showed that in the presence of Triton X-100, the air films became unstable, and thus the coal particles tended to be easily captured by the liquid drops.

### 1.3 Reference

- 1 Derjaguin, B. & Dukhin, S. Theory of flotation of small and medium-size particles. *Progress in Surface Science* **43**, 241-266 (1993).
- 2 Tchoukov, P. *et al.* Role of asphaltenes in stabilizing thin liquid emulsion films. *Langmuir* **30**, 3024-3033 (2014).
- 3 Masliyah, J., Zhou, Z. J., Xu, Z., Czarnecki, J. & Hamza, H. Understanding water-based bitumen extraction from Athabasca oil sands. *The Canadian Journal of Chemical Engineering* **82**, 628-654 (2004).
- 4 Pugh, R. Foaming, foam films, antifoaming and defoaming. *Advances in Colloid and Interface Science* **64**, 67-142 (1996).
- 5 Kennedy, M. J. *et al.* Bubble coarsening dynamics in fluorinated and non-fluorinated firefighting foams. *Colloids and Surfaces A: Physicochemical and Engineering Aspects* **470**, 268-279 (2015).
- 6 Schutt, E. G., Klein, D. H., Mattrey, R. M. & Riess, J. G. Injectable microbubbles as contrast agents for diagnostic ultrasound imaging: the key role of perfluorochemicals. *Angewandte Chemie International Edition* **42**, 3218-3235 (2003).
- 7 Vrij, A. Possible mechanism for the spontaneous rupture of thin, free liquid films. *Discussions of the Faraday Society* **42**, 23-33 (1966).
- 8 Manica, R., Klaseboer, E. & Chan, D. Y. Dynamic interactions between drops—a critical assessment. *Soft Matter* **4**, 1613-1616 (2008).
- 9 Xing, Y. *et al.* Recent experimental advances for understanding bubble-particle attachment in flotation. *Advances in colloid and interface science* **246**, 105-132 (2017).
- 10 Reynolds, O. IV. On the theory of lubrication and its application to Mr. Beauchamp tower's experiments, including an experimental determination of the viscosity of olive oil. *Philosophical Transactions of the Royal Society of London* **177**, 157-234 (1886).
- 11 Xie, L., Cui, X., Gong, L., Chen, J. & Zeng, H. Recent Advances in the Quantification and Modulation of Hydrophobic Interactions for Interfacial Applications. *Langmuir* **36**, 2985-3003 (2020).
- 12 Li, Z. *et al.* Wetting and spreading behaviors of nanodroplets: The interplay among substrate hydrophobicity, roughness, and surfactants. *The Journal of Physical Chemistry C* **120**, 15209-15215 (2016).
- 13 Feng, L., Manica, R., Grundy, J. S. & Liu, Q. Unraveling Interaction Mechanisms between Molybdenite and a Dodecane Oil Droplet Using Atomic Force Microscopy. *Langmuir* **35**, 6024-6031 (2019).
- 14 Yarin, A. L. Drop impact dynamics: splashing, spreading, receding, bouncing.... *Annu. Rev. Fluid Mech.* **38**, 159-192 (2006).
- 15 Kolinski, J. M., Mahadevan, L. & Rubinstein, S. M. Lift-off instability during the impact of a drop on a solid surface. *Physical review letters* **112**, 134501 (2014).

- 16 de Ruiter, J., van den Ende, D. & Mugele, F. Air cushioning in droplet impact. II. Experimental characterization of the air film evolution. *Physics of fluids* **27**, 012105 (2015).
- 17 Rioboo, R., Tropea, C. & Marengo, M. Outcomes from a drop impact on solid surfaces. *Atomization and Sprays* **11** (2001).
- 18 Pack, M., Kaneelil, P., Kim, H. & Sun, Y. Contact Line Instability Caused by Air Rim Formation under Nonsplashing Droplets. *Langmuir* **34**, 4962-4969 (2018).
- 19 Tsai, P., Hendrix, M. H., Dijkstra, R. R., Shui, L. & Lohse, D. Microscopic structure influencing macroscopic splash at high Weber number. *Soft Matter* **7**, 11325-11333 (2011).
- 20 Soto, D., De Larivière, A. B., Boutillon, X., Clanet, C. & Quéré, D. The force of impacting rain. *Soft matter* **10**, 4929-4934 (2014).
- 21 Mundo, C., Sommerfeld, M. & Tropea, C. Droplet-wall collisions: experimental studies of the deformation and breakup process. *International journal of multiphase flow* **21**, 151-173 (1995).

## 2 Literature Review

### 2.1 Liquid films

#### 2.1.1 Introduction

When two surfaces are approaching in liquid, a layer of liquid film will form. An essential industrial process involving liquid films is froth flotation. Flotation is a widely used technique to collect target solid materials based on the solid surface properties, especially the hydrophobicity<sup>1</sup>. The target particles could remain attached to the gas-liquid interface when air bubbles were generated into the slurry. The successful attachment is subjected to the bubble-particles interaction. Initially, this process is governed by the hydrodynamic force in the liquid phase; meanwhile, a layer of thin liquid film forms between the bubble and particle surface. And then the liquid film drains away, leading the rupture to rupture. It is followed by the growth of a three-phase (gas-liquid-solid) contact line until a stable wetting perimeter is reached. The bubble-particle attaching process can be described as a sequence of sub-steps<sup>2,3</sup>, as visualized in Figure 2.1:

(I). Collision. Here, the bubble approaches the particles until a contact distance.

(II). Attachment. It begins with the drainage and rupture of the liquid film and continues with contact line movement. This process involves the adhesion of the particle to the bubble when the particle is smaller than the air bubble, e.g., in mineral flotation, or the adhesion of the bubble to the particle when the air bubble is smaller than the particle, e.g., in plastic flotation<sup>4</sup>.

(III). Stability or detachment. This stage will determine the final status of bubble-particle interaction. For the stable case, the bubble will float to the top of the slurry, carrying the particles. But there might also be the detachment of the particles from bubbles, which occurs when the bubble-particle aggregates are unstable.

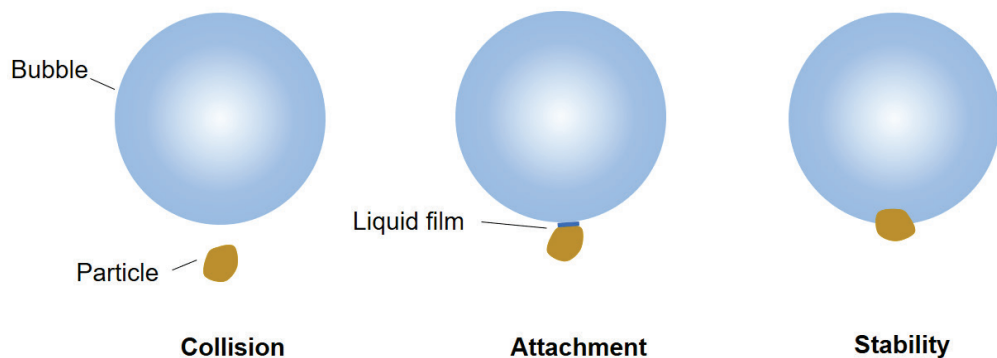


**Figure 2.1** Bubble-particle attaching process in mineral flotation

## 2.1.2 Collision

### 2.1.2.1 Collision efficiency

During the collisions, as shown in Figure 2.2, some particles will slide and then leave the air bubbles, while others will finally attach to the air bubble. The final status of the collision is determined by many factors, as detailed in this section.

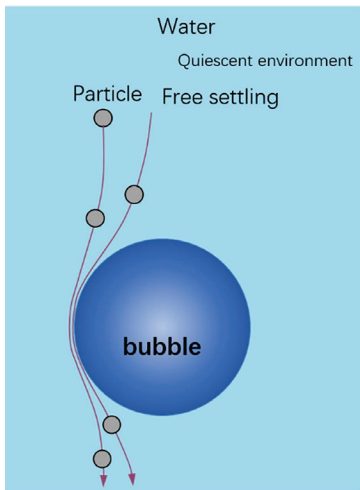


**Figure 2.2** Possible article-bubble collision case<sup>12</sup>, reprinted with permission.

Tremendous efforts have been made in investigating the collision process. Firstly, it is found that the relative position of bubbles and particles is of great importance, and the critical position is presented in Figure 2.3.

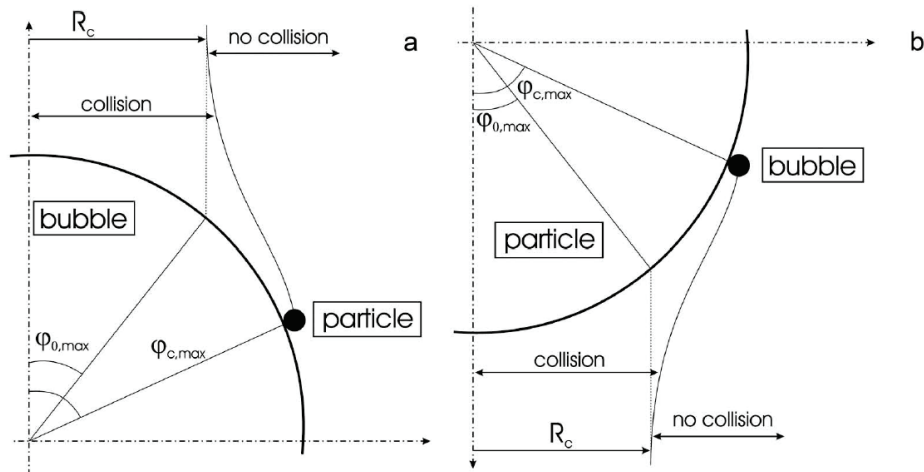


**Figure 2.3** Schematic of the collision of the bubble and particle: a). the particle is smaller than the bubble; b). the bubble is smaller than the particle.  $R_c$  is the grazing trajectory radius,  $\varphi_{0,max}$  maximum initial angle, and  $\varphi_{c,max}$  maximum collision angle<sup>5</sup>, reprinted with permission.

It is clear that when  $\varphi$  is smaller than  $\varphi_{c,max}$ , the collision may happen. Considering the interceptional, gravitational, and inertial effects,  $\varphi_{c,max}$  varies at different Re numbers<sup>6</sup>:

$$\varphi_{c,max} = 78.1 - 7.37 \log Re \text{ for } 20 < Re < 40 \quad \text{Eq. 2.1}$$

$$\varphi_{c,max} = 85.5 - 12.49 \log Re \text{ for } 1 < Re < 20 \quad \text{Eq. 2.2}$$

$$\varphi_{c,max} = 85.0 - 2.50 \log Re \text{ for } 0.1 < Re < 1 \quad \text{Eq. 2.3}$$

Besides, a concept called collision efficiency ( $E_c$ ), was proposed and described as<sup>3</sup>,

$$E_c = 1 - (1 - E_g)(1 - E_s)(1 - E_i) \quad \text{Eq. 2.4}$$

where  $E_g$ ,  $E_s$ , and  $E_i$  are efficiencies resulted from gravity, interception, and inertia, respectively.

And  $E_g$  is determined by the particle settling velocities  $U_p$  and bubble rise velocities  $U_b$ , as described as<sup>7</sup>,

$$E_g = \frac{U_p/U_b}{1+U_p/U_b} \quad \text{Eq. 2.5}$$

As for the interception part, it is based on the assumption that only the particle that is close enough to the bubble can be collected. Thus, the sizes of bubbles and particles play important roles here. And the  $E_s$  is obtained by<sup>8</sup>,

$$E_s = \frac{3d_p}{d_b} \quad \text{Eq. 2.6}$$

where  $d_p$  and  $d_b$  denote diameters of the particle and bubble, respectively.

The inertia effect is dependent on the Stokes number  $K_{Stokes}$ , and  $E_i$  is described as<sup>9</sup>:

$$E_i = \left( \frac{K_{Stokes}}{K_{Stokes}+0.2} \right)^2 \quad \text{Eq. 2.7}$$

And the Stokes number  $K_{Stokes}$  can be calculated by<sup>10</sup>,

$$K_{Stokes} = \left( \frac{\rho_p U_b d_p^2}{9\eta d_b} \right)^2 \quad \text{Eq. 2.8}$$

where  $\rho_p$  is the particle density, and  $\eta$  is the liquid dynamic viscosity.

Note that the inertial forces have ignorable effects on the collision efficiency when  $K_{Stokes} \ll 1/12$ .

In order to quickly calculate the colloid efficiency, a simple model has been proposed as<sup>11</sup>,

$$E_c = \frac{U_b/U_p}{1.02568U_b/U_p+0.74057} \quad \text{Eq. 2.9}$$



But it has to be mentioned that this simple model only works when  $0.4 \leq U_b/U_p \leq 25$ .

### 2.1.2.2 Collision forces

During the collision process, there are at least four components in the total collision force, i.e., inertial (including added mass), drag, micro-hydrodynamic, and gravity forces<sup>12</sup>. Those forces can vary with the changes of the relative positions of particles and bubbles, requiring the particle trajectories to be determined first. The shortest distance between particle and bubble ( $\delta$ ), the radial position of particle center ( $r$ ), and polar angle of particle center measured from vertical ( $\varphi$ ) can be determined by the following equations obtained from the Basset-Boussinesq-Oseen equation<sup>13</sup>:

$$\frac{dv_\delta}{dt} = \frac{v_\varphi^2}{r} - \frac{f_r v_\delta + v_s \cos \varphi}{\tau} + \Delta \quad \text{Eq. 2.10}$$

$$\frac{dv_\varphi}{dt} = -\frac{v_\delta v_\varphi}{r} - \frac{f_t v_\varphi - v_s \sin \varphi}{\tau} \quad \text{Eq. 2.11}$$

$$\frac{d\delta}{dt} = v_\delta = v_r \quad \text{Eq. 2.12}$$

$$\frac{d\varphi}{dt} = \frac{v_\varphi}{r} \quad \text{Eq. 2.13}$$

where,  $r = R_b + \delta + R_p$ ,  $\tau \equiv \frac{R_p^2(2\rho_p + \rho_f)}{9\mu}$ ,  $\mathbf{v}_s \equiv \frac{2R_p^2(\rho_p - \rho_f)}{9\mu} \mathbf{g}$ ,  $\Delta = \left(\frac{\delta_{crit}}{\delta}\right)^{200}$ , and  $t$  denotes time,  $\tau$  the viscous relaxation time,  $v_i$  velocities in the  $i$ -direction,  $v_s$  Stokes velocity,  $\Delta$  contact force,  $\delta_{crit}$  gap at which the repulsion becomes important,  $\mu$  dynamic viscosity,  $\rho_i$  density of particle ( $i=p$ ) or fluid ( $i=f$ );  $f_r$  and  $f_t$  are drag correction functions for the radial and tangential directions, respectively.

The components of the four forces are summarized in Table 2.1<sup>13</sup>.

**Table 2.1** The components of the four forces<sup>13</sup>

Force	Radial component	Tangential component
Inertia and added mass, $F_{i,IAM}$	$m_* \left( \frac{dv_\delta}{dt} - \frac{v_\varphi^2}{r} \right)$	$m_* \left( \frac{dv_\varphi}{dt} + \frac{v_\delta v_\varphi}{r} \right)$
Stokes drag, $F_{i,Stokes}$	$6\pi\mu R_p v_\delta$	$6\pi\mu R_p v_\varphi$
Microhydrodynamic drag, $F_{i,MHD}$	$(f_r - 1)6\pi\mu R_p v_\delta$	$(f_t - 1)6\pi\mu R_p v_\varphi$
Gravity, $F_{i,grav}$	$(m_p - m_f)g \cos(\varphi)$	$-(m_p - m_f)g \sin(\varphi)$

Note:  $m_i$  denotes the mass of particle ( $i=p$ ) or fluid ( $i=f$ ),  $m_* = m_p + m_f/2$

### 2.1.3 Attachment

After the collision, it is the attachment process, i.e., liquid film thinning and rupture, which is a prerequisite for the formation of the bubble-particle aggregate in flotation. The stability of the liquid film dominates the entire attachment. Researchers have done massive work to understand the attachment process by utilizing diverse instruments, designing experiments, proposing theoretical models and mechanisms. Follows are the details that have been done so far.

#### 2.1.3.1 Bubble-solid interaction forces

##### 2.1.3.1.1 Hydrodynamic force

When a curved surface is moving towards a flat surface at a low Reynolds number, as shown in Figure 2.4, the liquid flow can be considered to follow the Reynolds lubrication approximation.

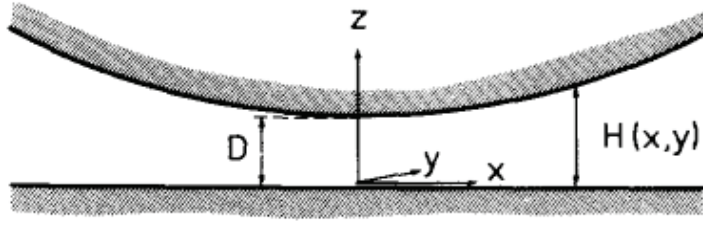


**Figure 2.4** A coordinate system between a curved surface and a flat surface<sup>14</sup>, reprinted with permission.

The momentum in the velocity field  $\mathbf{v}_T$  of a liquid with a shear viscosity  $\eta$  is obtained by,

$$\eta \frac{\partial^2}{\partial z^2} \mathbf{v}_T = \nabla_T p \quad \text{Eq. 2.14}$$

where  $p$  is the pressure in the liquid film. And  $\mathbf{v}_T = (v_x, v_y)$ ,  $\nabla_T = [\hat{x} \left( \frac{\partial}{\partial x} \right), \hat{y} \left( \frac{\partial}{\partial y} \right)]$ .

Under the conditions of  $\mathbf{v}_T = 0$  at  $z=0$  and  $z=H(x, y)$ , one can integrate the equation and get:

$$\mathbf{v}_T = \frac{1}{2\eta} z [z - H(x, y)] \nabla_T p \quad \text{Eq. 2.15}$$

Considering the equation of continuity  $\frac{\partial v_z}{\partial z} = -\nabla_T \cdot \mathbf{v}_T$ , the Eq.2.15 can be integrated under the conditions of  $v_z=0$  at  $z=0$ , and one can obtain:

$$v_z = -\frac{1}{2\eta} \nabla_T \cdot \left\{ \left[ \frac{1}{3} z^3 - \frac{1}{2} z^2 H(x, y) \right] \nabla_T p \right\} \quad \text{Eq. 2.16}$$

Regarding  $v_z$  as  $dH/dt$ , and one can obtain,

$$\frac{dH}{dt} = \frac{1}{12\eta} \nabla_T \cdot [H^3(x, y) \nabla_T p(x, y)] \quad \text{Eq. 2.17}$$

This equation can get the pressure as long as the velocity and  $H(x, y)$  are known. Here,  $H(x, y) = D + r^2/2R$ ;  $R$  is the radius of the liquid film, and  $r^2 = x^2 + y^2$ . Combining  $H(x, y)$  with Eq. 2.17, one can obtain:

$$\frac{dH}{dt} = \frac{1}{12\eta} \frac{1}{r} \frac{d}{dr} \left[ r H^3(r) \frac{dp(r)}{dr} \right] \quad \text{Eq. 2.18}$$

Eq. 2.18 can be further integrated under the conditions that  $dp/dr$  is finite at  $r=0$ ,

$$p(r) = p(\infty) - \frac{3\eta R}{H^2(r)} \frac{dH}{dt} \quad \text{Eq. 2.19}$$

By under the conditions of  $H \ll R$ , one can integrate the total pressure across the entire area and get the hydrodynamic force<sup>15</sup>:

$$F_h = \frac{6\pi\eta R^2}{H} \frac{dH}{t} \quad \text{Eq. 2.20}$$

### 2.1.3.1.2 van der Waals force

The van der Waals force is one of the two essential components in the classical DLVO theory. It defines the interatom interaction, including universal London dispersion force, Keesom orientation dipole-dipole force, and Debye induction interaction. The first force is universally present, while the last two are just for polars. In flotation, during the thinning of liquid films, the London dispersion force is in a short-range (usually less than 10nm). In the case of a sphere approaching towards a planar, the van der Waals interaction force is derived as<sup>69</sup>:

$$F_{vdw} = -\frac{2AR^3}{3(2R+D)^2D^2} \quad \text{Eq. 2.21}$$

where A denotes the Hamaker constant, R the sphere radius, D the distance between the sphere and the planar.

Eq. 2.21 can derive the following equation, based on the relative size of the sphere and planar:

$$F_{vdw} = \begin{cases} -\frac{AR}{6D^2}, & \text{for } D \ll R \\ -\frac{2AR^3}{3(2R+D)^4}, & \text{for } D \gg R \end{cases} \quad \text{Eq. 2.22}$$

In order to calculate van der Waals force, the key is to find the Hamaker constant A. And a non-retarded Hamaker constant for two macroscopic phases 1 and 2 interacting in a medium 3 can be calculated by,

$$A_{total} \approx \frac{3}{4} \kappa T \left( \frac{\varepsilon_1 - \varepsilon_3}{\varepsilon_1 + \varepsilon_3} \right) \left( \frac{\varepsilon_2 - \varepsilon_3}{\varepsilon_2 + \varepsilon_3} \right) + \frac{8h\nu_e}{8\sqrt{2}} \frac{(n_1^2 - n_3^2)(n_2^2 - n_3^2)}{(n_1^2 + n_3^2)^{\frac{1}{2}}(n_2^2 + n_3^2)^{\frac{1}{2}}[(n_1^2 + n_3^2)^{\frac{1}{2}} + (n_2^2 + n_3^2)^{\frac{1}{2}}]} \quad \text{Eq. 2.23}$$

where  $\varepsilon$  denotes the dielectric constant, n refractive index,  $\nu_e$  absorption frequency.

Notably, for the solid 1 and bubble 2 in a liquid 3, the Hamaker constant is  $A_{132}$ . If the individual Hamaker constant A can be extracted from the literature,  $A_{132}$  can be obtained by a combining law:

$$A_{132} = (\sqrt{A_{11}} - \sqrt{A_{33}})(\sqrt{A_{22}} - \sqrt{A_{33}}) \quad \text{Eq. 2.24}$$

where  $A_{11}$ ,  $A_{22}$ , and  $A_{33}$  are Hamaker constants of air, solid, and water, respectively.

In most flotation cases,  $A_{11}$ ,  $A_{22}$ , and  $A_{33}$  follow a sequence of  $A_{11} < A_{33} < A_{22}$ . Thus the  $A_{132}$  is negative. Therefore the total van der Waals force will be positive (or repulsive), which is detrimental to the particle-bubble aggregate.

### 2.1.3.1.3 Electrical double-layer force

The electrical double-layer force, together with the van der Waals force, forms the classical DLVO theory. The electrical double-layer force depends on the surface charge and the Debye length. Generally, a surface in a liquid is not neutrally charged. The surfaces in a liquid can carry charges in three mechanisms: a). The ionization and/or dissociation of surface components; b). The adsorption of ions in the solution; c). Charges transfer from one surface to the other. Since the surface is charging, its co-ions will be balanced by the counterions, forming an inner Stern layer (specifically adsorbed by the surface in the plane  $\delta$ ) and a Diffuse layer, also known as the diffuse electric double-layer. The potential at the boundary plane  $\delta$  is known as the Zeta ( $\zeta$ ) potential, which can be easily measured and approximately equal to the surface potential<sup>69</sup>.

Debye length ( $\lambda_D$ , or  $\kappa^{-1}$ ) shows how far the electrostatic effect of a charge carrier can persist. The magnitude of the electric potential will decrease by 1/e every one  $\kappa^{-1}$ . And  $\kappa^{-1}$  is calculated by,

$$\kappa^{-1} = \sqrt{\frac{\epsilon_r \epsilon_0 k_B T}{2 \times 10^3 N_A e^2 I}} \quad \text{Eq. 2.25}$$

where  $I$  is the ionic strength of the electrolyte and  $I = \frac{1}{2} \sum_{i=1}^n c_i z_i^2$ ,  $c$  is the molar concentration, and  $z$  is the ion charge number. And  $\epsilon_0$  denotes the permittivity of free space,  $\epsilon_r$  the dielectric constant,  $k_B$  the Boltzmann constant,  $T$  the temperature,  $N_A$  the Avogadro number,  $e$  the elementary charge.

Following the Hogg-Healy-Fuerstenau approximation rule, the electrical double-layer force can be obtained by,

$$F_{edl} = \frac{\epsilon_0 \epsilon \kappa^2}{2} \frac{2\psi_1 \psi_2 \cosh(\kappa h) - \psi_1^2 - \psi_2^2}{\sinh^2(\kappa h)} \quad \text{Eq. 2.26}$$

where  $\epsilon$  denotes the dielectric constants of the medium (water in this case),  $\epsilon_0$  the dielectric constants of vacuum,  $\psi_1$  and  $\psi_2$  the surface potentials of the air bubble and the particle.

It is worth noting that, similar to the van der Waals force, the electrical double-layer force is also varying with the shapes of the bodies of interest. For the sphere near a flat surface, the electrical double-layer force between two similar objects is described as,

$$F_{edl} = \kappa R Z e^{-\kappa D} \quad \text{Eq. 2.27}$$

where  $R$  is the sphere radius,  $D$  the distance between two bodies. And  $Z$  is constant of interaction, depending only on the surfaces' properties and calculated by,

$$Z = 64\pi\epsilon_0\epsilon \left(\frac{kT}{e}\right)^2 \tanh^2\left(\frac{ze\psi_0}{4kT}\right) \quad \text{Eq. 2.28}$$

where  $\psi_0$  is the surface potential of the object.

In flotation, the air bubble is carrying negative charges. However, the sign of the charge on the particle surfaces can be modified by adjusting the slurry conditions, making the electrical double-layer force to be selectively positive or negative.

#### 2.1.3.1.4 Hydrophobic force

It has been found that the liquid films between air bubbles and hydrophobic surfaces tend to rupture easily; even the DLVO theory suggests the van der Waals force and the electrical double-layer force are both repulsive<sup>16</sup>. This weird phenomenon has attracted researchers' interest and has been explained by different theories, especially the so-called hydrophobic force. Although the existence of hydrophobic force is still under debate, the popular models are summarized here for a fair comparison.

Initially, according to the magnitude of the measured attractive force, a single exponential function of the hydrophobic force is suggested to be<sup>17</sup>:

$$\frac{F}{R} = C_0 \exp\left(-\frac{H}{D_0}\right) \quad \text{Eq. 2.29}$$

where F denotes the force measured between two curved surfaces with the radius of curvature R, H the closest separation distance, D<sub>0</sub> the decay length, and C<sub>0</sub> a fitting constant.

The single exponential function is suitable for less hydrophobic surfaces, whose contact angle is smaller than 90°. As stronger hydrophobic interactions had been measured on a surface with a contact angle of larger than 90°, a more frequently-used double-exponential function was then proposed<sup>17</sup>,

$$\frac{F}{R} = C_1 \exp\left(-\frac{H}{D_1}\right) + C_2 \exp\left(-\frac{H}{D_2}\right) \quad \text{Eq. 2.30}$$

Here D<sub>1</sub> is in the range of 1-2nm, which is the same as D<sub>0</sub>. However, D<sub>2</sub> is in the range of 3-24nm.

Significantly for the bubble-flat surface attachment, Pan et al. modified the double-exponential function to define the pressure caused by the hydrophobic force<sup>18</sup>:

$$\Pi_h = \frac{C_1}{2\pi D_1} \exp\left(-\frac{H}{D_1}\right) + C_2 \exp\left(-\frac{H}{D_2}\right) \quad \text{Eq. 2.31}$$

It has been well-accepted that a power law might describe the hydrophobic force<sup>19</sup>,

$$\frac{F}{R} = -\frac{K}{6H^2} \quad \text{Eq. 2.32}$$

where K is the force constant. When it comes to an air bubble and KEX-coated surface system, K is fit to be  $7.2 \times 10^{-18} \text{ J}^{19}$ .

Apart from these models, Shi et al. proposed another approach to characterize the hydrophobic force from the perspective of interaction free energy<sup>20</sup>. For the nonsymmetric interactions between air bubbles and hydrophobized mica surfaces, the interaction free energy is,

$$W_H(h) = -C \exp\left(-\frac{h}{D_H}\right) \quad \text{Eq. 2.33}$$

where  $h$  is the distance between air bubbles the solid surfaces.  $D_H$  denotes the decay length, and  $C$  is another parameter, calculated by

$$C = \gamma + \gamma_{SW} - \gamma_{SA} \quad \text{Eq. 2.34}$$

Thus the hydrophobic force is calculated by,

$$\Pi_H = -\frac{dW_H}{dh} \quad \text{Eq. 2.35}$$

In the meantime, according to the famous Young's Equation:

$$\gamma_{SA} = \gamma_{WA} \cos\theta + \gamma_{SW} \quad \text{Eq. 2.36}$$

where  $\gamma_{WA}$ ,  $\gamma_{SA}$ ,  $\gamma_{SW}$  denote the interface energies for water-air, soild-air, and soild-water, respectively.  $\theta$  is the contact angle.

Combining the above equations, obtain the hydrophobic force can be obtained:

$$\Pi_H = -\left[\frac{\gamma_{WA}(1-\cos\theta)}{D_H}\right] \exp\left(\frac{-h}{D_H}\right) \quad \text{Eq. 2.37}$$

In their experiments, the decay length  $D_H$  is dependent on the hydrophobicity of the solid surface. When the contact angle is  $45^\circ$ ,  $D_H$  is  $0.8 \pm 0.1$  nm, while it becomes  $1.0 \pm 0.1$  nm when the contact angle increases to  $90^\circ$ . This equation and the single exponential function turn to possess a similar decay length.

On the other hand, other researchers believe the attraction might be due to cavity bridging, nanobubble/microbubble/submicrobubble bridging, the water structure near the solid surface, and electrostatic interactions between two patches oppositely charged, as detailed in the following section.

Gas cavities are formed due to the liquid film metastability during the approaching of one surface towards the other<sup>21</sup>. The existence of gas cavities can be proved by the changing of the refractive index and by the observation via AFM<sup>22</sup>. The liquid film's metastability might come from the sudden change of pressure caused by the surface asperity, the contamination, or the dissolved gas.

Nanobubble/microbubble/submicrobubble bridging is another critical hypothesis. Although the solubility of air in water is small, the dissolved air is still existing in the slurry. Zhang et al. successfully imaged the nanobubbles<sup>23,24</sup>. And the attraction can be fitted by the theoretical models based on the vapor bridging<sup>25,26</sup>. After the degassing

process, the measured hydrophobic forces are significantly decreased. But the hydrophobic forces are still detected, indicating that the nanobubble may not be the only reason for the hydrophobic attraction. Still, it does intensify the force to a long-range<sup>27</sup>. Faghiehnejad et al. suggested that the microbubbles and submicrobubbles are reasons why the long-range (hundreds of nanometers) hydrophobic forces exist, while nanobubbles are responsible for the short-range (several nanometers) hydrophobic force<sup>28</sup>.

Besides, the arrangement of water molecules near the solid changes with the surface hydrophobicity<sup>29</sup>. The water density near a hydrophobic surface is relatively smaller than that near a less hydrophobic surface. A low water density corresponds to a sparse bulk hydrogen bonding network, which is readily disturbed<sup>30</sup>. Work done by employing the sum-frequency vibrational spectroscopy (SFVS) confirms the water structure difference near different hydrophobic surfaces<sup>31-33</sup>.

In most flotation cases, the surfaces of both air bubbles and particles are not free of surfactants and ions, which will inevitably lead to adsorption in the form of patches, islands, or clusters<sup>34</sup>. When the patches are charged, the electrostatic interactions might be present during the thinning of the liquid films. Many researchers have studied the relation between the surface potential and the added surfactant, and the enhanced hydrophobic forces were observed with increasing surface charges by surfactant patches<sup>35,36</sup>. However, when adding the electrolyte to suppress the electric double-layer, the hydrophobic forces are not changing as predicted<sup>37</sup>, leaving the charged patch hypothesis less convincing.

### 2.1.3.2 Theoretical modes

#### 2.1.3.2.1 Stefan–Reynolds Model

Different models have been developed to understand the bubble-particle interaction in the context of flotation. The most important one is the Stefan-Reynolds model, which refers to the drainage of the liquid film between two immobile surfaces<sup>18</sup>. As the bubble approaches towards a flat surface, the film thinning velocity is,

$$\frac{\partial h}{\partial t} = -\frac{1}{12\mu r} \frac{\partial}{\partial r} \left( r h^3 \frac{\partial p}{\partial r} \right) \quad \text{Eq. 2.38}$$

where  $p$  denotes the hydrodynamic pressure,  $t$  time,  $h$  film thickness,  $\mu$  viscosity, and  $r$  the radial distance from the film center. After integrating the Eq. 2.38 twice under the conditions of  $p=0$  when  $r=\infty$ , and  $\partial p / \partial r=0$  when  $r=0$ , one can get,

$$\frac{dh}{dt} = \frac{2h^3 p}{3\mu R^2} \quad \text{Eq. 2.39}$$

where  $R$  denotes the film radius and  $p$  is the normal pressure balance along with a horizontal film based on that the flat film and no-slip boundary and described as,

$$p = p_\sigma - \Pi \quad \text{Eq. 2.40}$$



where  $p\sigma = 2\sigma/R$  is the capillary pressure ( $\sigma$  is the surface tension),  $R$  the film radius, and  $\Pi$  the total disjoining pressure.

Thus the film thinning velocity is described as,

$$\frac{dh}{dt} = -\frac{2h^3}{3\mu R^2} (p\sigma - \Pi) \quad \text{Eq. 2.41}$$

### 2.1.3.2.2 Modified Stefan–Reynolds Model

When the liquid film is between one immobile surface and one mobile surface, the model is accordingly modified as<sup>3</sup>,

$$\frac{dh}{dt} = -\frac{8h^3}{3\mu R^2} (P\sigma - \Pi) \quad \text{Eq. 2.42}$$

Experimental data show that surfactants can change the condition of an immobile surface to a mobile surface. That is to say, at a high surfactant concentration, a good agreement between the theoretical and experimental data can be obtained using the modified Stefan–Reynolds model. However, at low surfactant concentrations, both models will work.

### 2.1.3.2.3 Hydrodynamic model

Horn et al.<sup>38</sup> assumed the inertia and surface forces are negligible, and then they proposed the hydrodynamic force  $F_h$  is balanced by the restoring force  $F_k$  of the spring of the surface force apparatus, as shown:

$$F_h = F_k = k\Delta \quad \text{Eq. 2.43}$$

where  $\Delta$  is the deflection of the spring, whose spring constant is  $k$ .

Using  $L(t)$  as the position of the spring's distal end, one can obtain the relation between the film thickness  $h(t)$  and the spring deflection:

$$h(t) = \Delta(t) + L(t) \quad \text{Eq. 2.44}$$

And the distal end was driven at a constant speed  $V$  for a time  $t_s$ ; therefore  $L(t)$  is calculated by,

$$L(t) = \begin{cases} h_0 + Vt, & \text{for } 0 < t < t_s \\ h_0 + Vt_s, & \text{for } t \geq t_s \end{cases} \quad \text{Eq. 2.45}$$

where  $h_0$  is the initial separation.

Then the force can be extracted as,

$$F_h = \begin{cases} k(h - h_0 - Vt), & \text{for } 0 < t < t_s \\ k(h - h_0 - Vt_s), & \text{for } t \geq t_s \end{cases} \quad \text{Eq. 2.46}$$

Thus the separation can be resolved as long as the force is known.

When combining Eq. 2.44, 2.45, and 2.46, one can obtain the equation of motion:

$$-\frac{6\pi\eta R_g R_h}{kh} \frac{dh}{dt} f^* = \begin{cases} k(h - h_0 - Vt), & \text{for } 0 < t < t_s \\ k(h - h_0 - Vt_s), & \text{for } t \geq t_s \end{cases} \quad \text{Eq. 2.47}$$

One can solve the above equation numerically to obtain  $h(t)$ . Note that for the no-slip boundary conditions,  $f^*$  is equal to 1.

### 2.1.3.3 Experimental approaches

#### 2.1.3.3.1 Induction timer

Induction time ( $t_i$ ) is the minimum time need for the liquid film to drain to a critical rupture distance before rupture<sup>39</sup>. In the meantime, the sliding contact time ( $t_{con}$ ) is introduced as the time needed for a particle to slide along a bubble without significantly deforming the local bubble surface. Only when  $t_i$  is shorter than  $t_{con}$ , the attachment can occur. It is found that many factors can affect the  $t_i$ , mainly including particle sizes, particle properties, bubble sizes, particle composition, mineral liberation, etc<sup>40</sup>. Since the induction time is a complete result of the chemistry and hydrodynamics of the system, it provides kinetic information and is regarded as a better characterization of flotation than the thermodynamic quantified contact angle<sup>41</sup>.

On the other hand, however, instead of the direct utilization of a high-resolution camera to record the contact time of a bubble approaching a mineral surface, researchers alternatively use the critical time required for more than half of the experiments where the air bubble can pick particles up from a bed of particles as the induction time<sup>41</sup>, as shown in Figure 2.5. In the quartz-amine system, induction time decreased with increasing collector dosage and electrolyte concentration. And in the air bubble-bitumen attachment system, the induction time was long in process water in the presence of calcium ions<sup>42</sup>.

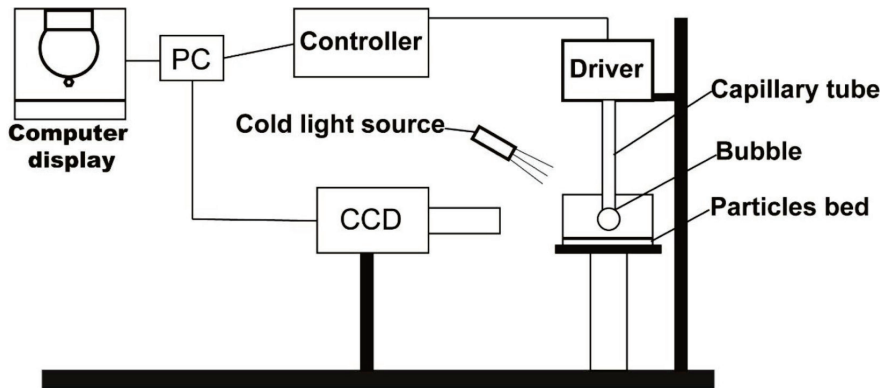


**Figure 2.5** An induction timer used by Li et al.,<sup>43</sup> reprinted with permission.

Besides, thanks to the development of high-resolution cameras, researchers can directly record the attachment process, including the induction time and contact time. A typical schematic is provided in Figure 2.6.

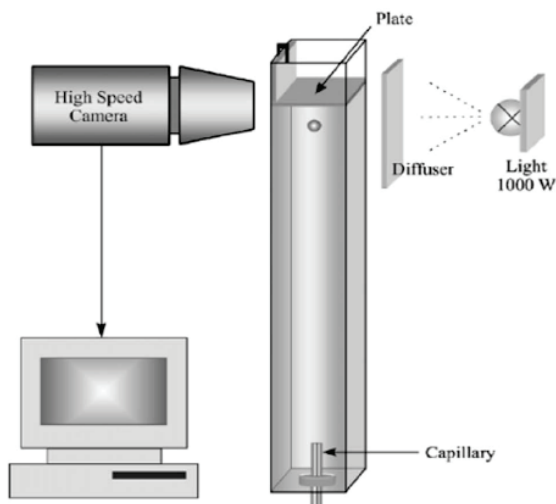


**Figure 2.6** A high-speed camera recording the rising of an air bubble to a solid surface<sup>44</sup>, reprinted with permission.

Another advantage of the high-resolution camera is that it can also directly visualize the shapes of both particles and air bubbles, allowing to conveniently investigate the effect of particle shape, roughness, and the deformation of air bubbles. However, the quality of the analysis is dependant on the best resolution the camera can reach. The results can be tricky if the image quality is not as well as one expects.

#### 2.1.3.3.2 Three dimensional (3D) imaging

The 3D imaging of liquid films can be obtained by calculating the interferogram patterns, which is similar to Newton's rings<sup>45</sup>. As shown in Figure 2.7, a bubble was generated by a capillary syringe, and it was driven towards the experimental cell substrate, confining a layer of thin liquid film between the bubble and the substrate. A polychromatic light beam went through the liquid film from the top, and the reflection beam signals were collected by the objective in a formation of interferogram patterns. The patterns were then processed to release the thickness results of the liquid films. Note that there is a pressure transducer inside the tube, whose purpose is to monitor the pressure. Using this device, the effect of heterogeneities of the film surface can be studied. However, its main limitation is that it can only be used to measure the movements in a tangential direction.

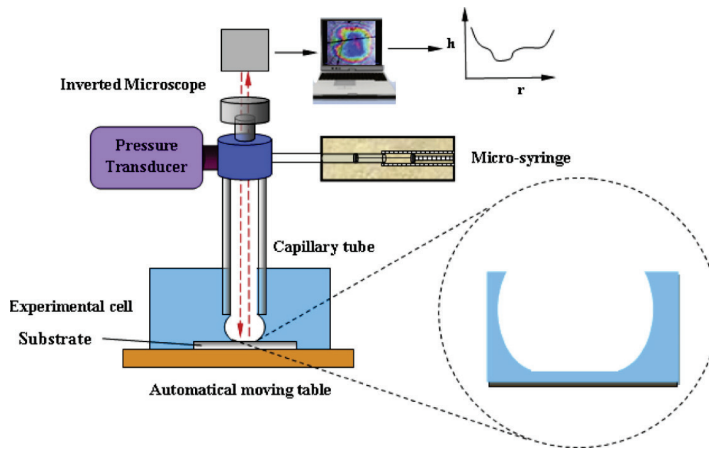


**Figure 2.7** A 3D imaging set-up of thin liquid film<sup>45</sup>, reprinted with permission.

### 2.1.3.3.3 Surface forces apparatus (SFA)

SFA was firstly invented by Winterton et al.<sup>46</sup> and Israelachvili<sup>47</sup> 50 years ago. The separation between two mica surfaces in water is measured by the optical multiple-beam interferometry. SFA allows the detection of tiny surface forces, including van der Waals, electrostatic double-layer, and so-called hydrophobic forces. Despite the fact that SFA can provide accurate force results, it possesses a primary limitation, which is that it can measure the forces between transparent flat materials<sup>48</sup>. Plus, the distance is inferred from the force measurements instead of the direct characterization. Later, Horn et al.<sup>49</sup> measured film thicknesses between air bubbles and flat mica surfaces (Figure 2.8) via a modified SFA. The light source here is the white light, whose interferometry patterns allow the determination of the zero-order of the film thickness. This is crucial for the measurement of the absolute thickness of the liquid films, especially in the case when the air bubble is deformed and exhibits a flat surface at the terminal stage of the film drainage process.

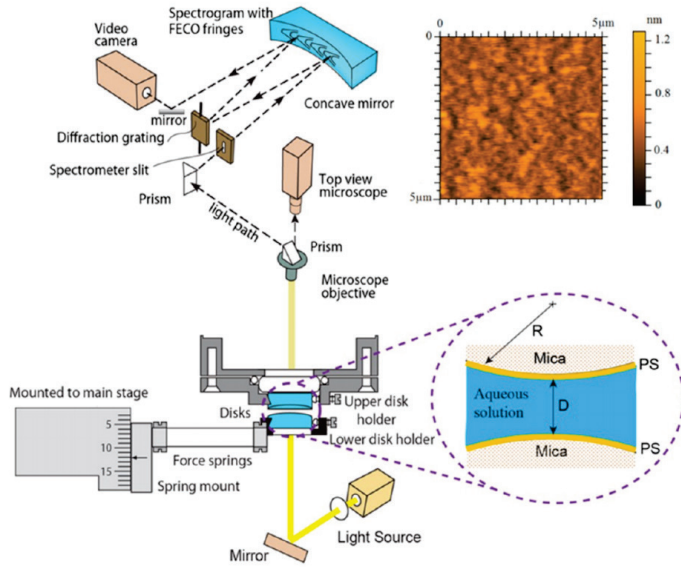


**Figure 2.8** A schematic of SFA<sup>50</sup>, reprinted with permission.

#### 2.1.3.3.4 Atomic Force Microscopy (AFM)

Invented in 1986<sup>51</sup>, AFM was first used to study the bubble-particle attachment in 1994 by Butt<sup>52</sup>. A sharp probe is attached to the end of a microcantilever (with a known spring constant) in a typical AFM. During the test process, the probe is driven towards the sample so that its tip will scan the surface. When an interaction between the tip and the sample appears, the cantilever will deform, detected by a laser beam focusing on the cantilever. Then the interaction can be calculated by Hooke's law. When air bubbles are attached to the cantilever, the bubble-particle attachment can be studied by AFM, as shown in Figure 2.9. Likewise, Ducker et al. changed the relative positions of the air bubble and the solid surface and also were able to measure the interaction in the air bubble-mineral system<sup>53</sup>.

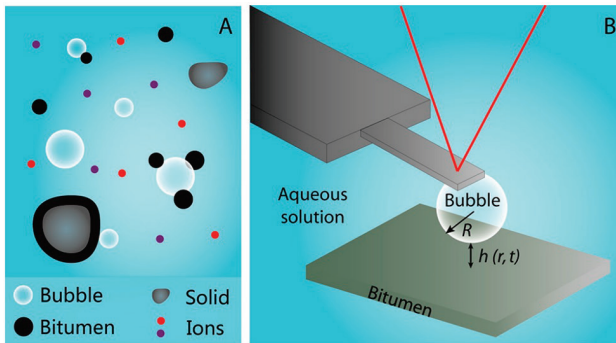


**Figure 2.9** Schematic of the AFM to investigate the bubble-particle attachment<sup>54</sup>, reprinted with permission.

Despite the fact that AFM is a powerful tool with so many advantages such as flexibility, small contact area, and simple configuration, it has its own limitations. Foremost, it is difficult to determine the correct order of the interferometry, given the formed bubbles. This limitation makes the AFM be a semi-quantitative technique to build the evolution of the thinning of liquid films. Due to the presence of surface forces and hydrodynamic effect<sup>55</sup>, the bubble can deform, and we can assume the air bubble deforms as a Hookean spring, which gives the actual distance as,

$$D = -z + \frac{d+interpret}{slope} + D_c \quad \text{Eq. 2.48}$$

where  $z$  denotes the displacement of the AFM piezo,  $d$  the cantilever's deflection,  $D_c$  the distance of rupture.

### 2.1.3.3.5 Reflection Interference Contrast Microscope (RICM)

RICM was initially developed in bioscience in 1964, employing monochromatic, polarized light to form the interference pattern of an object on a plane glass surface<sup>56</sup>. A schematic is provided in Figure 2.10 (a) to illustrate the principle.

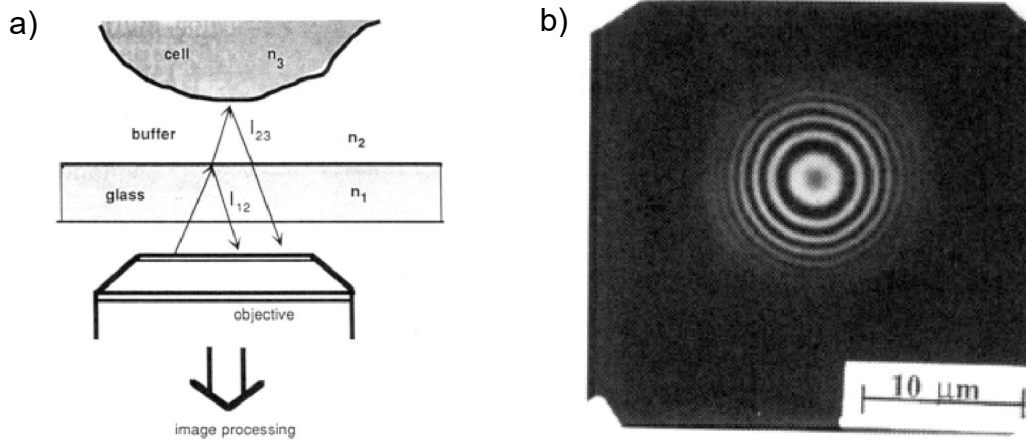


**Figure 2.10** Schematic and outcome of RICM<sup>57</sup>, reprinted with permission.

The sample is illuminated from the bottom, and then reflections occur at the glass surface and the basal cell membrane surface, resulting in  $I_{12}$  and  $I_{23}$ , respectively. The interference of  $I_{12}$  and  $I_{23}$  will form an interference pattern, as shown in Figure 2.10 (b). Note that the reflection at an interface from a medium of a higher optical density causes a phase shift ( $\delta$ ) of the light. In comparison, it does not occur at an interface with a lower optical density. The intensity ( $I$ ) on the RICM pattern is a function of the wavelength-dependent distance ( $\lambda \times d$ ), as shown here,

$$I(h(x,y), \lambda) = I_{12} + I_{23} + 2\sqrt{I_{12}I_{23}} \cos \left[ \frac{4\pi n_2 h(x,y)}{\lambda} + \delta \right] \quad \text{Eq. 2.49}$$

where  $h(x,y)$  denotes the distance at a specific position with the lateral position  $x$  and  $y$ ,  $I$  the resultant intensity,  $n_2$  the refractive index of the medium,  $\lambda$  the wavelength.

There are three main advantages of RICM: Firstly, the simplicity of the setup in comparison with other interferometric techniques; Secondly, the high lateral and out-of-plane resolutions; Lastly, the suitability for dynamic measurements<sup>58</sup>. However, there is an essential concern for RICM: the measurement of the absolute film thickness. Monochromatic wavelength interferometry could determine the film thickness only up to  $n\lambda/2$ , where  $n$  is unknown. Researchers employ dual-wavelength to obtain the absolute thickness of liquid films<sup>59</sup> by introducing an additional periodicity and boundary condition. This enables the measurement of absolute distances with an accuracy of 3 nm within a separation length of 0-0.8 $\mu\text{m}$ <sup>59</sup>. However, in flotation, the attachment of the particle to the air bubble can reach a range of micrometers, which is beyond the precision of the DW-RICM. Thus more work should be done here.

### 2.1.3.3.6 Combining the force measurement and film thickness measurement

The combination of AFM and RICM was first developed to study the mechanical properties of polyelectrolyte multilayer capsules, which allows the measurement of the interaction forces and the deformation of the soft surfaces<sup>60</sup>. Shi et al. introduced a similar set-up to study the bubble-mica attachment, as shown in Figure 2.11.

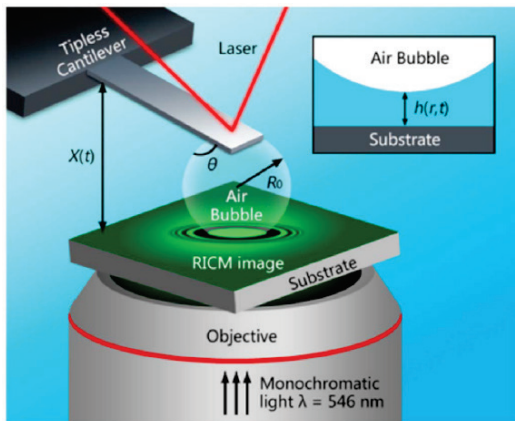


**Figure 2.11** Combined AFM and RICM<sup>20</sup>, reprinted with permission.

The hybrid instrument can release information from both the perspectives of the liquid film profiles and the forces. However, it is regarded as a simple combination of two techniques, still suffering from the individual drawbacks.

In addition, Zhang et al. developed a device called thin liquid film force apparatus (ITLFFA), as shown in Figure 2.12, attempting to measure the force and film profile simultaneously over a broad range of Reynolds numbers (0.01-50).



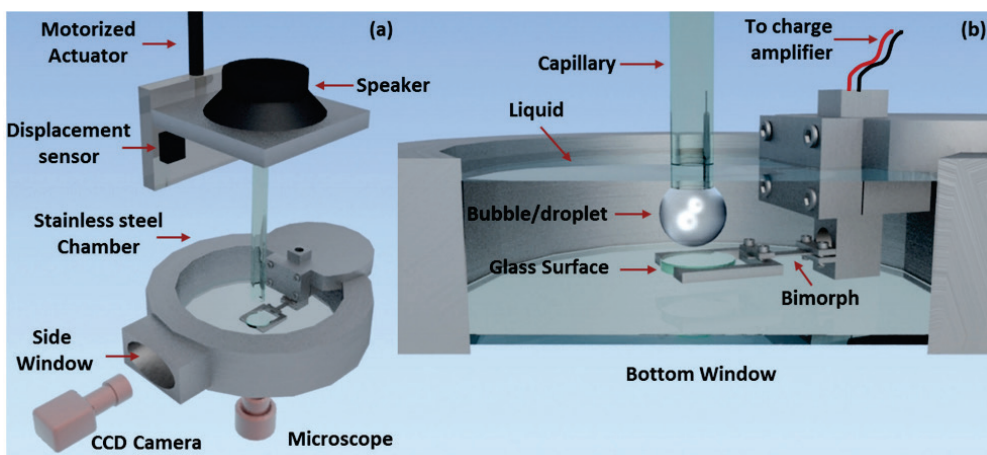


**Figure 2.12** Schematics of the thin liquid film force apparatus (ITLFFA)<sup>61</sup>, reprinted with permission.

ITLFFA has a stainless steel chamber with two windows: one is for the side-view to measure the contact angle and the attachment process, and the other is at the bottom, designed for the light beams to go through. A bimorph is inside the chamber and enclosed by a fluorinated ethylene propylene sheath. The bimorph connects with the transparent disc to detect the forces by recording the disc's position. A second wavelength light is also employed here to determine the zero-order accurately. However, two-wavelength light beams are not synchronized and can be further improved to ensure its reliability.

#### 2.1.3.4 General factors

In general, the factors that may play roles in the stability of liquid films can be summarized here, including surface wettability, roughness, bubble size, gas type, particle shape, approach velocity, and fluid properties (electrolyte concentration, liquid viscosity, temperature, and pressure). The details will be given in this section.

Wettability (hydrophobic or hydrophilic properties) is often related to intermolecular forces. Long-range attraction forces leading to destabilization of the wetting film at hydrophobic solid surfaces have been of particular interest for flotation separation, given that attachment of hydrophobic particles to the bubble is the fundamental step of the flotation process. The crucial process is the thinning and rupture of liquid film between the particle and the bubble<sup>62-65</sup>. The stability of the wetting film can be influenced by surface hydrophobicity: The higher the contact angle was, the larger the critical thickness, and the shorter lifetime of the wetting films had<sup>66,67</sup>. In the flotation of hydrophilic particles, the involved van der Waals force is repulsive. It changes to attractive when the refractive index of the solid is smaller than that of water<sup>68</sup>. If the electrostatic component is also repulsive, the wetting films should be stable, and the attachment of the particle to the bubble surface would not occur. On the other hand, it is well known that the liquid film between two hydrophobic surfaces (for example, the hydrophobic grain and the bubble) is unstable<sup>64</sup>. A widely-accepted concept is that the “hydrophobic interactions”



are attributed to the structural changes of boundary layers of water. The water density adjacent to the hydrophobic surfaces is lower than that in bulk water, called “hydrophobic gap”<sup>69</sup>. While water density close to hydrophilic surfaces is greater than that in bulk water<sup>70</sup>. The thickness of the depletion layer is about 0.2 nm or less<sup>71</sup>. When increasing the attraction between liquid and solid surfaces, the depletion will gradually disappear, indicating intermolecular forces.

In flotation, it is well-accepted that a tiny bubble is beneficial to recovery, which may be due to the increasing probability of collision ( $P_c$ ) of a particle colliding with a bubble with the decreasing size of bubbles. Researchers proposed different models based on bubble sizes:

For large bubble:

$$P_c = \frac{3D_p}{D_b} \quad \text{Eq. 2.50}$$

where  $D_b$  is the bubble size and  $D_p$  the particle size.

For intermediate bubble sizes:

$$P_c = \frac{3}{2} \left[ 1 + \frac{\left(\frac{3}{16}\right)Re^{0.72}}{1+0.249Re^{0.56}} \right] \left(\frac{D_p}{D_b}\right)^2 \quad \text{Eq. 2.51}$$

where  $Re$  is Reynolds Number.

For small bubbles:

$$P_c = \frac{3}{2} \left(\frac{D_p}{D_b}\right)^2 \quad \text{Eq. 2.52}$$

And a dimensionless stream function to derive  $P_c$  is shown here:

$$P_c = \left[ \frac{3}{2} + \frac{4Re^{0.72}}{15} \right] \left(\frac{D_p}{D_b}\right)^2 \quad \text{Eq. 2.53}$$

$P_c$  will increase when bubble size decrease in any equations above. The results agree well with flotation recoveries.

Tiny bubbles of gas nuclei with a size of 1-13.5  $\mu\text{m}$ , also known as picobubbles, naturally are found in liquids<sup>72,73</sup>. Picobubbles tend to easily attach particles compared to large bubbles because picobubbles exhibit relatively small ascending and rebound velocities from solid surfaces. Another reason is that picobubbles possess high surface free energy. Both experimental and practical results have shown that in the presence of tiny bubbles in flotation, the recoveries can be improved<sup>74,75</sup>.

In addition, the attachment of nanobubbles on solid surfaces de stabilizes liquid films. Via AFM, investigators proved that submicroscopic air bubbles are the origin of “hydrophobic interactions”<sup>76</sup>. When degassing the water, the “hydrophobic interactions”

decreased as well, further confirming the nanobubbles are responsible for the TLF instability<sup>77</sup>. Another evidence is that the “hydrophobic interactions” will disappear when the solid surface is hydrophobized without contact with the gas atmosphere<sup>78</sup>.

When changing gas types, the liquid film’s stability will change as well, which might be due to the formation of nanobubbles by nucleation. To quantify the difference in terms of the nanobubble generations between gas types, van Limbeek and Seddon<sup>79</sup> employed AFM to measure the average radii of curvature and diameters of nanobubbles. The amount of nanobubbles follows the order: Argon > Carbon Dioxide > Hydrogen > Oxygen > Helium > Nitrogen > Methane. It is known the solubility order of these gases is: Hydrogen > Helium > Methane > Nitrogen > Oxygen > Argon > Carbon Dioxide. Although opinions are saying the nucleation is related to gas solubility, the results here did not fully support it. And adsorption strength of the various gases is irrelative to nucleation<sup>80</sup>. The nucleation origin by the excess gas swelling the density-depleted layer near an immersed hydrophobic surface may also be not exact<sup>70,81</sup>. There is a lot of work needed to fully understand the role of gas types in nucleation, but at least tons of evidence have shown gas types can affect the nucleation and then the liquid film stability.

Before introducing the effects of other factors, it is necessary to mention the film thinning kinetics based on Stefan-Reynolds equation, which will be discussed later, as shown in Equation 2.54<sup>82</sup>.

$$\frac{dh}{dt} = -\frac{2fh^3\Delta P}{3\eta R_f^2} \quad \text{Eq. 2.54}$$

where  $f$  is one correction coefficient, and it is 4 for the nonsymmetric liquid film having a mobile interface between water and an air bubble, while  $f$  becomes 8 for foam films between two full-slip bubbles;  $h$  is the thickness of the liquid film;  $\Delta p$  is the driving pressure, and in this case, it is the pressure difference between bulk and film phases;  $\eta$  is the liquid viscosity;  $R_f$  is the film radius.

Rough and hydrophobic solid surfaces promote the generation of tiny bubbles by cavitation and film thinning kinetics<sup>83,84</sup>. For the rough solid surface, when the liquid film drains to the highest protrusions, the rupture will suddenly occur<sup>44</sup>. Therefore, the films' probability of rupturing on rough surfaces is significantly higher than that on a flat surface. And with increasing roughness or increasing the size of asperities, the attachment time decreases when an air bubble is approaching a solid surface. Besides, the surface roughness is proven to affect the wettability and the measured contact angle values. For example, for a smooth hydrophobic surface having a contact angle of 120°, the contact angle will increase to 150° as increasing the surface roughness<sup>85</sup>. One possible reason for the higher contact angles at rough hydrophobic surfaces is that the drop edge is “arrested” by the groove borders<sup>86</sup>. Also, the geometric constraint of solid surface results in structural changes of water compared to its bulk properties due to the hydrogen bonding network<sup>87</sup>. Quantitatively, the roughness makes the solid surfaces more hydrophobic, as described by the modified Young’s equation:

$$\cos\theta_w = r \cdot \cos\theta \quad \text{Eq. 2.55}$$

where  $\theta_w$  is the real contact angle, called “Wenzel contact angle”;  $\theta$  is the measured contact angle; and  $r$  is the ratio of real and geometrical areas of the surface, which is greater than 1 for rough surfaces.

As to the particle shape, it is generally accepted that irregular particles contribute to the rupture of liquid films. One evidence can be found in the measurement of induction time. For example, Verrelli et al.<sup>88,89</sup> investigated if the particle size can affect the induction time by a high-speed camera. It turned out that irregular particles achieved an induction time one order less than that of spherical particles. When it comes to flotation, the recovery of particles with sharp edges is higher than that of regular particles<sup>90</sup>.

A high liquid viscosity will engender a slow thinning speed. Another phenomenon related to liquid viscosities is called “apparent” slippage of the liquid over the hydrophobic surface. The origin of the slippage effect may be a decrease of liquid viscosity when it is near the solid surface. The viscosity reduction is due to the change in the structure of the liquid itself and is usually associated with the enhanced nucleation close to the hydrophobic surface<sup>91</sup>.

Approach velocity is one of the critical parameters that dominate the drainage process of liquid films, mainly by affecting the hydrodynamic forces. At a low approach speed within 100  $\mu\text{m}$ , there is barely a deformation of the bubble/drop. Traditionally, researchers use the Reynolds number to characterize the hydrodynamics instead of approach velocity. When  $\text{Re} > 50$ , apparent bubble deformations will occur. By measuring the interaction forces and spatiotemporal film thickness simultaneously, one can predict the first occurrence of the dimple and obtain the function showing how  $\text{Re}$  affects the drainage of liquid films<sup>92</sup>. TLFs formed when the bubble interacts with the hydrophilic silica surface reached the same equilibrium thickness (130nm) no matter what approaching speed was used. Approaching speed can only affect the shape of the TLFs and the required time to reach the final states but does not influence the stability of TLFs.

Electrolyte concentration mainly affects the thickness of the electrostatic double layer. As the increase of electrolyte concentration, the electrostatic double layer will be suppressed. In pure water, Debye Length ( $k^{-1}$ ) is  $10^{-6} \text{ m}$ <sup>93</sup>. However, in the 0.01 M NaCl solution,  $k^{-1}$  becomes 3.04nm<sup>68</sup>, significantly decreasing the contribution of electrostatic double-layer interaction during the drainage of liquid films. By recording the spatiotemporal profiles of liquid films, investigators found the electrolyte concentration had no effect on the draining rate at the initial thinning stage. However, as the films continued thinning, the barrier rim in 0.1 M KCl solution quickly reached the lower height, which led to a narrow pathway for the center liquid to drain, causing a longer time to get an equilibrium state. In addition, the equilibrium thickness of the liquid film in 0.1 M KCl solution is 17nm, obviously smaller than 130 nm in  $10^{-5} \text{ M}$  KCl solution<sup>92</sup>.

The temperature of the liquid is also an essential factor. Van Limbeek and Seddon<sup>79</sup> compared the size and amount of nanobubbles by nucleation at different temperatures and found that more nanobubbles were observed when rising temperatures. The optimal system temperature was 35-40 °C, in which the nucleation reached the maximum.

The pressure inside the liquid film may also affect film stability. One evidence is that the stable films formed when  $\Delta p$  in Eq. 2.55 reaches zero. Another idea is that changing the pressure of a liquid can facilitate the nucleation process. Ohgaki et al.<sup>94</sup> utilized a zero-clearance rotary pump under the condition of 0.6 MPa to generate 600 cm<sup>3</sup> per 1 dm<sup>3</sup> nanobubble, which is far more than that under the atmospheric pressure.

### 2.1.3.5 Other film rupture mechanism

The rupture of the TLFs is thermodynamically favorable if the change in the Gibbs free energy ( $\Delta G$ ) is negative<sup>95</sup>. Apart from the abovementioned forces that may lead to rupture, other mechanisms have also been proposed.

Capillary wave mechanism: Apart from surface forces, the film rupture might be attributed to the attractive disjoining pressure in the TLFs coupled with growing fluctuation waves<sup>96</sup>. Although surface tension tends to make the (bubble) surface flat, natural thermal motions can cause a certain roughness. Also, the surface profiles can be regarded as a sum of Fourier waves, proposed as surface light scattering theory in the 1920s<sup>96</sup>. These waves were originated from attractive forces (van der Waals force and electrostatic force), which would favor the disproportionation of a film and then cause deformations. The deformations would grow and lead to the following rupture when the wavelength ( $\Lambda$ ) of fluctuation reached critical wavelength ( $\Lambda_c$ ), as shown in following equations.

$$\Lambda = \left(\frac{2\pi}{p}\right)(\rho^2 + \sigma^2)^{-\frac{1}{2}} \quad \text{Eq. 2.56}$$

$$\Lambda_c = \left[-\frac{2\pi^2\gamma}{\left(\frac{d^2V}{dh^2}\right)_0}\right]^{\frac{1}{2}} \quad \text{Eq. 2.57}$$

where  $\gamma$  is interfacial tension;  $V$  free energy;  $p=2\pi/a$ ;  $h$  film thickness;  $\rho$  density;  $\sigma$  surface potential.

Nucleation mechanism<sup>97</sup>: Rupture is originated from defects or impurities in the film. In this case, the density fluctuation inside the film or the tiny gas bubbles play a significant role<sup>98</sup>. Specifically, nanobubbles work as a bridge between normal bubbles and other surfaces. Take the solid particle as an example: Gas nuclei or picobubbles on a particle surface can promote the attachment of larger bubbles, as shown in Figure 2.13. In other words, picobubbles make particles more hydrophobic, improving the probability of the particle attachment while lowering the likelihood of detachment<sup>75</sup>.

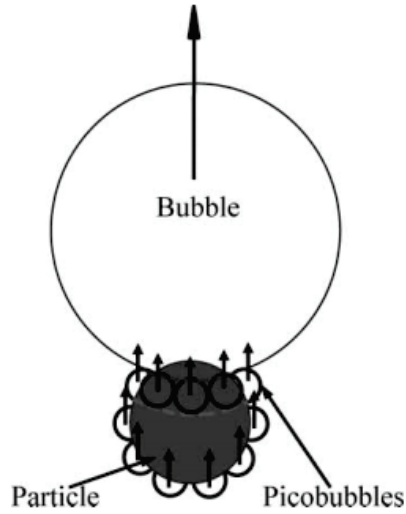


**Figure 2.13** Bridge role of picobubbles in solid-bubble attachment<sup>99</sup>, reprinted with permission.

## 2.1.4 Stability or detachment

The stability or detachment sub-step, also known as the wetting process, occurring right after the rupture of the liquid film, is also well-studied. This is a process of the evolution of the three-phase contact (TPC) line, which is relevant to the wetting or dewetting mechanisms. Factors, such as the solid surface properties (hydrophobicity, roughness, etc.) and liquid properties (surface tension, viscosity, etc.), will affect the final status of the three-phase contact line. Accordingly, several models have been proposed to illustrate this sub-step.

### 2.1.4.1 Detachment models

#### 2.1.4.1.1 Hydrodynamic model

The first one is the hydrodynamic model, based on the assumption that viscous dissipation controls the wetting process while the effect of the solid surface properties is not considered<sup>100,101</sup>. Here, the wetting process is quantified by the dynamic contact angle  $\theta^d$  via,

$$(\theta^d)^3 = (\theta^0)^3 \pm 9 \frac{\eta V}{\gamma_{lv}} \ln \left( \frac{L}{L_s} \right) \quad \text{Eq. 2.58}$$

where  $\theta^0$  denotes the equilibrium contact angle,  $\eta$  the liquid viscosity,  $\gamma_{lv}$  the surface tension of the liquid,  $L$  the characteristic capillary length ( $L = \sqrt{(2\gamma_{lv}/\rho g)}$ , where  $\rho$  is the liquid density), and  $L_s$  the slip length (in the order of molecular dimensions<sup>102</sup>). Note

that the positive sign corresponds to the advancing liquid movement, while the negative one corresponds to the receding case.

#### 2.1.4.1.2 Molecular-kinetic model

Instead of ignoring the solid surface, a second model, the molecular-kinetic model, is proposed, excluding the effect of the liquid, viscous dissipation<sup>103,104</sup>. The molecular-kinetic model is based on two assumptions: First, the entire interface follows the Laplace equation; Second, the energy dissipation appears only at the moving TPC after the adsorption and desorption process. In this scenario, the dynamic contact angle  $\theta^d$  is obtained by<sup>105</sup>,

$$\cos\theta^d = \cos\theta^0 \mp \frac{2\kappa T}{\gamma_{lv}\lambda^2} \operatorname{arcsinh}\left(\frac{V}{2K_w\lambda}\right) \quad \text{Eq. 2.59}$$

where  $k$  denotes the Boltzman constant,  $T$  the temperature,  $\lambda$  the distance between two adsorption or desorption sites, and  $K_w$  the quasi-equilibrium rate constant. In contrast to the hydrodynamic model, here, the negative sign applies to the advancing case, while the and positive sign is suitable in the receding case.

#### 2.1.4.1.3 Combined model

Through the abovementioned discussion, either the hydrodynamic model or the molecular-kinetic model can perfectly describe the wetting process. In practice, both the properties of liquid and solid should be carefully taken into account. Thus a combined model was finally proposed, and the dynamic contact angle  $\theta^d$  is given by,

$$\cos\theta^d = \arccos^3\left[\cos\theta^0 \mp \frac{2\kappa T}{\gamma_{lv}\lambda^2} \operatorname{arcsinh}\left(\frac{V}{2K_w\lambda}\right)\right] \pm 9 \frac{\eta V}{\gamma_{lv}} \ln\left(\frac{L}{L_s}\right) \quad \text{Eq. 2.60}$$

Many experiments have been done to test and compare the three models. It has to be mentioned that in a different context, the fittings models can change. For example, Hoffman's experimental results of a glass/silicone oils/air system were in good agreement with the hydrodynamic model<sup>106</sup>, but Hayes and Ralston fit the experimental data of a PET/aqueous glycerol/air system with the molecular-kinetic model<sup>107</sup>. In addition, it is found that the molecular displacement, i.e., the adsorption and desorption process, dominates the wetting of the polydimethylsiloxane oils. But the dependence of the dynamic contact angle on contact velocity remains elusive and cannot be explained by any of these models<sup>108</sup>.

#### 2.1.4.2 Detachment force measurement

It is accepted that detachment occurs when the detachment force overcomes the attachment force. Numerous experiments have been carried out to measure the detachment force so far.

AFM is a general approach here, given that it can directly provide the force information during the detachment. Ally et al.<sup>109,110</sup> used a colloid probe AFM to measure the detachment forces between bubbles and microparticles, as shown in Figure 2.14.

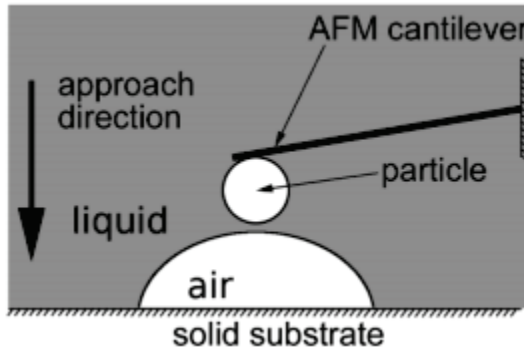


**Figure 2.14** Configuration of bubble-particle interaction by AFM<sup>109</sup>, reprinted with permission.

Another straightforward way to attain the detachment force is the microbalance technique. Wang et al.<sup>110</sup> employed a high-sensitivity microelectronic mechanical balance and measured the detachment of water drops from PDMS. And the schematic of the experimental set-up is shown in Figure 2.15.

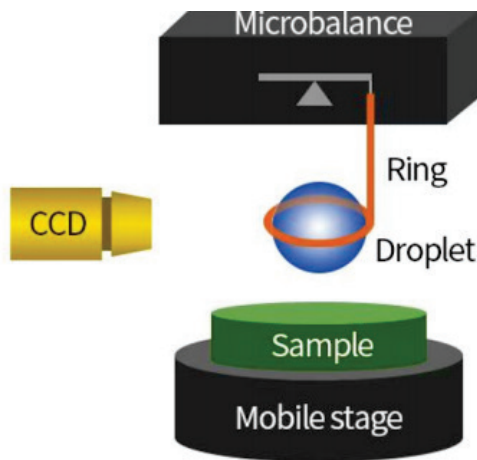


**Figure 2.15** Schematic of the adhesion force measurement method<sup>110</sup>, reprinted with permission.

Apart from the direct approaches, the detachment force can also be determined by the vibration technique, where the bubble-particle aggregate undergoes a simple harmonic motion<sup>111</sup>. The detachment force is a function of the critical amplitude and frequency of vibration. A typical set-up of this technique is provided in Figure 2.16.

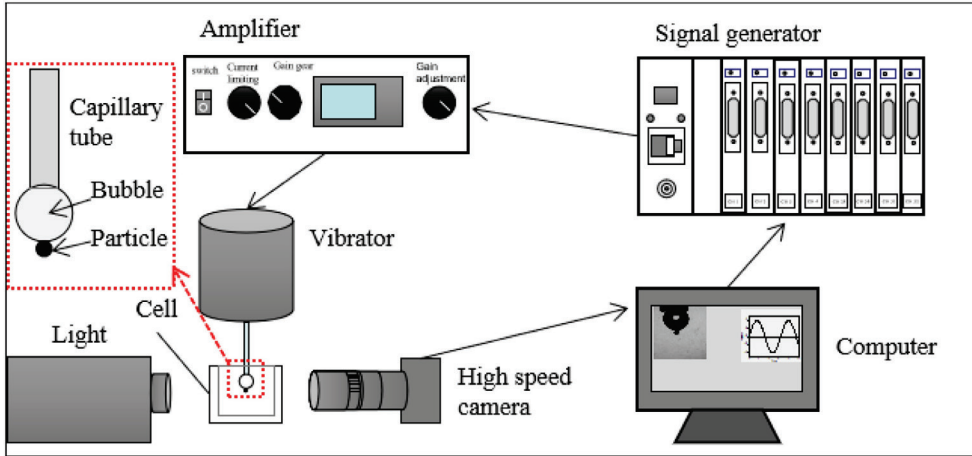


**Figure 2.16** Schematic of a vibration technique<sup>112</sup>, reprinted with permission.

### 2.1.4.3 Spreading speed

No matter what the dynamic contact angle changes, practically, TPC is a result of molecular interaction and fluid dynamics. And it is well appreciated that the TPC moves in a velocity, called spreading speed, defined as,

$$U_{TPC} = \frac{dr_{TPC}}{dt} \quad \text{Eq. 2.61}$$

where  $r_{TPC}$  is the three-phase contact line radius. And when  $U_{TPC}$  is zero, the spreading is completed.

Some researchers suggested the dissipation of liquid viscous dominated the spreading speed, and the primary resistance came from the bulk viscous friction. However, others believe that interaction between the surface and the liquid was the key. More pieces of evidence have been found to support the combination of both opinions<sup>113</sup>.

## 2.2 Air films

### 2.2.1 Introduction

Air films between solid surfaces and liquid droplets were firstly noticed by Worthington<sup>114,115</sup> in the 1870s. After that, they have received tremendous attention from researchers. The most commonly-seen air film in nature would be occurring during the rainfall. In practice, drop impacts on solid surfaces are a key element of many industrial processes, such as dust control, ink-jet printing, rapid spray cooling, fire suppression, spray coating and painting, plasma spraying, pesticide spraying, etc.<sup>116</sup> Understanding the evolution of the involved air films is of great importance to control and simulate the processes.



Take dust control in coal mining as an example to describe the role of air films. The collection of fine dust in coal mines remains a tough challenge, primarily as strict regulations on the environment have been globally implemented<sup>117</sup>. The main problems associated with coal dust consist of environmental, health, and safe issues<sup>118,119</sup>. Due to the respirable dust with a diameter of smaller than 75  $\mu\text{m}$ , workers exposed in underground coal mines suffer from many possible occupational diseases, including pneumoconiosis, silicosis, and advanced massive fibrosis<sup>120</sup>. Once getting diseases, workers cannot be easily cured because of the lack of effective therapeutic approaches<sup>121</sup>. To avoid the tragedies, the removal of dust particles has been investigated for decades. Currently, the suppression of dust is mainly achieved by several methods: a). fully enclosing dust generation resources (crusher, stage loader, belt, etc.); b). installation of curtains; c). ventilation; d). foam; e). water spray<sup>122-124</sup>. Among them, the water spray is a widely used approach to eliminate the dust substantially. Water spray takes effects as several roles in dust control: it can increase moisture in the air and enhance the coal wettability, and improve the airborne dust capture<sup>125</sup>. More specifically, dust capture involves the collision and attachment of dust particles towards water droplets<sup>126</sup>. The attachment process holds the key to a successful capture of dust, and it consists of the evolution of air films trapped between water drops and coal surfaces. Researchers found the air film was unstable during approach: when the separation distance reached a particular value, the rupture phenomenon would occur spontaneously, and the distance was defined as critical separation distance ( $d_c$ ), which varies from the nanometer scale to micrometer scale from case to case<sup>127,128</sup>.

Another example is ink-jet printing, one of the most promising methods for selectively depositing functional materials<sup>129,130</sup>. Ink-jet printing is also used in graphics and other conventional printing operations, displays<sup>131</sup>, plastic electronics<sup>132</sup>, solder dispensing for flip-chip manufacture<sup>133</sup>, rapid prototyping<sup>134</sup>, ceramic component manufacture<sup>135</sup>, enzyme-based sensors<sup>136</sup>, and tissue engineering<sup>137</sup>. In ink-jet printing, the liquids come from nozzles and are broken into droplets of sizes of 30-60  $\mu\text{m}$ <sup>138</sup>. Overall, the ink-jet printing process is composed of three steps: Firstly, liquid drops are generated; After that, droplets are positioning on a substrate; Lastly, the deposit is formed by drying or other solidification methods. To fully understand the impacts of the printed drop on the substrate, researchers need to recognize the involved interactions<sup>139</sup>. Apparently, the rupture of air film plays a significant role. The behavior of a liquid drop on impacting a solid surface is driven by inertial forces, capillary forces, and gravitational forces. The interactions between the individual drop and the substrate are of utmost importance in resolving printed objects. Furthermore, the resolution of the printed pattern is governed by the spreading of a liquid drop on a substrate. Thus a full understanding of air film rupture's role is beneficial to improving the ink-jet printers to achieve more advantageous results.

To investigate the evolution of air films, many technologies have been developed and utilized in this field. Besides, researchers summarized that solid surface properties like wettability and roughness, and liquid properties, including density, viscosity, and surface

tension, as well as the operations like the impact velocity, can influence the evolution of air films. More details will be provided in the following sections.

### 2.2.2 Experimental approaches

The drop impact on solid surfaces has been investigated for more than a century, and multiple imaging techniques have been used to characterize the air films.

These techniques start with direct high-speed imaging<sup>140-143</sup>. The most straightforward way is photography by CCD cameras. CCD cameras provide the evolution of the drop outlines during the impacts. Via this method, Rioboo et al.<sup>144</sup> summarized six possible outcomes of drop impact on a solid surface: deposition, prompt splash, corona splash, receding break-up, partial rebound, and complete rebound, as shown in Figure 2.17. The occurrence of the different outcomes is found to be closely related to the hydrophobicity of the solid surfaces.

Although the high-speed camera is the most direct technique to observe how the air film changes with time, its accuracy to measure the film thickness is limited to its resolution. Though the camera technology has been rapidly developing, the resolution ( $r$ ) is still limited to around 0.2 micrometers due to the relatively long wavelength ( $\lambda$ , 390nm-700nm) of the visible light and numerical aperture(NA). The following empirical equation explains their underlying relation<sup>145</sup>:

$$r = 0.61 \times \frac{\lambda}{NA} \quad \text{Eq. 2.62}$$

It is typical for the air film thickness to be less than 200 nm, indicating it is challenging to employ CCD cameras to measure the thickness of air films during the entire thinning process, despite the fact that they can still provide valuable information on the shape change of the liquid droplets as well as the contact angles formed when liquid drops sit on solid surfaces.

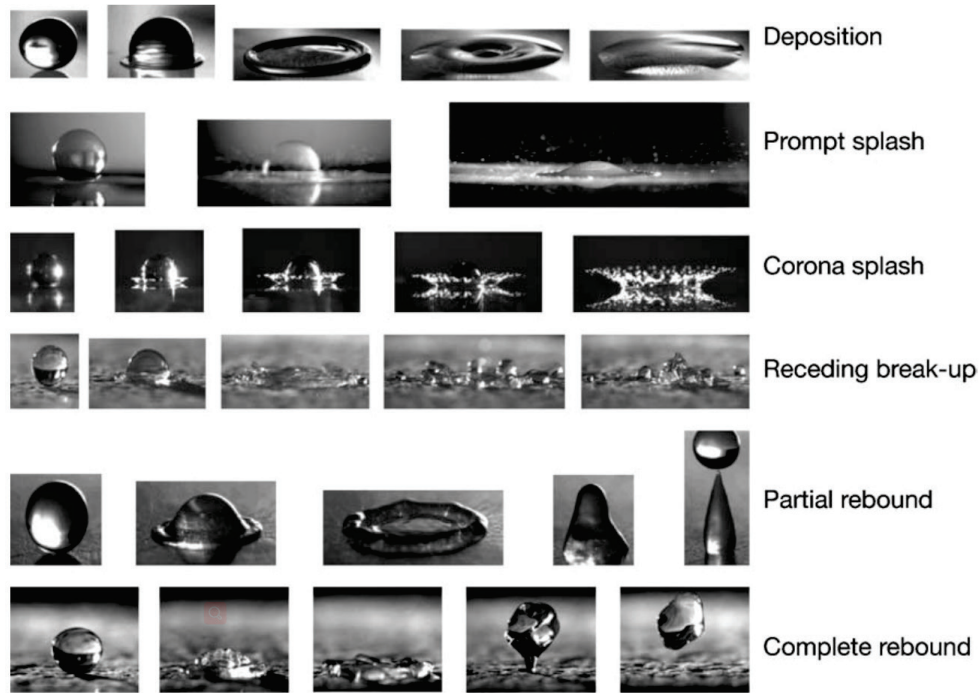


**Figure 2.17** Outcomes of liquid droplets impacting solid surfaces by CCD<sup>116</sup>, reprinted with permission.

X-ray phase-contrast imaging is another way to visualize the profile of the air film. Lee et al. employed X-ray phase-contrast imaging to track the dynamic changes in interfaces between air and liquid. The coherent nature of synchrotron X-rays strongly enhances the phase contrast of air-liquid interfaces with sharp black and white fringes<sup>146,147</sup>. Its schematic is shown in Figure 2.18.

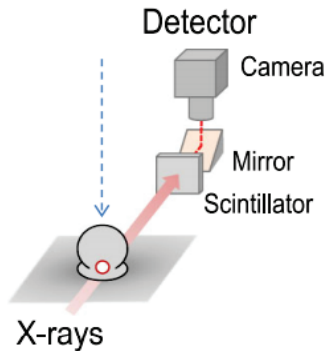


**Figure 2.18** Schematic of ultrafast x-ray phase-contrast imaging<sup>146</sup>, reprinted with permission.

In addition, the total internal reflection microscopy (TIRM) also allows researchers to characterize the dynamics of the drop profiles near the solid surface. When the droplet enters the evanescent field of the surface, the partially-transmitted light will capture images. The schematic is shown in Figure 2.19. Despite that TIRM can resolve nanometer scales, its range is limited and cannot determine the distance of more than 500 nm<sup>148</sup>.

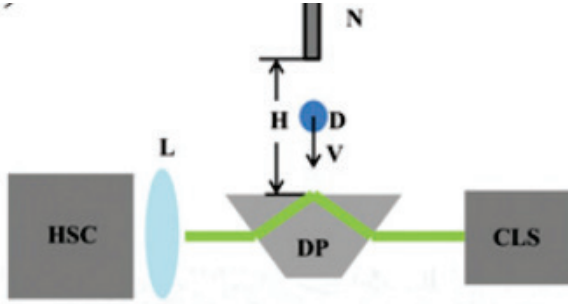


**Figure 2.19** Schematic of total internal reflection microscopy<sup>149</sup>, reprinted with permission.

In Figure 2.19, D denotes the water-glycerol drops. H is the height from a nozzle (N), above the substrate. A monochromatic light illuminates the dove prism (DP) from below. And the collimated light source (CLS) will excite an evanescent wave above the surface of the prism. Use a long working distance objective (L) to image the air films through the beam detected by the high-speed imaging sensor (HSC).

Reflection interference microscopy (RIM) is another popular way to observe the thin air films. This technique is based on the interference of light reflected from the two interfaces across the air film, as shown in Figure 2.20. To attain an accurate description, the finite illumination numerical aperture should be taken into consideration<sup>58,150,151</sup>. Recently it has been extensively applied to measure the thicknesses of the air films, such as that trapped between superhydrophobic surfaces<sup>152</sup>, and the drainage of air films during a drop floating or bouncing on a liquid bath<sup>153,154</sup>. However, there is a significant problem: the measurement of the absolute film thickness is elusive. Monochromatic wavelength interferometry fringes could calculate the film thickness of  $n\lambda/2$ , where  $\lambda$  is the light wavelength, and  $n$  is unknown. To overcome this difficulty, van der Veen et al.<sup>155</sup> used white light instead of a single wavelength light. By comparing the interference pattern with a known film profile between a spherical lens and a flat surface, the absolute thickness of air film up to 4000 nm having a perfect resolution of 40 nm can be extracted. Besides, a technique called dual-wavelength interferometry uses an additional wavelength light source<sup>156</sup>, which can measure the absolute film thickness. The frame rate of the high-speed cameras and the quality of the light will determine the time resolution. Currently, a frame rate of more than 100000 fps (frame per second) can be reached at the cost of recording only a small target area.

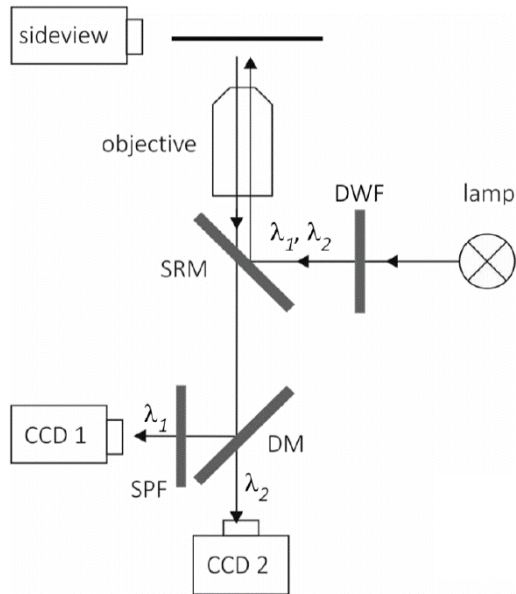


**Figure 2.20** Schematic of dual-wavelength reflection interference microscopy. (DWF: dual-wavelength filter; SRM: semi reflecting mirror; DM: dichroic mirror; SPF: short pass filter; CCD 1 and CCD 2: CCD cameras)<sup>156</sup>, reprinted with permission.

### 2.2.3 Theoretical models

Diverse mechanisms are trying to explain why the rupture of air film rupture:

The first well-accepted opinion is that the solid roughness causes the rupture during a process called “squeeze-out” of air between liquid droplets and solid surfaces. Kolinski et al. proposed that any discrete nanometer-height defects on a solid surface completely lead the air films to rupture<sup>157</sup>. Then, some scientists suggested that the collision of a droplet and a solid surface/particle was attributed to inertial impact, and the rupture happened when the thickness of air films reached the mean free path<sup>158,159</sup>. Based on this mechanism, it is not surprising to observe that some factors, such as the mass and size of droplets, the roughness, and the texture of the solid surfaces, significantly affect the air film stability. During the squeeze process, the gas pressure  $P_g$  is balanced with the capillary ( $P_\delta$ ) and inertial ( $P_i$ ) pressures of the liquid by  $P_g \sim P_\delta + P_i$ <sup>160-162</sup>. That is when the stable air film formed. However, many theoretical<sup>159,163-166</sup> and experimental<sup>128,167,168</sup> results show that the squeeze-out is irreversible, ultimately causing the contact of the liquid drop and the solid surface.

Besides, the intermolecular force is another reason for the rupture of the air rupture. Tran et al. observed the liquid bath deformed and the air film ruptured at a predictable distance from the lowest deformation, and the separation distance was calculated by a model considering van der Waals force<sup>162</sup>. The intermolecular forces between the drop and solid are postulated to be responsible for early merging, although there were no direct

measurements of the air film morphology during coalescence<sup>169-171</sup>. Furthermore, electrical interaction was also crucial for the capture of particles by droplets. Per coal dust was proved to carry charges on the order of  $10^{-10}$  elemental charges after pulverization. And the sign and amount of charge depended on moisture content, dust component, process method as well as particle size, etc.<sup>172-174</sup>. On the other hand, water exhibits the nature of hydrated excess protons in the formation of complex  $\text{H}_9\text{O}_4^+$  or  $\text{H}_5\text{O}_2^+$  due to thermal hopping, proton tunneling, or solvation effects<sup>175</sup>, while water is generally considered to be charge-neutral<sup>176</sup>. Additionally, surfactant-containing spray droplets can carry certain charges: Anionic surfactants lead the liquid to be negatively charged, and cationic surfactants tend to form positively-charged droplets, while the dissolution of nonionic surfactants into water creates small net positive charges<sup>177</sup>.

Apart from these, the effect of capillary waves was addressed by Lee et al.'s theory<sup>146</sup>. They proposed that the contact of droplets and the solid surface was related to the energy transfer through capillary waves during the retraction. The capillary waves converged at the center and attached the solid when the waves' propagation speed exceeded the retraction speed.

All the existing mechanisms promote the understanding of the collision of droplets and particles, but there is still much work needed to study the mechanisms further.

#### **2.2.4 Involved factors**

The solid surface properties that may affect the air films are summarized to be roughness, wettability, and other structural or chemical heterogeneity.

Roughness is the key to the rupture of air films. For rough surfaces, the rupture of air films is very common<sup>148</sup>. It is said that the asperities on solid surfaces cause the stochastic failure of the interstitial film<sup>178</sup>. Other investigators found that roughness played a vital role in splashing when liquid droplets impact solid surfaces. A large roughness could inhibit the formation of thin-sheet water during spreading and benefit the prompt splashing at the advancing contact line<sup>143</sup>. However, it is worthy to note that Kolinski et al.<sup>157</sup> found liquid droplets could bounce on atomically smooth super hydrophilic mica surfaces without touching the substrate, just like "skiing on the surfaces." This report indicates that there was a stable nanometer-scale air film between flat solid surfaces and water droplets.

The effect of the solid surface wettability on the air films is still remaining controversial. Some investigators claim there is no relation between wettability and air film evolution. One evidence is that the air entrainment volume is almost the same for the solid surfaces with contact angles of  $20^\circ$  to  $60^\circ$ <sup>146</sup>. For the bounce to happen, traditionally, it requires a non-wetting state, which can be achieved by using a superhydrophobic substrate<sup>179</sup> or a sublimating substrate of dry ice to stabilize the layer of vapor<sup>180</sup>, or by actively stabilizing a thin layer of air or vapor below the droplet by evaporation<sup>181-183</sup>. Another way to maintain the air layer is to oscillate the substrate to create a liquid<sup>153,154,184</sup> or soap film<sup>185</sup>.

And experimental results also show that the air films are stable during the entire impact process, no matter how hydrophilic or hydrophobic the substrates are<sup>148,186</sup>. However, it is also found that compared with hydrophobic surfaces, the air films ruptured so quickly and far that it is difficult to record when using hydrophilic solid surfaces<sup>187</sup>, which is known as “Wenzel state”<sup>188</sup>. The underlying mechanism may lie in that the water adsorption on a solid surface in the air varies with hydrophobicity. On the hydrophilic surface, the average thickness of the strongly hydrogen-bonded water layer increases to 2 molecular layers with increasing relative humidity (RH), beyond which the weakly hydrogen-bonded structure is dominant. On the hydrophobic surface, the adsorbed water layer consists predominantly of the weakly hydrogen-bonded structure, and its average thickness remains less than a monolayer<sup>189</sup>. At the same RH (>60%), there will be two monolayers of the ordered water layer on the hydrophilic surfaces, and the adsorbed water film possesses solid-like properties<sup>190</sup>. In contrast, the water layer on the hydrophobic surfaces is highly disordered and forms isolated clusters. The distinction of water adsorption may be the key reason for the rupture of air films in between.

As for the role of structure, it is found that microtextures have a profound effect on the macroscopic splash<sup>191</sup>. Two types of surfaces are compared: one is a smooth surface, and the other one is a grooved surface. It turns out that the groove structure can influence the spreading of the liquid lamella on the solid surface. The impacting drop spreads along the groove direction is similar to that on the smooth surface, but the solid pillars on the grooved surface obstruct the droplet spreading in a normal direction to the groove. Another impressive result is that the hydrophobicity of the grooved surface is enhanced on the grooved surface, leading to a stronger rebound of the liquid droplet on the grooved surface than that on the smooth surface<sup>192</sup>.

The primary liquid properties, including density, viscosity, viscoelasticity, will lead to different scenarios in terms of air films. The liquid density is critical because the heavier the drop is, the stronger the impact force  $F$  will be<sup>193</sup>. Similarly, a droplet with a large size may also refer to a more significant impact force during impact. Other investigators found factors like the velocity of impact, drop size and shape, and the liquid surface tension have essential effects on the mass and energy distribution of the ejected droplets<sup>194</sup>. By using ethanol, water, and a mixture of water-sucrose-ethanol, different surface tensions ( $22 < \sigma < 72 \text{ mN/m}$ ) and viscosities ( $1.0 < \mu < 2.9 \text{ mPas}$ ) can be obtained. It is found the deposition-splashing boundary is a function of impact velocity, liquid viscosity, and surface tension<sup>195</sup>. The viscosity will also affect the lamella's spreading after a drop impacting a smooth, dry surface. A larger viscosity leads to a longer time for the lamella to eject into thin sheets<sup>143</sup>.

Apart from those mentioned solid and liquid properties, other factors may also be of great importance to the air film evolution, like ambient pressure. Investigators have shown that decreasing the ambient pressure will suppress the splashing in drop impacts<sup>163,195</sup>. Besides, if the ambient pressure is lowered, droplet ejection is also suppressed<sup>143</sup>. Scientists also discovered the influence of ambient pressure on the maximal spreading diameter on hydrophobic microtextures: the maximal spreading diameter lamella

decreases, and directional splash can even be eliminated with a decreasing ambient pressure<sup>191</sup>.

Generally, the evolution of air films can be characterized by the dimensionless numbers: a). Capillary number  $Ca = \mu_g U_0 / \sigma$  for the gas phase; b). Weber number  $We = \rho_l U_0^2 R / \sigma$  for the liquid phase; c). Stokes number  $St = \rho_l U_0 R / \mu_g$  accounting for both the liquid and gas phases. In these dimensionless numbers,  $\mu_g$  is the viscosity of the gas,  $U_0$  the impact velocity,  $\rho_l$  the density of the droplet, and  $\sigma$  the surface tension of the droplet. We number is often considered the most important. At high We, away from the center, the curvature at the minimum air film thickness increases and finally reaches the maximum when the capillary pressure stops the approach of the droplet to the substrate, forming the kink height(s)<sup>128</sup>. Besides, researchers found the We number has a vital role on splash: at low We, there would be a complete rebound; at high We, there would be an advancing splash where the central area encircles an air region<sup>191</sup>.



## 2.3 Reference

- 1 Rao, S. R. *Surface chemistry of froth flotation: Volume 1: Fundamentals*. (Springer Science & Business Media, 2013).
- 2 Ralston, J., Dukhin, S. & Mishchuk, N. Wetting film stability and flotation kinetics. *Advances in Colloid and Interface Science* **95**, 145-236 (2002).
- 3 Nguyen, A. & Schulze, H. J. *Colloidal science of flotation*. Vol. 118 (CRC Press, 2003).
- 4 Pita, F. & Castilho, A. Separation of plastics by froth flotation. The role of size, shape and density of the particles. *Waste Management* **60**, 91-99 (2017).
- 5 Basařová, P., Machoň, V., Hubička, M. & Horn, D. Collision processes involving a single rising bubble and a larger stationary spherical particle. *International Journal of Mineral Processing* **94**, 58-66 (2010).
- 6 Schulze, H. Hydrodynamics of bubble-mineral particle collisions. *Mineral Processing and Extractive Metallurgy Review* **5**, 43-76 (1989).
- 7 Flint, L. & Howarth, W. The collision efficiency of small particles with spherical air bubbles. *Chemical Engineering Science* **26**, 1155-1168 (1971).
- 8 Sutherland, K. Physical chemistry of flotation. XI. Kinetics of the flotation process. *The Journal of Physical Chemistry* **52**, 394-425 (1948).
- 9 Derjaguin, B. & Dukhin, S. Theory of flotation of small and medium-size particles. *Progress in Surface Science* **43**, 241-266 (1993).
- 10 Basařová, P., Zawala, J. & Zedníková, M. Interactions between a Small Bubble and a Greater Solid Particle during the Flotation Process. *Mineral Processing and Extractive Metallurgy Review* **40**, 410-426 (2019).
- 11 Basařová, P. & Hubička, M. The collision efficiency of small bubbles with large particles. *Minerals Engineering* **66**, 230-233 (2014).
- 12 Li, S. *et al.* Experimental observations of bubble–particle collisional interaction relevant to froth flotation, and calculation of the associated forces. *Minerals Engineering* **151**, 106335 (2020).
- 13 Verrelli, D. I., Lee, A., Schwarz, M. P. & Koh, P. T. in *Ninth International Conference on Computational Fluid Dynamics in the Minerals and Process Industries (CFD2012)*, CSIRO, Australia, Melbourne, Australia, Accepted October.
- 14 Chan, D. Y. & Horn, R. The drainage of thin liquid films between solid surfaces. *The Journal of chemical physics* **83**, 5311-5324 (1985).
- 15 Parkinson, L. & Ralston, J. The interaction between a very small rising bubble and a hydrophilic titania surface. *The Journal of Physical Chemistry C* **114**, 2273-2281 (2010).
- 16 Laskowski, J. & Kitchener, J. The hydrophilic—hydrophobic transition on silica. *Journal of Colloid and Interface Science* **29**, 670-679 (1969).
- 17 Yoon, R.-H. & Mao, L. Application of extended DLVO theory, IV: derivation of flotation rate equation from first principles. *Journal of colloid and interface science* **181**, 613-626 (1996).
- 18 Pan, L. & Yoon, R.-H. Effects of electrolytes on the stability of wetting films: Implications on seawater flotation. *Minerals Engineering* **122**, 1-9 (2018).

- 19 Pan, L. & Yoon, R.-H. Measurement of hydrophobic forces in thin liquid films of water between bubbles and xanthate-treated gold surfaces. *Minerals Engineering* **98**, 240-250 (2016).
- 20 Shi, C. *et al.* Measuring forces and spatiotemporal evolution of thin water films between an air bubble and solid surfaces of different hydrophobicity. *ACS nano* **9**, 95-104 (2015).
- 21 Christensen, H. & Claesson, P. Cavitation and the interaction between macroscopic surfaces. *Science* **239**, 390-392 (1988).
- 22 Ishida, N., Sakamoto, M., Miyahara, M. & Higashitani, K. Optical observation of gas bridging between hydrophobic surfaces in water. *Journal of colloid and interface science* **253**, 112-116 (2002).
- 23 Zhang, X. H. *et al.* Degassing and temperature effects on the formation of nanobubbles at the mica/water interface. *Langmuir* **20**, 3813-3815 (2004).
- 24 Zhang, X. H., Li, G., Maeda, N. & Hu, J. Removal of induced nanobubbles from water/graphite interfaces by partial degassing. *Langmuir* **22**, 9238-9243 (2006).
- 25 Attard, P. Thermodynamic analysis of bridging bubbles and a quantitative comparison with the measured hydrophobic attraction. *Langmuir* **16**, 4455-4466 (2000).
- 26 Hampton, M. A., Donose, B. C. & Nguyen, A. V. Effect of alcohol–water exchange and surface scanning on nanobubbles and the attraction between hydrophobic surfaces. *Journal of colloid and interface science* **325**, 267-274 (2008).
- 27 Xing, Y., Gui, X. & Cao, Y. The hydrophobic force for bubble–particle attachment in flotation—a brief review. *Physical Chemistry Chemical Physics* **19**, 24421-24435 (2017).
- 28 Faghijnejad, A. & Zeng, H. Hydrophobic interactions between polymer surfaces: using polystyrene as a model system. *Soft Matter* **8**, 2746-2759 (2012).
- 29 Patel, A. J., Varilly, P. & Chandler, D. Fluctuations of water near extended hydrophobic and hydrophilic surfaces. *The Journal of Physical Chemistry B* **114**, 1632-1637 (2010).
- 30 Tabor, R. F., Grieser, F., Dagastine, R. R. & Chan, D. Y. The hydrophobic force: measurements and methods. *Physical Chemistry Chemical Physics* **16**, 18065-18075 (2014).
- 31 Tyrode, E. & Liljeblad, J. F. Water structure next to ordered and disordered hydrophobic silane monolayers: a vibrational sum frequency spectroscopy study. *The Journal of Physical Chemistry C* **117**, 1780-1790 (2013).
- 32 Sanders, S. E. & Petersen, P. B. Heterodyne-detected sum frequency generation of water at surfaces with varying hydrophobicity. *The Journal of Chemical Physics* **150**, 204708 (2019).
- 33 Wang, R. *et al.* Hydrophobic behavior of fluorite surface in strongly alkaline solution and its application in flotation. *Colloids and Surfaces A: Physicochemical and Engineering Aspects*, 125661 (2020).
- 34 Meyer, E. E., Lin, Q., Hassenkam, T., Oroudjev, E. & Israelachvili, J. N. Origin of the long-range attraction between surfactant-coated surfaces. *Proceedings of the National Academy of Sciences* **102**, 6839-6842 (2005).

- 35 Sáringer, S. r., Rouster, P. & Szilágyi, I. n. Regulation of the stability of titania nanosheet dispersions with oppositely and like-charged polyelectrolytes. *Langmuir* **35**, 4986-4994 (2019).
- 36 Adar, R. M., Andelman, D. & Diamant, H. Electrostatics of patchy surfaces. *Advances in Colloid and Interface Science* **247**, 198-207 (2017).
- 37 Xie, L., Cui, X., Gong, L., Chen, J. & Zeng, H. Recent Advances in the Quantification and Modulation of Hydrophobic Interactions for Interfacial Applications. *Langmuir* **36**, 2985-3003 (2020).
- 38 Horn, R. G., Vinogradova, O. I., Mackay, M. E. & Phan-Thien, N. Hydrodynamic slippage inferred from thin film drainage measurements in a solution of nonadsorbing polymer. *The Journal of Chemical Physics* **112**, 6424-6433 (2000).
- 39 Albijanic, B., Ozdemir, O., Nguyen, A. V. & Bradshaw, D. A review of induction and attachment times of wetting thin films between air bubbles and particles and its relevance in the separation of particles by flotation. *Advances in colloid and interface science* **159**, 1-21 (2010).
- 40 Wang, S., Albijanic, B., Tao, X. & Fan, H. Thin liquid film drainage mechanism between air bubbles and low-rank coal particles in the presence of surfactant. *Fuel Processing Technology* **186**, 18-24 (2019).
- 41 Yoon, R.-H. & Yordan, J. L. Induction time measurements for the quartz—amine flotation system. *Journal of Colloid and Interface Science* **141**, 374-383 (1991).
- 42 Gu, G., Xu, Z., Nandakumar, K. & Masliyah, J. Effects of physical environment on induction time of air-bitumen attachment. *International Journal of Mineral Processing* **69**, 235-250 (2003).
- 43 Li, Y. *et al.* Application of compound reagent H511 in the flotation removal of unburned carbon from fly ash. *Colloids and Surfaces A: Physicochemical and Engineering Aspects*, 124699 (2020).
- 44 Krasowska, M. & Malysa, K. Kinetics of bubble collision and attachment to hydrophobic solids: I. Effect of surface roughness. *International Journal of Mineral Processing* **81**, 205-216 (2007).
- 45 Karakashev, S. I., Stöckelhuber, K. W., Tsekov, R. & Heinrich, G. Bubble rubbing on solid surface: Experimental study. *Journal of colloid and interface science* **412**, 89-94 (2013).
- 46 Tabor, D. & Winterton, R. The direct measurement of normal and retarded van der Waals forces. *Proc. R. Soc. Lond. A* **312**, 435-450 (1969).
- 47 Israelachvili, J. & Tabor, D. Measurement of van der Waals dispersion forces in the range 1.4 to 130 nm. *Nature Physical Science* **236**, 106 (1972).
- 48 Connor, J. N. & Horn, R. G. Extending the surface force apparatus capabilities by using white light interferometry in reflection. *Review of scientific instruments* **74**, 4601-4606 (2003).
- 49 Horn, R. G., Bachmann, D. J., Connor, J. & Miklavcic, S. The effect of surface and hydrodynamic forces on the shape of a fluid drop approaching a solid surface. *Journal of physics: condensed matter* **8**, 9483 (1996).
- 50 Xie, L., Shi, C., Cui, X. & Zeng, H. Surface forces and interaction mechanisms of emulsion drops and gas bubbles in complex fluids. *Langmuir* **33**, 3911-3925 (2017).

- 51 Binnig, G., Quate, C. F. & Gerber, C. Atomic force microscope. *Physical review letters* **56**, 930 (1986).
- 52 Butt, H.-J. A technique for measuring the force between a colloidal particle in water and a bubble. *Journal of Colloid and Interface Science* **166**, 109-117 (1994).
- 53 Ducker, W. A., Xu, Z. & Israelachvili, J. N. Measurements of hydrophobic and DLVO forces in bubble-surface interactions in aqueous solutions. *Langmuir* **10**, 3279-3289 (1994).
- 54 Xie, L. *et al.* Probing the interaction mechanism between air bubbles and bitumen surfaces in aqueous media using bubble probe atomic force microscopy. *Langmuir* **34**, 729-738 (2018).
- 55 Wang, W. *et al.* Review and perspectives of AFM application on the study of deformable drop/bubble interactions. *Advances in colloid and interface science* **225**, 88-97 (2015).
- 56 Curtis, A. The mechanism of adhesion of cells to glass: a study by interference reflection microscopy. *The Journal of cell biology* **20**, 199-215 (1964).
- 57 Raedler, J. & Sackmann, E. On the measurement of weak repulsive and frictional colloidal forces by reflection interference contrast microscopy. *Langmuir* **8**, 848-853 (1992).
- 58 Wiegand, G., Neumaier, K. R. & Sackmann, E. Microinterferometry: three-dimensional reconstruction of surface microtopography for thin-film and wetting studies by reflection interference contrast microscopy (RICM). *Applied optics* **37**, 6892-6905 (1998).
- 59 Schilling, J., Sengupta, K., Goennenwein, S., Bausch, A. R. & Sackmann, E. Absolute interfacial distance measurements by dual-wavelength reflection interference contrast microscopy. *Physical Review E* **69**, 021901 (2004).
- 60 Dubreuil, F., Elsner, N. & Fery, A. Elastic properties of polyelectrolyte capsules studied by atomic-force microscopy and RICM. *The European Physical Journal E* **12**, 215-221 (2003).
- 61 Zhang, X. *et al.* Simultaneous measurement of dynamic force and spatial thin film thickness between deformable and solid surfaces by integrated thin liquid film force apparatus. *Soft Matter* **12**, 9105-9114 (2016).
- 62 Dai, Z., Dukhin, S., Fornasiero, D. & Ralston, J. The inertial hydrodynamic interaction of particles and rising bubbles with mobile surfaces. *Journal of Colloid and Interface Science* **197**, 275-292 (1998).
- 63 Dai, Z., Fornasiero, D. & Ralston, J. Particle–bubble attachment in mineral flotation. *Journal of colloid and interface science* **217**, 70-76 (1999).
- 64 Nguyen, A. & Schulze, H. Electrical double-layer forces. *Colloidal science of flotation* **118**, 323 (2004).
- 65 Schulze, H. & Stöckelhuber, W. Flotation as a heterocoagulation process: Possibilities of calculating the probability of the microprocesses, rupture of the intervening thin liquid film, and progress in modeling of the overall process. *Coagulation and Flocculation, (Edited by H. Stechemesser and B. Dobiáš)*, 455-517 (2005).
- 66 Schulze, H., Stöckelhuber, K. & Wenger, A. The influence of acting forces on the rupture mechanism of wetting films—nucleation or capillary waves. *Colloids and Surfaces A: Physicochemical and Engineering Aspects* **192**, 61-72 (2001).

- 67 Stöckelhuber, K. W., Schulze, H. J. & Wenger, A. in *Trends in Colloid and Interface Science XV* 11-16 (Springer, 2001).
- 68 Israelachvili, J. N. *Intermolecular and surface forces*. (Academic press, 2011).
- 69 Sendner, C., Horinek, D., Bocquet, L. & Netz, R. R. Interfacial water at hydrophobic and hydrophilic surfaces: Slip, viscosity, and diffusion. *Langmuir* **25**, 10768-10781 (2009).
- 70 Doshi, D. A., Watkins, E. B., Israelachvili, J. N. & Majewski, J. Reduced water density at hydrophobic surfaces: Effect of dissolved gases. *Proceedings of the National Academy of Sciences* **102**, 9458-9462 (2005).
- 71 Janeček, J. & Netz, R. R. Interfacial water at hydrophobic and hydrophilic surfaces: Depletion versus adsorption. *Langmuir* **23**, 8417-8429 (2007).
- 72 Johnson, B. D. & Cooke, R. C. Generation of stabilized microbubbles in seawater. *Science* **213**, 209-211 (1981).
- 73 Yount, D. Growth of bubbles from nuclei. *Supersaturation and bubble formation in fluids and organisms*, 131-164 (1989).
- 74 Dziensiewicz, J. & Pryor, E. An investigation into the action of air in froth flotation. *Trans. IMM., London* **59**, 455-491 (1950).
- 75 Shimoiizaka, J. & Matsuoka, I. in *Proc. XIV International Mineral Processing Congress, Toronto, Canada*. 17-23.
- 76 Attard, P. Nanobubbles and the hydrophobic attraction. *Advances in colloid and interface science* **104**, 75-91 (2003).
- 77 Meyer, E. E., Lin, Q. & Israelachvili, J. N. Effects of dissolved gas on the hydrophobic attraction between surfactant-coated surfaces. *Langmuir* **21**, 256-259 (2005).
- 78 Ishida, N., Inoue, T., Miyahara, M. & Higashitani, K. Nano bubbles on a hydrophobic surface in water observed by tapping-mode atomic force microscopy. *Langmuir* **16**, 6377-6380 (2000).
- 79 van Limbeek, M. A. & Seddon, J. R. Surface nanobubbles as a function of gas type. *Langmuir* **27**, 8694-8699 (2011).
- 80 Seddon, J. R. *et al.* Dynamic dewetting through micropancake growth. *Langmuir* **26**, 9640-9644 (2010).
- 81 Dammer, S. M. & Lohse, D. Gas enrichment at liquid-wall interfaces. *Physical review letters* **96**, 206101 (2006).
- 82 Sheludko, A. Thin liquid films. *Advances in Colloid and Interface Science* **1**, 391-464 (1967).
- 83 Ryan, W. L. & Hemmingsen, E. A. Bubble formation in water at smooth hydrophobic surfaces. *Journal of colloid and interface science* **157**, 312-317 (1993).
- 84 Gerth, W. A. & Hemmingsen, E. A. Heterogeneous nucleation of bubbles at solid surfaces in gas-supersaturated aqueous solutions. *Journal of Colloid and Interface Science* **74**, 80-89 (1980).
- 85 Extrand, C. Criteria for ultralyophobic surfaces. *Langmuir* **20**, 5013-5018 (2004).
- 86 Sedev, R., Fabretto, M. & Ralston, J. Wettability and surface energetics of rough fluoropolymer surfaces. *The Journal of Adhesion* **80**, 497-520 (2004).

- 87 Mezger, M. *et al.* On the origin of the hydrophobic water gap: an X-ray reflectivity and MD simulation study. *Journal of the American Chemical Society* **132**, 6735-6741 (2010).
- 88 Verrelli, D. I., Koh, P. T. & Nguyen, A. V. Particle–bubble interaction and attachment in flotation. *Chemical Engineering Science* **66**, 5910-5921 (2011).
- 89 Verrelli, D. I., Bruckard, W. J., Koh, P. T., Schwarz, M. P. & Follink, B. Particle shape effects in flotation. Part 1: Microscale experimental observations. *Minerals Engineering* **58**, 80-89 (2014).
- 90 Hassas, B. V. *et al.* Effect of roughness and shape factor on flotation characteristics of glass beads. *Colloids and Surfaces A: Physicochemical and Engineering Aspects* **492**, 88-99 (2016).
- 91 Vinogradova, O. I. Drainage of a thin liquid film confined between hydrophobic surfaces. *Langmuir* **11**, 2213-2220 (1995).
- 92 Zhang, X., Manica, R., Tchoukov, P., Liu, Q. & Xu, Z. Effect of Approach Velocity on Thin Liquid Film Drainage between an Air Bubble and a Flat Solid Surface. *The Journal of Physical Chemistry C* **121**, 5573-5584 (2017).
- 93 Winterhalter, M. & Helfrich, W. Effect of surface charge on the curvature elasticity of membranes. *The Journal of Physical Chemistry* **92**, 6865-6867 (1988).
- 94 Ohgaki, K., Khanh, N. Q., Joden, Y., Tsuji, A. & Nakagawa, T. Physicochemical approach to nanobubble solutions. *Chemical Engineering Science* **65**, 1296-1300 (2010).
- 95 Van Oss, C. J. *Interfacial forces in aqueous media*. (CRC press, 2006).
- 96 Mandelstam, L. L. Mandelstam, Ann. Phys.(Leipzig) 41, 608 (1913). *Ann. Phys.(Leipzig)* **41**, 608 (1913).
- 97 Derjaguin, B. & Gutop, J. Doklad Akad Nauk SSSR. *Moscow* **153**, 859 (1963).
- 98 Jacobs, K., Herminghaus, S. & Mecke, K. R. Thin liquid polymer films rupture via defects. *Langmuir* **14**, 965-969 (1998).
- 99 Fan, M. & Tao, D. A study on picobubble enhanced coarse phosphate froth flotation. *Separation Science and Technology* **43**, 1-10 (2008).
- 100 Cox, R. The dynamics of the spreading of liquids on a solid surface. Part 1. Viscous flow. *Journal of Fluid Mechanics* **168**, 169-194 (1986).
- 101 Voinov, O. Hydrodynamics of wetting. *Fluid dynamics* **11**, 714-721 (1976).
- 102 Thompson, P. A. & Robbins, M. O. Simulations of contact-line motion: slip and the dynamic contact angle. *Physical review letters* **63**, 766 (1989).
- 103 Blake, T. & Haynes, J. Kinetics of liquidliquid displacement. *Journal of colloid and interface science* **30**, 421-423 (1969).
- 104 Ruckenstein, E. & Dunn, C. Slip velocity during wetting of solids. *Journal of Colloid and Interface Science* **59**, 135-138 (1977).
- 105 Blake, T. & De Coninck, J. The influence of solid–liquid interactions on dynamic wetting. *Advances in colloid and interface science* **96**, 21-36 (2002).
- 106 Hoffman, R. L. A study of the advancing interface. I. Interface shape in liquid–gas systems. *Journal of colloid and interface science* **50**, 228-241 (1975).
- 107 Hayes, R. A. & Ralston, J. Forced liquid movement on low energy surfaces. *Journal of colloid and interface science* **159**, 429-438 (1993).
- 108 Ranabothu, S. R., Karnezis, C. & Dai, L. L. Dynamic wetting: hydrodynamic or molecular-kinetic? *Journal of colloid and interface science* **288**, 213-221 (2005).

- 109 Ally, J., Kappl, M., Butt, H.-J. r. & Amirfazli, A. Detachment Force of Particles from Air– Liquid Interfaces of Films and Bubbles. *Langmuir* **26**, 18135-18143 (2010).
- 110 Ally, J., Kappl, M. & Butt, H.-J. r. Adhesion of particles with sharp edges to air– liquid interfaces. *Langmuir* **28**, 11042-11047 (2012).
- 111 Xing, Y. *et al.* Effect of surface roughness on the detachment between bubble and glass beads with different contact angles. *Powder Technology* **361**, 812-816 (2020).
- 112 Zhang, Y., Xing, Y., Ding, S., Cao, Y. & Gui, X. Effect of vibration mode on detachment of low-rank coal particle from oscillating bubble. *Powder Technology* **356**, 880-883 (2019).
- 113 Phan, C. M., Nguyen, A. V. & Evans, G. M. Combining hydrodynamics and molecular kinetics to predict dewetting between a small bubble and a solid surface. *Journal of colloid and interface science* **296**, 669-676 (2006).
- 114 Worthington, A. Proc. R. Soc. London. (1876).
- 115 Worthington, A. (Nature Publishing Group, 1877).
- 116 Yarin, A. L. Drop impact dynamics: splashing, spreading, receding, bouncing.... *Annu. Rev. Fluid Mech.* **38**, 159-192 (2006).
- 117 Daood, S. S. *et al.* Pollutant and corrosion control technology and efficient coal combustion. *Energy & Fuels* **31**, 5581-5596 (2017).
- 118 Zhang, G., Zhang, L., Fan, H. & Hu, E. Concentration, enrichment, and partitioning behavior of heavy metals in ash from a down-fired furnace burning anthracite coal. *Energy & Fuels* **31**, 9381-9392 (2017).
- 119 Zhou, Q., Qin, B., Wang, J., Wang, H. & Wang, F. Effects of preparation parameters on the wetting features of surfactant-magnetized water for dust control in Luwa mine, China. *Powder Technology* **326**, 7-15 (2018).
- 120 Beck, T., Seaman, C., Shahan, M. & Mischler, S. Open-air sprays for capturing and controlling airborne float coal dust on longwall faces. *Mining engineering* **70**, 42 (2018).
- 121 Li, J. *et al.* TAK1 inhibition attenuates both inflammation and fibrosis in experimental pneumoconiosis. *Cell discovery* **3**, 17023 (2017).
- 122 Colinet, J., Listak, J. M., Organiscak, J. A., Rider, J. P. & Wolfe, A. L. *Best practices for dust control in coal mining.* (2010).
- 123 Seibel, R. J. *Dust control at a transfer point using foam and water sprays.* Vol. 97 (US Dept. of the Interior, Bureau of Mines, 1976).
- 124 Han, F., Wang, D., Jiang, J. & Zhu, X. A new design of foam spray nozzle used for precise dust control in underground coal mines. *International Journal of Mining Science and Technology* **26**, 241-246 (2016).
- 125 Organiscak, J. Examination of water spray airborne coal dust capture with three wetting agents. *Transactions of Society for Mining, Metallurgy, and Exploration, Inc* **334**, 427 (2013).
- 126 Cheng, L. Collection of airborne dust by water sprays. *Industrial & Engineering Chemistry Process Design and Development* **12**, 221-225 (1973).
- 127 Kolinski, J. M., Mahadevan, L. & Rubinstein, S. M. Lift-off instability during the impact of a drop on a solid surface. *Physical review letters* **112**, 134501 (2014).

- 128 de Ruiter, J., van den Ende, D. & Mugele, F. Air cushioning in droplet impact. II. Experimental characterization of the air film evolution. *Physics of fluids* **27**, 012105 (2015).
- 129 De Gans, B. J., Duineveld, P. C. & Schubert, U. S. Inkjet printing of polymers: state of the art and future developments. *Advanced materials* **16**, 203-213 (2004).
- 130 Calvert, P. Inkjet printing for materials and devices. *Chemistry of materials* **13**, 3299-3305 (2001).
- 131 Bharathan, J. & Yang, Y. Polymer electroluminescent devices processed by inkjet printing: I. Polymer light-emitting logo. *Applied Physics Letters* **72**, 2660-2662 (1998).
- 132 Siringhaus, H. *et al.* High-resolution inkjet printing of all-polymer transistor circuits. *Science* **290**, 2123-2126 (2000).
- 133 Hayes, D. J., Wallace, D. B. & Royall Cox, W. in *Proceedings-SPIE the International Society for Optical Engineering*. 242-247 (Citeseer).
- 134 Sachs, E., Cima, M., Williams, P., Brancazio, D. & Cornie, J. Three dimensional printing: rapid tooling and prototypes directly from a CAD model. *Journal of Engineering for Industry* **114**, 481-488 (1992).
- 135 Seerden, K. A. *et al.* Ink-jet printing of wax-based alumina suspensions. *Journal of the American Ceramic Society* **84**, 2514-2520 (2001).
- 136 Setti, L. *et al.* An amperometric glucose biosensor prototype fabricated by thermal inkjet printing. *Biosensors and Bioelectronics* **20**, 2019-2026 (2005).
- 137 Nakamura, M. *et al.* Biocompatible inkjet printing technique for designed seeding of individual living cells. *Tissue engineering* **11**, 1658-1666 (2005).
- 138 Park, J. & Moon, J. Control of colloidal particle deposit patterns within picoliter droplets ejected by ink-jet printing. *Langmuir* **22**, 3506-3513 (2006).
- 139 Derby, B. Inkjet printing of functional and structural materials: fluid property requirements, feature stability, and resolution. *Annual Review of Materials Research* **40**, 395-414 (2010).
- 140 Thoroddsen, S., Etoh, T. & Takehara, K. Air entrapment under an impacting drop. *Journal of Fluid Mechanics* **478**, 125-134 (2003).
- 141 van Dam, D. B. & Le Clerc, C. Experimental study of the impact of an ink-jet printed droplet on a solid substrate. *Physics of Fluids* **16**, 3403-3414 (2004).
- 142 Thoroddsen, S., Etoh, T., Takehara, K., Ootsuka, N. & Hatsuki, Y. The air bubble entrapped under a drop impacting on a solid surface. *Journal of Fluid Mechanics* **545**, 203-212 (2005).
- 143 Latka, A., Strandburg-Peshkin, A., Driscoll, M. M., Stevens, C. S. & Nagel, S. R. Creation of prompt and thin-sheet splashing by varying surface roughness or increasing air pressure. *Physical review letters* **109**, 054501 (2012).
- 144 Rioboo, R., Tropea, C. & Marengo, M. Outcomes from a drop impact on solid surfaces. *Atomization and Sprays* **11** (2001).
- 145 Farsari, M., Filippidis, G. & Fotakis, C. Fabrication of three-dimensional structures by three-photon polymerization. *Optics letters* **30**, 3180-3182 (2005).
- 146 San Lee, J., Weon, B. M., Je, J. H. & Fezzaa, K. How does an air film evolve into a bubble during drop impact? *Physical review letters* **109**, 204501 (2012).
- 147 Agbaglah, G. *et al.* Drop impact into a deep pool: vortex shedding and jet formation. *Journal of fluid mechanics* **764** (2015).



- 148 Kolinski, J. M., Mahadevan, L. & Rubinstein, S. Drops can bounce from perfectly hydrophilic surfaces. *EPL (Europhysics Letters)* **108**, 24001 (2014).
- 149 Josserand, C. & Thoroddsen, S. T. Drop impact on a solid surface. *Annual review of fluid mechanics* **48**, 365-391 (2016).
- 150 Gingell, D. & Todd, I. Interference reflection microscopy. A quantitative theory for image interpretation and its application to cell-substratum separation measurement. *Biophysical Journal* **26**, 507-526 (1979).
- 151 Wiegand, G., Jaworek, T., Wegner, G. & Sackmann, E. Studies of structure and local wetting properties on heterogeneous, micropatterned solid surfaces by microinterferometry. *Journal of colloid and interface science* **196**, 299-312 (1997).
- 152 Manukyan, G., Oh, J., Van Den Ende, D., Lammertink, R. G. & Mugele, F. Electrical switching of wetting states on superhydrophobic surfaces: a route towards reversible Cassie-to-Wenzel transitions. *Physical review letters* **106**, 014501 (2011).
- 153 Couder, Y., Fort, E., Gautier, C.-H. & Boudaoud, A. From bouncing to floating: noncoalescence of drops on a fluid bath. *Physical review letters* **94**, 177801 (2005).
- 154 Terwagne, D., Vandewalle, N. & Dorbolo, S. Lifetime of a bouncing droplet. *Physical Review E* **76**, 056311 (2007).
- 155 van der Veen, R. C., Tran, T., Lohse, D. & Sun, C. Direct measurements of air layer profiles under impacting droplets using high-speed color interferometry. *Physical Review E* **85**, 026315 (2012).
- 156 de Ruiter, J., Mugele, F. & van den Ende, D. Air cushioning in droplet impact. I. Dynamics of thin films studied by dual wavelength reflection interference microscopy. *Physics of fluids* **27**, 012104 (2015).
- 157 Kolinski, J. M. *et al.* Skating on a film of air: drops impacting on a surface. *Physical review letters* **108**, 074503 (2012).
- 158 Chander, S., Alaboyun, A. & Aplan, F. in *Proceedings of the Third Symposium on Respirable Dust in the Mineral Industries*. 193-202 (Society for Mining, Metallurgy & Exploration Littleton, CO).
- 159 Duchemin, L. & Josserand, C. Curvature singularity and film-skating during drop impact. *Physics of Fluids* **23**, 091701 (2011).
- 160 Klaseboer, E., Manica, R. & Chan, D. Y. Universal behavior of the initial stage of drop impact. *Physical review letters* **113**, 194501 (2014).
- 161 Bouwhuis, W., Hendrix, M. H., van der Meer, D. & Snoeijer, J. H. Initial surface deformations during impact on a liquid pool. *Journal of fluid mechanics* **771**, 503-519 (2015).
- 162 Tran, T., de Maleprade, H., Sun, C. & Lohse, D. Air entrainment during impact of droplets on liquid surfaces. *Journal of Fluid Mechanics* **726**, R3 (2013).
- 163 Mandre, S., Mani, M. & Brenner, M. P. Precursors to splashing of liquid droplets on a solid surface. *Physical review letters* **102**, 134502 (2009).
- 164 Hicks, P. D. & Purvis, R. Air cushioning and bubble entrapment in three-dimensional droplet impacts. *Journal of Fluid Mechanics* **649**, 135-163 (2010).
- 165 Hicks, P. D. & Purvis, R. Liquid–solid impacts with compressible gas cushioning. *Journal of Fluid Mechanics* **735**, 120-149 (2013).
- 166 Duchemin, L. & Josserand, C. Rarefied gas correction for the bubble entrapment singularity in drop impacts. *Comptes Rendus Mécanique* **340**, 797-803 (2012).

- 167 Driscoll, M. M. & Nagel, S. R. Ultrafast interference imaging of air in splashing dynamics. *Physical review letters* **107**, 154502 (2011).
- 168 de Ruiter, J., Oh, J. M., van den Ende, D. & Mugele, F. Dynamics of collapse of air films in drop impact. *Physical review letters* **108**, 074505 (2012).
- 169 Pan, K.-L. & Law, C. K. Dynamics of droplet–film collision. *Journal of fluid mechanics* **587**, 1-22 (2007).
- 170 Gilet, T. & Bush, J. W. Droplets bouncing on a wet, inclined surface. *Physics of Fluids* **24**, 122103 (2012).
- 171 Tang, X., Saha, A., Law, C. K. & Sun, C. Nonmonotonic response of drop impacting on liquid film: mechanism and scaling. *Soft matter* **12**, 4521-4529 (2016).
- 172 Page, S. J. Relationships between electrostatic charging characteristics, moisture content, and airborne dust generation for subbituminous and bituminous coals. *Aerosol Science & Technology* **32**, 249-267 (2000).
- 173 Johnston, A., Vincent, J. & Jones, A. Measurements of electric charge for workplace aerosols. *The Annals of occupational hygiene* **29**, 271-284 (1985).
- 174 Nieh, S. & Nguyen, T. MEASUREMENT AND CONTROL OF ELECTROSTATIC CHARGES ON PULVERIZED COAL IN A PNEUMATIC PIPELINE\*. *Particulate science and technology* **5**, 115-130 (1987).
- 175 Marx, D., Tuckerman, M. E., Hutter, J. & Parrinello, M. The nature of the hydrated excess proton in water. *Nature* **397**, 601 (1999).
- 176 Gong, X. *et al.* A charge-driven molecular water pump. *Nature nanotechnology* **2**, 709 (2007).
- 177 Tessum, M. W. & Raynor, P. C. Effects of spray surfactant and particle charge on respirable coal dust capture. *Safety and health at work* **8**, 296-305 (2017).
- 178 Pack, M., Kaneelil, P., Kim, H. & Sun, Y. Contact Line Instability Caused by Air Rim Formation under Nonsplashing Droplets. *Langmuir* **34**, 4962-4969 (2018).
- 179 Richard, D. & Quéré, D. Bouncing water drops. *EPL (Europhysics Letters)* **50**, 769 (2000).
- 180 Antonini, C., Bernagozzi, I., Jung, S., Poulikakos, D. & Marengo, M. Water drops dancing on ice: how sublimation leads to drop rebound. *Physical review letters* **111**, 014501 (2013).
- 181 Chandra, S. & Avedisian, C. On the collision of a droplet with a solid surface. *Proc. R. Soc. Lond. A* **432**, 13-41 (1991).
- 182 Biance, A.-L., Chevy, F., Clanet, C., Lagubeau, G. & Quéré, D. On the elasticity of an inertial liquid shock. *Journal of Fluid Mechanics* **554**, 47-66 (2006).
- 183 Tran, T., Staat, H. J., Prosperetti, A., Sun, C. & Lohse, D. Drop impact on superheated surfaces. *Physical review letters* **108**, 036101 (2012).
- 184 Gilet, T., Terwagne, D., Vandewalle, N. & Dorbolo, S. Dynamics of a bouncing droplet onto a vertically vibrated interface. *Physical review letters* **100**, 167802 (2008).
- 185 Gilet, T. & Bush, J. W. The fluid trampoline: droplets bouncing on a soap film. *Journal of Fluid Mechanics* **625**, 167-203 (2009).
- 186 de Ruiter, J., Lagraauw, R., Mugele, F. & van den Ende, D. Bouncing on thin air: how squeeze forces in the air film during non-wetting droplet bouncing lead to momentum transfer and dissipation. *Journal of fluid mechanics* **776**, 531-567 (2015).

- 187 van der Veen, R. C. *et al.* How microstructures affect air film dynamics prior to drop impact. *Soft matter* **10**, 3703-3707 (2014).
- 188 Wenzel, R. N. Resistance of solid surfaces to wetting by water. *Industrial & Engineering Chemistry* **28**, 988-994 (1936).
- 189 Chen, L., He, X., Liu, H., Qian, L. & Kim, S. H. Water Adsorption on Hydrophilic and Hydrophobic Surfaces of Silicon. *The Journal of Physical Chemistry C* **122**, 11385-11391 (2018).
- 190 Zhao, G. *et al.* Structure and properties of water film adsorbed on mica surfaces. *The Journal of chemical physics* **143**, 104705 (2015).
- 191 Tsai, P., Hendrix, M. H., Dijkstra, R. R., Shui, L. & Lohse, D. Microscopic structure influencing macroscopic splash at high Weber number. *Soft Matter* **7**, 11325-11333 (2011).
- 192 Kannan, R. & Sivakumar, D. Drop impact process on a hydrophobic grooved surface. *Colloids and Surfaces A: Physicochemical and Engineering Aspects* **317**, 694-704 (2008).
- 193 Soto, D., De Larivière, A. B., Boutillon, X., Clanet, C. & Quéré, D. The force of impacting rain. *Soft matter* **10**, 4929-4934 (2014).
- 194 Mundo, C., Sommerfeld, M. & Tropea, C. Droplet-wall collisions: experimental studies of the deformation and breakup process. *International journal of multiphase flow* **21**, 151-173 (1995).
- 195 Xu, L., Zhang, W. W. & Nagel, S. R. Drop splashing on a dry smooth surface. *Physical review letters* **94**, 184505 (2005).

### 3 Measurement of Instability of Thin Liquid Films by Synchronized Tri-wavelength Reflection Interferometry Microscope\*

\* The material contained in this chapter has been published in *Langmuir*, reused with permission. Full citation: Gao Y, Pan L. *Measurement of instability of thin liquid films by synchronized tri-wavelength reflection interferometry microscope. Langmuir. 2018 Oct 22;34(47):14215-25.*

#### 3.1 Introduction

Quantification of critical rupture thickness of the thin liquid films (TLFs) of water formed between air bubbles and surfaces is fundamental to many processes ranging from ore beneficiation,<sup>1</sup> bitumen extraction,<sup>2,3</sup> firefighting foam generation,<sup>4,5</sup> and theranostic applications.<sup>6</sup> All of these applications involve the interactions between air bubbles and other surfaces in water.<sup>7</sup> Ore beneficiation by the froth flotation process, for instance, involves a collision of dispersed air bubbles and solid particles in water. When air bubbles are brought sufficiently closer to the surfaces of particles in water, the TLF formed between them ruptures followed by a spreading of three-phase contact lines.<sup>8-10</sup>

The rupture of the TLFs is thermodynamically spontaneous when the change in the Gibbs free energy ( $\Delta G$ ) is less than zero.<sup>11</sup> For instance, the TLF of pure water between two air bubbles, i.e. a foam film, is highly unstable. From a fluid dynamic perspective, the film rupture is manifested as a catastrophically bridging of two surfaces in water accompanied by a vanishing of the confining liquid films. The film rupture might be attributed to the attractive disjoining pressures ( $\Pi$ ) in the TLFs coupled with a growth of fluctuation waves.<sup>12,13</sup> A positive  $\Pi$  resists film thinning resulting in the formation of an equilibrium film.<sup>14</sup> When the  $\Pi$  becomes negative, the film becomes unstable and ruptures at a critical rupture thickness ( $h_c$ ). This model assumes that the rupture occurs at  $h_c$ , at which the gradient of the disjoining pressure reaches a critical value.<sup>15,16</sup> The negative  $\Pi$  might originate from hydrophobic force,<sup>17-19</sup> electrostatic double layer force,<sup>20-23</sup> van der Waals force,<sup>24</sup> or a combination of these forces.<sup>25</sup> To validate this model, accurate measurements of  $h_c$  and  $\Pi$  are prerequisite. Measurements of  $\Pi$  in unstable TLFs have been described elsewhere.<sup>17,26</sup>

Over the last few decades, researchers have experimentally measured the critical rupture thickness of unstable TLFs between two surfaces.<sup>27-30</sup> These measurements were conducted by bringing two surfaces into close proximity, with the separation distance, i.e. film thickness of the TLFs, monitored by means of the microinterferometry technique.<sup>31</sup> Early research efforts have been focused on foam films<sup>27</sup> and wetting films.<sup>28-30</sup>

Much of past research showed that the critical rupture thickness varied with water chemistry, surface hydrophobicity, and bubbles sizes.<sup>16,22,29,32,33</sup> For example, Yoon et al. showed that the  $h_c$  value increased from 60 nm to 140 nm when the water contact angles

of hydrophobic silica surfaces increased from  $75^\circ$  to  $103^\circ$ .<sup>29</sup> These  $h_c$  values were obtained with 4-mm size air bubbles. A similar study showed that the  $h_c$  value was approximately 205 nm when an air bubble of 1.2 mm in radius was moved towards a hydrophobic glass surface of a water contact angle of  $62.5^\circ$ .<sup>34</sup> Recently, Shi et al. showed that the  $h_c$  was approximately 11 nm in 100 mM NaCl solutions between a 60-100  $\mu\text{m}$  radius air bubble and a hydrophobic surface of  $90^\circ$  water contact angle.<sup>26</sup> It is evident that the previously reported  $h_c$  values were largely inconsistent even though the water contact angles of solid surfaces were closely the same. Despite that many possible theories for film rupture have been proposed,<sup>35,36</sup> the underlying reason for such discrepancies is yet to be elucidated. Blake and Kitchener commented that the critical rupture thickness might be sensitive to surface asperity or trace contamination.<sup>30</sup>

The study of wetting films is often subjected to a scrutiny of surface contamination,<sup>37</sup> surface roughness,<sup>38</sup> and nanobubble formation.<sup>39</sup> Soft materials, such as air bubbles and oil droplets in water, are smooth at an atomic level by surface tensions.<sup>40</sup> However, the inconsistency regarding the  $h_c$  values is still ubiquitous.<sup>19,41</sup> For instance, the  $h_c$  value was estimated to be approximately 3 nm for the TLFs between two micrometer-sized oil droplets in 0.5 M NaCl solutions,<sup>19</sup> and  $\sim 5\text{nm}$  between two identical air bubbles (radii 74  $\mu\text{m}$ ).<sup>42</sup> These results were obtained through AFM force measurements. On the contrary, spatiotemporal profiles of TLFs between two millimeter-sized air bubbles showed that the film ruptured at an  $h_c$  in the range of 25-35 nm.<sup>41</sup> Noticeably, the sizes of liquid droplets or air bubbles used in those measurements are different due to instrumental limitations. The sizes of droplets employed in the AFM measurements are in the order of 100  $\mu\text{m}$ , while those used in SFA or Scheludko cells are in the order of 1 mm.

Despite the fact that the technique for measuring the film thickness has been established since 1960s, the determination of critical rupture thickness for highly unstable TLFs is challenging.<sup>33</sup> The conventional monochromatic interferometry method involves a step in determining the orders of fringes. For stable TLFs, the order of fringes can be back calculated from the reference point, at which the equilibrium film thickness is reached. For unstable TLFs, a determination of the film thickness is difficult due to a lack of reference points. One assumption might be that the TLF ruptures at an  $h_c$  of 60-220 nm.<sup>15</sup> Other verification methods might include 1) direct force measurement,<sup>17,43</sup> and 2) characterization of spatial deformation of the TLFs.<sup>18</sup> The latter method is established in that the spatial deformation is governed by the hydrodynamic force which is dependent on both film thickness and approaching speed. These calibration methods might not be applicable to the case when the  $h_c$  is beyond 220 nm, where both the surface and hydrodynamic forces become negligible.

Recent advances have been made to obtain accurate information on critical rupture thickness of the TLFs. A dual-wavelength interferometry technique was introduced to determine the separation distance between air bubbles and solid surfaces,<sup>34</sup> which was originally developed by Schilling et al.<sup>44</sup> This method records monochromatic interference fringes at two different wavelengths separately. From two recorded videos, one can determine the absolute thickness of the equilibrium film. In a similar manner,

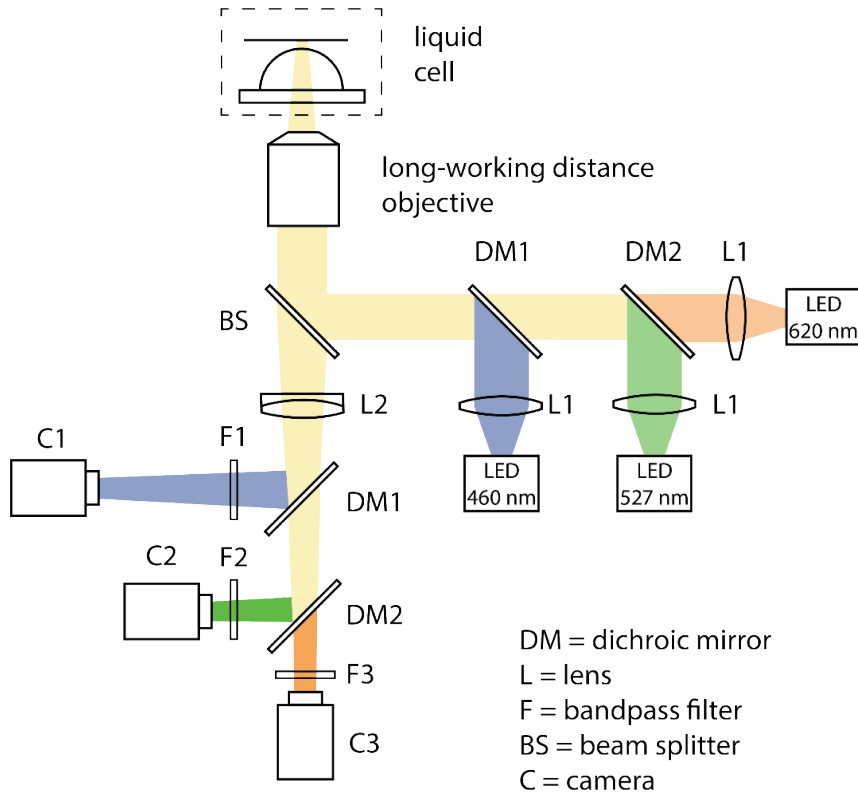
Yoon and Yordan converted the intensity of interference fringes to the reflectance at two different wavelengths ( $\lambda = 533$  and  $600$  nm), which were in turn used to determine the film thickness.<sup>29</sup> Both methods assume that each measurement is reproducible, which might be the case for equilibrium films and unstable films with a consistent  $h_c$ . Other calibration method includes white-light interferometry technique that yields an accurate measurement of film thicknesses.<sup>45,46</sup> This method generates the fringes of equal chromatic orders (FECO) by directing the white light transmitted through a thin gap to a spectrometer. From the FECO images, Horn and his colleagues were able to determine the time evolution of the separation distance of mercury droplets and a mica surface in electrolyte solutions as well as between air bubbles and solid surfaces.<sup>47,48</sup> Unfortunately, this method might be limited to axially symmetric TLFs.

An ability to accurately determine the critical rupture thickness of highly unstable TLFs is essential to better understand the underlying mechanisms of film rupture. In the present work, a Synchronized Tri-wavelength Interferometry Microscope (STRIM) was developed in-house to determine the film thickness between two surfaces in water. The STRIM technique was built using off the shelf optical components coupled with an inverted microscope. The three synchronized high-speed cameras record monochromatic interference fringes at three different wavelengths simultaneously at a rate of 150-300 frames per seconds. These fringes are then analyzed to determine the film thickness using a least square method or a trial-and-error method. The STRIM technique allows for an accurate film thickness measurement without any calibrations. The objective of these experiments is to better understand the effect of air bubble sizes and different hydrophobic surfaces on film instability. The result will be used to discuss rupture mechanisms of TLFs between two hydrophobic surfaces in water.

## 3.2 Instrumentation

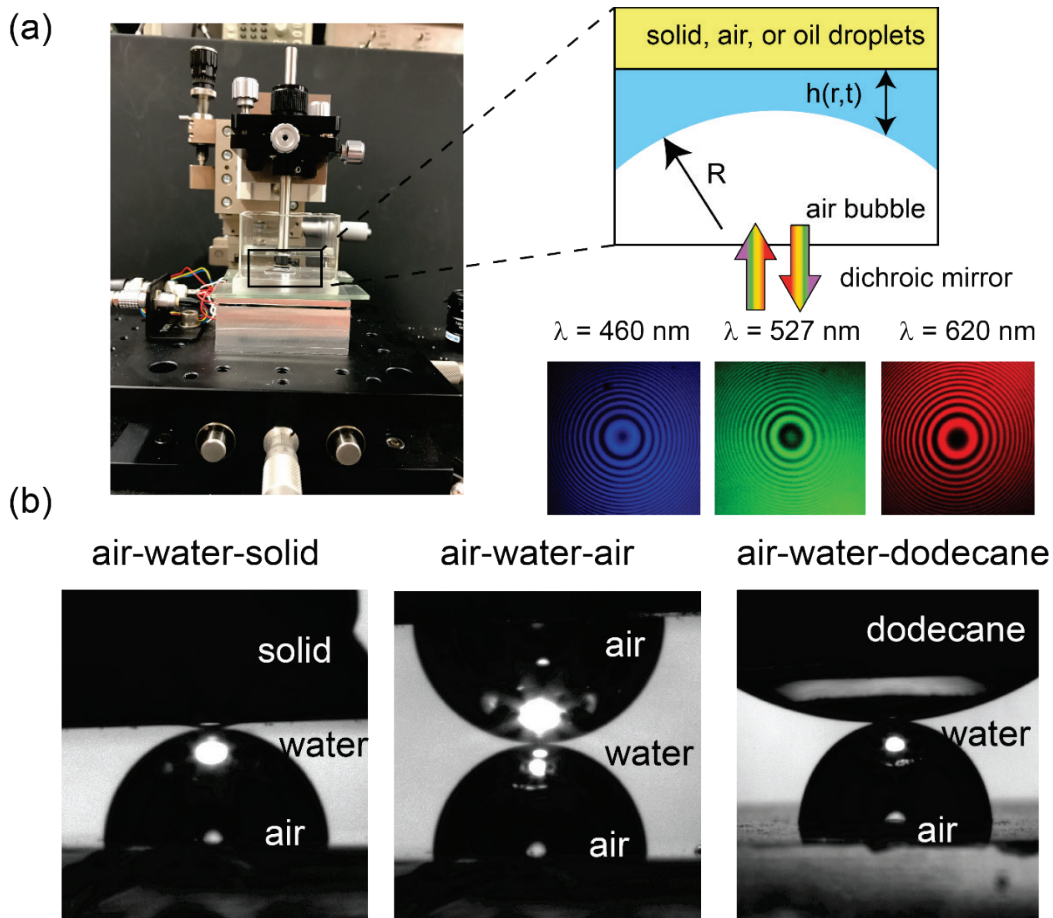
### Instrument Design

Fig. 3.1 shows an optical setup of the Synchronized Tri-Wavelength Reflection Interferometry Microscopy (STRIM) that was developed in this work. The STRIM instrument is built upon an Olympus IX73 inverted microscope using a customized 3-wavelength high-power LED system for white-light illumination. This illumination system combines the output of three LEDs into a single collimated beam. In this system, three color LEDs (PT121-TE, luminous) are used as light source and controlled by a high-current LED driver (DK-136M, luminous). The colored light emitted from the LED array are collimated using aspheric condenser lenses, and subsequently combined using two dichroic mirrors (DM1 and DM2) having cut-off wavelengths of 495 nm and 565 nm, respectively. Passive heat sink modules are used for the LEDs to eliminate vibrations from the fans used. All optomechanical components and optical elements were obtained from Thorlabs and Chroma.



**Figure 3.1** Optical setup of the Synchronized Tri-wavelength Reflection Interferometry Microscope (STRIM).

Fig. 3.2a shows a photo of a STRIM system that was designed and developed to study the interactions between a hemispherical air bubble and a surface in water. The surface can be a flat solid surface, a hemispherical air bubble, or a hemispherical liquid droplet as shown in Fig. 3.2b. In using this instrument, a customized liquid cell module is mounted on an IX73 inverted microscope. The liquid cell module sits on a piezo stage that allows the cell module to move up and down with a maximum travelling distance of 15  $\mu\text{m}$ . A multi-axis translational stage is installed to control the positions of air bubbles and substrates. In each experiment, a hemispherical air bubble is placed on the bottom of a glass container filled with water. The air bubble is brought closer to the upper surface by the piezo stage. The closing of the two surfaces formed a thin liquid film in between.



**Figure 3.2** a) a photo and schematic representation of the STRIM instrument developed in this study. b) side-view images of air-water-solid, air-water-air, and air-water-dodecane interaction.

When light passes through the liquid gap, the interference of two reflected light beams at the adjoining curved interface creates an interference pattern. The interference fringes of different wavelengths exit the microscope, and are separated by means of two dichroic mirrors (DM1 and DM2). The fringe images are captured by three synchronized CMOS cameras (Grasshopper3, FLIR) at different wavelengths. Short-pass filters ( $d\lambda = 10 \text{ nm}$  with 90% peak transmission) are installed in front of each camera with central wavelengths of 620, 527, and 460 nm, respectively. A frequency generator (AFG1022, Tektronix) is used to trigger cameras and control the frame rate. These cameras are capable of recording images at a maximum rate of 300 frames per second at a 600 x 600 pixel resolution. An infinity-corrected long-working distance objective (Mitutoyo) is used to observe optical fringes. The magnification of the objective can be calibrated using a standard stage micrometer (Thorlabs).



The interference fringes are used to determine the film thickness based on the principle of interferometry. By analyzing the changes in intensities at each pixel point across the interference fringes, the film thickness  $h$  over a range of  $r$  and  $t$  can be determined, where  $r$  is the radial distance from the symmetry axis of the liquid film and  $t$  is the elapsed time.<sup>49</sup> The image processing is done using a custom-written Matlab program. The underlying principle will be described in the following session.

### Thickness Measurement

In principle, when light waves pass through a thin gap between two surfaces, a fraction of the light waves are reflected at two adjoining interfaces. The two reflected light waves are superimposed creating an interference pattern. Depending on the geometry of the thin gap, the interference fringe pattern might vary. For a hemispherical air bubble against a flat surface in water, Newton's rings are formed.

The intensity profile of the interference pattern is given as,<sup>44</sup>

$$I = I_1 + I_2 + 2\sqrt{I_1 I_2} \cos\left(\frac{4\pi n h}{\lambda} + \delta\right) \quad (1)$$

where  $I_1$  and  $I_2$  are the intensities of light waves reflected from two adjoining interfaces of the thin liquid films. In Eq. (1), the optical path length ( $2nh$ ) is a product of twice the film thickness ( $h$ ) of the thin gap and the reflective index ( $n$ ) of the medium in which the light propagates,  $\lambda$  is the light wavelength, and  $\delta$  is the phase shift of the light reflected from the interfaces. The  $\delta$  value is determined from the reflective indexes ( $n, k$ ) of the media using a matrix of a multilayer system.<sup>50</sup> Herein,  $\delta = \pi$  and  $0$  in the thin liquid films formed between an air bubble and a silicon surface, and between two air bubbles, respectively. The film thickness calculation at the outer region of the TLF might be corrected due to the change in the optical path associated with the curvature of the air bubbles.<sup>51</sup> In the present work, the film thickness is determined at the maximum radial position of consideration ( $r_{\max}$ ), where the inclination angle is in the range of  $1.8^\circ - 6.0^\circ$ . Thus, no corrections should be necessary in this work.

Newton's rings consist of concentrically alternating bright and dark rings. From the fringes,  $I_{\max}$  and  $I_{\min}$  values are the maximum and minimum intensities in each pattern when phase differences ( $4\pi n h/\lambda + \delta$ ) are even and odd multiples of  $\pi$ , respectively. At  $\delta=0$ , the film thickness at the maximum ( $I_{\max}$ ) and minimum ( $I_{\min}$ ) intensities are the even and odd multiples of  $\lambda/4n$ , respectively. Eq. [1] might be modified as,

$$\frac{2I - (I_{\max} + I_{\min})}{I_{\max} - I_{\min}} = \cos\left(\frac{4\pi n h}{\lambda} + \delta\right) \quad (2)$$

From Eq. (2),  $h$  can be determined if  $I_{\max}$ ,  $I_{\min}$  and  $n$  are known. In Eq. (2), the orders of fringes  $n$  are commonly determined from the reference point, at which the TLF reaches equilibrium.

However, a determination of value  $n$  may be challenging if the film ruptures at a thickness of above 200 nm. The three-wavelength interferometry method solves this challenge. Eq. (2) is a system of non-linear equations, and thus the  $h$  and  $n$  values can be determined using a least square approach when at least three  $I$  vs.  $\lambda$  data are available.

Alternatively, one can determine the order of fringes using a trial-and-error method. In using this method, the film thickness  $h(t)$  at a fixed  $r$  is iteratively determined from Eq. (2) using arbitrarily chosen fringe orders ( $n$ ) until the experimental data obtained at different  $\lambda$  overlaps. The trial-and-error method produces experimental data with high precision and accuracy, and the result will be discussed in the follow-up session.

### 3.3 Experimental section

#### Materials

Single-side polished silicon wafers were used as substrates in this study. Prior to thickness profile measurements, they were cleaned in a freshly-prepared piranha solution ( $\text{H}_2\text{SO}_4:\text{H}_2\text{O}_2 = 7:3$  by volume) at a temperature of 80 °C for 3 minutes, rinsed with deionized (DI) water, and dried in a nitrogen gas stream. A fraction of cleaned silicon wafers were rendered hydrophobic by immersing them in freshly prepared octadecyltrichlorosilane (OTS, 95%, Alfa Aesar) in toluene solutions. The surface hydrophobicity of the substrates was controlled by varying OTS concentrations and immersion duration. The hydrophobicity was determined by measuring water contact angles on the substrates using the sessile drop technique.<sup>52</sup> In preparing solutions, toluene solvent was dehydrated using 3Å molecular sieves to minimize self-polymerization of OTS molecules.<sup>53</sup> DI water with a resistivity of above 18.0 MΩ·cm was obtained from a Barnstead water purification system (Thermo Scientific). All glassware were cleaned in a saturated potassium hydroxide in isopropanol solution overnight, rinsed with DI water, and dried under a laminar hood.

For measuring bubble-bubble and bubble-oil interactions, hydrophobic quartz plates were used to anchor an air bubble or an oil droplet on surfaces. Polished fused quartz plates of 1/16" thick were obtained from Technical Glass Product and were cleaned in a piranha solution using the same procedure as described in the previous paragraph. The cleaned quartz plates were rendered hydrophobic by immersing them in a  $10^{-3}$  M OTS-in-toluene solution for 30 minutes, subsequently cleaned in chloroform ultrasonically for 5 minutes to remove excess OTS molecules on surfaces, and dried in a particle-free nitrogen gas stream. The obtained hydrophobic quartz plates exhibited water contact angles of 90°. The chemical n-Dodecane (99%) was purchased from Alfa Aesar and used as oil without further purification.

#### Experimental Procedures

Experimental studies have been undertaken for three cases: 1) bubble-solid interaction, 2) bubble-bubble interaction, and 3) bubble-oil interaction as shown in Fig. 2b. Air bubbles

of varying radii ( $R = 100 \mu\text{m} - 1.2 \text{ mm}$ ) were carefully placed on a hydrophobic quartz plate in a liquid cell using a gas-tight syringe. For interactions between two bubbles, the air bubble on the upper plate was created using a droplet transfer method.<sup>54</sup> In using this method, an air bubble was transferred from a mildly hydrophobized quartz plate to the upper hydrophobic quartz plate in water. The three-phase contact line for the air bubbles was assumed to be fixed with an unperturbed contact angle of  $90^\circ$ . The droplet transfer method was also employed to prepare a dodecane droplet on the upper quartz plate. The dodecane droplet exhibited a water contact angle of approximately  $150^\circ$  on hydrophobic solid surface along the water/dodecane/solid three-phase contact line, and the curvature radius of the dodecane droplet ( $R_d$ ) was estimated to be 3.0-5.0 mm. Since the curvature radius of the dodecane droplet was much larger than that of the air bubble, the principal radius of TLFs was the same as the radius of the air bubble.

An alignment procedure was carefully followed to ensure that the droplets were aligned at the same axis of symmetry. In this process, the position was adjusted by an xyz translational stage until the two reflected light from the two parabolic-shaped adjoining interfaces of the TLF overlapped with each other. A side-view camera was used to assist the alignment process.

The measurements were conducted in water and a  $10^{-2}$  M NaCl solution. In the  $10^{-2}$  M NaCl solutions, the Debye length ( $\kappa^{-1}$ ) is 3.04 nm.<sup>55</sup> In this case, the contributions from the electrostatic double-layer interaction ( $\Pi_e$ ) to the total disjoining pressure ( $\Pi$ ) is negligible at a separation distance of above 20 nm. Therefore, only the van der Waals dispersion and hydrophobic forces are considered in the context of the surface forces.

An air bubble was moved towards a fixed upper surface at a constant nominal velocity for a total travel distance of  $8 \mu\text{m}$ . The air bubble was then held at its final position for 15 seconds. Prior to each experiment, the upper plate was lowered until the initial closest distance was approximately  $6 \mu\text{m}$ , where an interference fringe became lightly visible in the camera. A piezoelectric-driven z-stage was used to move up the air bubble. The piezo was driven by a piezo controller (PDU150Cl, PiezoDriver), and the input signals were controlled using a National Instruments (NI) CompactDAQ platform system.

## 3.4 Results

### Bubbles vs Hydrophilic Solids

To illustrate both the accuracy and precision of the STRIM technique, we first present the result of an air bubble against a hydrophilic silica surface in DI water. In DI water, both van der Waals dispersion and electrostatic double-layer forces are monotonically repulsive, and thus a stable wetting film is maintained.<sup>56</sup> Fig. 3.3 shows the timed evolution of the interference fringes between an air bubble of  $835 \mu\text{m}$  in radius and a hydrophilic silicon surface. The air bubble was brought closer to the silicon surface at a constant nominal driving velocity of  $0.7 \mu\text{m/s}$ . Fig. 3.3b shows the pixel value of the center of the interference fringes as a function of the elapsed time at different

wavelengths. The intensity profiles were then used to determine the film thickness *vs.* elapsed time using the trial-and-error method as described above. In this case, the equilibrium film thickness was below 200 nm, and thus the order of fringes was zero.

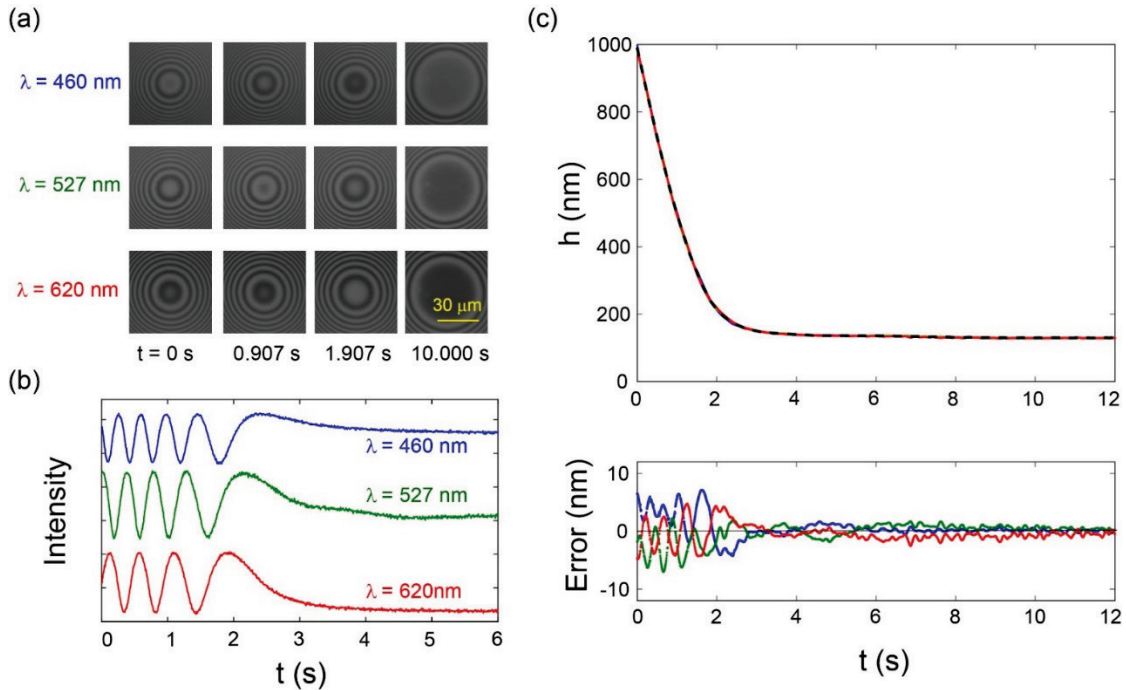


**Figure 3.3** Analysis of the interference fringes obtained at three different wavelengths to obtain the film thickness. a) a timed series of interference fringes at  $\lambda = 460$ , 527 and 60 nm; b) changes in pixel intensity at the center of the fringes as a function of time; c) film thickness as a function of the time at three different wavelengths. The smoothed film thickness is shown in black dashed line. The RMS error of the film thickness measurement is below 3 nm.

From the intensity profiles, the time evolution of film thicknesses at the center of the film,  $h(r=0,t)$  can be determined, with the result shown in Fig. 3.3c. The  $h$  *vs.*  $t$  plot was shown with the reference time  $t = 0$ , at which the closest separation distance was 1  $\mu\text{m}$ . As shown, the film thickness data obtained at three different wavelengths overlapped with each other. Also shown in Fig. 3c is the difference ( $\Delta h$ ) between each experimental data point and the smoothed value. The maximum error (peak-to-valley) was 10 nm and the RMS error was 1.41 nm, confirming the accuracy of film thickness measurements.

Note that the film thickness measurement at  $h > 400$  nm (RMS = 2.73 nm) exhibits less precision compared to those at  $h < 400$  nm (RMS = 0.76 nm). The poorer precision in film thickness measurements at  $h > 400$  nm might be attributed to two reasons associated with camera exposure time and image quality. First, the measurement is affected by thinning velocity. During the initial stage of film thinning, *i.e.*  $h > 400$  nm, the film thinning was governed by an external approach. During the later stage, *i.e.*  $h < 400$  nm, film thinning was decelerated by a repulsive surface force, and the film eventually

reached equilibrium. Since the camera's exposure time was fixed at 0.7 ms, the slower thinning velocity contributes to a higher resolution in film thickness measurements. Secondly, the lower precision might be attributed to a lower contrast of the interference fringes at  $h > 400$  nm compared to those obtained at  $h < 400$  nm.

The obtained  $h$  data along the radial extents ( $r$ ) of the film were used to construct the spatiotemporal thickness profile  $h(r,t)$ , with the result shown in Fig. 3.4. The data points in blue, green and red represent the film thickness data obtained at  $\lambda = 460, 527$  and  $620$  nm, respectively. At  $h > 300$  nm, the bubble/water interface exhibited a near-parabolic shape. As  $h$  was further decreased to below 300 nm, the bubble/water interface became flattened at the equilibrium thickness ( $h_e$ ). During this stage, the continuous approach of the air bubble expanded the extents of the flattened air bubble. Also shown in Fig. 3.4 is the difference,  $\Delta h$ , between experimental data points and a smoothed six-order polynomial fit. In this case, there are a total of 57 experimental data points, of which the maximum  $\Delta h$  is 3.8 nm and the RMS error is 0.6 nm, validating the accuracy of the measurement.

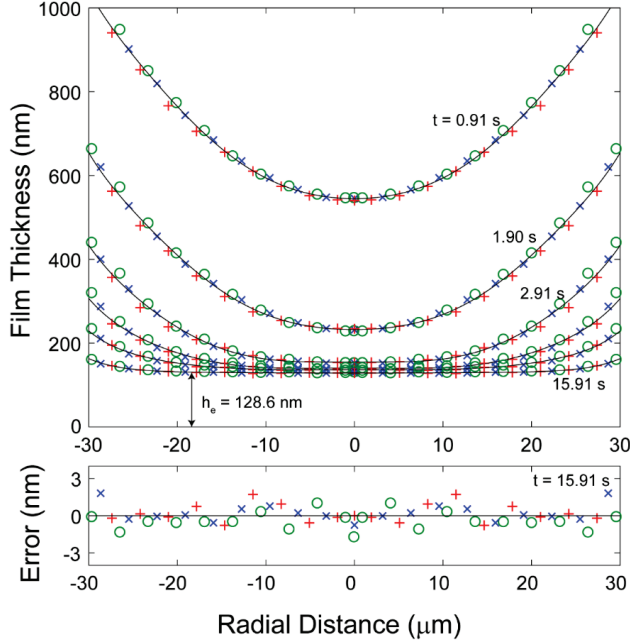


**Figure 3.4** Spatiotemporal thickness profiles of the thin liquid film (TLF) formed between an air bubble of 0.835 mm in radius and a hydrophilic silicon surface in water at an approaching velocity of  $0.7 \mu\text{m/s}$ .

The equilibrium thickness was determined to be 128 nm, which matched well with the theory. The disjoining pressure can be predicted using the classic DLVO theory,

$$\begin{aligned} \Pi &= \Pi_d + \Pi_e \\ &= -\frac{A_{132}}{6\pi h^3} - \frac{\epsilon\epsilon_0\kappa^2}{2\sinh(\kappa h)} \left[ (\psi_1^2 + \psi_2^2) \operatorname{cosech}(\kappa h) - 2\psi_1\psi_2 \coth(\kappa h) \right] \end{aligned} \quad (3)$$

In Eq. (3),  $\Pi_d$  and  $\Pi_e$  represent the contributions from the van der Waals and double-layer forces, respectively. The  $A_{132}$  ( $= -1 \times 10^{-20}$  J) is the Hamaker constant for the interaction between solid **1**, air **2**, and water **3** as calculated from the Lifshitz theory in the wetting films of water formed on silicon.<sup>55</sup> The second term represents the Hogg-Healey-Fuerstenau (HHF) approximation,<sup>57</sup> which is a function of double-layer potentials of silica ( $\psi_1$ ) and bubble ( $\psi_2$ ), respectively. Using  $\kappa^{-1} = 60$  nm,  $\psi_1 = -46$  mV,  $\psi_2 = -80$  mV, and  $p_c = 172$  N/m<sup>2</sup>, the Eq. (3) yields that  $h_e = 128$  nm, which agrees well with experimental data. Note that the  $h_e$  varies with  $p_c$  and  $\Pi$ . The former is governed by bubble sizes ( $R$ ) and surface tension of water ( $\gamma$ ), while the latter is determined by surface potentials and electrolyte concentrations. Thus, the equilibrium thickness can be reduced by adding electrolytes and reducing bubble sizes.<sup>30</sup>

### Bubble vs Hydrophobic Solids

In the case of an air bubble against a hydrophobic solid, the arising attractive hydrophobic force overcomes the repulsive van der Waals dispersion force, causing the film to rupture.<sup>18,30,49</sup> Fig. 3.5 compares two examples of the spatiotemporal thickness profiles of wetting films formed on hydrophobic quartz surfaces with two different sizes of air bubbles. The equilibrium contact angles of water on the hydrophobic surfaces are  $95^\circ$ , as measured by the sessile droplet method. The bubble size can be determined by fitting spatial thickness profiles at  $h > 1$   $\mu\text{m}$  to an unperturbed spherical shape using  $h = h_o + r^2/2R$ , where  $h_o$  is a fitting parameter,  $r$  is the radial distance from the axis of symmetry, and  $R$  is the bubble radius.<sup>58</sup> The  $R$  values were determined to be a) 0.942 mm and b) 0.169 mm, respectively. These experiments were carried out by moving the air bubble against the solid surface at a nominal velocity of  $0.7$   $\mu\text{m/s}$ .

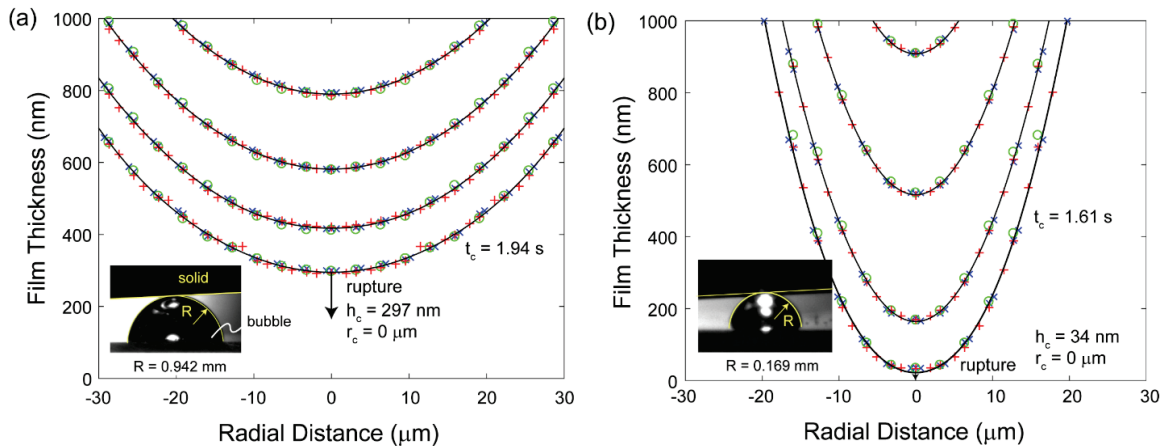


**Figure 3.5** Comparison of spatiotemporal thickness profiles of the thin liquid films (TLFs) of water between an air bubble of a) 0.942 mm and b) 0.169 mm in radius and a hydrophobic silicon surface of a water equilibrium contact angle of  $90^\circ$  in  $10^{-2}$  M NaCl solutions. The time interval between two adjacent profiles is 0.5 s.

The spatiotemporal profiles obtained using hydrophobic solid surfaces as the substrate show that a sudden rupture occurred within one video frame ( $\Delta t = 6$  ms), as indicated by arrows. At this moment, the closest separation distance is defined as the critical rupture thickness,  $h_c$ . From this point and beyond, the air bubble was plunged catastrophically onto the hydrophobic solid surface, signifying an onset of bubble-solid attachment. As shown in Fig. 3.5, the critical rupture thickness ( $h_c$ ) of one experiment using a 0.94 mm-radius air bubble was 297 nm, while that obtained at  $R = 0.169$  mm was 34 nm. The film rupture was followed by a spreading of the three-phase contact line until a finite contact angle (or receding angle) was established. The receding angles of the air bubbles on hydrophobic silicon surfaces in a  $10^{-2}$  M NaCl solution were determined to be approximately  $90^\circ$ .

Other characteristic of unstable TLFs include spatiotemporal profiles. The air bubble initially maintained a spherical shape at a large separation distance and became deformed by the external forces. For large air bubbles ( $R = 0.942$  mm), the air-water interface exhibited a near-parabolic shape, with the minimal separation distance occurring at the axis of symmetry prior to the film rupture. Such an unperturbed profile was attributed to a large critical rupture thickness ( $h_c = 297$  nm), at which both the hydrodynamic and surface forces were negligible.

For smaller bubbles, the extents of interfacial deformation at the air/water interface can be estimated by dividing capillary pressure ( $p_c$ ) from the total force ( $F$ ). The total force in TLFs consists of hydrodynamic and surface forces, with the former being determined using the Reynolds lubrication theory,<sup>59,60</sup>

$$F = \frac{6\pi\mu R^2}{h} \frac{dh}{dt} \quad (4)$$

where  $dh/dt$  is the thinning velocity, and  $\mu$  is viscosity. Eq. (4) shows that the hydrodynamic force is proportional to bubble radius while inversely proportional to film thickness. The  $p_c$  is equal to  $2\gamma/R$ , where  $R$  is the bubble radius and  $\gamma$  is the surface tension of water. At  $R = 0.169$  mm,  $h = 50$  nm and  $dh/dt = 0.7$   $\mu\text{m/s}$ , the hydrodynamic force is small ( $F = 7.53$  nN) while  $p_c$  is large ( $p_c = 852$  N/m<sup>2</sup>). These two factors result in a small deformation. The interfacial deformation of the TLFs under an influence of both hydrodynamic and surface forces has been numerically modelled using a combination of the lubrication theory and Young-Laplace equation,<sup>43,61</sup> and thus will not be discussed in the present work.

To further examine the effect of bubble sizes on the instability of wetting films formed on hydrophobic surfaces, a series of experiments were carried out with over 25 substrates over a 10-day experimental period. All substrates were prepared using the same procedure, and the water contact angle on each substrate was approximately  $95^\circ$ . Fig. 3.6 shows the result of the critical rupture thickness obtained at three different bubble size ranges. At  $R = 0.13$ – $0.26$  mm, the  $h_c$  values were narrowly distributed in a region of 17–55 nm with a medium rupture thickness of 27 nm with a few exceptions of above 60 nm.



When the bubble size was increased to 0.45-0.58 mm and 0.71-0.88 mm, the distribution of  $h_c$  became wider. For instance, at  $R = 0.71-0.88$  mm, over 90% of  $h_c$  values were distributed in the range of 57-184 nm, a range that was significantly wider than those obtained with small air bubbles. In addition, the mean rupture thickness was increased to 57 nm and 122 nm at  $R = 0.45-0.58$  mm and  $R = 0.71-0.88$  mm, respectively. This confirms that the critical rupture thickness decreases with decreasing the sizes of air bubble.

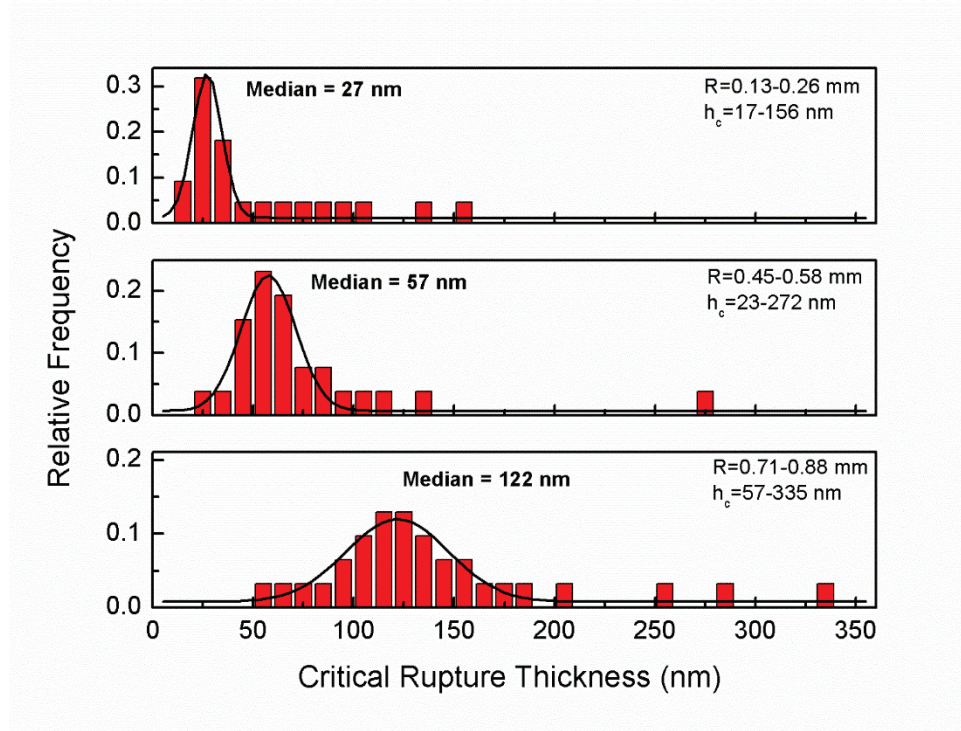


**Figure 3.6** Results of the critical rupture thicknesses of the TLF between air bubbles and hydrophobic silicon surfaces with water contact angles of  $90^\circ$ .

### Bubble vs Bubble

Measurements were extended to the interaction between two air bubbles in  $10^{-2}$  M NaCl solutions. The surfaces of air bubbles in water are atomically smooth due to the capillary pressure inside the air bubbles. Therefore, the effect of surface roughness is ignored. Fig. 3.7 shows the spatiotemporal thickness profiles of the TLFs between air bubbles of same radius at a)  $R = 0.915$  mm and b)  $R = 0.217$  mm. These experiments were conducted at an approaching velocity of  $0.7 \mu\text{m/s}$  in  $10^{-2}$  M NaCl solutions. For air bubbles which had  $R = 0.91$  mm, the TLF initially maintained the spherical shape at  $h > 300$  nm, where both hydrodynamic and surface forces were negligible. The film started to flatten at the radial extent when the closest separation distance was decreased to approximately 100 nm at  $t = 3.0$  s. As the lower air bubble was driven further towards the upper bubble surface, a dimple gradually developed. The dimple formation was attributed to the development of repulsive hydrodynamic forces. The rising repulsive forces were balanced by the surface



tension force, causing an interfacial deformation.<sup>62</sup> As the film continued to thin and reach a critical rupture thickness ( $h_c$ ), the film ruptured catastrophically. The  $h_c$  was determined from the last fringe image before the two air bubbles merged into one. At  $R = 0.915$  mm, the film ruptured at  $h_c = 40$  nm and  $r_c = 20$   $\mu$ m. The  $r_c$  is defined as the radial position where the film was ruptured. In general,  $r_c$  is where the closest separation distance occurs.

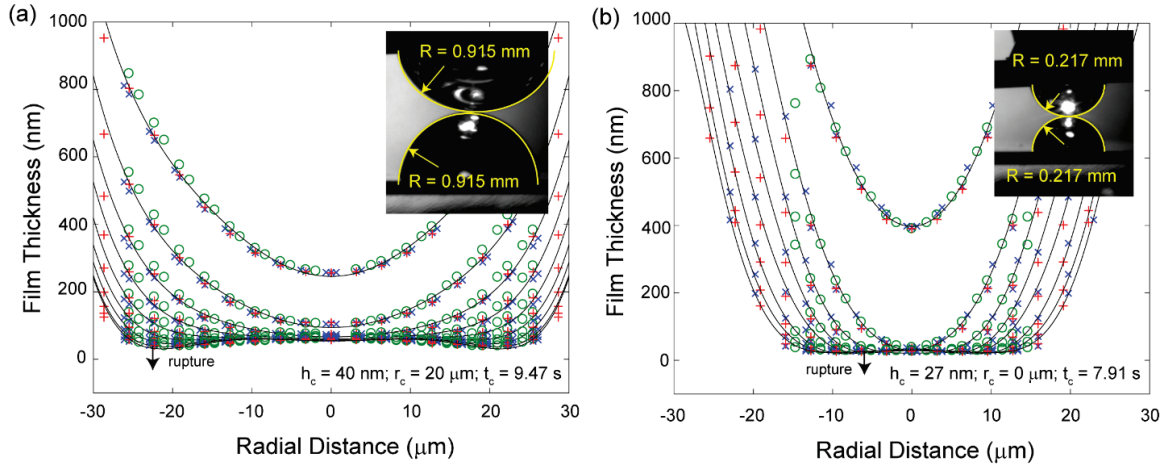


**Figure 3.7** Time evolution of spatiotemporal film profiles of TLFs formed between two air bubbles in  $10^{-2}$  M NaCl solutions at bubble sizes of a) 0.915  $\mu$ m and b) 0.217  $\mu$ m. The time interval between two adjacent profiles is 1 s.

For smaller air bubbles ( $R = 0.217$  mm), a flat film was formed. The flattened film expanded at the radial extent when the lower air bubble was driven towards the upper air bubble surfaces. During this stage, film thickness at the flat film region remained at the closest separation distance of approximately 30 nm. The film ruptured at  $h_c = 27$  nm,  $r_c \approx 7$   $\mu$ m, and  $t_c = 7.91$  s.

Fig. 3.8 shows the result of  $h_c$  obtained at different bubble radii. A total of 15 experiments were conducted over a 3-day experimental period. It was found that the  $h_c$  values increased with increasing bubble sizes. For instance, the  $h_c$  value increased from 26 nm at  $R = 0.25$  mm to 38 nm at  $R = 0.95$  mm. The reproducibility of the critical rupture thickness data was found to be within 5 nm. Note that the critical rupture thickness obtained in foam films between two air bubbles was much smaller and narrowly ranged than those obtained in wetting films formed on hydrophobic surfaces. The result indicates that there might be additional factors causing the rupture of wetting films compared to those for foam film. It is worthy of mentioning that with air bubbles of approximately 0.25 mm in radius, the critical rupture thickness of foam films is comparable to those of wetting films formed on hydrophobic surfaces having water with contact angles of  $95^\circ$ . The present result indicates that the use of small air bubbles with the sizes of below 0.25 mm eliminates some factors that being responsible for the film rupture.

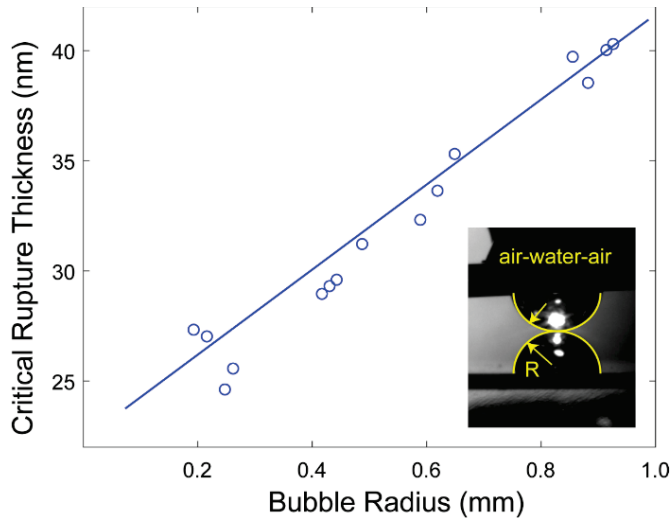


**Figure 3.8** Effect of bubble sizes on critical rupture thickness ( $h_c$ ) of the TLFs between two air bubbles.

### Bubble vs Dodecane

To further demonstrate the effect of surface hydrophobicity on critical rupture thickness, we investigated the interaction between air bubbles and dodecane droplets. Fig. 3.9 shows the result obtained between air bubbles and dodecane droplets in  $10^{-2}$  M NaCl solutions. Dodecane in  $10^{-2}$  M NaCl solution has a surface tension of 47 mN/m. Thus, the dodecane droplet in water is less hydrophobic than the air bubbles in water. The radius of the dodecane droplet was approximately 4.0 mm, while the sizes of air bubbles varied from 0.20 mm to 0.95 mm. The radii of the TLFs were determined experimentally from the spatiotemporal profiles. Three cases are shown, with  $R = 0.803$ , 0.645 and 0.307 mm, respectively. At  $R = 0.802$  mm, the critical rupture thickness  $h_c$  was found to be 30 nm. The  $h_c$  value decreased to 26 nm and 24 nm when the bubble radius ( $R$ ) was reduced to 0.645 and 0.307 mm, respectively.

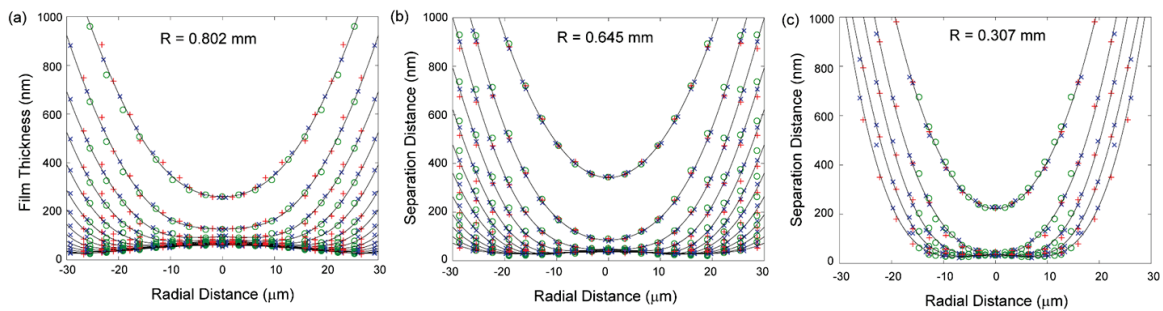


**Figure 3.9** Timed evolution of film profiles of the thin liquid films formed between an 8-mm diameter droplet of dodecane and an air bubble in  $10^{-2}$  M NaCl solutions using different sizes of air bubbles.

Other characteristics of the instability of TLFs include  $r_c$  and  $t_c$  as shown in Table 3.1. A comparison of the spatiotemporal profiles shows that the deformation of the TLF for larger air bubbles was much more significant than that for smaller air bubbles. For instance, the  $r_c = 28.12 \mu\text{m}$  at  $R = 0.803 \text{ mm}$ . When the  $R$  value was reduced to  $0.307 \text{ mm}$ , the  $r_c$  was reduced to  $7.19 \mu\text{m}$ , correspondingly. The interfacial deformation slowed down the thinning of film drainage, and subsequently increased the critical rupture time. As shown in Table 1, the critical rupture time,  $t_c$ , was decreased from  $15.65 \text{ s}$  at  $R = 0.803 \text{ mm}$  to  $5.39 \text{ s}$  at  $R = 0.307 \text{ mm}$ .

**Table 3.1** Characteristic parameters of film rupture at different bubble radius.

$R$ (mm)	$h_c$ (nm)	$t_c$ (s)	$r_c$ ( $\mu\text{m}$ )
0.802	30	15.65	28.12
0.645	26	12.27	12.81
0.307	24	5.39	7.19

Fig. 3.10 shows the critical rupture thickness of the TLFs formed between dodecane droplets and air bubbles of varying radii ranging from  $0.2 \text{ mm}$  to  $0.95 \text{ mm}$ . As shown, the  $h_c$  value decreased monotonically with decreasing bubble size. For instance, the  $h_c$  value decreased from  $32 \text{ nm}$  at  $R = 0.95 \text{ mm}$  to  $22 \text{ nm}$  at  $R = 0.20 \text{ mm}$ . The reduction in  $h_c$  values with decreasing bubble size might be attributed to a reduction in wave motions. Nevertheless, the result obtained in the asymmetric TLFs between air bubbles and dodecane droplets is consistent with those obtained in foam films between two air bubbles.

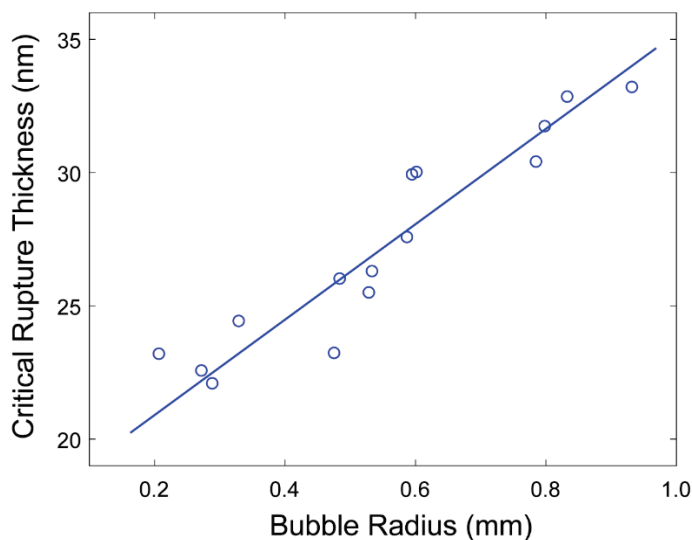


**Figure 3.10** Effect of bubble sizes on critical rupture thickness of the TLF of water between a droplet of dodecane and an air bubble in  $10^{-2}$  M NaCl solution.

### 3.5 Discussion

The present study provides direct experimental evidence that foam films in the absence of repulsive electrostatic double-layer forces are unstable and film rupture is spontaneous. The critical rupture thickness was found to have a range of 25-37 nm at bubble sizes of 0.20-0.95 mm. These values obtained in the present work were found to be larger than those obtained by AFM,<sup>42</sup> but comparable to those measured by bringing two millimeter-sized air bubbles into close proximity.<sup>41,63</sup> The present result agrees well with previous findings that the critical rupture thickness of foam films decreases with decreasing bubble size.<sup>13,63,64</sup>

Compared to the foam films formed between two air bubbles, the TLFs formed between air bubbles and dodecane droplets have slightly smaller critical rupture thicknesses. For instance, at  $R = 0.4$  mm, the  $h_c$  value between dodecane droplets and air bubbles was approximately 25 nm, while that obtained between two air bubbles was approximately 30 nm. Likewise, at  $R = 0.9$  mm, the  $h_c = 33$  nm for air-dodecane interaction, while  $h_c = 40$  nm for air-air interaction. The smaller critical rupture thickness obtained between dodecane droplets and air bubbles might be associated with a weaker hydrophobic interaction between oil droplets and air bubbles compared to those between two air bubbles.<sup>11,65</sup> It has been shown that air bubbles are more hydrophobic than both dodecane and hydrophobic substrates with water contact angles of  $95^\circ$ .<sup>65</sup> This result is consistent with the previous result on the coalescence of two air bubbles in water.<sup>66,67</sup>

Both air bubble and dodecane oil in water might be considered atomically smooth by large capillary pressures, and thus the effect of surface roughness can be negligible.<sup>40</sup> It has been shown that the  $h_c$  decreased with decreasing bubble sizes in both foam films and TLFs between air bubbles and dodecane droplets in water. Since film rupture is governed

by both attractive surface forces and surface fluctuational waves, the “true”  $h_c$  might be defined when the vibration of air bubbles is completely diminished.<sup>63</sup>

In this analysis, we extrapolated the  $h_c$  vs  $R$  curves to the  $h_c$  values at  $R = 0$  mm, where the film rupture is caused purely by attractive surface forces. The intercept of the fitted curves at  $R = 0$  mm in Fig. 8 and Fig. 10 yields that  $h_c = 20$  nm for foam films and  $h_c = 16$  nm for TLFs between an air bubble and a dodecane droplet. These values were obtained in  $10^{-2}$  M NaCl solutions, at which repulsive electrostatic double-layer forces minimized.

Assuming that the film rupture is driven by attractive surface forces at  $R = 0$  mm, the magnitudes of waves can be determined by subtracting the “true”  $h_c$  from the measured  $h_c$  values at different bubbles sizes. It has been found that the magnitudes of vibration of the bubble-bubble interaction increased from  $\sim 8$  nm at  $R = 0.3$  mm to  $\sim 18$  nm at  $R = 0.8$  mm. Likewise, the vibration magnitudes for bubble-dodecane interaction increased from  $\sim 8$  nm at  $R = 0.3$  mm to  $\sim 17$  nm at  $R = 0.8$  mm. Surprisingly, the magnitudes of waves for asymmetric TLFs are comparable to those for the symmetric TLFs between two air bubbles. Based on the present result, we concluded that the rupture of the TLF between two soft surfaces might be driven by hydrophobic interactions along with the additional factor contributing from the spontaneous growth of surface fluctuational waves. Note that the magnitudes of fluctuational waves obtained from the present work are comparable to the previous work.<sup>63</sup>

Compared to the TLF formed between two soft surfaces, the studies of wetting films on hydrophobic surfaces might be subjected to a scrutiny of surface contamination due to adsorption of trace dusts, nanobubbles, and other substances. Our present result shows that the  $h_c$  values obtained in wetting films formed on hydrophobic solid surfaces are correlated to bubble sizes. The critical rupture thickness obtained in the wetting films was much more widely distributed than those obtained between two soft surfaces. Some rupture events occurred at a film thickness above 250 nm, at which the effect of surface and hydrodynamic forces were negligible. The solid surfaces were polished silicon surfaces with an RMS roughness of below  $3\text{\AA}$ , and thus it is reasonable to assume that film rupture is not related to surface roughness. Even though the hydrophobic (OTS) coating might slightly increase surface roughness, surface roughness cannot be solely responsible for film rupture at a distance greater than 150 nm. One theory suggested that the rupture of the wetting films might be associated with a formation of “nanobubbles” in the vicinity of the hydrophobic surfaces.<sup>39</sup> In light of this, the rupture of the wetting films is essentially the rupture of foam films governed by attractive surface forces. In this regard, the critical rupture thickness should be independent of bubble sizes. In fact, we have shown that at  $R = 0.13\text{-}0.26$  mm, rupture thickness can be as small as 18 nm, at which the hydrophobic interaction might become the dominant factor.

It is unlikely that the wave motion as discussed above can cause the rupture of the wetting films on hydrophobic surfaces at a distance of 150 nm or above, at which the  $\Pi$  is negligible.<sup>24</sup> Instead, we hypothesize that a reduction in the critical rupture thickness with

decreasing the sizes of air bubbles might be associated with dissolved gas molecules in TLFs. When the film thickness is decreased to the critical rupture thickness, the dissolved gas molecules form a gas channel between air bubbles and hydrophobic solid surfaces causing the film to rupture. It should be noted that the formation of a gas channel is a random process, and its size might be associated with the volume of TLFs as well as the gas solubility. However, the rupture mechanism of unstable wetting films is rather complex and the proposed hypothesis will be tested in further investigation.

For an exceptionally large  $h_c$  of 300 nm or above, we cannot exclude the possibility of the adsorption of trace hydrocarbon contaminants from the water or from the air during the sample preparation, despite the effort taken to minimize surface contaminations. These trace contaminations are invisible under the light microscope. These nano-sized airborne contaminants are hydrophobic, and therefore be responsible for film rupture once being adsorbed on surfaces.<sup>68</sup>

The present result sheds new light onto the instability of TLFs with air bubbles. The STRIM technique achieves a  $\sim 1$  nm resolution in film thickness over a range of 0-1  $\mu\text{m}$  for unstable TLFs. The technique can be readily extended to study droplet-droplet and droplet-plate interaction in different media, such as immiscible liquid,<sup>69</sup> air,<sup>70,71</sup> and supercritical liquids.<sup>72,73</sup>

### 3.6 Summary and conclusions

In this work, a newly developed Synchronized Tri-wavelength Reflection Interferometry Microscope (STRIM) technique was in house developed to study the instability of unstable thin liquid films (TLFs) between air bubbles and various hydrophobic surfaces for the first time. The STRIM technique uses three synchronized high-speed cameras that record monochromatic interference fringes at three different wavelengths simultaneously. These three sets of monochromatic interference fringes can be used to obtain spatiotemporal profiles without any assumptions. The accuracy of the film thickness measurements was found to be within 1 nm over a range of 0- 200 nm and within 3 nm over the range of 200 – 1000 nm.

Results obtained between air bubbles and hydrophobic silicon surfaces showed that the critical rupture thicknesses scattered over a range of 57 – 335 nm, with a median rupture thickness of 122 nm, at bubble sizes of 0.71-0.88 mm. When the bubble sizes were reduced to 0.13-0.26 mm, the range of the critical rupture thicknesses was reduced to 17-156 nm, with a median rupture thickness of 27 nm. The present result indicates that the rupture of wetting films formed on hydrophobic surfaces might be associated with a formation of gas channels that effectively bridges hydrophobic solid plates and air bubbles in water.

Compared to wetting films formed on hydrophobic surfaces, the rupture thickness for foam films between two air bubbles in a  $10^{-2}$  M NaCl solution was much more consistent in the range of 22-45 nm. The critical rupture thicknesses were found to increase with

increasing bubble sizes, which is attributed to the increased fluctuation waves at the air/water interface. This result was compared with those obtained between one air bubble and one droplet of dodecane. It was found that the critical rupture thickness obtained between the air bubble and the droplet of dodecane was smaller than those obtained between two air bubbles, indicating that the critical rupture thickness of TLFs is correlated to the hydrophobicities of the interacting surfaces.

### 3.7 Reference

- 1 Derjaguin, B. V. & Dukhin, S. S. Theory of flotation of small and medium-size particles. *Trans. Inst. Min. Metall.* **70**, 221-246 (1961).
- 2 Tchoukov, P. *et al.* Role of Asphaltenes in Stabilizing Thin Liquid Emulsion Films. *Langmuir* **30**, 3024-3033, doi:10.1021/la404825g (2014).
- 3 Masliyah, J., Zhou, Z. J., Xu, Z., Czarnecki, J. & Hamza, H. Understanding Water-Based Bitumen Extraction from Athabasca Oil Sands. *The Canadian Journal of Chemical Engineering* **82**, 628-654, doi:doi:10.1002/cjce.5450820403 (2004).
- 4 Pugh, R. J. Foaming, foam films, antifoaming and defoaming. *Adv. Colloid Interface Sci.* **64**, 67-142 (1996).
- 5 Kennedy, M. J. *et al.* Bubble coarsening dynamics in fluorinated and non-fluorinated firefighting foams. *Colloids and Surf., A* **470**, 268-279, doi:<https://doi.org/10.1016/j.colsurfa.2015.01.062> (2015).
- 6 Schutt, E. G., Klein, D. H., Mattrey, R. M. & Riess, J. G. Injectable Microbubbles as Contrast Agents for Diagnostic Ultrasound Imaging: The Key Role of Perfluorochemicals. *Angew. Chem. Int. Ed.* **42**, 3218-3235, doi:doi:10.1002/anie.200200550 (2003).
- 7 Xing, Y. *et al.* Recent experimental advances for understanding bubble-particle attachment in flotation. *Advances in colloid and interface science* **246**, 105-132 (2017).
- 8 Ralston, J., Dukhin, S. S. & Mishchuk, N. A. Wetting film stability and flotation kinetics. *Adv. Colloid Interface Sci.* **95**, 145-236 (2002).
- 9 Yoon, R.-H. & Mao, L. Application of extended DLVO theory, IV: derivation of flotation rate equation from first principles. *Journal of colloid and interface science* **181**, 613-626 (1996).
- 10 Scheludko, A., Tschaljowska, S. & Fabrikant, A. Contact between a gas bubble and a solid surface and froth flotation. *Special Discussions of the Faraday Society* **1**, 112-117, doi:10.1039/SD9700100112 (1970).
- 11 van Oss, C. J. *Interfacial Forces in Aqueous Media*. 2nd Edition edn, (CRC Press, 2006).
- 12 Vrij, A. Possible mechanism for the spontaneous rupture of thin, free liquid films. *Discussions of the Faraday Society* **42**, 23-33 (1966).
- 13 Ivanov, I. B., Radoev, B., Manev, E. & Scheludko, A. Theory of the critical thickness of rupture of thin liquid films. *Transactions of the Faraday Society* **66**, 1262-1273, doi:10.1039/TF9706601262 (1970).
- 14 Derjaguin, B. On the repulsive forces between charged colloid particles and on the theory of slow coagulation and stability of lyophobic sols. *Transactions of the Faraday Society* **35**, 203-215, doi:10.1039/TF9403500203 (1940).
- 15 Schulze, H. J. Einige Untersuchungen über das Zerreißen dünner Flüssigkeitsfilme auf Feststoffoberflächen. *Colloid. Polym. Sci.* **253**, 730-737, doi:10.1007/BF02464456 (1975).



- 16 Mahnke, J., Schulze, H. J., Stckelhuber, K. W. & Radoev, B. Rupture of thin wetting films on hydrophobic surfaces: Part I: methylated glass surfaces. *Colloids Surf., A* **157**, 1-9 (1999).
- 17 Pan, L. & Yoon, R.-H. Measurement of hydrophobic forces in thin liquid films of water between bubbles and xanthate-treated gold surfaces. *Minerals Engineering* **98**, 240-250 (2016).
- 18 Pan, L., Jung, S. & Yoon, R. H. Effect of hydrophobicity on the stability of the wetting films of water formed on gold surfaces. *J. Colloid Interface Sci.* **361**, 321-330, doi:10.1016/j.jcis.2011.05.057 (2011).
- 19 Tabor, R. F., Wu, C., Grieser, F., Dagastine, R. R. & Chan, D. Y. C. Measurement of the Hydrophobic Force in a Soft Matter System. *The Journal of Physical Chemistry Letters* **4**, 3872-3877, doi:10.1021/jz402068k (2013).
- 20 Manica, R., Connor, J. N., Carnie, S. L., Horn, R. G. & Chan, D. Y. C. Dynamics of Interactions Involving Deformable Drops: Hydrodynamic Dimpling under Attractive and Repulsive Electrical Double Layer Interactions. *Langmuir* **23**, 626-637, doi:doi:10.1021/la0620760 (2007).
- 21 Jiang, L., Krasowska, M., Fornasiero, D., Koh, P. & Ralston, J. Electrostatic attraction between a hydrophilic solid and a bubble. *Physical Chemistry Chemical Physics* **12**, 14527-14533 (2010).
- 22 Aronson, M. P. & Princen, H. M. Aqueous films on silica in the presence of cationic surfactants. *Colloid. Polym. Sci.* **256**, 140-149, doi:10.1007/BF01679172 (1978).
- 23 Alexandrova, L., Pugh, R. J., Tiberg, F. & Grigorov, L. Confirmation of the Heterocoagulation Theory of Flotation. *Langmuir* **15**, 7464-7471, doi:10.1021/la981618d (1999).
- 24 Vrij, A. & Overbeek, J. T. G. Rupture of thin liquid films due to spontaneous fluctuations in thickness. *J. Am. Chem. Soc.* **90**, 3074-3078, doi:10.1021/ja01014a015 (1968).
- 25 Tchaliowska, S., Herder, P., Pugh, R., Stenius, P. & Eriksson, J. C. Studies of the contact interaction between an air bubble and a mica surface submerged in dodecylammonium chloride solution. *Langmuir* **6**, 1535-1543, doi:10.1021/la00100a002 (1990).
- 26 Shi, C. *et al.* Measuring forces and spatiotemporal evolution of thin water films between an air bubble and solid surfaces of different hydrophobicity. *ACS nano* **9**, 95-104 (2014).
- 27 Scheludko, A. Thin liquid films. *Adv. Colloid Interface Sci.* **1**, 391-464, doi:10.1016/0001-8686(67)85001-2 (1967).
- 28 Exerowa, D., Zacharieva, M., Cohen, R. & Platikanov, D. Dependence of the Equilibrium Thickness and Double-Layer Potential of Foam Films on the Surfactant Concentration. *Colloid. Polym. Sci.* **257**, 1089-1098 (1979).
- 29 Yoon, R. H. & Yordan, J. L. The Critical Rupture Thickness of Thin Water Films on Hydrophobic Surfaces. *J. Colloid Interface Sci.* **146**, 565-572 (1991).
- 30 Blake, T. D. & Kitchener, J. A. Stability of aqueous films on hydrophobic methylated silica. *J Chem Soc, Faraday Trans 1* **68**, 1435-1442 (1972).

- 31 Derjaguin, B. V. Theory of Capillary Condensation and Related Capillary Effects. Calculation of Spreading Action of Polymolecular Liquid Films. *Zh. Fiz. Khim.* **14**, 137-147 (1940).
- 32 Xie, L. *et al.* Interaction Mechanisms between Air Bubble and Molybdenite Surface: Impact of Solution Salinity and Polymer Adsorption. *Langmuir* **33**, 2353-2361, doi:10.1021/acs.langmuir.6b04611 (2017).
- 33 Mahnke, J., Schulze, H. J., Stckelhuber, K. W. & Radoev, B. Rupture of thin wetting films on hydrophobic surfaces. Part II: fatty acid Langmuir-Blodgett layers on glass surfaces. *Colloids and Surf., A* **157**, 11-20 (1999).
- 34 Zhang, X. *et al.* Simultaneous measurement of dynamic force and spatial thin film thickness between deformable and solid surfaces by integrated thin liquid film force apparatus. *Soft Matter* **12**, 9105-9114 (2016).
- 35 Sharma, A. & Ruckenstein, E. An analytical nonlinear theory of thin film rupture and its application to wetting films. *J. Colloid Interface Sci.* **113**, 456-479 (1986).
- 36 Sharma, A. & Ruckenstein, E. Dewetting of solids by the formation of holes in macroscopic liquid films. *J. Colloid Interface Sci.* **133**, 358-368, doi:[https://doi.org/10.1016/S0021-9797\(89\)80044-X](https://doi.org/10.1016/S0021-9797(89)80044-X) (1989).
- 37 Ducker, W. A., Xu, Z. & Israelachvili, J. N. Measurements of Hydrophobic and DLVO Forces in Bubble-Surface Interactions in Aqueous Solutions. *Langmuir* **10**, 3279-3289 (1994).
- 38 Krasowska, M. & Malysa, K. Kinetics of bubble collision and attachment to hydrophobic solids: I. Effect of surface roughness. *Int. J. Miner. Process.* **81**, 205-216, doi:<https://doi.org/10.1016/j.minpro.2006.05.003> (2007).
- 39 Stöckelhuber, K. W., Radoev, B., Wenger, A. & Schulze, H. J. Rupture of Wetting Films Caused by Nanobubbles. *Langmuir* **20**, 164-168, doi:10.1021/la0354887 (2004).
- 40 Tabor, R. F., Grieser, F., Dagastine, R. R. & Chan, D. Y. C. The hydrophobic force: measurements and methods. *PCCP* **16**, 18065-18075, doi:10.1039/C4CP01410C (2014).
- 41 Wang, L. Drainage and rupture of thin foam films in the presence of ionic and non-ionic surfactants. *Int. J. Miner. Process.* **102-103**, 58-68, doi:<https://doi.org/10.1016/j.minpro.2011.09.012> (2012).
- 42 Vakarelski, I. U. *et al.* Dynamic interactions between microbubbles in water. *Proc. Natl. Acad. Sci.* **107**, 11177-11182, doi:10.1073/pnas.1005937107 (2010).
- 43 Chan, D. Y. C., Klaseboer, E. & Manica, R. Theory of non-equilibrium force measurements involving deformable drops and bubbles. *Adv. Colloid Interface Sci.* **165**, 70-90, doi:DOI 10.1016/j.cis.2010.12.001 (2011).
- 44 Schilling, J., Sengupta, K., Goennenwein, S., Bausch, A. R. & Sackmann, E. Absolute interfacial distance measurements by dual-wavelength reflection interference contrast microscopy. *Physical Review E* **69**, 021901, doi:10.1103/PhysRevE.69.021901 (2004).
- 45 Israelachvili, J. N. Thin film studies using multiple-beam interferometry. *J. Colloid Interface Sci.* **44**, 259-272, doi:[http://dx.doi.org/10.1016/0021-9797\(73\)90218-X](http://dx.doi.org/10.1016/0021-9797(73)90218-X) (1973).

- 46 Glovnea, R. P., Forrest, A. K., Olver, A. V. & Spikes, H. A. Measurement of Sub-Nanometer Lubricant Films Using Ultra-Thin Film Interferometry. *Tribology Letters* **15**, 217-230, doi:10.1023/a:1024809102533 (2003).
- 47 Connor, J. N. & Horn, R. G. Measurement of Aqueous Film Thickness between Charged Mercury and Mica Surfaces: A Direct Experimental Probe of the Poisson–Boltzmann Distribution. *Langmuir* **17**, 7194-7197, doi:10.1021/la0155505 (2001).
- 48 Pushkarova, R. A. & Horn, R. G. Surface forces measured between an air bubble and a solid surface in water. *Colloid Surface A* **261**, 147-152, doi:DOI 10.1016/j.colsurfa.2004.10.132 (2005).
- 49 Pan, L. & Yoon, R.-H. Hydrophobic forces in the wetting films of water formed on xanthate-coated gold surfaces. *Faraday Discuss.* **146**, 325-340, doi:10.1039/b926937a (2010).
- 50 Macleod, H. A. *Thin-film optical filters, 3rd Ed.*, (Institute of Physics, 2001).
- 51 Wiegand, G., Neumaier, K. R. & Sackmann, E. Microinterferometry: Three-Dimensional Reconstruction of Surface Microtopography for Thin-Film and Wetting Studies by Reflection Interference Contrast Microscopy (RICM). *Appl. Opt.* **37**, 6892-6905, doi:10.1364/AO.37.006892 (1998).
- 52 Li, D., Cheng, P. & Neumann, A. W. Contact angle measurement by axisymmetric drop shape analysis (ADSA). *Adv. Colloid Interface Sci.* **39**, 347-382, doi:[https://doi.org/10.1016/0001-8686\(92\)80065-6](https://doi.org/10.1016/0001-8686(92)80065-6) (1992).
- 53 McGovern, M. E., Kallury, K. M. R. & Thompson, M. Role of Solvent on the Silanization of Glass with Octadecyltrichlorosilane. *Langmuir* **10**, 3607-3614, doi:10.1021/la00022a038 (1994).
- 54 Vakarelski, I. U. *et al.* Bubble Colloidal AFM Probes Formed from Ultrasonically Generated Bubbles. *Langmuir* **24**, 603-605, doi:10.1021/la7032059 (2008).
- 55 Israelachvili, J. *Intermolecular and Surface Force - 3rd ed.*, (Academic Press, 2011).
- 56 Churaev, N. V. & Zorin, Z. M. Wetting films. *Adv. Colloid Interface Sci.* **40**, 109-146, doi:Doi: 10.1016/0001-8686(92)80073-7 (1992).
- 57 Hogg, R., Healy, T. W. & Fuerstenau, D. W. Mutual coagulation of colloidal dispersions. *Trans. Faraday Soc.* **62**, 1638 - 1651, doi:10.1039/TF9666201638 (1966).
- 58 Carnie, S. L., Chan, D. Y. C., Lewis, C., Manica, R. & Dagastine, R. R. Measurement of Dynamical Forces between Deformable Drops Using the Atomic Force Microscope. I. Theory. *Langmuir* **21**, 2912-2922, doi:10.1021/la0475371 (2005).
- 59 Horn, R. G., Vinogradova, O. I., Mackay, M. E. & Phan-Thien, N. Hydrodynamic slippage inferred from thin film drainage measurements in a solution of nonadsorbing polymer. *J. Chem. Phys.* **112**, 6424-6433, doi:10.1063/1.481274 (2000).
- 60 Hardy, W. & Bircumshaw, I. Boundary Lubrication. Plane Surfaces and the Limitations of Amontons' Law. *Proceedings of the Royal Society of London. Series A, Containing Papers of a Mathematical and Physical Character* **108**, 1-27 (1925).

- 61 Chan, D. Y. C., Klaseboer, E. & Manica, R. Film drainage and coalescence  
between deformable drops and bubbles. *Soft Matter* **7**, 2235-2264 (2011).
- 62 Platikanov, D. Experimental Investigation on the Dimpling & of Thin Liquid  
Films. *J Phys. Chem.* **68**, 3619-3624, doi:doi:10.1021/j100794a030 (1964).
- 63 Radoev, B. P., Scheludko, A. D. & Manev, E. D. Critical thickness of thin liquid  
films: Theory and experiment. *J. Colloid Interface Sci.* **95**, 254-265,  
doi:[https://doi.org/10.1016/0021-9797\(83\)90094-2](https://doi.org/10.1016/0021-9797(83)90094-2) (1983).
- 64 Manev, E., Scheludko, A. & Exerowa, D. Effect of surfactant concentration on  
the critical thicknesses of liquid films. *Colloid. Polym. Sci.* **252**, 586-593,  
doi:10.1007/BF01558157 (1974).
- 65 Du, Q., Freysz, E. & Shen, Y. R. Surface Vibrational Spectroscopic Studies of  
Hydrogen Bonding and Hydrophobicity. *Science* **264**, 826-828 (1994).
- 66 Wang, L. G. & Yoon, R. H. Hydrophobic forces in thin aqueous films and their  
role in film thinning. *Colloid Surface A* **263**, 267-274, doi:DOI  
10.1016/j.colsurfa.2004.12.045 (2005).
- 67 Angarska, J. K. *et al.* Detection of the Hydrophobic Surface Force in Foam Films  
by Measurements of the Critical Thickness of the Film Rupture. *Langmuir* **20**,  
1799-1806, doi:10.1021/la0357514 (2004).
- 68 Li, Z. *et al.* Effect of airborne contaminants on the wettability of supported  
graphene and graphite. *Nat. Mater* **12**, 925, doi:10.1038/nmat3709  
<https://www.nature.com/articles/nmat3709#supplementary-information> (2013).
- 69 Shi, C. *et al.* Long-Range Hydrophilic Attraction between Water and  
Polyelectrolyte Surfaces in Oil. *Angew. Chem. Int. Ed.* **55**, 15017-15021,  
doi:doi:10.1002/anie.201608219 (2016).
- 70 van der Veen, R. C. A., Tran, T., Lohse, D. & Sun, C. Direct measurements of air  
layer profiles under impacting droplets using high-speed color interferometry.  
*Physical Review E* **85**, 026315, doi:10.1103/PhysRevE.85.026315 (2012).
- 71 Hendrix, M. H. W., Bouwhuis, W., van der Meer, D., Lohse, D. & Snoeijer, J. H.  
Universal mechanism for air entrainment during liquid impact. *J. Fluid Mech.*  
**789**, 708-725, doi:10.1017/jfm.2015.757 (2016).
- 72 Wan, J., Kim, Y. & Tokunaga, T. K. Contact angle measurement ambiguity in  
supercritical CO<sub>2</sub>-water-mineral systems: Mica as an example. *International  
Journal of Greenhouse Gas Control* **31**, 128-137,  
doi:<https://doi.org/10.1016/j.ijggc.2014.09.029> (2014).
- 73 Saraji, S., Goual, L., Piri, M. & Plancher, H. Wettability of Supercritical Carbon  
Dioxide/Water/Quartz Systems: Simultaneous Measurement of Contact Angle  
and Interfacial Tension at Reservoir Conditions. *Langmuir* **29**, 6856-6866,  
doi:10.1021/la3050863 (2013).

## 4 Understanding the Mechanism of Froth Flotation of Molybdenite Using Oily Collectors from a Perspective of Thinning and Rupture of Thin Liquid Film\*

\*The material contained in this chapter has been submitted to a peer-reviewed journal: *Minerals Engineering*.

### 4.1 Introduction

Molybdenum is an essential metal that is used in high-strength steel alloys and other chemical applications <sup>1</sup>. To date, over 50% of molybdenum production comes from molybdenite in porphyry Cu-Mo ores <sup>2</sup>. The head grade of molybdenite in these ore bodies is typically less than 0.1% <sup>3</sup>, and froth flotation has been commonly used in concentrating molybdenite from copper sulfides and other gangue minerals <sup>4,5</sup>.

Froth flotation of molybdenite is governed by the anisotropic structure of molybdenite crystals, which is in turn affected by operational factors such as grinding conditions, collectors, pH, and types of gangue minerals <sup>5-7</sup>. Molybdenite crystal consists of S-Mo-S sandwich-like layers held together by weak van der Waals bonds <sup>7</sup>. Upon crushing and grinding, a molybdenite particle may comprise two types of surfaces: face surfaces created by a rupture of weak S-S van der Waals bonds and edge surfaces created by a rupture of strong covalent Mo-S bonds within the S-Mo-S layer <sup>8</sup>. When being immersed in water, molybdenite particles exhibit anisotropic surface properties. The face surface is hydrophobic, while the edge surface is hydrophilic due to a strong interaction with water molecules <sup>9</sup>. The face-to-edge ratio of individual molybdenite particles impacts flotation performance <sup>10</sup>. Fine grinding yields fine molybdenite particles with a high edge-to-face ratio, while coarse grinding yields coarse molybdenite particles with a low edge-to-face ratio. It has been shown previously that the flotation recovery of molybdenite at a particle size of 20  $\mu\text{m}$  reaches 100%, while the flotation recovery is decreased to 75% as the particle size is reduced to less than 10  $\mu\text{m}$  <sup>11</sup>. Recent studies revealed by AFM and STM show that there are nano-sized clusters of edge patches on face surfaces <sup>12,13</sup>, which may also impact the flotation performance.

Much of the previous R&D has been devoted to the development of flotation collectors for molybdenite <sup>14,15</sup>. Due to the anisotropic surface properties of molybdenite crystals, different collectors have been developed <sup>16-18</sup>. Hydrocarbon oils are common collectors for molybdenite <sup>5</sup>. These hydrocarbon oils, such as kerosene and diesel, are readily adsorbed on molybdenite faces by hydrophobic interaction <sup>19</sup>. Since most of the hydrocarbon oils are practically insoluble in water, they are present in the oil emulsions in the forms of oil droplets by agitation <sup>20</sup> and/or ultrasonication <sup>10</sup>. It has been previously shown that oils with relatively higher dispersibility in water exhibit a better froth flotation performance <sup>21</sup>. The collector performance of hydrocarbon oils improves with increasing the length of its carbon chains <sup>22-25</sup>. However, an oily collector with a long hydrocarbon chain exhibits a relatively low dispersibility in water, resulting in a decrease in mineral

recovery. In this regard, the addition of emulsifying agents improves the flotation performance<sup>26,27</sup>. Furthermore, studies show that a better performance is obtained with blended oils compared to single oil<sup>28,29</sup>. This is attributed to the adsorption of blended oils on edge surfaces. Furthermore, sulfated coconut oil is found to be effective for its ability to adsorb on molybdenite edges<sup>30</sup>.

The adsorption of insoluble oil collectors on molybdenite surfaces involves collision, attachment, and spreading of micro-sized oil droplets on molybdenite surfaces. During the conditioning process, oil droplets collide and adhere to particles' surfaces<sup>31</sup>. The attachment of oily collectors on molybdenite surfaces is attributed to attractive van der Waals and hydrophobic interactions<sup>32</sup>. The electrostatic double-layer force is typically repulsive between oils and molybdenite surfaces. The suppression of the EDL force by lowering pH and/or increasing electrolyte concentrations facilitates the attachment process<sup>32,33</sup>. Once the oil droplets attach to molybdenite faces, they spread quickly on molybdenite surfaces until an equilibrium contact line is established. The contact angles of oil droplets on the molybdenite surfaces are above 100°<sup>34</sup>. The adsorption of oily collectors on molybdenite faces results in an increase in surface hydrophobicity of molybdenite and, consequently, the flotation kinetics. It has been shown that the water contact angles ( $\theta$ ) on molybdenite faces are in the range of 70-80 degrees<sup>6,7,30,35</sup>. Upon the adsorption of oily collectors (e.g., diesel and kerosene), the water contact angles on molybdenite face surfaces are increased by 8-10°<sup>29,31,36,37</sup>.

Despite much previous efforts on the development of new collectors, there are few studies on understanding its governing mechanism involved. Many questions remain, such as how oil collectors are adsorbed on molybdenite surfaces and how the adsorbed oil droplets impact the stability and rupture of the thin liquid films (TLFs). In this study, the effect of insoluble oily collectors on the thinning and rupture of the TLFs between air bubbles and molybdenite faces has been investigated by monitoring the spatial and temporal evolution of the TLFs using synchronized tri-wavelength reflection interferometry microscope (STRIM)<sup>38</sup>. Two hydrocarbon oils have been studied and compared, and they are kerosene and dodecane. The oil collectors are dispersed in water by ultrasonication, and the oil drop sizes in the emulsions are determined using an optical method coupled with image processing. The molybdenite surfaces are hydrophobized by immersing mineral samples in oil emulsions of different oil dosage. The temporal and spatial evolution of the TLFs during the approach is monitored by recording and analyzing multi-colored fast-changing interference fringes. The rupture mechanism will be discussed in the context of surface forces, drop size, as well as film deformation.

## 4.2 Materials and experiments

### 4.2.1 Materials

A fresh cleavage (face) surface of a layered molybdenite mineral was prepared by peeling off the top layer using masking tape (Scotch-Blue, 3M). The molybdenite face surface

was naturally hydrophobic with a water contact angle of 70°. Deionized (DI) water was obtained from a laboratory-scale water purification system (Barnard, Thermo Fisher). The DI water used in this study had a resistance of 18.1 mΩ cm or above. Two types of aliphatic hydrocarbon oils were used in this study. They were n-dodecane (99%) and kerosene (99%). Both were obtained from Alfa Aesar, and they were used as received. Sodium chloride (NaCl) was used as an electrolyte. The NaCl (purity: 99.98%) was obtained from Alfa Aesar. They were thermally treated at 500 °C overnight to remove organics prior to the use.

#### **4.2.2 Oil emulsion**

Both dodecane and kerosene are aliphatic hydrocarbon oils, and they have low solubility in water. In this study, oil emulsions were prepared by dispersing oils in the aqueous solutions using an ultrasonic cleaner for 5 minutes. The oil concentration in oil emulsions varied from 0.01% to 1.0%.

Both the size distribution and density of oil drops in the oil emulsions are determined by analyzing oil images using the ImageJ software. A drop of the oil emulsion solution was placed on a cleaned glass slide and then covered by a clean cover glass. Prior to the size measurement experiments, glass slides were cleaned by immersing them in a boiling Piranha solution at a temperature of 85-100 °C for 15 minutes, followed by rinsing them with amounts of DI water and dried with a compressed N<sub>2</sub> stream. The cleaned glass slide was hydrophilic with a water contact angle of less than 5°, and therefore oil drops in oil emulsion solutions were unlikely attached to surfaces of the glass slides. Images of oil drops in the oil emulsions were taken under a 20x objective using a CMOS camera. The pictures were processed using the ImageJ software to obtain the number of drops over a single picture frame (200 μm × 210 μm) as well as size distribution.

#### **4.2.3 Contact Angle Measurements**

Molybdenite face surface was naturally hydrophobic with a water contact angle of 60-80°. In this study, molybdenite substrates were immersed in oil emulsion solutions for 5 minutes. Upon the treatment in oil emulsion solutions, molybdenite substrates were transferred to a glass container filled with DI water for the contact angle measurements. The contact angle measurements were conducted using the captive bubble method. At least three measurements were taken, and the average data was reported.

#### **4.2.4 Bubble-molybdenite attachment**

The attachment process between air bubbles and molybdenite face surfaces is investigated by monitoring the spatial and temporal evolution of the TLFs during the bubble-molybdenite attachment using the synchronized tri-wavelength reflection interferometry microscope (STRIM). Figure 4.1 shows a schematic drawing of a STRIM instrument that is used to study the bubble-molybdenite interaction. A hemispherical air

bubble was initially fixated on an optically-flat fused quartz plate by means of a micro-syringe. To fixate an air bubble on the lower quartz surface, the plate was rendered hydrophobic by a methylation process<sup>39</sup>. The hydrophobized plate exhibited a water contact angle of above 90°. A molybdenite substrate was attached to a multi-axis translational stage with its face surface facing downward. The molybdenite sample was lowered to the air bubble to a closest separation distance of approximately 6-10  $\mu\text{m}$  by means of a manual translational stage. A side-view camera was used to assist the alignment process. An infinity-corrected 20 $\times$  long-working distance objective (Mitutoyo) was used to monitor optical fringes. The magnification was calibrated using a standard microscope calibration slide (Thorlabs). Three synchronized cameras recorded the interference fringes simultaneously at a rate of 150 frames per second at wavelengths of 460 nm, 526nm, and 620nm, respectively<sup>40</sup>.

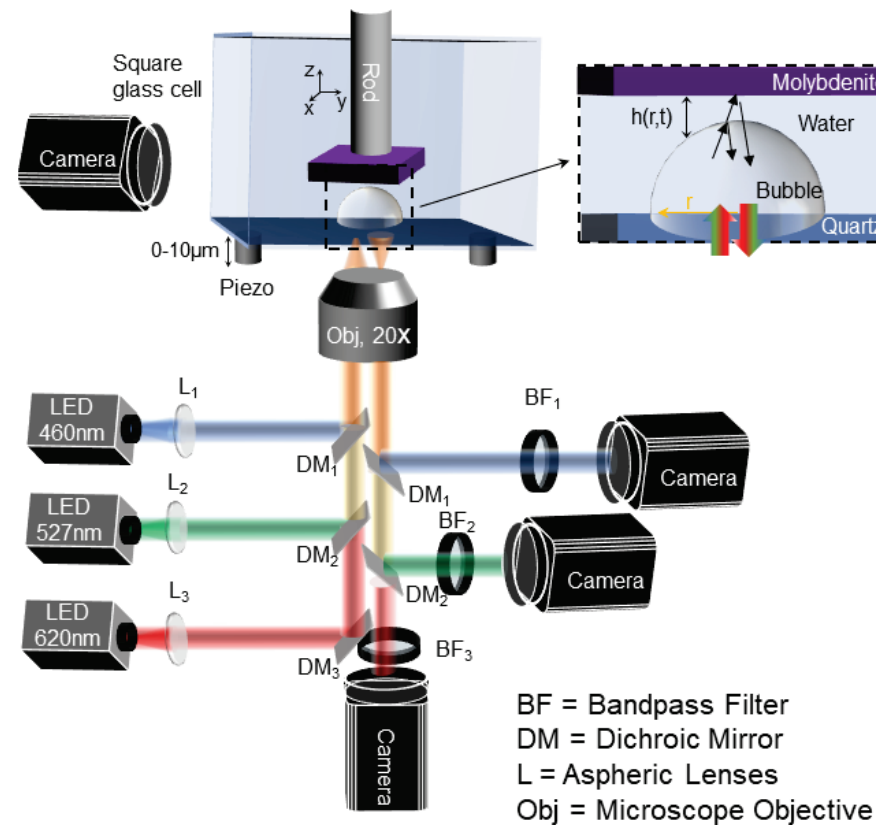


**Figure 4.1** A schematic representation of synchronized tri-wavelength reflection interferometry microscope (STRIM) that is used to study thinning and rupture of TLFs during the bubble-molybdenite attachment process.



The STRIM instrument monitors the spatial and temporal evolutions of the TLFs during the bubble-mineral approach. Different from the monochromatic interferometry technique, STRIM uses three synchronized cameras to record fast-evolving interference fringes at three different wavelengths. This configuration enables an accurate determination of fringe orders and, consequently, the film thicknesses over the range of 0–5  $\mu\text{m}$  with a resolution of 1–3 nm<sup>39</sup>. The interference fringes are processed to determine the spatiotemporal thickness profile of the TLFs using the equation below:

$$\frac{2I - (I_{\max} + I_{\min})}{I_{\max} - I_{\min}} = \cos\left(\frac{4\pi nh}{\lambda} + \delta\right) \quad (1)$$

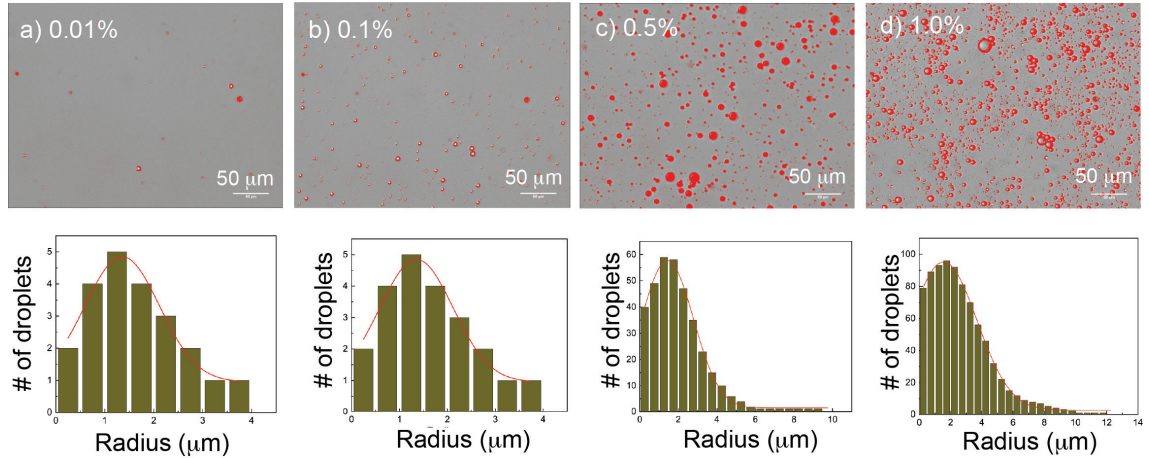
where  $I_{\max}$  and  $I_{\min}$  are the maximum and minimum intensity values in each fringe order,  $h$  is the film thickness,  $n$  is the reflective index of the medium,  $\lambda$  is the light wavelength, and  $\delta$  is the phase shift of the light reflected from the interfaces. The  $\delta$  value is determined from the reflective indexes ( $n$ ,  $k$ ) of the interference layers using a matrix of a multilayer system<sup>41</sup>. For molybdenite, the values of  $\delta$  is approximately zero at  $\lambda = 460$ , 526, and 620 nm, respectively. The order of fringes is determined using a trial-and-error method. In using this method, the film thickness as a function of time,  $h(t)$ , at a given radial position is iteratively determined using arbitrarily chosen fringe orders until the thickness data obtained at three different wavelengths overlap with each other. By determining the film thickness data along the radial direction, the spatiotemporal thickness profile,  $h(r, t)$ , can be then constructed. The image processing is carried out using a custom-written Matlab program. In this study, the film thickness was determined at a maximum radial position of 25–35  $\mu\text{m}$ , where the inclination angle was below 1.5°. Therefore, a correction associated with the deflection of light beams at two interfaces across the TLF due to the changes in bubble curvatures can be neglected<sup>42</sup>.

## 4.3 Results and discussion

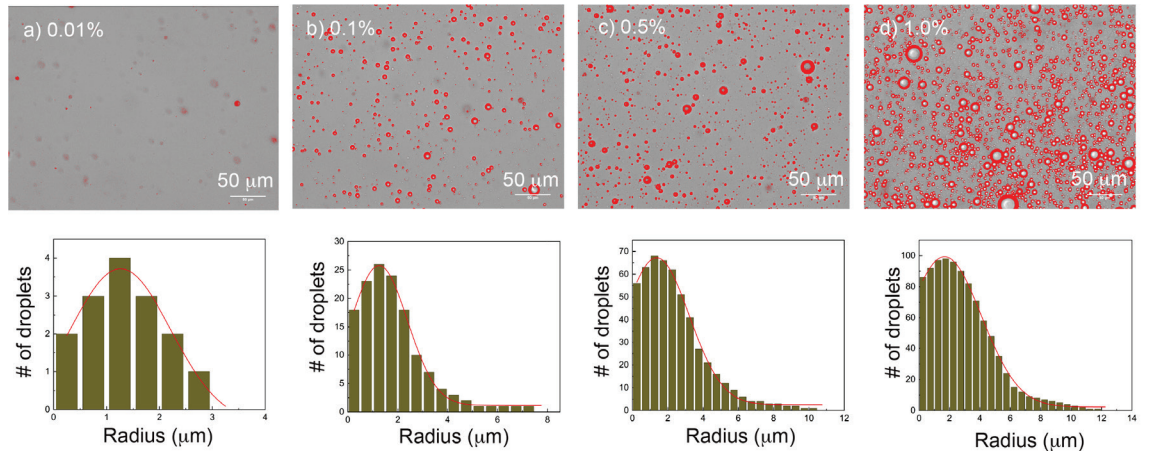
### 4.3.1 Oil Emulsion

Figure 4.2 shows microscopic images of oil drops in the dodecane emulsions of a) 0.01%, b) 0.1%, c) 0.5% and d) 1.0% dodecane dosage. Dodecane oils were dispersed in DI water using an ultrasonic cleaner for 5 minutes. As shown, the number and density of oil drops in oil emulsions increase with increasing oil dosages from 0.01% to 1.0%. Size analysis of the oil drops in the oil emulsions were conducted using the Image J software, and the result is shown in Figure 4.2. The size distribution data was fitted to a Gaussian distribution model to determine the mode, medium, and mean drop sizes. It is shown that the model fits the experimental data well with a coefficient of determination ( $R^2$ ) of 0.90 - 0.98. Table 1 shows mode, median, mean, and maximum oil drop size as well as the number of drops over one picture frame (200  $\mu\text{m} \times 210 \mu\text{m}$ ) at different oil dosages from 0.01% to 1.0%. It has been shown that the medium drop size in the dodecane emulsion increases from 1.42  $\mu\text{m}$  at 0.01 % dodecane dosage, to 2.12  $\mu\text{m}$  and 2.78  $\mu\text{m}$  at 0.5 % and 1.0% dodecane dosage, respectively. The maximum drop size ( $R_{\max}$ ) is increased from  $\mu.72 \mu\text{m}$  at 0.01% dodecane dosage to 11.86  $\mu\text{m}$  at 1.0% dodecane dosage. A higher

percentage of large oil drops with a diameter of above 6  $\mu\text{m}$  observed at 1.0% dodecane dosage may be attributed to a less mechanical energy per unit mass of oil during the emulsification process compared to that used in dispersing 0.01% dodecane in DI water. In addition, this may also be attributed to the coagulation of micron-sized oil drops due to the hydrophobic interaction<sup>43</sup>.



**Figure 4.2** Photos and size distribution of dodecane drops in the aqueous emulsions of DI water at a) 0.01%, b) 0.1%, c) 0.5%, and d) 1.0% oil dosage.



**Figure 4.3** Photos and size distribution of kerosene drops in the aqueous emulsion of DI water at a) 0.01%, b) 0.1%, c) 0.5%, and d) 1.0% oil dosage.

Figure 4.3 shows photos and size distribution of kerosene drops in the oil emulsions at a) 0.01%, b) 0.1%, c) 0.5%, and d) 1.0% oil dosage. Similar results were observed with kerosene compared to dodecane, *i.e.*, the number of oil drops in the oil emulsions increases with increasing kerosene concentrations in DI water. The median size of the oil drops increases from 4.48  $\mu\text{m}$  at 0.1% kerosene dosage, to 5.45  $\mu\text{m}$  and 6.30  $\mu\text{m}$  at 0.5%

and 1.0% kerosene dosage, respectively. The maximum size of kerosene drops in the oil emulsion also increases from 8.86  $\mu\text{m}$  at 0.1% oil dosage to 12.39  $\mu\text{m}$  at 1.0% oil dosage.

By comparing size analysis data obtained with two different oil collectors, kerosene exhibits a better dispersibility in DI water than dodecane. We have shown that at 0.5% kerosene dosage, the density of drops in the oil emulsion with kerosene was approximately 50% higher than that with dodecane. The higher dispersibility of kerosene in water compared to dodecane may be attributed to a high solubility of kerosene in water ( $\sim 0.02 \text{ g/L}$  at  $20 \text{ }^\circ\text{C}$ )<sup>44</sup> compared to that of dodecane in water ( $\sim 3.7 \times 10^{-6} \text{ g/L}$  at  $25 \text{ }^\circ\text{C}$ )<sup>45</sup>.

**Table 4.1** Various drop sizes and the number of drops in dodecane and kerosene emulsions at different oil dosages.

Oil	Conc. (wt%)	Mode size ( $\mu\text{m}$ )	Median size ( $\mu\text{m}$ )	Mean size ( $\mu\text{m}$ )	Maximum size ( $\mu\text{m}$ )	# of drops
Dodecane	0.01%	1.29	1.42	1.75	3.72	15
	0.1%	1.32	1.93	3.97	8.72	140
	0.5%	1.43	2.12	4.93	10.16	355
	1.0%	1.58	2.78	6.29	11.86	825
Kerosene	0.01%	1.35	1.64	2.00	3.77	20
	0.1%	1.41	2.27	4.48	8.86	221
	0.5%	1.46	2.54	5.45	10.29	518
	1.0%	1.62	2.98	6.30	12.39	950

#### 4.3.2 Surface hydrophobicity by contact angle measurement

Flotation recovery of molybdenite minerals without any collectors was reported in the range of 15-40%<sup>19</sup>. The floatability of molybdenite is attributed to the natural hydrophobicity of molybdenite face surfaces. The oily collectors increase the hydrophobicity of molybdenite face surfaces, and consequently, the flotation recovery. Figure 4.4 shows examples of bright-field images of the molybdenite face surfaces before and after the treatment in the dodecane or kerosene emulsion solutions at different oil concentrations. The images were taken under the microscope using a 20x long-working

distance objective. These images were taken at one specific location, but these images shown were representative. On the bare molybdenite face surface, the surface is flat with no impurities observed. At 0.1% dodecane dosage, there are many oil drops observed with diameters in the range of 1-5  $\mu\text{m}$  on surfaces. Given the optical limit, nano-sized oil droplets can not be detected. At 1.0% oil dosage, there are a significant fraction of oil drops with diameters of 20-50  $\mu\text{m}$  appeared on surfaces. A similar result was obtained with kerosene as the collector.

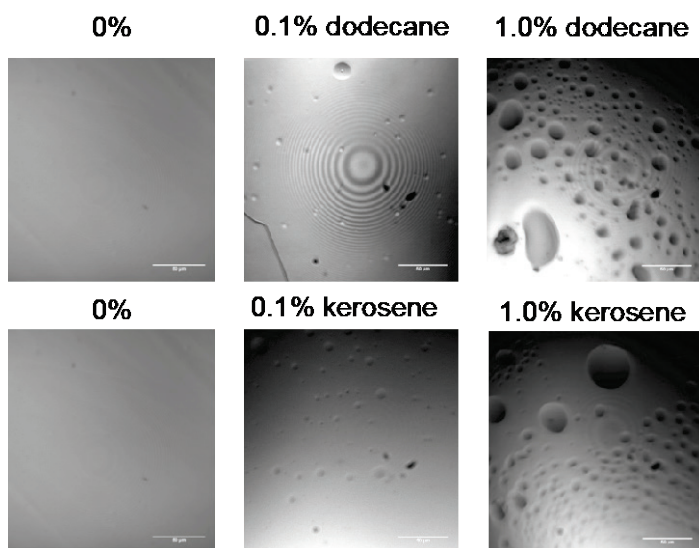


**Figure 4.4** Bright-field microscope images of molybdenite face surface with and without treated with kerosene emulsions at different oil dosages.

The surface hydrophobicity of molybdenite face surfaces with and without oil emulsion treatments is characterized by contact angle measurements using the captive bubble method. Molybdenite substrates are immersed in the oil emulsion at different oil dosage for 5 minutes, and they are then transferred to a square glass cell filled with DI water for the contact angle measurements. Figure 4.5 shows the equilibrium water contact angles on molybdenite surfaces after being treated in oil emulsion solutions. As shown, the equilibrium water contact angle is  $67^\circ$ . The equilibrium water contact angle increases after the adsorption of oil droplets on surfaces. For instance, with kerosene, the water contact angle of the emulsion-treated molybdenite surface is increased to  $75^\circ$  at 0.01% kerosene dosage. The water contact angle continues to increase with increasing the kerosene dosage, reaches a plateau of  $81^\circ$  at 1% kerosene dosage. The result suggests that the adsorption of kerosene on molybdenite surfaces increases the surface hydrophobicity of molybdenite face surfaces, which is consistent with the previous findings<sup>19</sup>.

The increase in surface hydrophobicity of the molybdenite face surfaces obtained with dodecane is less significant than that obtained with kerosene. For instance, the water

contact angle of the molybdenite face surfaces reaches  $76^\circ$  at 0.1% dodecane dosage compared to  $80^\circ$  at 0.1% kerosene dosage. The maximum water contact angle obtained at 1.0% dodecane dosage reaches  $81^\circ$ , which is slightly less than that obtained with kerosene. The higher hydrophobicity of the molybdenite face surfaces obtained with kerosene might be attributed to higher coverage of kerosene drops on molybdenite face surfaces as well as a higher hydrophobicity of kerosene compared to dodecane <sup>46</sup>.

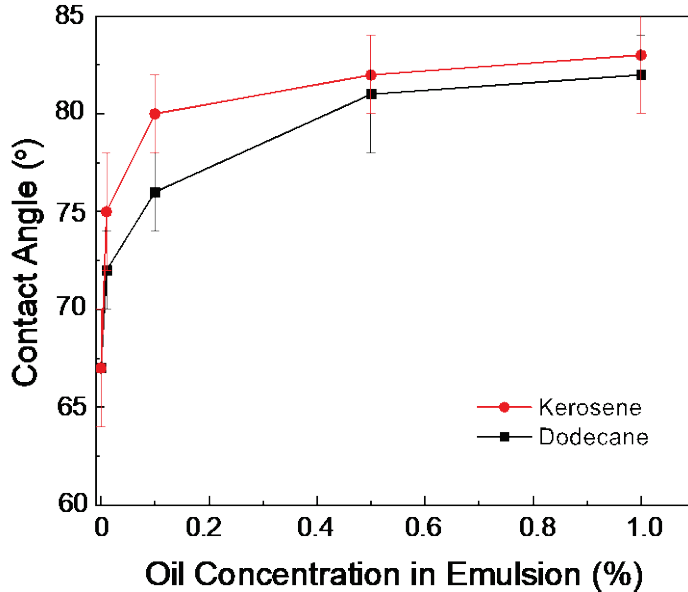


**Figure 4.5** Effect of oil types and oil concentration in the oil emulsions on the equilibrium water contact angle on molybdenite face surfaces using captive bubble method.

### 4.3.3 Stability of Thin Liquid Films (TLFs)

Stability and rupture of the TLFs on molybdenite face surfaces with and without the treatments of emulsified oils are examined by approaching a hemispherical air bubble to a horizontal molybdenite surface in DI water externally by means of a piezo device. The external approaching speed is 700 nm/s. Figure 4.6 shows a) time series of interference fringes obtained at three different wavelengths and b) spatiotemporal thickness profiles of the thin liquid films formed on molybdenite face surfaces. The  $t = 0$  s is arbitrarily chosen when the closest separation distance is 1000 nm. The diameter of the air bubble was 0.72 mm, and the equilibrium film thickness ( $h_e$ ) of the TLFs on freshly peeled molybdenite face surface was 68 nm. A stable film was formed due to a balance between capillary pressure and a repulsive electrostatic double-layer force between two negatively charged surfaces. Despite that the molybdenite face surface was naturally hydrophobic, the hydrophobic interaction was not strong enough to overcome the repulsive double-layer force at least at a distance of beyond 68 nm.

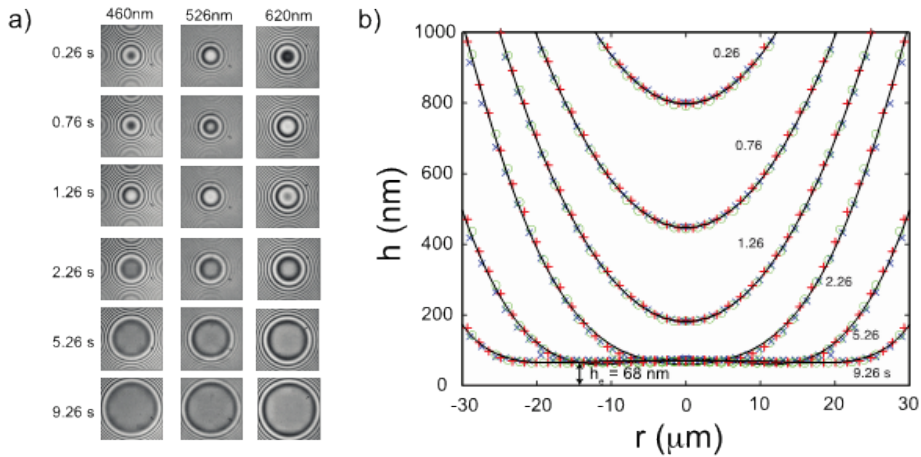


**Figure 4.6** The spatiotemporal evolution of the thin liquid films of DI water when an air bubble approaches a freshly peeled molybdenite face surface. (a) interference fringes obtained at three different wavelengths, (b) spatiotemporal profiles of the thin liquid films (TLFs).

Figure 4.7 shows bubble-molybdenite attachment result obtained with a molybdenite substrate treated in a 0.1% dodecane emulsion. Upon its contact in a dodecane emulsion solution for 5 minutes, the molybdenite sample was transferred to a glass cell for the film stability measurement. The result shows that the TLF was unstable formed on a dodecane-treated molybdenite face surface. During the initial phase of the film drainage, when the closest separation distance was above 400 nm, the film thinning was governed by the external drive with a negligible impact from both hydrodynamic and disjoining pressures. This is reflected by a gap of equal space between two spatial profiles obtained at a timed interval of 0.3 seconds. At a separation distance of below 400 nm, the film thinning was decelerated due to a rising hydrodynamic force. When the film thinned to a critical rupture thickness ( $h_c$ ), the film ruptured. In an example shown in Figure 4.7, the film ruptured at  $h_c = 181$  nm at  $t = 1.55$  s. Shortly after the film rupture, the three-phase contact line spread lightly within a few milliseconds until an equilibrated contact angle was established along the three-phase contact line.

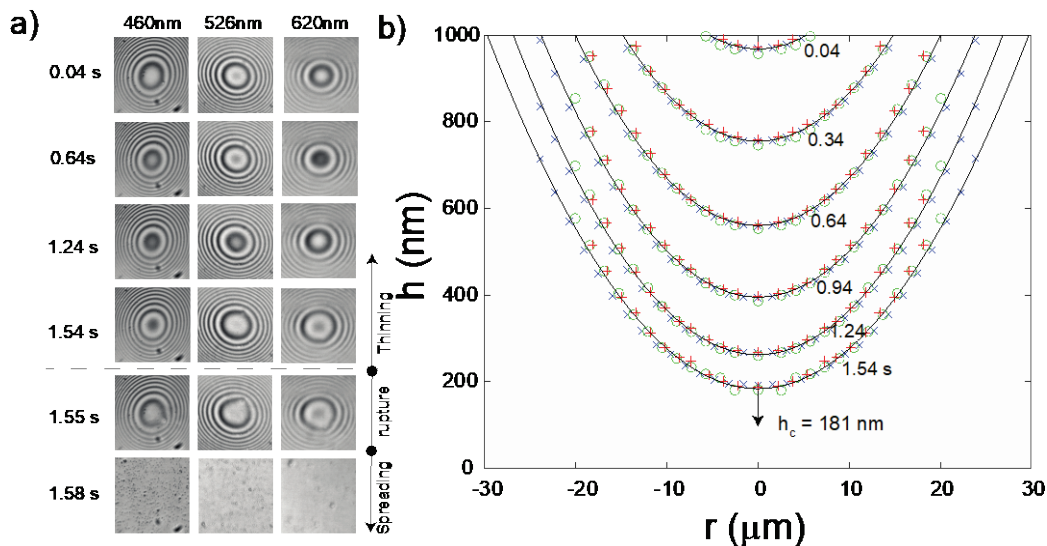


**Figure 4.7** The evolution of the TLFs when an air bubble approaches towards a molybdenite face surface treated with 0.1% emulsified dodecane solutions. (a) interference images; (b) spatiotemporal thickness profiles.

As claimed previously by one author of this present work, film stability is governed by many factors, including disjoining pressure, surface asperity, nanobubbles, etc<sup>38,47,48</sup>. An attractive disjoining pressure results in a rupture of the TLF, while a repulsive disjoining pressure stabilizes the TLF. The disjoining pressures in the TLF can be determined from the spatiotemporal thickness profiles and reflected by the kinetics of thinning. Figure 4.8 compares the kinetics of the thinning of the TLFs on molybdenite face surfaces treated in the kerosene or dodecane emulsion solutions at different oil concentrations. The result is shown as the minimum separation distance as a function of time from the initial closest separation distance of 1000 nm to a critical rupture thickness. As shown, the thinning kinetics decreases slightly with increasing dodecane concentrations in the dodecane emulsions. The deaccelerated film thinning may be associated with the coverage of micron-sized oil droplets on molybdenite face surfaces as shown in Figure 4.4. The presence of surface protrusions (i.e., adsorbed oil droplets) effectively prevents the liquid from draining to the edge of the TLFs. Similar phenomena were observed with kerosene as the collector. Nevertheless, no apparent acceleration of the film thinning was observed, suggesting that the overall disjoining pressures are repulsive in the TLF. It is unlikely that the repulsive disjoining pressure observed at a distance of above 100 nm is responsible for the film rupture.



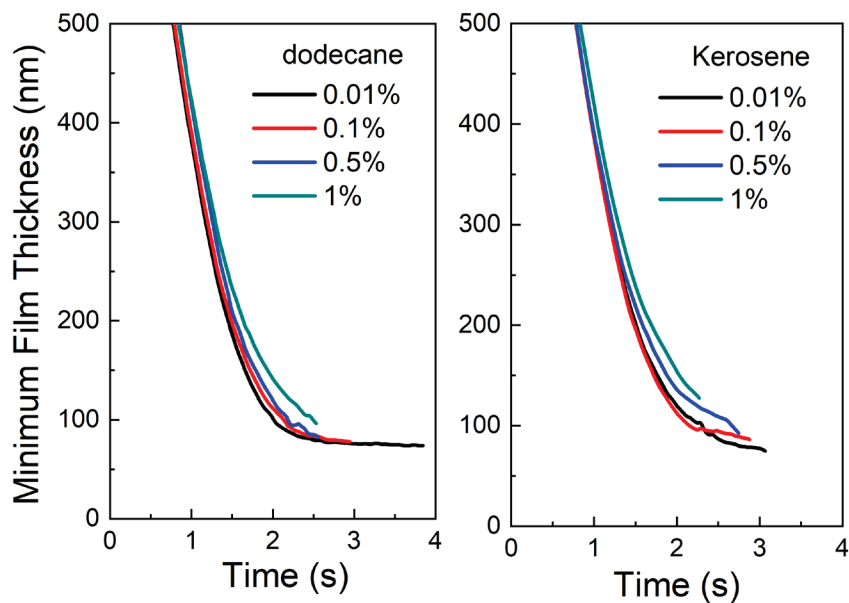


**Figure 4.8** Kinetics of thinning of the TLFs formed between air bubbles and molybdenite surfaces treated with dodecane and kerosene emulsions solutions.

Instead, the film rupture is attributed to the interaction between air bubbles and oil droplets on adsorbed on molybdenite surfaces by hydrophobic interaction. Unlike ionic collectors that adsorb on mineral surfaces and form a monolayer with a thickness of a few nanometers<sup>49,50</sup>, oil droplets are adsorbed on molybdenite surfaces in the forms of isolated patches. In this regard, the rupture mechanism depends on both sizes and morphology of oil droplets on molybdenite surfaces.



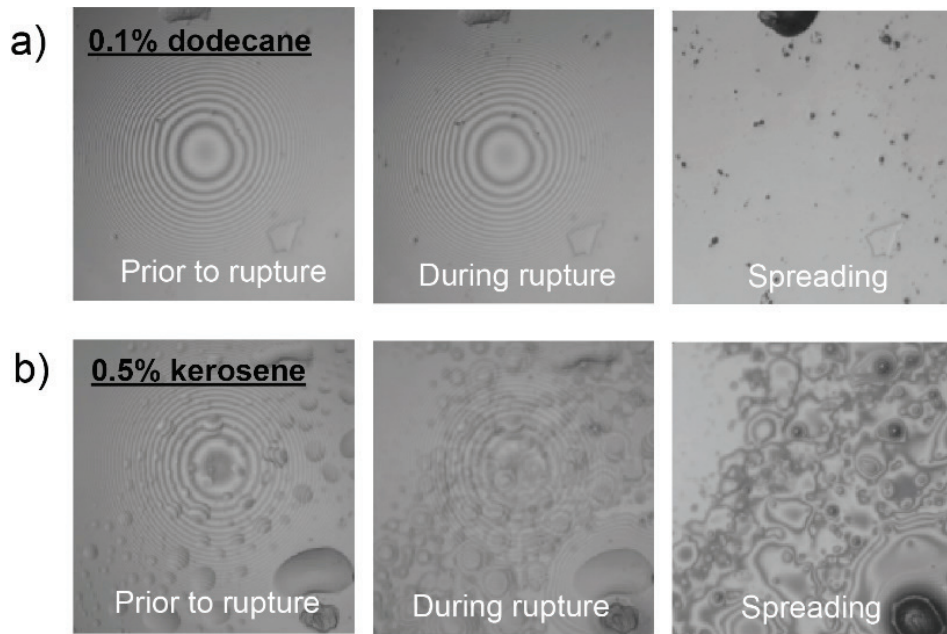


**Figure 4.9** Film rupture between air bubbles and molybdenite surfaces treated in oil emulsions at a) 0.1% dodecane and b) 0.5% kerosene dosage.

To better reveal the rupture mechanisms involved in the use of oily collectors, detailed analysis of the interference fringes during the film rupture is investigated. Figure 4.9a shows a series of the interference fringe images prior to and after the film rupture after the molybdenite substrate is treated in 0.1% dodecane emulsion. As shown, there are a few micro-sized oil droplets adsorbed on molybdenite face surfaces. It is possible that there are many submicron-sized droplets on molybdenite face surfaces, which cannot be detected optically. The film rupture seems to occur when the bubble touches a surface protrusion on the molybdenite surface at an overall separation distance of  $\sim 100\text{-}300$  nm. This surface protrusion is believed to be the submicron-sized oil droplets on molybdenite face surfaces that reduce the separation distance between the air bubble and the oil droplet. The film rupture is followed by a lighting spreading of a three-phase contact line as shown in Figure 4.9a.

Figure 4.9b shows the interference fringes of the TLF prior to and after the film rupture when the molybdenite substrate is treated in a 0.5% kerosene solution. As shown, large oil droplets are found on molybdenite face surfaces. As shown, the bubble's approach to oil-adsorbed molybdenite surfaces results in a bubbles' deformation. The presence of large oil droplets on the molybdenite surface not only slows down thinning kinetics but also impacts the rupture thickness. The result from over 20 experiments shows that film ruptures at a separation distance of  $100\text{-}350$  nm between the air bubble and the molybdenite surface. The actual separation distance between the bubble and the oil

droplet prior to the film rupture cannot be accurately determined due to the sizes of the oil droplets. It is anticipated that the film ruptures at a distance of below 100 nm.

Figure 4.10 shows a schematic diagram of two mechanisms involved in the film rupture with oily collectors used. In the first mechanism (mode I), the film rupture is attributed to surface asperities, i.e., submicron-sized oil droplets. During the film drainage, the presence of submicron-sized oil droplets has a minimal impact on both the thinning kinetics. In addition, the pressure built in the TLF due to both hydrodynamic and surface forces has a negligible effect on the oil droplet, and the submicron-sized oil droplets are considerably non-deformable. Therefore, the film rupture may occur when the air bubble is in very close proximity of the submicron-sized oil droplet to a real critical rupture thickness (real  $h_c$ ). In this regard, the film rupture is strongly dependent on the heights of the submicron-sized oil droplets. We have shown that the  $h_c$  values determined experimentally between air bubbles and molybdenite surfaces (or measured  $h_c$ ) are distributed over a wide range of 100-350 nm.

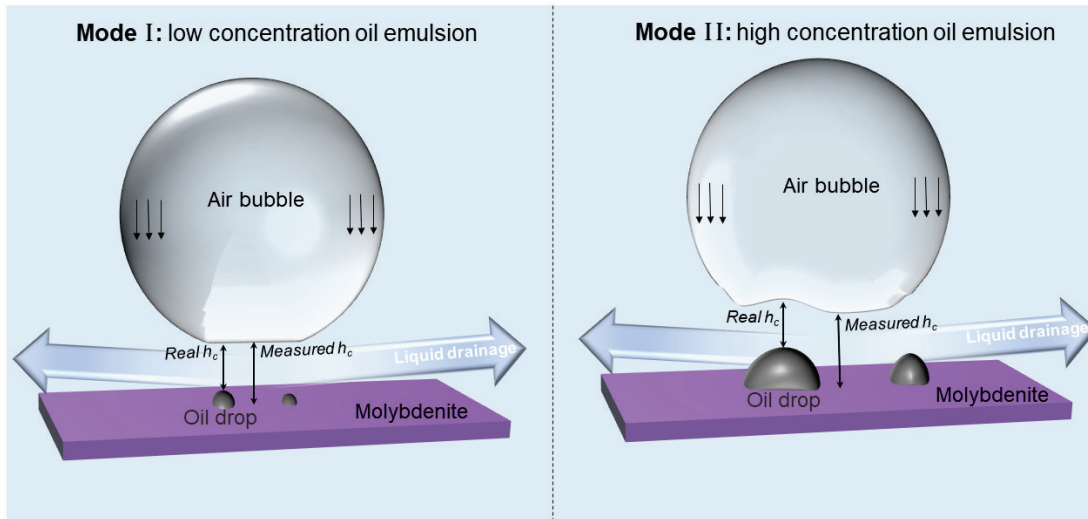


**Figure 4.10** A schematic of two different mechanisms involved in the film rupture.

The second mechanism (mode II) involves the interaction between air bubbles and large oil drops, which occurs when using high oil concentrations of oil emulsions. This results in a bubble deformation. In this regard, the film stability is governed by the interactions between air bubbles and oil droplets dominantly<sup>51</sup>. It has been previously shown that the film rupture between air bubbles and oil droplets at a critical rupture thickness of 30-50 nm. Regardless of the types of mechanisms involved, the rupture of TLFs between air bubbles and oil droplets is the onset of the film spreading process and, consequently, the bubble-molybdenite attachment process.

Based on the two film rupture mechanisms discussed above, one of the hypotheses is that the occurrence of the film rupture depends on the coverage of oil droplets on molybdenite surfaces, which is proportional to oil dosage as well as oil dispersibility. To validate these two hypotheses, film stability measurements were conducted on molybdenite substrates treated with oil emulsion solutions. A total of 25 independent experiments were conducted at each experimental variable. Figure 4.11 shows the occurrence of the film rupture events of the TLF formed between air bubbles and freshly peeled molybdenite surfaces. On the molybdenite face surface without the treatment of oil emulsions, in 23 out of 25 experiments, stable films were formed. The TLF became less stable with increasing the dodecane dosage in the oil emulsion solutions. At 1% dodecane concentration, the TLFs in all 25 experiments are unstable, resulting in the film rupture. A similar result was obtained using kerosene as the collector. Compared to the result obtained with dodecane, kerosene performs better in destabilizing the TLFs. For molybdenite surfaces treated with 0.5% kerosene emulsion, the TLF was unstable in all 25 film stability measurements. The present result validates both hypotheses, suggesting that the oil dispersibility plays a critical role in destabilizing the TLFs.

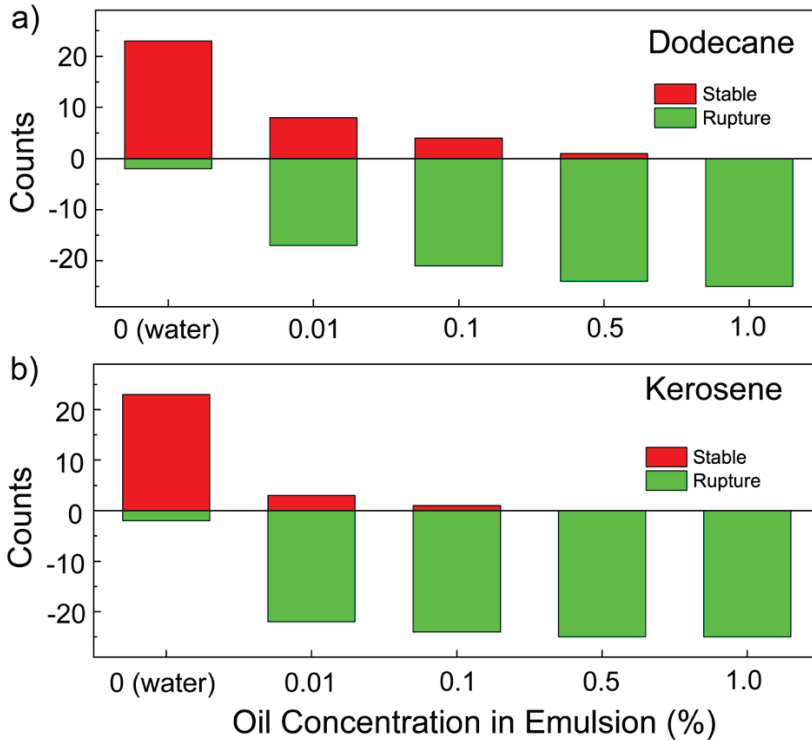


**Figure 4.11** Effect of a) dodecane and d) concentration in oil emulsion on the occurrence of rupture of thin liquid films on molybdenite face surfaces treated in the oil emulsion solutions.

#### 4.4 Summary and conclusion

The effect of oil collectors on the stability and rupture of TLFs between air bubbles and molybdenite face surfaces has been studied by monitoring the spatial and temporal evolution of the thin liquid films (TLFs) as well as the morphology of molybdenite face surfaces using synchronized tri-wavelength reflection interferometry microscope (STRIM) technique. Oil emulsion solutions are prepared by dispersing hydrocarbon oil (dodecane/kerosene) in DI water using an ultrasonic cleaner. It has been shown that both kerosene and dodecane oils are present as micron-sized oil droplets in DI water. The result obtained from the film stability measurements shows that the TLFs formed between air bubbles and freshly peeled molybdenite surfaces are stable due to the presence of a repulsive electrostatic double-layer force.

Hydrocarbon oils in oil emulsions adsorb on hydrophobic molybdenite face surfaces spontaneously in forms of isolated oil patches, resulting in an increase in surface hydrophobicity. The result obtained from the film stability measurement shows that the TLFs between air bubbles and collector-treated molybdenite surfaces become unstable and rupture despite that the kinetics of thinning of TLFs are nearly the same with and without oil collector treatment. When the molybdenite surfaces are covered with a large quantity of hydrocarbon oils, the kinetics of thinning is decelerated due to the presence of oil droplets for the liquid in the TLF to drain.

The film rupture may be in various forms. When nano-sized oil droplets were attached on molybdenite surfaces, the rupture occurs when the closest separation distance between the two reaches a real critical rupture thickness of 30-50 nm. For large oil droplets adsorbed on molybdenite face surfaces, which happened in high collector dosage, the observational rupture thicknesses significantly vary, but the real critical rupture thicknesses maintain the same. In this regard, film stability depends on oil drop sizes as well as surface chemistry of TLFs. It has also been shown that the occurrence of the film rupture largely depends on the density of oil drops adsorbed on molybdenite face surfaces. Kerosene exhibits a better dispersibility than dodecane, leading to higher coverage of oils on molybdenite surfaces at the same oil dosage. The fundamental knowledge gained from this work is critical for developing both processes and new chemicals for the flotation of molybdenite minerals.

## 4.5 References

- 1 Yin, Z. *et al.* Evaluation of l-cysteine as an eco-friendly depressant for the selective separation of MoS<sub>2</sub> from PbS by flotation. *Journal of Molecular Liquids* (2019).
- 2 Bulatovic, S. M. *Handbook of flotation reagents: chemistry, theory and practice: Volume 1: flotation of sulfide ores.* (Elsevier, 2007).
- 3 Yuan, D., Cadien, K., Liu, Q. & Zeng, H. Separation of talc and molybdenite: challenges and opportunities. *Minerals Engineering* **143**, 105923 (2019).
- 4 Wie, J. M. & Fuerstenau, D. The effect of dextrin on surface properties and the flotation of molybdenite. *International journal of mineral processing* **1**, 17-32 (1974).
- 5 Castro, S., Lopez-Valdivieso, A. & Laskowski, J. Review of the flotation of molybdenite. Part I: Surface properties and floatability. *International Journal of Mineral Processing* **148**, 48-58 (2016).
- 6 Yang, B., Song, S. & Lopez-Valdivieso, A. Effect of particle size on the contact angle of molybdenite powders. *Mineral Processing and Extractive Metallurgy Review* **35**, 208-215 (2014).
- 7 Chander, S. & Fuerstenau, D. On the natural floatability of molybdenite. *Trans. AIME* **252**, 62-69 (1972).
- 8 Han, S. *et al.* Band-gap transition induced by interlayer van der Waals interaction in MoS<sub>2</sub>. *Physical Review B* **84**, 045409 (2011).
- 9 Laskowski, J. & Kitchener, J. The hydrophilic—hydrophobic transition on silica. *Journal of Colloid and Interface Science* **29**, 670-679 (1969).
- 10 Song, S., Zhang, X., Yang, B. & Lopez-Mendoza, A. Flotation of molybdenite fines as hydrophobic agglomerates. *Separation and Purification Technology* **98**, 451-455 (2012).
- 11 Dickinson, R. G. & Pauling, L. The crystal structure of molybdenite. *Journal of the American Chemical Society* **45**, 1466-1471 (1923).
- 12 López-Valdivieso, A., Madrid-Ortega, I., Valdez-Pérez, D., Yang, B. & Song, S. in *Proceedings of the 9th International Mineral Processing Conference, Santiago, Chile.* 20-23.
- 13 Komiyama, M. *et al.* Crater structures on a molybdenite basal plane observed by ultra-high vacuum scanning tunneling microscopy and its implication to hydrotreating. *Journal of Molecular Catalysis A: Chemical* **215**, 143-147 (2004).
- 14 Hsu, L. Effects of oxygen and sulfur fugacities on the scheelite-tungstenite and powellite-molybdenite stability relations. *Economic Geology* **72**, 664-670 (1977).
- 15 Smith, J. & Bhappu, R. in *Paper presented at the AIME Pacific Southwest Mineral Industry Conference.*
- 16 Ramirez, A., Gutierrez, L. & Laskowski, J. S. Use of “oily bubbles” and dispersants in flotation of molybdenite in fresh and seawater. *Minerals Engineering* **148**, 106197 (2020).
- 17 He, T., Wan, H., Song, N. & Guo, L. The influence of composition of nonpolar oil on flotation of molybdenite. *Minerals Engineering* **24**, 1513-1516 (2011).

- 18 Rebolledo, E., Laskowski, J. S., Gutierrez, L. & Castro, S. Use of dispersants in flotation of molybdenite in seawater. *Minerals Engineering* **100**, 71-74 (2017).
- 19 Lin, Q.-q. *et al.* Flotation mechanisms of molybdenite fines by neutral oils. *International Journal of Minerals, Metallurgy, and Materials* **25**, 1-10 (2018).
- 20 Rubio, J., Capponi, F., Rodrigues, R. & Matiolo, E. Enhanced flotation of sulfide fines using the emulsified oil extender technique. *International Journal of Mineral Processing* **84**, 41-50 (2007).
- 21 Lin, Q.-q. *et al.* Recovery of molybdenum and copper from porphyry ore via iso-flotability flotation. *Transactions of Nonferrous Metals Society of China* **27**, 2260-2271 (2017).
- 22 Crozier, R. & RD, C. Flotation reagent practice in primary and by-product molybdenum recovery. (1979).
- 23 Xia, Y. & Peng, F. Selection of frothers from residual organic reagents for copper-molybdenite sulfide flotation. *International Journal of Mineral Processing* **83**, 68-75 (2007).
- 24 Hui, W., Gu, G.-H., Fu, J.-G., Li, C. & Ye, H. Study of the interfacial interactions in the molybdenite floatation system. *Journal of China University of Mining and Technology* **18**, 82-87 (2008).
- 25 Song, S. & Lopez-Valdivieso, A. Computational studies on interaction between air bubbles and hydrophobic mineral particles covered by nonpolar oil. *Journal of colloid and interface science* **212**, 42-48 (1999).
- 26 Hoover, R. & Malhotra, D. Emulsion flotation of molybdenite. *Flotation--A. M. Gaudin Memorial* (1976).
- 27 Nishkov, I., Lazarov, D., Marinov, M., Beas, E. & Henriquez, C. in *Proceedings of IV Meeting of the Southern Hemisphere on Mineral Technology and III Latin-American Congress on Froth Flotation, Concepción, Chile.* 20-23.
- 28 Smit, F. & Bhasin, A. Relationship of petroleum hydrocarbon characteristics and molybdenite flotation. *International Journal of Mineral Processing* **15**, 19-40 (1985).
- 29 He, T. *et al.* Improving fine molybdenite flotation using a combination of aliphatic hydrocarbon oil and polycyclic aromatic hydrocarbon. *Results in Physics* **12**, 1050-1055 (2019).
- 30 Kelebek, S. Critical surface tension of wetting and of floatability of molybdenite and sulfur. *Journal of Colloid and Interface Science* **124**, 504-514 (1988).
- 31 Miki, H., Hirajima, T., Muta, Y., Suyantara, G. P. W. & Sasaki, K. Effect of sodium sulfite on floatability of chalcopyrite and molybdenite. *Minerals* **8**, 172 (2018).
- 32 Feng, L., Manica, R., Grundy, J. S. & Liu, Q. Unraveling Interaction Mechanisms between Molybdenite and a Dodecane Oil Droplet Using Atomic Force Microscopy. *Langmuir* **35**, 6024-6031 (2019).
- 33 Peng, H. *et al.* Study of the Effect of Sodium Sulfide as a Selective Depressor in the Separation of Chalcopyrite and Molybdenite. *Minerals* **7**, 51 (2017).
- 34 Zanin, M., Ametov, I., Grano, S., Zhou, L. & Skinner, W. A study of mechanisms affecting molybdenite recovery in a bulk copper/molybdenum flotation circuit. *International Journal of Mineral Processing* **93**, 256-266 (2009).

- 35 Beaussart, A., Parkinson, L., Mierczynska-Vasilev, A. & Beattie, D. A. Adsorption of modified dextrans on molybdenite: AFM imaging, contact angle, and flotation studies. *Journal of colloid and interface science* **368**, 608-615 (2012).
- 36 You, X., Li, L. & Lyu, X. Flotation of molybdenite in the presence of microemulsified collector. *Physicochemical Problems of Mineral Processing* **53** (2017).
- 37 Suyantara, G. P. W., Hirajima, T., Miki, H. & Sasaki, K. Floatability of molybdenite and chalcopyrite in artificial seawater. *Minerals Engineering* **115**, 117-130 (2018).
- 38 Gao, Y. & Pan, L. Measurement of Instability of Thin Liquid Films by Synchronized Tri-wavelength Reflection Interferometry Microscope. *Langmuir* (2018).
- 39 Gao, Y. *et al.* Adsorption of a novel reagent scheme on scheelite and calcite causing an effective flotation separation. *Journal of Colloid and Interface Science* **512**, 39-46 (2018).
- 40 Gao, Y., Jung, S. & Pan, L. Interaction and instability of air films between bituminous coal surfaces and surfactant droplets. *Fuel* **274**, 117839 (2020).
- 41 Macleod, H. A. *Thin-film optical filters*. (CRC press, 2017).
- 42 de Ruiter, J., Mugele, F. & van den Ende, D. Air cushioning in droplet impact. I. Dynamics of thin films studied by dual wavelength reflection interference microscopy. *Physics of fluids* **27**, 012104 (2015).
- 43 Van den Tempel, M. Stability of oil-in-water emulsions II: Mechanism of the coagulation of an emulsion. *Recueil des Travaux Chimiques des Pays-Bas* **72**, 433-441 (1953).
- 44 Dagaut, P. On the kinetics of hydrocarbons oxidation from natural gas to kerosene and diesel fuel. *Physical Chemistry Chemical Physics* **4**, 2079-2094 (2002).
- 45 Sutton, C. & Calder, J. A. Solubility of higher-molecular-weight normal-paraffins in distilled water and sea water. *Environmental Science & Technology* **8**, 654-657 (1974).
- 46 Othman, N., Mat, H. & Goto, M. Separation of silver from photographic wastes by emulsion liquid membrane system. *Journal of membrane science* **282**, 171-177 (2006).
- 47 Pan, L. & Yoon, R.-H. Measurement of hydrophobic forces in thin liquid films of water between bubbles and xanthate-treated gold surfaces. *Minerals Engineering* **98**, 240-250 (2016).
- 48 Pan, L. & Yoon, R.-H. Effects of electrolytes on the stability of wetting films: Implications on seawater flotation. *Minerals Engineering* **122**, 1-9 (2018).
- 49 Zhang, W., Honaker, R. & Groppo, J. Flotation of monazite in the presence of calcite part I: Calcium ion effects on the adsorption of hydroxamic acid. *Minerals Engineering* **100**, 40-48 (2017).
- 50 Li, C. & Gao, Z. Tune surface physicochemical property of fluorite particles by regulating the exposure degree of crystal surfaces. *Minerals Engineering* **128**, 123-132 (2018).

## 5 Stability of Thin Liquid Films between Dodecane Drops and Hydrophobic Surfaces\*

\* The material contained in this chapter is in preparation for submission.

### 5.1 Introduction

Thin liquid films (TLFs) are formed when two surfaces are brought closer to each other in a liquid medium<sup>1</sup>. Stability of the TLFs governs many industrial applications ranging from oil recovery by waterflooding<sup>2</sup>, froth flotation<sup>3</sup>, and others<sup>4</sup>. Depending on the nature of individual application, the film rupture may or may not be desired. For instance, in the froth flotation, an attachment of micro-sized oil droplets on hydrophobic particles across a TLF of water is desired for improving the floatability of the minerals. From a thermodynamical perspective, the film rupture is spontaneous when the changes in Gibbs free energy associated with the film rupture process is negative<sup>5</sup>. From a perspective of surface forces, the TLFs rupture may occur when the surface forces are attractive<sup>6</sup>.

Previous efforts have been devoted to the fluid mechanics of thin liquid film between air bubbles and between air bubbles and various flat surfaces<sup>6-9</sup>. Different experimental approaches along with the numerical modelling were taken to better understand the physics of film thinning, rupture and spreading of the TLFs. These experimental approaches include a) thickness measurement by bringing two surfaces together<sup>10,11</sup>, b) direct force measurements between two surfaces<sup>12,13</sup>, and c) determining both forces and separation distances between two approaching surfaces<sup>14-16</sup>. Numerical modeling based on the Lubrication theory coupled with the Young-Laplace equation have been developed to predict both the thinning and interfacial deformation of the TLFs<sup>17,18</sup>. By matching the experimentally obtained force or film thickness data with the model prediction, one can determine the surface forces across the TLFs accurately<sup>19</sup>. It was shown that not only the fluid dynamics parameters, but also the surface forces, impact the dynamics of TLFs<sup>20,21</sup>. An attractive surface force accelerates the film thinning, while a repulsive surface force decelerates it. The TLFs may reach the equilibrium by a formation of an equilibrated film, or they may rupture at a critical rupture thickness.

Recent efforts have been devoted to the drainage of the TLFs between oil droplets and solid surfaces<sup>22-24</sup> and between two oil droplets<sup>25</sup>. The physics involved in the drainage of the TLFs between two oil droplets or between one oil droplet and one flat solid surface are identical to that in which air bubbles are involved. It has been experimentally confirmed that the lubrication theory coupled with the DLVO theory models the drainage of the TLFs successfully with immobile boundary conditions at both the oil/water and solid/water interfaces. The immobile boundary condition at the oil-water interfaces in the Stokes flow is attributed to an adsorption of trace impurities at the interface<sup>26</sup>.

Understanding the stability of the TLFs between oil droplets and solid surfaces and between two oil droplets is critical to the desired performance of many engineering



applications, in which the film rupture may or may not be desired. One of key metrics of the film stability is the critical rupture thickness, which is defined as the closest separation distance between two surfaces before the two surfaces are emerged<sup>27</sup>. The larger the critical rupture thickness, the less stable the TLF. It was shown recently that the critical rupture thickness between dodecane droplets and molybdenite face surfaces decreases by suppressing the repulsive double-layer forces. As a consequence, the TLF is being exposed to the impact of both the attractive van der Waals and hydrophobic forces<sup>22</sup>. A recent study on the critical rupture thickness of the TLFs between n-Alkane droplets and hydrophobic gold surfaces seems to suggest that the critical rupture thickness increases with increasing the attractive forces across the TLFs<sup>23</sup>. No statistics on critical rupture thickness data has been reported previously. One major difference between these two measurements is the sizes of alkane droplets used, which may contribute to the differences in the critical rupture thickness. Unfortunately, detailed studies on the stability of the TLFs between oils and hydrophobic surfaces were rare, and statistical data on the critical rupture thickness is unavailable.

In this work, stability of the TLFs between alkane drops and hydrophobic mineral surfaces in the electrolyte solution was investigated by measuring spatiotemporal evolution of the film thicknesses of the TLFs using the Synchronized Tri-wavelength Reflection Interferometry Microscopy technique. Two atomically flat mineral samples were used including talc and molybdenite. Measurements were conducted with different radius of alkane droplets ranging from 0.1 mm to 1 mm in radius and in different electrolyte solutions. The disjoining pressure parameters were determined by matching experimentally obtained spatiotemporal thickness profiles with the model. The result were discussed in the context of disjoining pressure, capillary pressure, and others.

## **5.2 Material and method**

### **5.2.1 Materials**

Dodecane (purity: 99%) was obtained from Alfa Aesar, and it was used without further purification. Well-crystallized molybdenite and talc samples were used in this study, they were obtained from Ward's science. In each experiment, a freshly peeled layer of the mineral sample was created by taping off the top layer of the mineral sample. De-ionized (DI) water was obtained from a laboratory water purification system (Thermo Fisher). The resistance of the DI water was above 18.1 m $\Omega$ -cm. Sodium chloride (NaCl, purity = 99.999%) was obtained from Alfa Aesar. Prior to the use, the NaCl powders were treated at a temperature of 500°C for 5 hrs to decompose a trace amount of organic residues.

### **5.2.2 Contact Angle Measurements**

Contact angle measurements were conducted using the captive bubble and captive oil methods. In using this method, a mineral sample was fixed on a stage with a clean and flat surface facing vertically downwards. An air bubble or an oil drop was generated

using a syringe. The air bubble or oil droplet rises and spread on the flat mineral surface until a stable three-phase contact line was formed. The angle between the surface of the water and the outline of the contact solid surface is described as the contact angle ( $\theta$ ). At least three measurements were taken, and the average data was reported.

### 5.2.3 Evolution of TLF

Stability and rupture of the thin liquid films (TLFs) were characterized by monitoring spatial and temporal evolution of the TLFs using the synchronized tri-wavelength reflection interferometry microscopy (STRIM). Figure 1 shows the STRIM set-up that was used to study the stability of TLF formed between dodecane oil and flat mineral surfaces. An oil drop of dodecane was placed on the lower quartz plate. For the dodecane oil beads up on the lower quartz plate, the quartz plate was hydrophobized by immersing in  $10^{-5}$ M OTS for 10-20 seconds. In water, dodecane oil beaded up on the weakly hydrophobized quartz plate with the angle between the surface of the oil and outline of the contact solid surface of approximately  $90^\circ$ . The mineral sample was brought closer to the apex of the oil droplet to a distance of approximately 6-10  $\mu\text{m}$ . The changes in the interference fringes of the thin liquid films (TLFs) were recorded using three synchronized CMOS cameras at a rate of 150 frames per second, while the oil droplet is approaching the flat mineral surface at an approaching of approximately 700 nm/s. The maximum travel distance was 10  $\mu\text{m}$ .

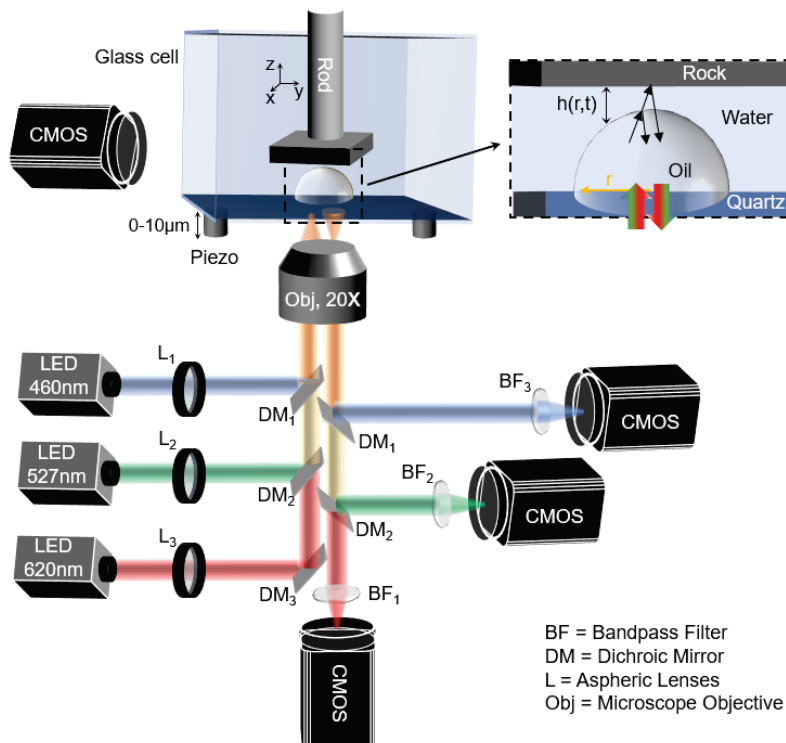


**Figure 5.1** Schematic of the synchronized tri-wavelength reflection interferometry microscopy (STRIM) used in this work

The interference fringes are processed to determine the spatiotemporal film thickness profile using the equation below:

$$\frac{2I - (I_{max} + I_{min})}{I_{max} - I_{min}} = \cos\left(\frac{4\pi nh}{\lambda} + \delta\right) \quad (1)$$

where  $I_{max}$  and  $I_{min}$  are the maximum and minimum intensities at each order,  $h$  is the film thickness,  $n$  is the reflective index of the medium,  $\lambda$  is the light wavelength, and  $\delta$  is the phase shift of the light reflected from the interfaces. The  $\delta$  value was determined from the reflective indexes ( $n, k$ ) of the interference layers using a matrix of a multilayer system. The order of fringes is determined using a trial-and-error method. In using this method, the film thickness as a function of time,  $h(t)$ , at a given radial position is iteratively determined using arbitrarily chosen fringe orders until the thickness data obtained at three different wavelengths overlap with each other. By determining the film thickness data along the radial direction, the spatiotemporal thickness profile,  $h(r,t)$ , can be then constructed. The image processing is carried out using a custom-written Matlab program. No correction was made associated with the deflection of light beams at two interfaces across the TLF, since the area of interest was limited to a maximum radial position of 25-35  $\mu\text{m}$ .

#### 5.2.4 Modeling

Dynamics of liquid film drainage between the oil droplet and flat solid surfaces can be described by the Lubrication theory as

$$\frac{\partial h}{\partial t} = \frac{1}{12\mu r} \frac{\partial}{\partial r} \left( rh^3 \frac{\partial p}{\partial r} \right) \quad (2)$$

where  $p$  is the excess pressure in the thin liquid film relative to the bulk liquid,  $h$  is the film thickness, and  $\mu$  is the liquid viscosity. The model assumes a non-slip boundary condition at the oil-liquid interface during film drainage of the TLF. The use of immobile boundary condition at the air-water interface and oil-water interface is justified previously by matching the experimental data with model.

The hydrodynamic pressure is balanced by the curvature pressure and disjoining pressure using the augmented Young-Laplace equation as,

$$p + \Pi = \frac{2\gamma}{R} - \frac{\gamma}{r} \frac{\partial}{\partial r} \left( r \frac{\partial h}{\partial r} \right) \quad (3)$$

where  $\Pi$  is the disjoining pressure in the film and  $\gamma$  is the interfacial tension at the oil-water interface. The  $\gamma$  value at the dodecane-water interface is 52  $\text{mN/m}^{28}$ . We assume that  $\gamma$  varies slightly with the electrolyte concentrations. The disjoining pressure consists of van der Waals force, electrostatic double-layer force, and hydrophobic force<sup>29,30</sup>.

$$\Pi = \Pi_{vdW} + \Pi_{elec} + \Pi_{hb} \quad (4)$$

Where  $\Pi_{vdW}$ ,  $\Pi_{elec}$ ,  $\Pi_{hb}$  are disjoining pressures due to van der Waals dispersion forces, electrostatic double-layer force, and hydrophobic forces.

The evolution of thin film drainage and the deformation of the oil-water interface can be modeled numerically if the initial and boundary conditions. The initial condition includes a) parabolic profile of the air-liquid interface, b) initial separation distance, c) approaching velocity. Other boundaries are identical to those proposed previously. The disjoining pressure parameters were iteratively determined when the experimental profile data matches with the model prediction.

## 5.3 Results and discussions

### 5.3.1 Effect of NaCl concentration on the TLF stability between dodecane drops and talc

The change of the electrolyte concentration will modify the thickness of the electrical double-layer. In this section, the electrolyte was set to be NaCl, which is commonly seen in film-related researches. Its effects on the stability of TLF between dodecane drop and talc were studied by contact angle measurement and the thinning evolution by the STRIM system.

#### 5.3.1.1 Contact angles of dodecane drops on talc

The contact angle is a primary way to characterize the solid surface hydrophobicity. The oil drops were placed on the talc surface in NaCl solutions with a concentration range of 0-1000mM, and the results are provided in Figure 2.

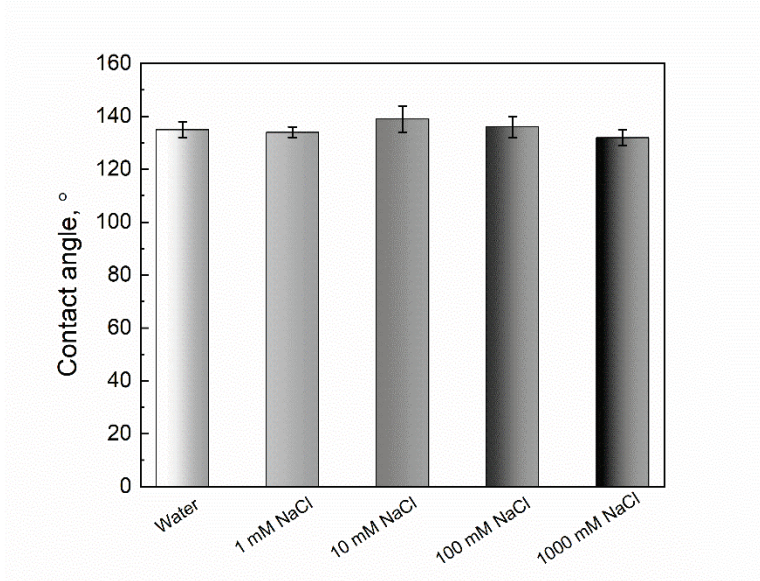


**Figure 5.2** Contact angles of dodecane drops on talc at different NaCl concentrations

As shown in Figure 2, in the DI water, the oil contact angle is about  $138^\circ$ , indicating that the talc surface is oleophilic. As the NaCl concentrations increase, the contact angles slightly increased and then decreased. But when taking the experimental errors into account, the contact angles can be regarded to maintain identical with various NaCl concentrations. Contact angles are thermodynamically quantified, and it will be of interest to compare the thinning process of TLF, which is providing provides kinetic information.

#### 5.3.1.2 TLF thinning process by STRIM

We observed two different scenarios of the TLF stability when changing the NaCl concentrations: stable films and film ruptures. The former occurred when the NaCl concentration was nearly zero, and the later appeared when the NaCl concentrations are more than 1 mM. To better describe two cases, we took the water and 10 mM NaCl solution as examples, and the evolution of TLFs are presented in Figure 3 and Figure 4, respectively.

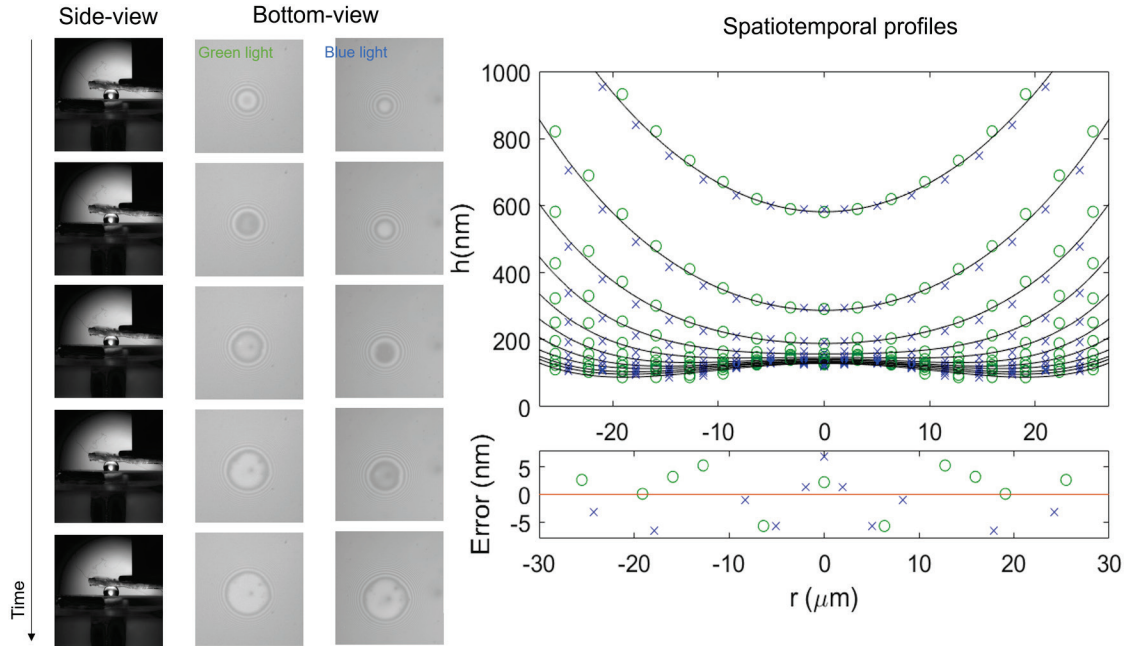


**Figure 5.3** A stable film in water between a dodecane drop and talc

Figure 3 shows the film drainage between a dodecane drop and talc. The first column is showing a sequence of images during the film thinning taken from the side view. Due to the limitation of the camera's resolution, the change of the film thicknesses cannot be observed by these images. Next to the side-view images are the bottom view fringes by two light beams, green and blue, with a wavelength of 520 nm and 460 nm, respectively. As the dodecane drop approaches the talc surface, the center area is expanding and remaining stable with the continuously nearing. Note that two sets of the bottom-view images were taken simultaneously, and the different intensities by two light beams will give the same film thickness value. After extracting the film thickness data out of the bottom-view images based on the methods introduced previously, we are able to reconstruct the evolution of the film thinning process, as shown in the spatiotemporal profiles shown in Figure 3. Green and blue symbols are the raw experimental data from the green and blue light, respectively. The gap between the two lines denotes the thickness change during an interval of 1 s. A narrow gap indicates a small thinning velocity. It is clear that as the separation distance is decreasing, the thinning velocity is correspondingly reduced, until to zero when the stable status of the TLF reaches. Note that the shape of the film is not maintaining spheric and causes a dimple due to the hydrodynamic forces generated by the pressure change in the liquid film. Thus, the closet separation distance at the equilibrium status is not the center of the film, but a little off to a position where  $r$  is equal to  $21.35 \mu\text{m}$ . And the equilibrium thickness is  $117 \mu\text{m}$  in the example shown in Figure 3. The below subgraph shows that the errors for two-wavelength light resources are falling into a narrow range of 5 nm, confirming the accuracy of the STRIM system.

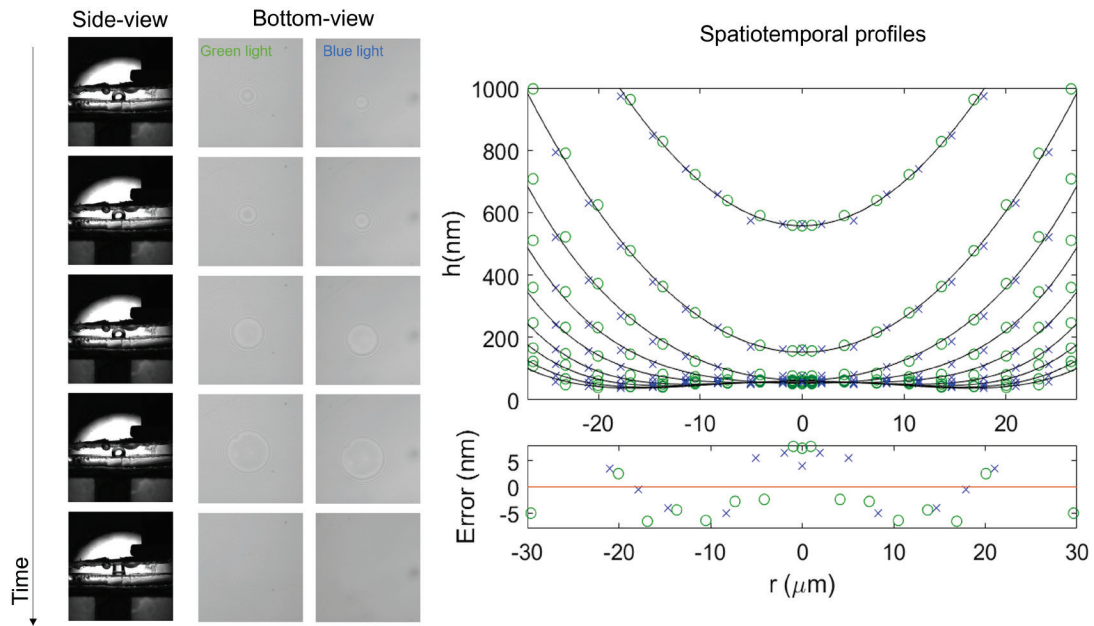


**Figure 5.4** The film ruptures in water between a dodecane drop and talc

As shown in Figure 4, when the water is replaced by 10 mM NaCl solution, the film becomes unstable and ruptures at the critical moment. The rupture can be found through the last one of the side-view images. Besides, both the bottom-view fringes from green and blue light beams suddenly disappear, which is consistent with the side-view images. And the film thinning data are extracted and presented in the form of spatiotemporal profiles in Figure 4. Similar to that in Figure 3, the thinning velocity decreases when the dodecane drop was driven towards the talc surface. And a dimple also appears in the meantime. However, when the closest separation distance reaches 58 nm, the film suddenly occurs at a position of 17.52  $\mu\text{m}$  off the center. The accuracy of experimental data is confirmed again by the small range of error.

To better explore the effect of NaCl concentrations on the thinning process of TLF between dodecane and talc, statistic experiments were then launched, and the results of



the final critical thicknesses at different NaCl concentrations are shown in Figure 5.

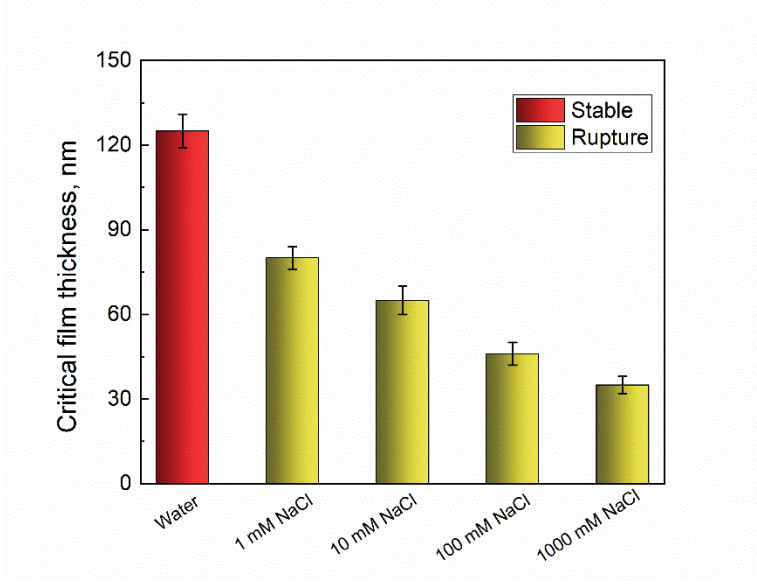


**Figure 5.5** Effects of NaCl concentrations on critical TLF thicknesses between dodecane drops and talc

In Figure 5, the radius of the dodecane drop size is approximately 0.5 mm. In water, the TLF reached equilibrium status at a thickness of around 120 nm. However, when the NaCl solution has a concentration that is greater than 1 mM, the films become unstable and rupture. And the critical rupture thickness is decreased from 86 nm to 34 nm as the NaCl concentration increase from 1 mM to 1000 mM, which might be mainly due to the suppression of electrical double-layer with increasing NaCl concentrations. Although the final critical thicknesses are crucial, the thinning kinetics of TLFs may also release meaningful information, as summarized in Figure 6.

As shown in Figure 6, in the initial stage, the thinning velocity maintains the same, i.e. 500 nm/s, which is the driving speed of the external piezo driver. When the medium is water, the thinning line is the top one, corresponding to the lowest thinning velocity compared with other NaCl solutions. And the water film will reach an equilibrium thickness of 120 nm, when the total pressure, including capillary pressure and disjoining pressure, is entirely balanced. On the other hand, with the increase of NaCl concentration, the thinning velocity keeps slightly increasing. And the NaCl films rupture in 1-1000 NaCl solutions, while the critical rupture thickness decrease with increasing NaCl



concentrations, as described in Figure 5.

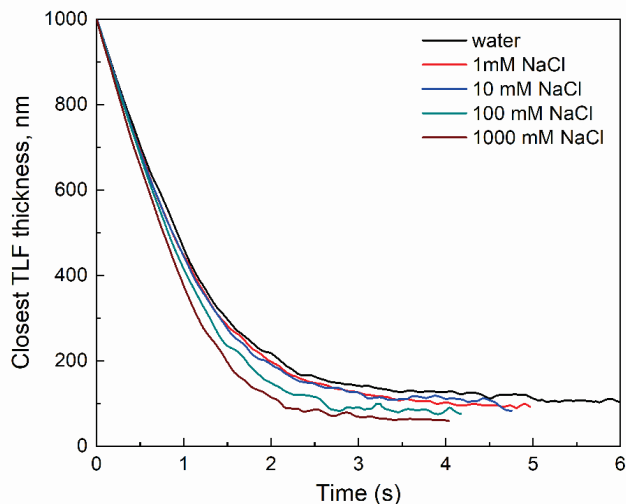


**Figure 5.6** Effects of NaCl concentrations on thinning kinetics of TLF between dodecane drops and talc

### 5.3.2 Effect of dodecane drop size on the TLF stability between dodecane drops and talc

The capillary pressure is adjusted by changing the dodecane drop size. In this section, the dodecane size was adjusted by controlling the drop volume. A set of statistic experiments in 1 mM NaCl solutions were launched via the STRIM system. And the critical thicknesses are provided in Figure 7.

In Figure 7, it is clear that the size of the dodecane drops significantly affects the stability of the TLFs. When the dodecane drop is small with a radius of 0.1-0.2 mm, all films rupture, and the critical rupture thicknesses are approximately 60 nm. When increasing the dodecane drop sizes to 0.6 mm, the critical rupture thickness increases to 75 nm. However, when further increased, the films become stable with the equilibrium film thicknesses in the range of 90-140 nm. The thinning details will be uncovered by the thinning kinetics in Figure 8.

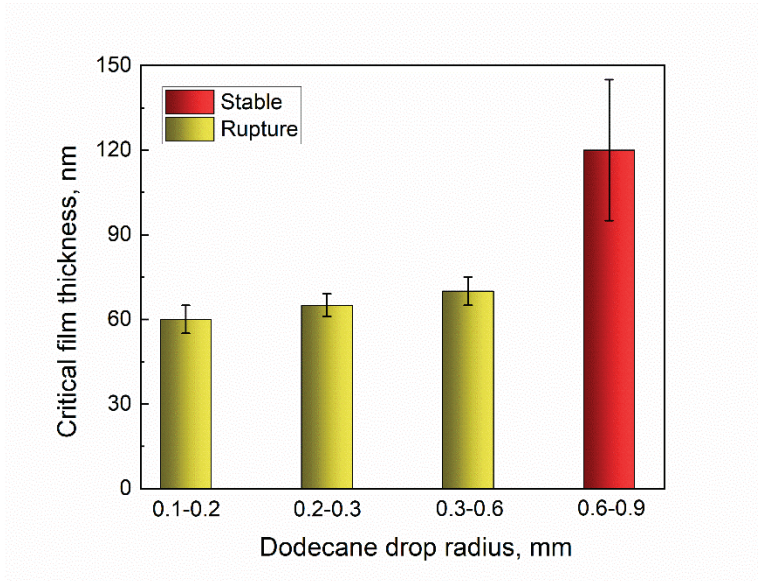


**Figure 5.7** Effects of dodecane drop size on critical TLF thicknesses between dodecane drops and talc

Figure 8 tells the significant differences among the thinning kinetics with various dodecane drop sizes. With the increase of dodecane drop sizes, thinning velocity slightly decreased after the film thicknesses thinned to below 800 nm. More remarkable thinning velocities appeared when the film thicknesses are smaller than 600 nm. This indicates that capillary pressure takes effects in a long-range distance. Compared with the small dodecane drops, the ones with a radius of 0.6-0.9mm corresponds to a more prominent slow-down of thinning. Although the thinning velocities for the dodecane drops with a size of below 0.6 mm increase with increasing drop size, the thinning kinetics almost remain the same, and the final rupture thicknesses are also close.

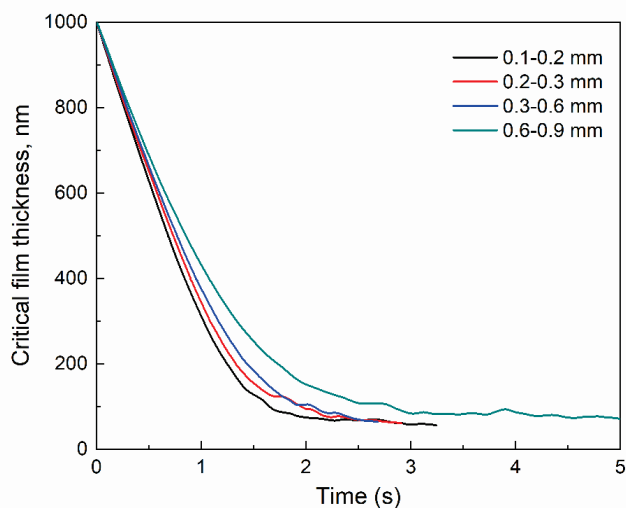


**Figure 5.8** Effects of dodecane drop size on thinning kinetics of TLF between dodecane drops and talc

### 5.3.3 Comprehensive understanding of the effects of the dodecane drop size and NaCl concentration on the TLF stability between dodecane drops and talc

In this section, a more systematic set of experiments were launched to change the dodecane drop sizes at NaCl concentrations ranging from 0 to 1000 mM. The film stabilities were summarized in Figure 9, and more detailed data with critical thickness/equilibrium thickness and the film deformations were provided in the Appendix section.

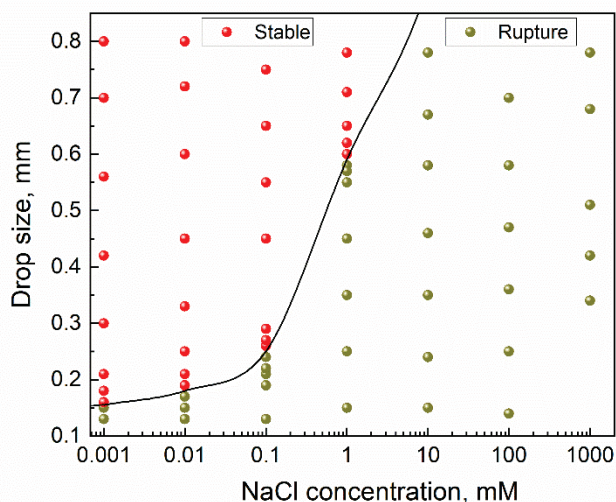


**Figure 5.9** The stabilities of TLFs between talc and dodecane drops with different sizes at different NaCl concentrations

Figure 9 contains a lot of useful information. The line in the graph is showing the boundary of stable and rupture films on talc. When the NaCl concentration is low, only small dodecane drops can lead to film ruptures. The required critical drop size is below 0.2 mm. However, when the NaCl concentration increases to over 0.1 mM, the critical drop size increases significantly to be more than 0.5 mm. When the NaCl concentrations further increase to 10 mM, the TLFs will always rupture. Overall, either decreasing the oil drop size or increasing NaCl concentration will benefit the TLF rupture. The fundamental mechanism might be lying in the DLVO theory, as given in Figure 10.

That shown in Figure 10 are the disjoining pressure calculated by the DLVO theory as well as the capillary pressure. On the left is describing the case of the stable film. In this case, the capillary pressure is initially greater than the disjoining pressure, which makes the drainage of the liquid films possible. However, the disjoining pressure increase with increasing electrical double-layer interaction, corresponding to the slow-down of the thinning velocity. When the capillary pressure is equal to the disjoining pressure, the liquid films become stable, and equilibrium thicknesses will be reached. When decreasing the dodecane drop size, the capillary pressure will increase, as well as the difference of the capillary pressure and disjoining pressure. Thus the thinning will continue, and the rupture will then tend to occur. And when increasing the NaCl concentration, the Debye length will decrease, and the effective range of the negative electrical interaction will be shortened. And the disjoining pressure will decrease, correspondingly.

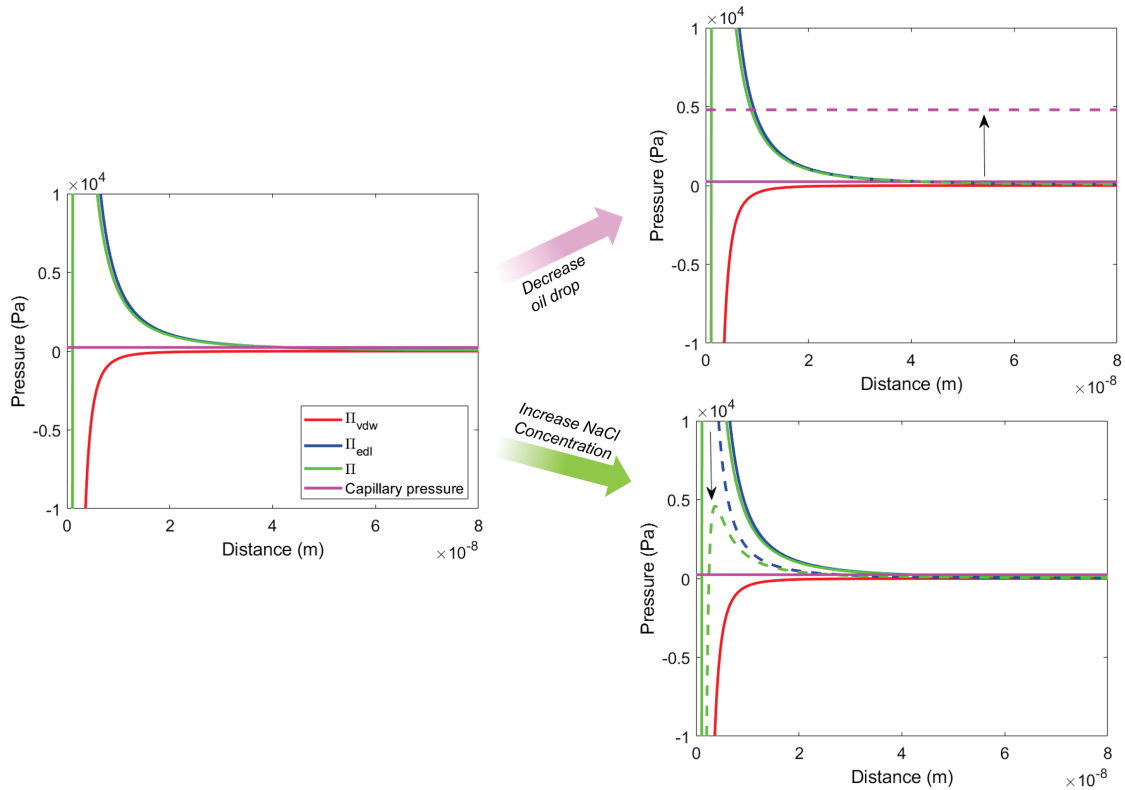
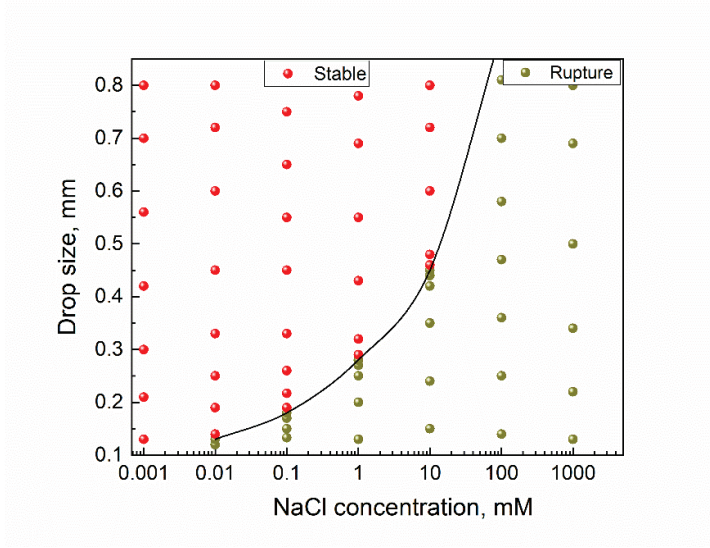


**Figure 5.10** Explanation of the effects of the dodecane drop size and NaCl concentration on the TLF stability between dodecane drops and talc

### 5.3.4 On other hydrophobic minerals

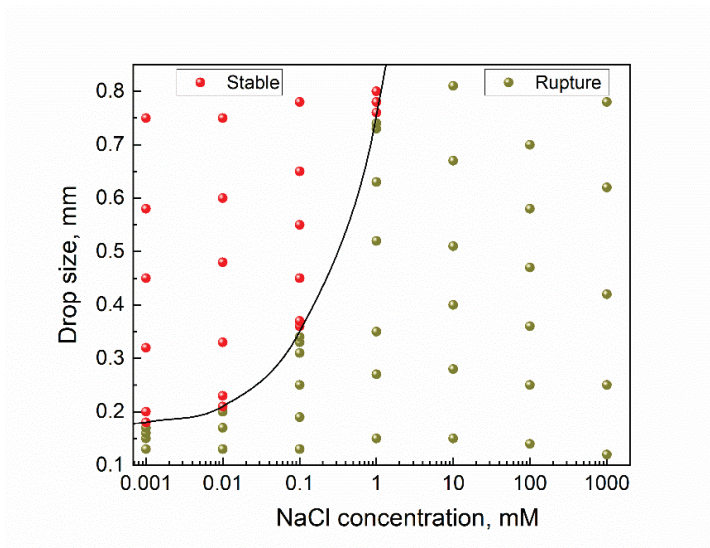
To test if the conclusions drawn on talc are universal, molybdenite and hydrophobic quartz were investigated following the same study protocol. The statistic experiments of the TLF stabilities between dodecane drops and molybdenite/hydrophobized quartz at various NaCl concentrations are summarized in Figure 11 and Figure 12, respectively.

In Figure 11, the stability boundary follows a similar trend to that in Figure 10. However, here the TLFs on the molybdenite surface require the critical dodecane drops for rupture to be smaller than that on talc at the same NaCl concentration. For example, when the NaCl concentration is 1 mM, the film on molybdenite ruptures when the dodecane drop is below 0.44 mm, but the value on talc is 0.56 mm. In the meantime, when the NaCl concentration is 100 mM and above, all the films rupture for the dodecane drops that have a radius smaller than 0.8 mm.



**Figure 5.11** The stabilities of TLFs between molybdenite and dodecane drops with different sizes at different NaCl concentrations

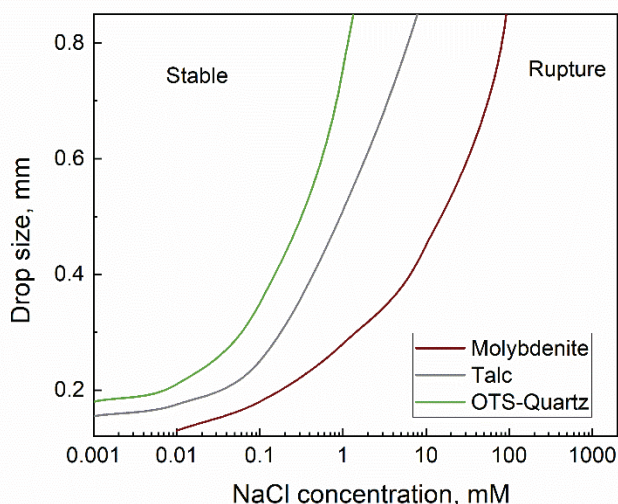
In contrast, Figure 12 tells a different story, where the films tend to be less stable than those on talc under the same conditions. If 1 mM NaCl concentration is still taken as an example, it is easy to observe that dodecane drops smaller than 0.74 mm will cause ruptures, while that for molybdenite and talc are 0.44 mm and 0.56 mm, respectively. And similar to the talc case, when the NaCl concentration is higher than 10 mM, the films always rupture. Overall, the stability boundaries contain a lot of information, and they are worth being compared in a separate graph, as shown in Figure 13.



**Figure 5.12** The stabilities of TLFs between hydrophobized quartz and dodecane drops with different sizes at different NaCl concentrations

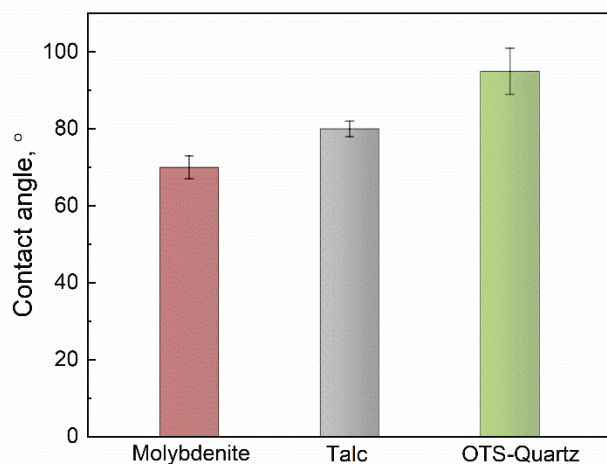


Figure 13 shows the comparison of stability boundaries in molybdenite-dodecane, talc-dodecane, and hydrophobized quartz-dodecane systems. The rupture zones have areas with the following sequence: OTS-quartz > talc > molybdenite, indicating under the same conditions, the liquid films on molybdenite are the most stable, while that on OTS-quartz are easiest to rupture. So there should be other factors than just the capillary pressure and disjoining pressure that can modify the film stability. We hypothesized that the intrinsic surface properties, especially the hydrophobicity, play a crucial role. Thus, as a standard procedure to characterize the surface hydrophobicity, the captive method to obtain the contact angles was employed in this work. And the results are provided in Figure 14.



**Figure 5.13** Comparison of stability boundaries for molybdenite-dodecane, talc-dodecane, and hydrophobized quartz-dodecane systems

It is shown in Figure 14 that the contact angle of the air bubble in the DI water on the molybdenite surface is about 70, while that on talc and hydrophobized quartz surfaces are 78 and 90, respectively. Interestingly, the sequence of the contact angles is the same as the rupture zone areas in Figure 13. That is to say, the liquid films on surfaces that are more hydrophobic tend to be unstable and ready to rupture. This might be due to the fact that the water densities near the hydrophobic surfaces are smaller than that are less hydrophobic<sup>31</sup> and thus easy to be broken during the drainage of the liquid films.



**Figure 5.14** Comparison of water contact angles on molybdenite, talc, and hydrophobized quartz

## 5.4 Summary and conclusions

The stability of water films confined between oil and hydrophobic solid surfaces is characterized by the STRIM technique. Results showed that stable water films form between oil drops and the abovementioned hydrophobic surfaces in DI water, and the equilibrium thickness decrease from 150 nm to 60 nm when reducing the oil drop radius from 0.9 mm to 0.2mm. But the water films become unstable and suddenly rupture when further decreasing oil drop sizes. Besides, increasing electrolyte concentrations and increasing surface hydrophobicity are also found to facilitate the water film ruptures. And the critical rupture thicknesses of water films decrease when reducing the size of oil drops or rising electrolyte concentrations. In the meantime, the thinning kinetics remain the same no matter how the experimental conditions varied.

The rupture of water films is mainly due to the negative disjoining pressure, which is the resultant force of capillary force and surface forces, especially the electronic double-layer force. However, the existence of hydrophobicity force cannot be well supported at the current stage. But the water films tend to rupture on more hydrophobic surface compared to the surface with less hydrophobicity. Summaries of the water film stabilities are provided in the forms of stability maps for different mineral surfaces, which can guide the selection of appropriate conditions in the relevant industrial processes.



## 5.5 Reference

- 1 Ralston, J., Dukhin, S. & Mishchuk, N. Wetting film stability and flotation kinetics. *Advances in Colloid and Interface Science* **95**, 145-236 (2002).
- 2 Thomas, S. Enhanced oil recovery-an overview. *Oil & Gas Science and Technology-Revue de l'IFP* **63**, 9-19 (2008).
- 3 Ramirez, A., Gutierrez, L. & Laskowski, J. S. Use of “oily bubbles” and dispersants in flotation of molybdenite in fresh and seawater. *Minerals Engineering* **148**, 106197 (2020).
- 4 Wie, J. M. & Fuerstenau, D. The effect of dextrin on surface properties and the flotation of molybdenite. *International journal of mineral processing* **1**, 17-32 (1974).
- 5 Xuefen, Z., Guiwu, L., Xiaoming, W. & Hong, Y. Molecular dynamics investigation into the adsorption of oil–water–surfactant mixture on quartz. *Applied surface science* **255**, 6493-6498 (2009).
- 6 Krasowska, M., Malysa, K. & Beattie, D. A. Recent advances in studies of bubble-solid interactions and wetting film stability. *Current Opinion in Colloid & Interface Science* **44**, 48-58 (2019).
- 7 Pan, L., Jung, S. & Yoon, R.-H. Effect of hydrophobicity on the stability of the wetting films of water formed on gold surfaces. *Journal of colloid and interface science* **361**, 321-330 (2011).
- 8 Atluri, V., Gao, Y., Wang, X., Pan, L. & Miller, J. D. The influence of polysaccharides on film stability and bubble attachment at the talc surface. *Mining, Metallurgy & Exploration* **36**, 71-80 (2019).
- 9 Pan, L. & Yoon, R.-H. Effects of electrolytes on the stability of wetting films: Implications on seawater flotation. *Minerals Engineering* **122**, 1-9 (2018).
- 10 Pan, L., Jung, S. & Yoon, R.-H. A fundamental study on the role of collector in the kinetics of bubble–particle interaction. *International journal of mineral processing* **106**, 37-41 (2012).
- 11 Liu, B. *et al.* Coalescence of bubbles with mobile interfaces in water. *Physical review letters* **122**, 194501 (2019).
- 12 Shi, C., Xie, L., Zhang, L., Lu, X. & Zeng, H. Probing the interaction mechanism between oil droplets with asphaltenes and solid surfaces using AFM. *Journal of colloid and interface science* **558**, 173-181 (2020).
- 13 Weiss, H. *et al.* Structure and Dynamics of Confined Liquids: Challenges and Perspectives for the X-ray Surface Forces Apparatus. *Langmuir* **35**, 16679-16692 (2019).
- 14 Zhang, X. *et al.* Simultaneous measurement of dynamic force and spatial thin film thickness between deformable and solid surfaces by integrated thin liquid film force apparatus. *Soft Matter* **12**, 9105-9114 (2016).
- 15 Zhang, X., Manica, R., Tchoukov, P., Liu, Q. & Xu, Z. Effect of approach velocity on thin liquid film drainage between an air bubble and a flat solid surface. *The Journal of Physical Chemistry C* **121**, 5573-5584 (2017).

- 16 Shi, C. *et al.* Measuring forces and spatiotemporal evolution of thin water films between an air bubble and solid surfaces of different hydrophobicity. *ACS nano* **9**, 95-104 (2015).
- 17 Liu, B., Manica, R., Xu, Z. & Liu, Q. The boundary condition at the air-liquid interface and its effect on film drainage between colliding bubbles. *Current Opinion in Colloid & Interface Science* (2020).
- 18 Chan, D. Y., Klaseboer, E. & Manica, R. Film drainage and coalescence between deformable drops and bubbles. *Soft Matter* **7**, 2235-2264 (2011).
- 19 Pan, L. & Yoon, R.-H. Measurement of hydrophobic forces in thin liquid films of water between bubbles and xanthate-treated gold surfaces. *Minerals Engineering* **98**, 240-250 (2016).
- 20 Xing, Y., Gui, X. & Cao, Y. The hydrophobic force for bubble-particle attachment in flotation—a brief review. *Physical Chemistry Chemical Physics* **19**, 24421-24435 (2017).
- 21 Xie, L., Cui, X., Gong, L., Chen, J. & Zeng, H. Recent Advances in the Quantification and Modulation of Hydrophobic Interactions for Interfacial Applications. *Langmuir* **36**, 2985-3003 (2020).
- 22 Feng, L., Manica, R., Grundy, J. S. & Liu, Q. Unraveling Interaction Mechanisms between Molybdenite and a Dodecane Oil Droplet Using Atomic Force Microscopy. *Langmuir* **35**, 6024-6031 (2019).
- 23 Huang, K. & Yoon, R.-H. Surface Forces in the Thin Liquid Films (TLFs) of Water Confined between n-Alkane Drops and Hydrophobic Gold Surfaces. *Langmuir* **35**, 15681-15691 (2019).
- 24 Aston, D. E. & Berg, J. C. Quantitative analysis of fluid interface-atomic force microscopy. *Journal of colloid and interface science* **235**, 162-169 (2001).
- 25 Tabor, R. F., Wu, C., Grieser, F., Dagastine, R. R. & Chan, D. Y. Measurement of the hydrophobic force in a soft matter system. *The journal of physical chemistry letters* **4**, 3872-3877 (2013).
- 26 Manica, R., Klaseboer, E. & Chan, D. Y. Force balance model for bubble rise, impact, and bounce from solid surfaces. *Langmuir* **31**, 6763-6772 (2015).
- 27 Gao, Y. & Pan, L. Measurement of instability of thin liquid films by synchronized tri-wavelength reflection interferometry microscope. *Langmuir* **34**, 14215-14225 (2018).
- 28 Zeppieri, S., Rodríguez, J. & López de Ramos, A. Interfacial tension of alkane+ water systems. *Journal of Chemical & Engineering Data* **46**, 1086-1088 (2001).
- 29 Yoon, R.-H. & Aksoy, B. S. Hydrophobic forces in thin water films stabilized by dodecylammonium chloride. *Journal of colloid and interface science* **211**, 1-10 (1999).
- 30 Liang, Y., Hilal, N., Langston, P. & Starov, V. Interaction forces between colloidal particles in liquid: Theory and experiment. *Advances in colloid and interface science* **134**, 151-166 (2007).

## 6 Interaction Forces between Water Droplets and Solid Surfaces Across Air Films\*

\* The material contained in this chapter has been published in *ACS omega*, reused with permission. Full citation: Gao Y, Jung S, Pan L. *Interaction Forces between Water Droplets and Solid Surfaces across Air Films*. *ACS omega*. 2019 Sep 27;4(15):16674-82.

### 6.1 Introduction

The impact of water droplets on solid surfaces is not only important from a fundamental perspective<sup>1</sup>, but also relevant to many technological applications, including dust control<sup>2</sup>, spray coating<sup>3</sup>, and pesticide control<sup>4,5</sup>. On superhydrophobic surfaces, falling water drops bounce off the surfaces<sup>6</sup>. On hydrophilic surfaces, water drops wet the surfaces readily<sup>7</sup>. Depending on the nature of the applications, wetting processes may or may not be beneficial. For dust suppression, it is desirable to have dust particles be wetted by liquid so that they settle to the ground.

The drop impact phenomena was first studied by Worthington<sup>8</sup>. Since then, numberless previous research efforts have been devoted to tracking the impact dynamics of drops<sup>9</sup>. A liquid drop's impact on a solid surface and/or a free surface is a complex process<sup>10,11</sup>, as it involves splashing<sup>12,13</sup>, crown formation<sup>14</sup>, spreading<sup>15</sup> and bouncing<sup>16</sup>. During the impact, an air film is formed between the water droplet and the solid surface. The presence of the intervening air film has significant effects on the impact dynamics of liquid drops<sup>17-20</sup>. The draining of the intervening air film builds up pressure within the air layer<sup>21</sup>, flattening the bottom of the droplet prior to coalescence. This leads to a delay in the wetting/merging process<sup>10,22</sup>. During the later stage of the impact, the intervening air film collapses<sup>23,24</sup>, resulting in the spreading of liquid drops on solid surfaces, or a merging of two free surfaces.

Despite of numerous investigations into drops' impacts on surfaces, very few studies were devoted to directly measuring the thickness profile of the air films during impact<sup>22,25,26</sup>. Previous studies have been focused on the instability of thin liquid films (TLFs)<sup>27-30</sup>. It has been found that the rupture thicknesses of TLFs are on the order of 100 nm<sup>31-35</sup>. The rupture thickness of the air film was found to be larger on the order of a few hundreds of nanometers, up to a few micrometers. The thickness of the air film has been previously measured using interferometry<sup>36,37</sup> and total internal reflection microscopy<sup>38</sup>. Using these techniques, it has been found that the air film ruptures at a thickness of 200-500 nm when two free silicon oil surfaces are brought closely together<sup>36,39</sup>. The authors claimed that at this distance or below, the van der Waals force becomes dominant and is responsible for the film rupture. For a water droplet impacting on a microscope glass slide, the critical rupture thicknesses of the air film are in the range of 250-400 nm<sup>40</sup>. Follow-up study indicates that the critical rupture thickness remains the same regardless of the hydrophobicity of solid surfaces and surface tensions of aqueous liquid drops<sup>37</sup>.

The exact value of the critical rupture thickness depends on the size of surface irregularities.

The rupture of the air films might be attributed to several mechanisms. Intermolecular force may be considered the major driving force for the film rupture<sup>37</sup>. In this case, the film rupture occurs when the separation distance within the acting range of attractive intermolecular forces. There might be two types of forces acting within the air gap between the two surfaces. The van der Waals force is monotonically attractive, which might be responsible for bringing the two surfaces into contact<sup>36</sup>. Another type of attractive forces leading to the film rupture might be electrostatic interaction between two oppositely charged surfaces. Other mechanisms/factors might include surface asperity<sup>37</sup>, which effectively reduces actual distance between the free water surface and the solid surface. However, no research has been conducted to accurately determine the intermolecular force between water droplets and solid surfaces across air films. The mechanism leading to the breakup of the air film is still elusive.

An accurate determination of the spatiotemporal thickness profile of a fast-evolving air film is a prerequisite to characterize the dynamics of air film draining and, subsequently, to determine the intermolecular force between two surfaces. This analysis involves a determination of the orders of each interference pattern. The authors of the present work previously improved the dual-wavelength interferometry technique by including a third synchronized and high-speed camera that recorded the interference fringes at the third wavelength<sup>41</sup>. The STRIM technique improves the accuracy of film thickness measurements to 10 nm or better over the range of 0 – 4  $\mu\text{m}$ , which is suitable to investigate highly unstable air films. Coupled with high-speed cameras, the STRIM is able to reconstruct the spatiotemporal thickness profiles of the air films.

In the present work, measurements have been carried out on polished solid surfaces of varying hydrophobicity by bringing water droplets towards flat solid surfaces at an approaching speed of approximately 600-1000 nm/s. During the course of approaching, the spatiotemporal thickness profiles of the air films are determined from the fast-evolving interference fringes. The film profile data are then analyzed to determine the critical rupture thickness and the kinetics of approach. From the kinetics data, the interaction force is determined. To further test the hypothesis that the water-solid interaction is sensitive to surface hydrophobicity, experiments are carried out on the basal surfaces of various layered minerals. These mineral surfaces exhibit varying surface hydrophobicity, and they are all atomically flat. The force results are discussed in the context of electrostatic forces.

## 6.2 Results

### 6.2.1 Water vs. Quartz

Figure 1 shows both a side view (a) and a bottom view (b) of the interaction between a water droplet and a flat solid surface in air. The bottom view was shown as a set of the interference fringes recorded at  $\lambda = 460, 527,$  and  $620$  nm, respectively (Figure 1b). In one experiment, a water droplet was brought towards a flat hydrophobic quartz surface by an external drive at a nominal velocity of approximately  $600$  nm/s. When the two surfaces were brought in close proximity on the order of  $100$  nm to a few micrometers, the water droplet plunged onto the solid surface manifested by a rupture of the air film. The rupture of the air film was followed by a spreading of the three-phase contact line. The spreading process occurred within a few milliseconds or less, and a finite contact angle was formed as shown from the side-view images (Figure 1a).

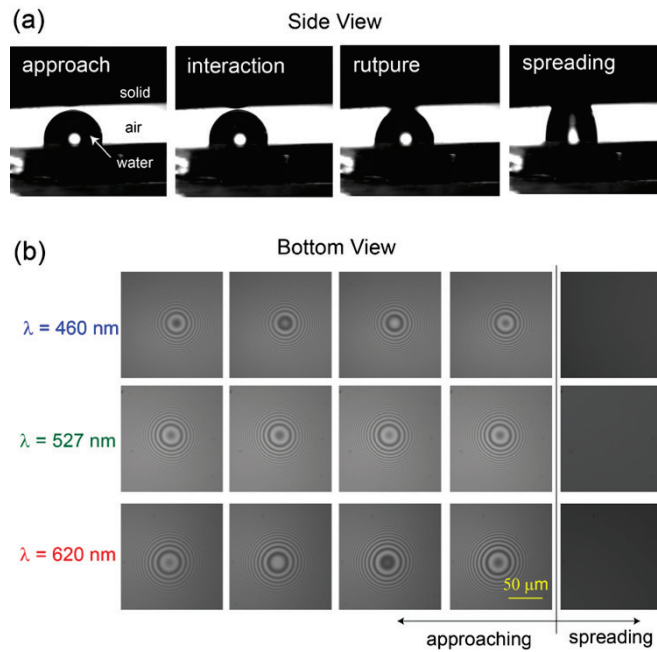


**Figure 6.1** Side view (a) and bottom view (b) of the interaction between water droplets and hydrophobic quartz surfaces.

The obtained three-wavelength interference fringes were analyzed to determine the separation distance. Figure 2 shows the spatiotemporal thickness profile of the air film between a water droplet and a hydrophobic quartz surface having a water contact angle ( $\theta_w$ ) of  $96^\circ$ . The data points in blue, green and red represent the experimental data obtained at  $\lambda = 460, 527,$  and  $620$  nm, respectively. The solid lines at each spatial profile were obtained using a polynomial fit. It was found that the fitted curves matched with

experimental data well. What also shown in Figure 2 is the difference ( $\Delta h$ )/error between experimental data and the polynomial fit. The maximum  $\Delta h$  is 20 nm and the RMS error is 5.93 nm. The profile shows that the water droplet maintained spherical during the interaction with the solid surfaces, validating the approach taken to determine interaction force as described in the aforementioned paragraph. On the hydrophobic quartz surface of  $\theta_w = 96^\circ$ , the critical rupture distance was found to be 45 nm.

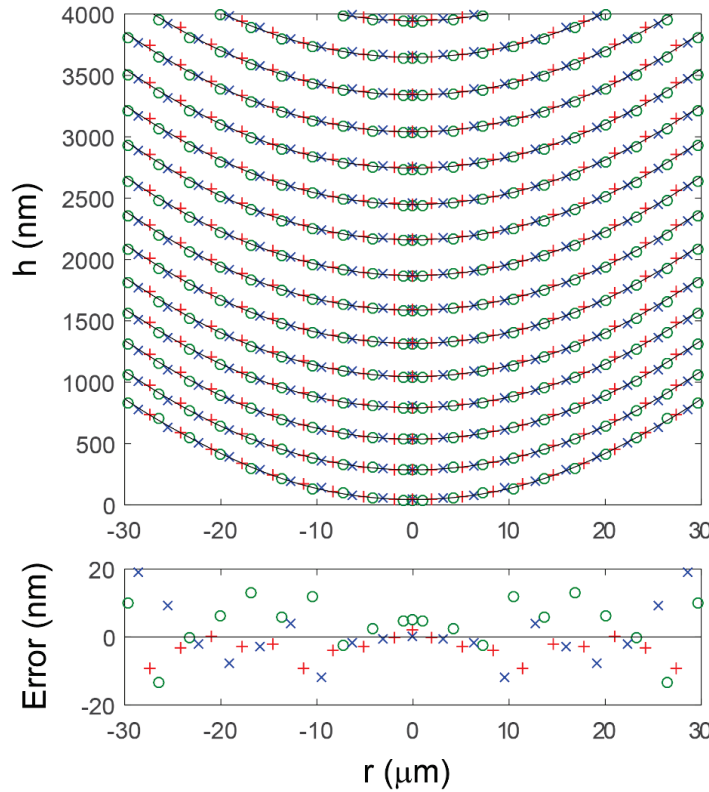


**Figure 6.2 a)** Spatiotemporal thickness profiles of the air film between a drop of DI water and a flat quartz surface having  $\theta_w$  of  $96^\circ$  and the difference ( $\Delta h$ ) between experimental data and the polynomial fit.

Figure 3 compares the spatiotemporal profile of the separation distances on quartz surfaces having different surface hydrophobicity. These quartz substrates exhibited water contact angles of  $96^\circ$ ,  $65^\circ$ ,  $35^\circ$ , and  $25^\circ$ , respectively. The lines shown in the profiles are polynomial fits to the spatial thickness profile data. The  $t = 0$  is when the closest separation distance is  $4 \mu\text{m}$ . As shown, the critical rupture distance ( $h_c$ ) was found to be 226 nm on the weakly hydrophobic quartz surface having  $\theta_w$  of  $65^\circ$ . The  $h_c$  values were increased to 865 and 1428 nm on quartz surfaces having  $\theta_w = 35^\circ$  and  $25^\circ$ , respectively. Our statistical study conducted on over 50 substrates shows that the  $h_c$  values increased with decreasing surface hydrophobicity of solids, confirming the accuracy of experimental data reported in this manuscript (see the supporting materials).

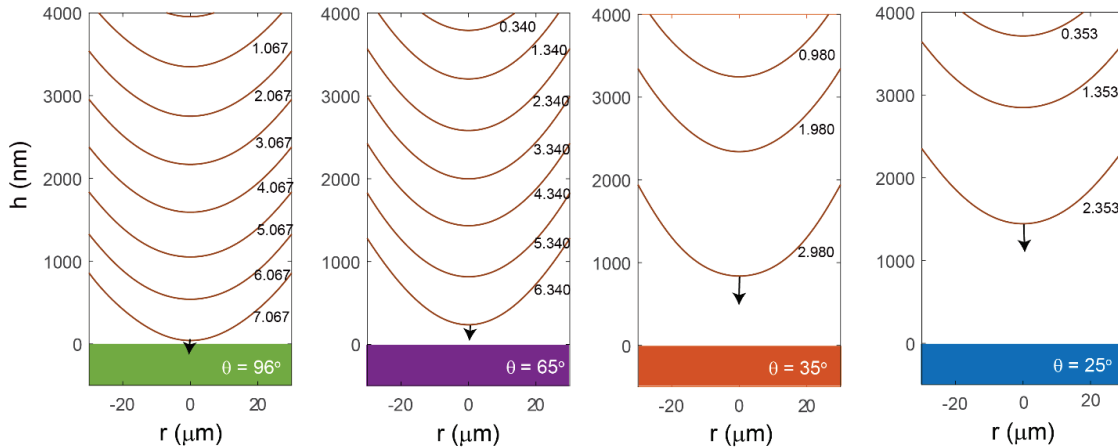


**Figure 6.3** Effect of surface hydrophobicity on spatiotemporal profiles of the air films between water droplets and quartz surfaces.

Note that the critical rupture distance was found to be above  $2 \mu\text{m}$  on very hydrophilic surfaces having  $\theta_w < 20^\circ$ . At this distance or above, the interference fringes were barely visible and therefore a determination of the rupture thickness became challenging. In this communication, the result obtained on very hydrophilic surfaces will not be discussed.

Other characteristics of the spatiotemporal profiles include the kinetics of approach. The two adjacent spatial profiles were collected at an interval of 1 seconds. As shown in Figure 3, the water droplet accelerated towards the hydrophilic solid surfaces as reflected by a wider gap between two adjacent spatial profiles obtained on the hydrophilic surfaces than those obtained on the hydrophobic surfaces. To further quantify the kinetics of approach, Figure 4 shows the effect of surface hydrophobicity on both the kinetics of approach ( $h$  vs.  $t$ ) and the approaching velocity ( $V$  vs.  $t$ ). The result shows that the approaching velocity remained constantly on hydrophobic surfaces of  $\theta_w = 96^\circ$  during the course of approaching. The kinetics of approach was deaccelerated as the two surfaces were brought closer together. On the hydrophilic surface having  $\theta_w = 25^\circ$ , however, the kinetics were accelerated with a maximum velocity of approximately  $-3,800 \text{ nm/s}$ . This result suggests that the kinetics of approach increases with decreasing surface hydrophobicity of solids.

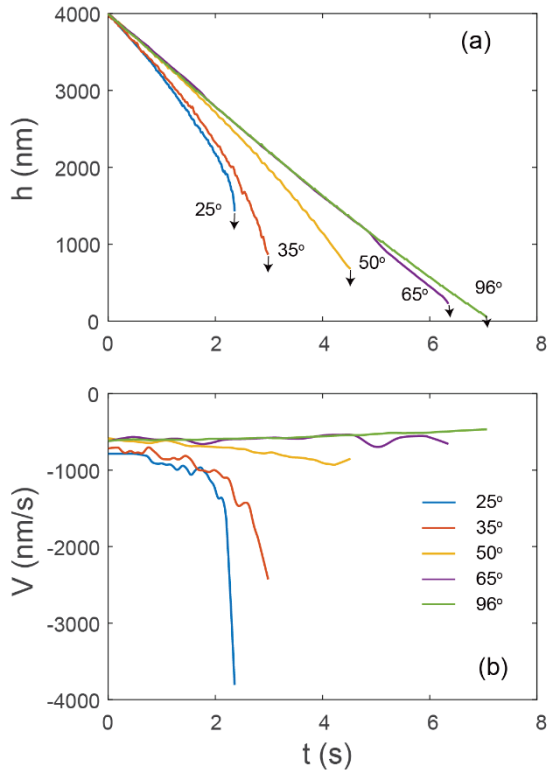


**Figure 6.4** Effect of hydrophobicity on the kinetics of film thinning (a) and approaching velocity (b).

**Table 6.1** Characteristics of the rupture of air films formed between water droplets and solid surfaces.

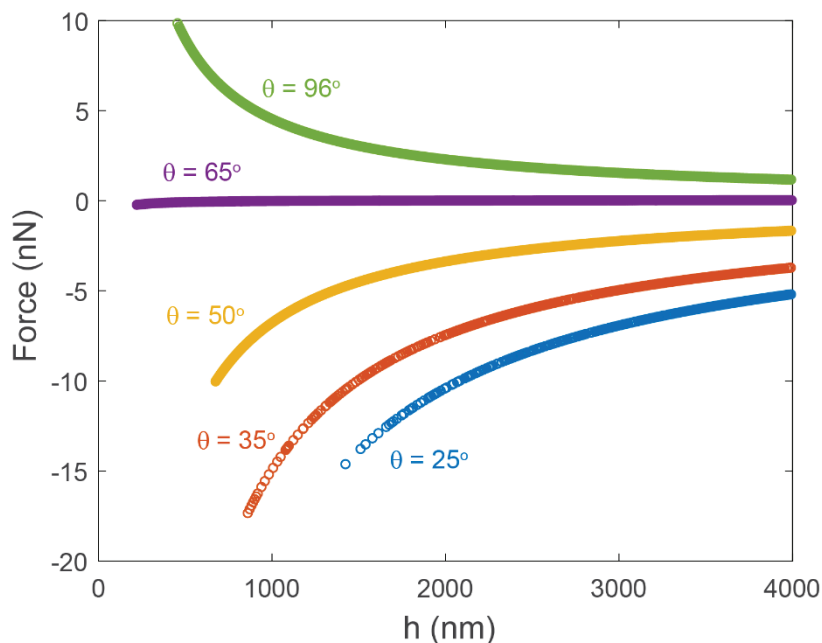
$\theta_w$ (°)	$t_c$ (s)	$h_c$ (nm)	$\Delta V_c$ (nm/s)
96	7.07	45	-133
65	6.30	226	58
50	4.52	679	312
35	2.99	865	1800
25	2.36	1428	3200



Table 1 summarizes several characteristics of the rupture of air films, including water contact angle ( $\theta_w$ ), critical rupture distance ( $h_c$ ), critical rupture velocity ( $\Delta V_c$ ), and critical rupture time ( $t_c$ ). The critical rupture velocity is defined as the difference between the terminal approaching velocity and the external driving velocity prior to the film rupture, as  $\Delta V_c = V_t - dh_e/dt$ . The  $\Delta V_c$  value is influenced dominantly by the interaction force between two surfaces. It has been found that the  $\Delta V_c$  was increased by reducing surface hydrophobicity of the solid surfaces. The negative value obtained on the hydrophobic surface having  $\theta_w = 96^\circ$  might be associated with repulsive electrostatic forces (columbic force), which will be discussed in detail in the following paragraphs.

The critical rupture time ( $t_c$ ) is defined as the total time spent from the initial closest separation distance of  $4 \mu\text{m}$  to the critical rupture distance. As shown, the critical rupture time decreases with decreasing surface hydrophobicity. The reduced  $t_c$  with decreasing  $\theta_w$  might be attributed to two reasons: 1) an increase in critical rupture thickness, and 2) an accelerated kinetics of approaching. Evidently, all characteristics signify an increase in attraction forces between water drops and solids with decreasing surface hydrophobicity.

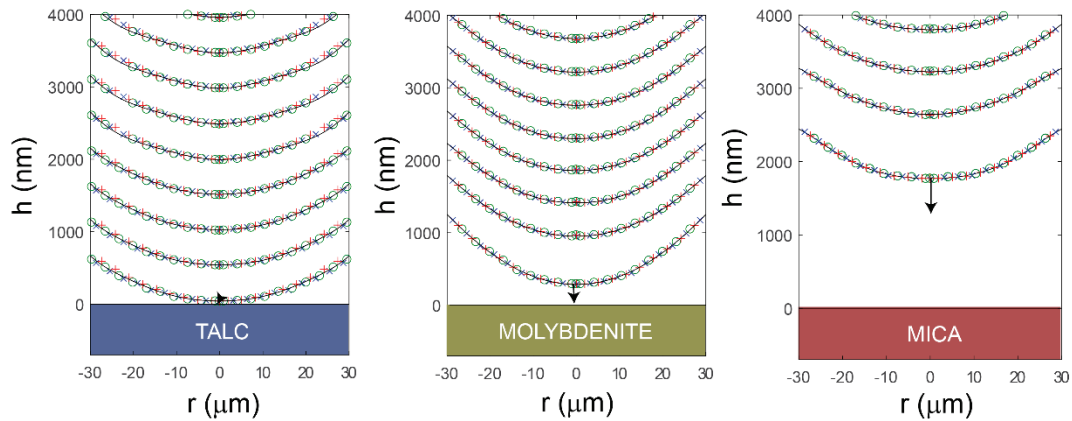
To better understand the underlying mechanisms involved in faster thinning kinetics observed on hydrophilic surfaces, the interaction force was determined using Equation (7). In Equation (7),  $\mu = 1.825 \times 10^{-5} \text{ kg/m}\cdot\text{s}$  at  $20^\circ\text{C}$ , the radius of curvature ( $a$ ) was determined by fitting individual spatial profile using Equation (4), and  $dh_e/dt = -600 \text{ nm/s}$ . Figure 5 shows the interaction forces between water drops and solid surfaces having different water contact angles. The result shows that the interaction force is attractive with hydrophilic quartz surfaces. The force becomes less attractive with increasing surface hydrophobicity of the quartz substrates. On hydrophobic surfaces having  $\theta_w = 65^\circ$ , the interaction force becomes almost zero, with a weak attraction at a distance of below  $500 \text{ nm}$ . The interaction force becomes net repulsive on very hydrophobic surfaces ( $\theta_w = 96^\circ$ ). Evidently, the result on interaction forces between water droplets and solid surfaces across air films is consistent with the result for kinetics of approach.



**Figure 6.5** Effect of surface hydrophobicity on the Interaction forces between water droplets and silica surfaces across air films.

### 6.2.2 Water vs. Minerals

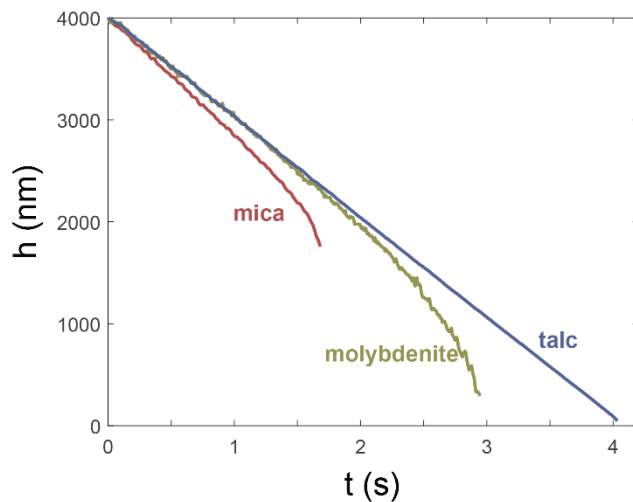
To further test the hypothesis that both the interaction and the rupture thickness of the air films are relevant to the surface hydrophobicity rather than surface functional groups, the second part of this work is to study the interaction forces between water droplets and natural mineral surfaces. A variety of layered minerals were used as the model surfaces, including muscovite mica, molybdenite, and talc. These mineral surfaces exhibit different degrees of surface hydrophobicities. Mica is naturally hydrophilic, while molybdenite and talc are naturally hydrophobic. The measurements were conducted on the basal planes of mineral surfaces which were atomically flat.



**Figure 6.6** Spatiotemporal profiles of water droplets against layered mineral surfaces.

Figure 6 shows the spatiotemporal profiles obtained when water droplets approach three mineral surfaces at a nominal approaching velocity of 1000 nm/s. As shown, the water droplet steadily approached a talc surface and plunged onto the surface at a closest separation distance of 43.5 nm. The critical rupture distance was determined to be 1767 nm and 288 nm on mica and molybdenite surfaces, respectively.

Also shown from the spatiotemporal profiles (Figure 6) is the kinetics of approach. It has been shown that the kinetics was faster on mica surfaces than obtained on molybdenite and talc surfaces. Figure 7 compares the kinetics of approach obtained on three different mineral surfaces. The external driving velocity was 1000 nm/s. As shown, the kinetics curve was linear on talc surfaces with no significant accelerations during the course of approach. On molybdenite surface, acceleration occurred at a closest separation distance of below 2000 nm. On mica surface, which is very hydrophilic, an accelerated approaching was evident at a distance of above 3000 nm.



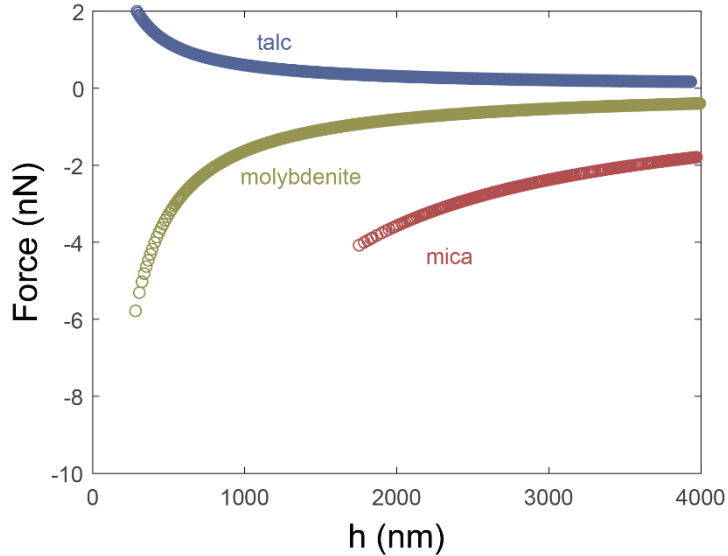
**Figure 6.7** Thinning kinetics of air films between water droplets and mineral substrates.

Table 2 summarizes several characteristics of natural mineral systems, including  $\theta_w$ ,  $h_c$ ,  $t_c$ , and  $\Delta V_c$ . The result suggests that 1) the  $h_c$  value decreases with increasing surface hydrophobicity ( $\theta_w$ ), and 2) the kinetics of approach increases with decreasing  $\theta_w$ . All data signify that the results obtained with natural mineral surfaces coincide with that obtained with chemically functionalized quartz surfaces, indicating that the water-solid interaction is sensitive to the surface hydrophobicity of solids rather than the surface functional groups.

**Table 6.2** Characteristics of thinning and rupture of air films between water droplets and different mineral surfaces.

Substrates	Mica	Molybdenite	Talc
$\theta$ (°)	10	65	90
$h_c$ (nm)	1767	288	43.5
$t_c$ (s)	4.03	3.84	1.68
$\Delta V_c$ (nm/s)	2425	1100	67

Figure 8 shows the interaction forces between water droplets and mineral surfaces. The results were determined from the spatiotemporal profiles shown in Figure 6 using Equation (7). As shown, the interaction force was weakly attractive between water droplets and talc surfaces, and became more attractive on surfaces of less hydrophilic such as molybdenite and mica. The interaction force result is in a good agreement with the surface hydrophobicity data, as the intermolecular force became more attractive with decreasing the surface hydrophobicity of mineral surfaces.



**Figure 6.8** Interaction forces between water droplets and a variety of natural mineral surfaces.

### 6.3 Discussion

As presented in the Results section, the critical rupture thickness of the air film between a water droplet and a solid surface increases exponentially with decreasing surface hydrophobicity. This finding was also found to be applicable to natural mineral surfaces regardless of surface functional groups. For instance, chemically hydrophobized quartz surfaces expose hydrocarbon when immersed in water. Talc's basal surface is composed of a silicon-oxygen tetrahedral, with magnesium-oxygen/hydroxyl octahedral in between. The basal surface does not contain hydroxyl groups which render the surface hydrophobic<sup>42</sup>. Molybdenite's basal plane has sulfur elements exposed on its surface. When immersed in water, molybdenite's basal surface exhibits natural hydrophobicity<sup>43</sup>. All of these hydrophobic surfaces exhibit a critical rupture distance of less than 300 nm when in close proximity to a water droplet.

The increase in the critical rupture thickness with decreasing surface hydrophobicity of solid surfaces might be explained using the thermodynamic principle and the mechanical mechanism. Thermodynamically, the free energy change ( $\Delta G$ ) associated with the wetting of solid surfaces by water is given as<sup>44</sup>,

$$\Delta G = \gamma_{sl} - \gamma_s - \gamma_{lv} \quad (1)$$

where  $\gamma_{sl}$ ,  $\gamma_s$  and  $\gamma_{lv}$  are the interfacial tensions between solid and water, between solid and air, and between liquid and air, respectively. Using Young's equation, it might be modified to,

$$\Delta G = -\gamma_{lv}*(1+\cos\theta) \quad (2)$$

where  $\theta$  is the water contact angle of solid surfaces. According to Equation (2), the free energy change ( $\Delta G$ ) becomes more negative when decreasing the surface hydrophobicity of solid surfaces (i.e., increasing  $\cos\theta$ ), indicating that hydrophilic surfaces can be wetted by water more easily than hydrophobic surfaces. The free energy change reaches a maximum of  $-2\gamma_{lv}$  on hydrophilic surfaces with  $\theta_w = 0^\circ$ . This thermodynamic analysis provides perspectives on the critical rupture distance.

Mechanically, the wetting of solid surfaces by water might occur when the gradient of the interaction force exceeds the spring constant or effective elastic constant of a water free surface<sup>45,46</sup>. For the case of drops, the spring constant is proportional to surface tension of liquid<sup>47</sup>. Prior to the rupture of an air film, the elastic force balances the interaction force, maintaining the water droplet spherical. When the attractive force exceeds a critical value, the air film ruptures and followed by a spreading of water on a solid surface. Both Figure 5 and Figure 8 suggest that the rupture of air films might occur when the gradient of interaction force exceeds in the range of 9.7 mN/m and 20 mN/m for water droplets having radii of 400-550  $\mu\text{m}$ . For very hydrophobic surfaces ( $\theta > 80^\circ$ ), we have shown that the rupture of air films occurred at a closest separation distance of below 100 nm, where the total force might be slightly attractive or repulsive. At this distance or below, the bridging of water droplets and solid surfaces might be attributed to additional factors, *e.g.* surface asperity, despite of great efforts to minimize surface contaminations during the surface preparation.

Another characteristic of the water-surface interaction is the kinetics of approach. It was found that the kinetics of approach increases with decreasing surface hydrophobicity of the substrates. The fast approach kinetics observed on hydrophilic surfaces is attributed to a strong attractive force. Figures 5 and 8 show the total interaction force between water droplets and flat solid surfaces that have different degrees of hydrophobicity. The total force is consisted of surface force and hydrodynamic force. The viscosity of air is two orders smaller than that of water ( $\mu=1.825 \times 10^{-5} \text{ kg/m}\cdot\text{s}$  at 20  $^\circ\text{C}$ ), and, therefore, the hydrodynamic force between two surfaces in air at a low approach speed (*i.e.* 600-1000 nm/s) is considerably negligible. In this regard, the measured force is mainly contributed from surface forces.

The calculated forces are fitted to an  $F = c/h$  function, where  $c$  is a constant and  $h$  is the separation distance. Figure 9 shows the fitting result with  $c$  values listed. It was found that the use of a  $c/h$  function fits the force data well, indicating that the measured surface force between two surfaces might be electric force following Coulomb's law<sup>48</sup>. These water droplets might carry opposite charges from hydrophilic solid surfaces, while the hydrophobic surfaces might carry similar charges as water droplets.

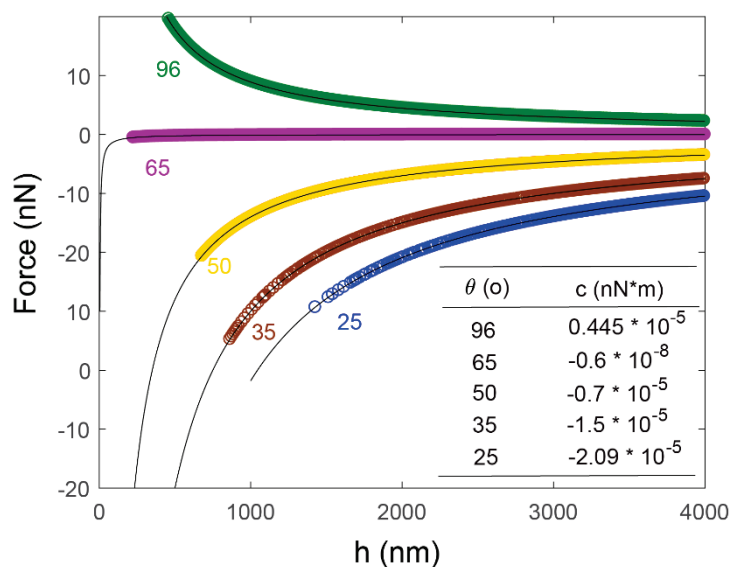


**Figure 6.9** Fitting of obtained force curves on quartz plates with  $F = c/h$  function.

Water drops used in this study were formed by passing DI water from a syringe through a micro-sized stainless steel needle. Electrical double layers are formed when DI water flows through a metal needle. Since the inner surfaces of the stainless steel tubing are negatively charged, this results in positive charges on surfaces of water droplets. The carried charges by the water droplet are achieved due to the charge separation when a water droplet is released from a stainless-steel needle to the quartz plate (i.e., an insulator). In this regard, the water droplet might carry excess hydrated proton on the surfaces of water droplets in the formation of  $H_9O_4^+$ ,  $H_3O^+$  or  $H_5O_2^+$ , causing the droplets to carry charges up to  $4.5 * 10^{-6} C/m^2$  <sup>49,50</sup>.

Negative charges on hydrophilic surfaces might be attributed to the adsorption of water molecules on their surfaces<sup>51</sup>. At ambient conditions, water molecules might adsorb on solid surfaces to form pitches or islands with a few nanometers in thickness<sup>52-55</sup>. The adsorption of water molecules renders the solid surfaces negatively charged due to the  $OH^-$  ion transfer. We have also shown that the negative charges on solid surfaces decrease with increasing the hydrophobicity of solids. Hydrophobic surfaces have difficulty adsorbing water molecules; however, the mechanism for which the hydrophobic surfaces carrying positive charge is still not clear.

## 6.4 Conclusion and Summary

In this work, we have studied the kinetics of thinning and rupture of air films formed between liquid droplets of DI water and mineral surfaces using the newly developed Synchronized Tri-wavelength Reflection Interferometry Microscopy (STRIM) technique. The spatiotemporal thickness profiles of the air film during the interaction between water

droplets and flat solid surface were determined with a 10 nm resolution over the distance of 0–4  $\mu\text{m}$ . The effect of surface hydrophobicity on the critical rupture thickness of the air film was studied. By determining the evolution of the pressure within the air gap, we have determined the interaction force between water droplets and solid surfaces across an air film for the first time.

The results showed that water droplets spread on solid surfaces spontaneously, regardless of the surface hydrophobicity. The critical rupture thickness of the air films increases exponentially with decreasing the surface hydrophobicity of solid surfaces. The critical rupture thickness was found to be above 2  $\mu\text{m}$  on a very hydrophilic quartz surface having a water contact angle of below 20°.

An acceleration of approaching was found between water droplets and hydrophilic solid surfaces. The acceleration in the film thinning was attributed to the presence of attractive surface forces. These interactions were strongly attractive on hydrophilic surfaces, and became less attractive with increased hydrophobicity of the surfaces. These attractive forces might be electric forces. The charging status was found to be more relevant to the hydrophobicity of surfaces, indicating that the charges on solid surfaces might be associated with the adsorption of water molecules on surfaces. This work provides fundamental insights into the wetting of solid surfaces by water drops, and the surface forces revealed between water droplets and solid surfaces across an air film are new additions to the field of surface forces.

## 6.5 Materials and Experiments

### 6.5.1 Materials

Polished fused quartz plates were used as substrates in this study and were obtained from Technical Glass Product. The RMS roughness of the quartz plates was less than 0.3 nm. Prior to the hydrophobization process, the substrates were cleaned in a freshly prepared piranha solution ( $\text{H}_2\text{SO}_4:\text{H}_2\text{O}_2 = 3:1$ , by volume) at a temperature of 80 °C for 15 minutes. The substrates were then cleaned with amounts of de-ionized (DI) water to remove acid residue on surfaces and dried in an ultrapure  $\text{N}_2$  stream. The obtained quartz plates were free of contaminants, hydrophilic, and could be wetted by water completely. Minerals samples, including molybdenite, mica, and talc, were obtained from various sources. These mineral samples were well crystallized. A freshly exposed surface was prepared on each of the minerals by peeling off the top layer with an adhesive tape. DI water was supplied by a Barnstead water purification system (Thermo Fisher). The resistance of the DI water was above 18.2  $\text{M}\Omega\cdot\text{cm}$ .

Hydrophobic quartz surfaces were prepared through a methylation process. Methyltrichlorosilane (MTS, 95%) and octadecyltrichlorosilane (OTS, 95%) were used as the chemicals. In this experiment, cleaned and dried quartz plates were immersed in a freshly prepared silane-in-toluene solution. The surface hydrophobicity was controlled by



varying concentrations of chemicals and immersion times. The hydrophobized quartz plates were taken out of the toluene solution and were cleaned with chloroform followed by isopropanol solutions in an ultrasonic cleaner for half an hour to remove residual chemicals on surfaces. The plates were then dried in an ultrapure N<sub>2</sub> streams in a fume hood and stored temporarily in a clean glass container. All chemicals used were ACS grade. The toluene solution was de-hydrated using 3 Å beaded molecular sieves (Alfa Aesar) before the use.

### 6.5.2 Experimental setup

Figure 10 shows a schematic diagram of the experimental set-up used for studying the interaction between water droplets and solid surfaces. In this experiment, a water droplet is brought towards an upper flat solid surface at a constant nominal velocity. As it approaches, the separation distance between the two surfaces is determined using the Synchronized Tri-wavelength Reflection Interferometry Microscope (STRIM)<sup>41</sup>. STRIM records multi-colored interference fringes of an air gap between a hemispherical water droplet and a flat solid surface. The fringe patterns are then used to determine the spatiotemporal thickness profile of the air film which reflects the dynamics of water droplets under the influence of surface and hydrodynamic forces. In addition, a side-view camera is used to capture the contact angle images as well as the evolution of the moving contact line. Experiments are conducted at the ambient condition (70 °F and 30-55% humidity).

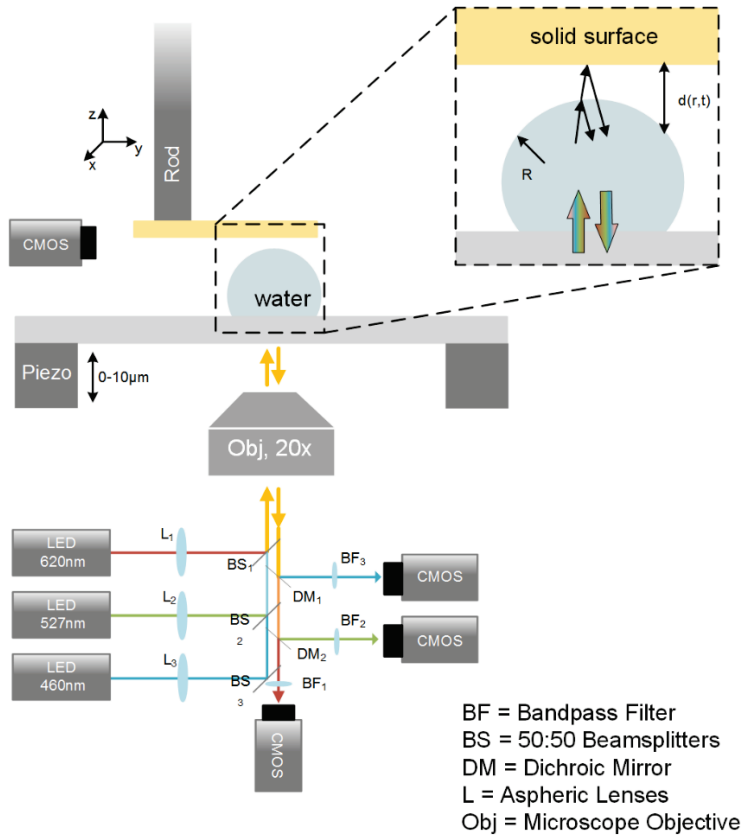


**Figure 6.10** A schematic drawing of an experimental set-up for measuring the spatiotemporal thickness profile of air films between water droplets and flat solid surfaces.

In using STRIM technique, colored light beams are generated using three high-power color LEDs. These colored light beams are collimated and combined using beam combiners. A 20x infinity-corrected long working distance objective (Mitutoyo) is used. The incident light beam illuminates and then gets reflected at two adjoining interfaces of an air layer between the water droplet and the solid surface. The two reflected beams interfere and form a “Newton rings” pattern. The fringe pattern exits the microscope, and is separated by dichroic mirrors to interference patterns of different wavelengths. Three cameras are synchronized to capture images simultaneously at a rate of 150 frames per seconds. Short-pass optical filters are placed at the front of each camera to create a monochromatic image.

Image processing of the interference fringes is conducted using a self-programmed MATLAB code based on the principle of interferometry<sup>56</sup>. Details can be found in the previous publication<sup>41</sup>. The recorded patterns are processed to obtain spatiotemporal profiles of the air film between water droplets and solid surfaces. The analysis of fringe images starts with a determination of the film thickness at the symmetric axis (*i.e.*,  $r = 0$ ). In this analysis, the orders of the fringes are determined when the thickness curves

obtained at three distinct wavelengths overlap with each other. By solving for the distance ( $h$ ) along the radial coordinates ( $r$ ), the spatiotemporal thickness profile of the air film,  $h(r, t)$ , is obtained. The critical rupture distance ( $h_c$ ) is defined as the minimum separation distance prior to the coalescence. The spatiotemporal thickness profile of the air film is also referred to as the spatiotemporal shape profile of the water droplet, since the solid surface is non-deformable.

### 6.5.3 Experimental procedure

In each experiment, a water droplet is placed on a polished fused quartz plate. The water droplet is created using a gas-tight micro-syringe with a stainless steel micro-needle. The radii of the water droplets are in the range of 440 – 570  $\mu\text{m}$ . To form a hemispherical droplet on the surface, the quartz surface is rendered hydrophobic by immersing the substrates in a  $10^{-3}$  M OTS-in-toluene solution for 1-3 hours. The hydrophobized quartz plate is rinsed with chloroform followed by isopropanol to remove residue chemicals on its surface. The hydrophobized quartz plate exhibits a water contact angle of above  $90^\circ$ . The quartz plate sits on a customized piezo-controlled z-stage, with a 1.5-inch ID aperture. This configuration allows light beams to pass through a piezoelectric Z-stage and illuminate the air film directly. The piezo stage can travel at a maximum of 7  $\mu\text{m}$  at a nominal velocity of 0 - 2  $\mu\text{m/s}$ .

A series of experiments are conducted by bringing a water droplet towards a flat mineral surface across an air film. Initially, the mineral surface is lowered manually to a closest separation distance of 5-10  $\mu\text{m}$ . At this distance or below, the interference fringe becomes slightly visible. This is followed by bringing the water droplet towards the upper surface at a nominal velocity of 600-1200 nm/s, while recording three-colored fringes simultaneously. Each experiment generates three sets of monochromatic fringe images at  $\lambda = 460, 527, \text{ and } 620$  nm, respectively. The images are processed to determine spatiotemporal profiles, which can be used to determine the interaction forces using the method described in the following paragraphs.

### 6.5.4 Force calculation

The interaction force between a water droplet and a flat surface across an air film is determined by solving the pressure distribution in the thin gap formed between the two surfaces. The pressure gradient within the gap is governed by the Reynolds lubrication equation<sup>57,58</sup>,

$$\frac{\partial p}{\partial r} = \frac{6\mu}{h^3} \frac{dh}{dt} r \quad (3)$$

where  $\mu$  is the viscosity of the air,  $h$  is the separation distance,  $r$  is the radial position and  $t$  is time. The water droplet remains spherical during the process as reflected by the

experimentally obtained spatiotemporal profiles, and therefore the separation distance can be represented as,

$$h(r,t) \approx h_0 + \frac{r^2}{2a} = h_0(1+s^2) \quad (4)$$

where  $h_0$  is the closest separation distance,  $a$  is the radius of curvature, and  $s = r/(2ah_0)^{1/2}$ . By substituting Equation (4) into Equation (3), one obtains

$$\frac{\partial p}{\partial s} = \frac{12\mu a}{h_0^2} \frac{dh_0}{dt} \frac{s}{(1+s^2)^3} \quad (5)$$

By integrating Equation (5), one obtains the pressure distribution along the radial position under one boundary condition  $p = p_\infty$  at  $r = a$ ,

$$p(s,t) - p_\infty = -\frac{3\mu a}{h_0^2} \left( \frac{dh_0}{dt} - \frac{dh_e}{dt} \right) \frac{1}{(1+s^2)^2} \quad (6)$$

where  $dh_e/dt$  is the approaching velocity at the outer region ( $r = a$ ). The  $dh_e/dt$  is equal to the external approaching velocity. Therefore, the forces due to the interaction between two surfaces can be determined by integrating the pressure distribution over the total area,

$$F = \int_0^\infty (p - p_\infty) 2\pi(2ah_0) s ds = -\frac{6\pi\mu a^2}{h_0} \left( \frac{dh_0}{dt} - \frac{dh_e}{dt} \right) \quad (7)$$

In Equation (7), both  $h_0$  and  $dh_0/dt$  can be determined from the spatiotemporal profiles obtained experimentally from interference fringes. The  $a$  value can be determined using Equation (4). The force data are presented as a function of the closest separation distance  $h_0$ .

## 6.6 Reference

- 1 Jossierand, C. & Thoroddsen, S. T. Drop impact on a solid surface. *Annual review of fluid mechanics* **48**, 365-391 (2016).
- 2 Chander, S., Alaboyun, A. & Aplan, F. in *Proceedings of the Third Symposium on Respirable Dust in the Mineral Industries*. 193-202.
- 3 Roisman, I. V., Horvat, K. & Tropea, C. Spray impact: Rim transverse instability initiating fingering and splash, and description of a secondary spray. *Physics of Fluids* **18**, 102104, doi:10.1063/1.2364187 (2006).
- 4 Kumar, M., Kulkarni, M. A., Chembu, N. G., Banpurkar, A. & Kumaraswamy, G. Aqueous dispersions of lipid nanoparticles wet hydrophobic and superhydrophobic surfaces. *Soft Matter* **14**, 205-215, doi:10.1039/C7SM01817G (2018).
- 5 Song, M. *et al.* Controlling liquid splash on superhydrophobic surfaces by a vesicle surfactant. *Science advances* **3**, e1602188 (2017).
- 6 Gauthier, A., Symon, S., Clanet, C. & Quéré, D. Water impacting on superhydrophobic macrottextures. *Nature communications* **6**, 8001 (2015).
- 7 Rioboo, R., Marengo, M. & Tropea, C. Time evolution of liquid drop impact onto solid, dry surfaces. *Exp. Fluids* **33**, 112-124 (2002).
- 8 Worthington Arthur, M. & Clifton Robert, B. XXVIII. On the forms assumed by drops of liquids falling vertically on a horizontal plate. *Proceedings of the Royal Society of London* **25**, 261-272, doi:10.1098/rspl.1876.0048 (1877).
- 9 Yarin, A. L. DROP IMPACT DYNAMICS: Splashing, Spreading, Receding, Bouncing.... *Annual Review of Fluid Mechanics* **38**, 159-192, doi:10.1146/annurev.fluid.38.050304.092144 (2006).
- 10 Kolinski, J. M. *et al.* Skating on a Film of Air: Drops Impacting on a Surface. *Phys. Rev. Lett.* **108**, 074503, doi:10.1103/PhysRevLett.108.074503 (2012).
- 11 Bird, J. C., Mandre, S. & Stone, H. A. Short-Time Dynamics of Partial Wetting. *Phys. Rev. Lett.* **100**, 234501, doi:10.1103/PhysRevLett.100.234501 (2008).
- 12 Mandre, S. & Brenner, M. P. The mechanism of a splash on a dry solid surface. *J. Fluid Mech.* **690**, 148-172, doi:10.1017/jfm.2011.415 (2011).
- 13 Xu, L., Zhang, W. W. & Nagel, S. R. Drop Splashing on a Dry Smooth Surface. *Phys. Rev. Lett.* **94**, 184505, doi:10.1103/PhysRevLett.94.184505 (2005).
- 14 Roisman, I. V. & Tropea, C. Impact of a drop onto a wetted wall: description of crown formation and propagation. *J. Fluid Mech.* **472**, 373-397, doi:10.1017/S0022112002002434 (2002).
- 15 Ukiwe, C. & Kwok, D. Y. On the Maximum Spreading Diameter of Impacting Droplets on Well-Prepared Solid Surfaces. *Langmuir* **21**, 666-673, doi:10.1021/la0481288 (2005).
- 16 Zhang, R., Hao, P. & He, F. Rapid bouncing of high-speed drops on hydrophobic surfaces with microcavities. *Langmuir* **32**, 9967-9974 (2016).
- 17 Tang, X., Saha, A., Law, C. K. & Sun, C. Bouncing drop on liquid film: Dynamics of interfacial gas layer. *Physics of Fluids* **31**, 013304, doi:10.1063/1.5063257 (2019).

- 18 Langley, K., Li, E. Q. & Thoroddsen, S. T. Impact of ultra-viscous drops: air-film gliding and extreme wetting. *J. Fluid Mech.* **813**, 647-666, doi:10.1017/jfm.2016.840 (2017).
- 19 de Ruiter, J., Lagraauw, R., Mugele, F. & van den Ende, D. Bouncing on thin air: how squeeze forces in the air film during non-wetting droplet bouncing lead to momentum transfer and dissipation. *Journal of fluid mechanics* **776**, 531-567 (2015).
- 20 Lee, J. S., Weon, B. M., Je, J. H. & Fezzaa, K. How Does an Air Film Evolve into a Bubble During Drop Impact? *Phys. Rev. Lett.* **109**, 204501, doi:10.1103/PhysRevLett.109.204501 (2012).
- 21 Mandre, S., Mani, M. & Brenner, M. P. Precursors to Splashing of Liquid Droplets on a Solid Surface. *Phys. Rev. Lett.* **102**, 134502, doi:10.1103/PhysRevLett.102.134502 (2009).
- 22 Dell'Aversana, P., Tontodonato, V. & Carotenuto, L. Suppression of coalescence and of wetting: The shape of the interstitial film. *Physics of Fluids* **9**, 2475-2485, doi:10.1063/1.869471 (1997).
- 23 Lo, H. Y., Liu, Y. & Xu, L. Mechanism of contact between a droplet and an atomically smooth substrate. *Physical Review X* **7**, 021036 (2017).
- 24 Pack, M. *et al.* Failure mechanisms of air entrainment in drop impact on lubricated surfaces. *Soft Matter* **13**, 2402-2409, doi:10.1039/C7SM00117G (2017).
- 25 Li, E. Q. & Thoroddsen, S. T. Time-resolved imaging of a compressible air disc under a drop impacting on a solid surface. *J. Fluid Mech.* **780**, 636-648, doi:10.1017/jfm.2015.466 (2015).
- 26 De Ruiter, J., Lagraauw, R., Van Den Ende, D. & Mugele, F. Wettability-independent bouncing on flat surfaces mediated by thin air films. *Nature physics* **11**, 48 (2015).
- 27 Shi, C. *et al.* Measuring forces and spatiotemporal evolution of thin water films between an air bubble and solid surfaces of different hydrophobicity. *ACS nano* **9**, 95-104 (2014).
- 28 Xing, Y. *et al.* Recent experimental advances for understanding bubble-particle attachment in flotation. *Advances in colloid and interface science* **246**, 105-132 (2017).
- 29 Chan, D. Y., Klaseboer, E. & Manica, R. Theory of non-equilibrium force measurements involving deformable drops and bubbles. *Advances in colloid and interface science* **165**, 70-90 (2011).
- 30 Pan, L., Jung, S. & Yoon, R.-H. Effect of hydrophobicity on the stability of the wetting films of water formed on gold surfaces. *Journal of colloid and interface science* **361**, 321-330 (2011).
- 31 Xie, L. *et al.* Interaction Mechanisms between Air Bubble and Molybdenite Surface: Impact of Solution Salinity and Polymer Adsorption. *Langmuir* **33**, 2353-2361, doi:10.1021/acs.langmuir.6b04611 (2017).
- 32 Aronson, M. P. & Princen, H. M. Aqueous films on silica in the presence of cationic surfactants. *Colloid. Polym. Sci.* **256**, 140-149, doi:10.1007/BF01679172 (1978).

- 33 Yoon, R. H. & Yordan, J. L. The Critical Rupture Thickness of Thin Water Films on Hydrophobic Surfaces. *J. Colloid Interface Sci.* **146**, 565-572 (1991).
- 34 Mahnke, J., Schulze, H. J., Stckelhuber, K. W. & Radoev, B. Rupture of thin wetting films on hydrophobic surfaces: Part I: methylated glass surfaces. *Colloids Surf., A* **157**, 1-9 (1999).
- 35 Mahnke, J., Schulze, H. J., Stckelhuber, K. W. & Radoev, B. Rupture of thin wetting films on hydrophobic surfaces. Part II: fatty acid Langmuir-Blodgett layers on glass surfaces. *Colloids and Surf., A* **157**, 11-20 (1999).
- 36 Couder, Y., Fort, E., Gautier, C. H. & Boudaoud, A. From Bouncing to Floating: Noncoalescence of Drops on a Fluid Bath. *Phys. Rev. Lett.* **94**, 177801, doi:10.1103/PhysRevLett.94.177801 (2005).
- 37 de Ruiter, J., Mugele, F. & van den Ende, D. Air cushioning in droplet impact. I. Dynamics of thin films studied by dual wavelength reflection interference microscopy. *Physics of fluids* **27**, 012104 (2015).
- 38 Kolinski, J. M., Mahadevan, L. & Rubinstein, S. M. Lift-Off Instability During the Impact of a Drop on a Solid Surface. *Phys. Rev. Lett.* **112**, 134501, doi:10.1103/PhysRevLett.112.134501 (2014).
- 39 Tran, T., de Maleprade, H., Sun, C. & Lohse, D. Air entrainment during impact of droplets on liquid surfaces. *Journal of Fluid Mechanics* **726**, R3 (2013).
- 40 van der Veen, R. C. A., Tran, T., Lohse, D. & Sun, C. Direct measurements of air layer profiles under impacting droplets using high-speed color interferometry. *Physical Review E* **85**, 026315, doi:10.1103/PhysRevE.85.026315 (2012).
- 41 Gao, Y. & Pan, L. Measurement of Instability of Thin Liquid Films by Synchronized Tri-Wavelength Reflection Interferometry Microscope. *Langmuir* **34**, 14215-14225 (2018).
- 42 Du, H. & Miller, J. D. A molecular dynamics simulation study of water structure and adsorption states at talc surfaces. *Int. J. Miner. Process.* **84**, 172-184, doi:<https://doi.org/10.1016/j.minpro.2006.09.008> (2007).
- 43 Castro, S., Lopez-Valdivieso, A. & Laskowski, J. S. Review of the flotation of molybdenite. Part I: Surface properties and floatability. *Int. J. Miner. Process.* **148**, 48-58, doi:<https://doi.org/10.1016/j.minpro.2016.01.003> (2016).
- 44 Israelachvili, J. *Intermolecular and Surface Force - 3rd ed.*, (Academic Press, 2011).
- 45 Cappella, B. & Dietler, G. Force-distance curves by atomic force microscopy. *Surf. Sci. Rep.* **34**, 1-104, doi:[https://doi.org/10.1016/S0167-5729\(99\)00003-5](https://doi.org/10.1016/S0167-5729(99)00003-5) (1999).
- 46 Butt, H. J. Measuring electrostatic, van der Waals, and hydration forces in electrolyte solutions with an atomic force microscope. *Biophys. J.* **60**, 1438-1444, doi:10.1016/S0006-3495(91)82180-4 (1991).
- 47 Attard, P. & Miklavcic, S. J. Effective Spring Constant of Bubbles and Droplets. *Langmuir* **17**, 8217-8223, doi:10.1021/la010969g (2001).
- 48 Halliday, D., Resnick, R. & Walker, J. *Fundamentals of Physics Extended, 10th Edition.* (Wiley, 2013).

- 49 Choi, D. *et al.* Spontaneous electrical charging of droplets by conventional pipetting. *Scientific Reports* **3**, 2037, doi:10.1038/srep02037 <https://www.nature.com/articles/srep02037#supplementary-information> (2013).
- 50 Marx, D., Tuckerman, M. E., Hutter, J. & Parrinello, M. The nature of the hydrated excess proton in water. *Nature* **397**, 601-604, doi:10.1038/17579 (1999).
- 51 Gouveia, R. F. & Galembeck, F. Electrostatic charging of hydrophilic particles due to water adsorption. *Journal of the American chemical society* **131**, 11381-11386 (2009).
- 52 Xu, K., Cao, P. & Heath, J. R. Graphene Visualizes the First Water Adlayers on Mica at Ambient Conditions. *Science* **329**, 1188-1191, doi:10.1126/science.1192907 (2010).
- 53 Arai, T., Sato, K., Iida, A. & Tomitori, M. Quasi-stabilized hydration layers on muscovite mica under a thin water film grown from humid air. *Scientific Reports* **7**, 4054, doi:10.1038/s41598-017-04376-3 (2017).
- 54 Furukawa, H. *et al.* Water adsorption in porous metal–organic frameworks and related materials. *Journal of the American Chemical Society* **136**, 4369-4381 (2014).
- 55 Wang, C.-y., Groenzin, H. & Shultz, M. J. Direct observation of competitive adsorption between methanol and water on TiO<sub>2</sub>: an in situ sum-frequency generation study. *Journal of the American Chemical Society* **126**, 8094-8095 (2004).
- 56 Macleod, H. A. *Thin-film optical filters, 3rd Ed.*, (Institute of Physics, 2001).
- 57 Pan, L., Jung, S. & Yoon, R. H. Effect of hydrophobicity on the stability of the wetting films of water formed on gold surfaces. *J. Colloid Interface Sci.* **361**, 321-330, doi:10.1016/j.jcis.2011.05.057 (2011).
- 58 Carnie, S. L., Chan, D. Y. C., Lewis, C., Manica, R. & Dagastine, R. R. Measurement of Dynamical Forces between Deformable Drops Using the Atomic Force Microscope. I. Theory. *Langmuir* **21**, 2912-2922, doi:10.1021/la0475371 (2005).



## 7 Interaction and Instability of Air Films Between Bituminous Coal Surfaces and Surfactant Droplets\*

\* The material contained in this chapter has been published in *Fuel*, reused with permission. Full citation: *Gao Y, Jung S, Pan L. Interaction and instability of air films between bituminous coal surfaces and surfactant droplets. Fuel. 2020 Aug 15;274:117839.*

### 7.1 Introduction

Particulates are ubiquitous in our daily life and in a variety of industrial applications. In the coal mining industry, large quantities of fine particles are produced in a wide range of processes, such as blasting and crushing of rock materials<sup>1</sup>. These fine particles quickly become airborne, leading to the creation of dust in the environment<sup>2,3</sup>. The dust remains suspended for days and creates a long-lasting health hazard to workers. An example is a respirable coal mine dust (RCMD), which is generated during underground coal mining. These RCMD particles have sizes of below 10  $\mu\text{m}$ . When inhaled by miners, the RCMD particles are deposited in the distal airways and gas-exchange regions of the lungs. Overexposure to RCMD causes coal workers' pneumoconiosis (CWP), a lung disease that can be fatal in its most severe form<sup>4-6</sup>.

Dust control during coal mining operations has been achieved through the utilization of ventilation systems, water sprayers, and flooded-bed scrubbers<sup>7</sup>. These control techniques reduce dust concentrations in the working environment and minimize dust explosion and health risks<sup>8</sup>. For instance, water spray produces small liquid droplets as a mist that collects suspended dust particles. In longwall and continuous mining operations, water is sprayed at cutting faces<sup>9</sup>, preventing fine particles from becoming airborne<sup>10</sup>. Flooded-bed scrubbers have been installed in continuous miners to capture airborne dust particles<sup>11-13</sup>. The dust-laden air is drawn into a metal mesh panel with water sprayed at the front. The mesh effectively captures and retains fine dust particles. The flooded-bed scrubber system achieves an overall capture efficiency of above 90%<sup>7</sup>.

Previous research efforts have primarily been devoted to understanding the mechanisms involved in the suppression of airborne dust particles using water sprays from a perspective of surface wettability<sup>14-16</sup>. Since coal is naturally hydrophobic and not easily wetted by water<sup>17</sup>, coal particles adhere to the surface of water droplets. For hydrophilic particles that are wettable by water, these particles penetrate the surfaces and collected inside the water droplets. Retaining dust particles inside the droplets creates free surfaces, which results in an improved dust capture efficiency<sup>18</sup>.

Conventionally, the efficiency of wetting agents on the capture of dust particles by water sprays has been studied by surface tension<sup>19</sup> and contact angle measurements<sup>18,20</sup>. It has been shown that the use of wetting agents leads to improved performance of dust suppression by water sprays<sup>8,21</sup>. Wetting agents reduces the surface tension of spray

liquids and increases the wettability of coal surfaces<sup>18,21-25</sup>. In particular, an increase in the wettability of coal benefits the capture of ultrafine particles<sup>26</sup>. It has been shown that the velocity required for dust particles to penetrate a liquid surface reduces dramatically with a decrease in contact angle and surface tension of liquids<sup>19</sup>. Alternatively, the efficiency of wetting agents has been characterized by dust sink experiments, also known as Walker's tests<sup>27</sup>. In using this method, a given amount of fine coal samples are placed on the surface of a surfactant solution, and the time it takes for particles to sink into the solution is recorded. The wetting rate is defined as the weight of dust particles that penetrate surfaces of the wetting liquids per second. It has been found that the wetting rate increases with increasing surfactant concentrations<sup>28,29</sup>. Results obtained from the sink experiments are comparable to those of dust capture tests<sup>8</sup>.

Despite the many studies into the effect of surfactants on dust suppression by water sprays, few of them have been devoted to understanding how dust particles are captured by liquid droplets. During the collision of a particle with a water droplet, an air film is formed<sup>30</sup>. The drainage of the air film builds up the hydrodynamic pressure, resisting the thinning of the air film<sup>31</sup>. If attractive surface forces are present across the air films, the thinning of the air film is accelerated<sup>32</sup>. However, the mechanisms involved during the thinning and rupture of the air films between aqueous droplets and bituminous coal surfaces have not been revealed.

In the present work, fundamental mechanisms involved in the capture of coal particles by water/surfactant sprays is examined by studying the thinning of air films between aqueous droplets and polished bituminous coal surfaces. Experiments are conducted by steadily approaching a hemispherical aqueous liquid droplet towards a polished bituminous coal surface while monitoring interference fringes of the air films using a newly developed Synchronized Tri-Wavelength Reflection Interferometry Microscope (STRIM). The STRIM enables an accurate determination of spatial and temporal evolutions of the air films over the range of 0-4  $\mu\text{m}$ . Measurements are conducted with liquid droplets of both non-ionic and anionic surfactant solutions. Results will be discussed in the context of film instability and kinetics of film thinning.

## **7.2 Materials and Experimental**

### **7.2.1 Materials**

Bituminous coal samples are obtained from a coal washing plant in the United States. They are clean products from a dense medium cyclone (DMC). The moisture and ash contents in the samples are 0.93% and 6.20%, respectively, determined using the ASTM D3174 method<sup>33</sup>. The coal samples are crushed into 1/2" x 1/2" small pieces using a hammer. The surfaces of the samples are polished using a series of polishing steps, including a coarse polish with 30-grit sandpapers, a fine polish with 600-grit sandpapers followed by 1500-grit sandpapers, and finally, an ultrafine polish using 0.5  $\mu\text{m}$  alumina powders. The polished coal exhibits mirror-like smooth surfaces. The surface roughness

of the polished coal surface is determined using atomic force microscopy (AFM). The measurement is conducted in a contact mode using the Asylum MFP-3D AFM. Fig. 1a) shows the AFM surface morphology image of a polished coal surface and Fig. 1b) shows the height profiles of the two selected lines, as shown in Fig. 1a). As shown, the RMS surface roughness values of two selected height profiles are 3.1 and 12.9 nm, respectively. The overall RMS surface roughness of the polished coal surface is 5.77-7.10 nm.

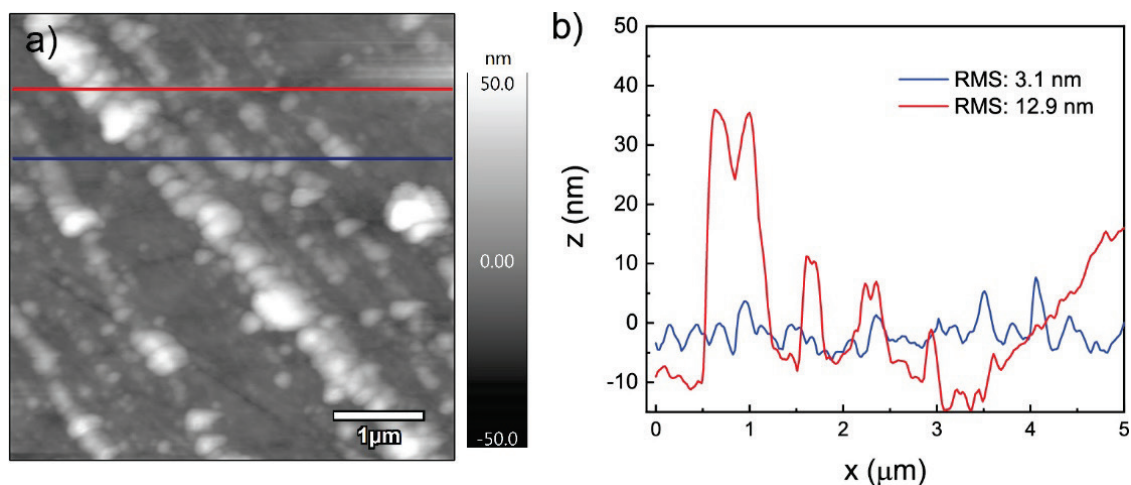


**Figure 7.1** a) Surface morphology of a polished bituminous coal surface determined by atomic force microscopy (AFM), b) height profiles on two color-coded lines.

Three types of surfactants are used in this study<sup>21</sup>. They are Triton™ X-100, sodium dodecyl sulfate (SDS), and sodium dioctyl sulfosuccinate (AOT). Triton X-100 is a non-ionic surfactant, while both SDS and AOT are anionic surfactants. All chemicals (99% purity or above) are obtained from Alfa Aesar or Sigma-Aldrich, and they are used as received without further purification. Deionized (DI) water is supplied from a Barnard water purification system (Thermo Fisher). The resistivity of the DI water is above 18.1 mΩ·cm.

## 7.2.2 Contact angle measurements

Contact angles of aqueous solutions on polished coal surfaces are determined using the sessile drop technique. A customized contact angle goniometer is used for this study. A small liquid droplet is carefully placed on a polished coal surface, and the contact angle is captured by a side-view camera. All experiments are repeated at least three times and averaged data is presented.

### 7.2.3 Instability of Air Film via STRIM

The objective of this work is to understand better the mechanism involved in the capture of dust particles by water droplets. Attachment between bituminous coal surfaces and water droplets is examined by monitoring spatial and temporal evolution of the air films between water droplets and polished coal surfaces. In this study, a water droplet approaches a polished coal surface steadily across an air film. During the approach, the spatial and temporal profile of the air film is determined by monitoring the interference fringes of the air films by STRIM. Different from the conventional monochromatic interferometry technique, STRIM uses three synchronized cameras to record fast-evolving interference fringes at three different wavelengths. This configuration enables an accurate determination of the fringe orders and, consequently, the film thicknesses over the range of 0 - 5  $\mu\text{m}$  with a resolution of 1-3 nm<sup>34</sup>. Details on the instrumental design can be found elsewhere<sup>35</sup>.

Fig. 2 shows a schematic drawing of the STRIM instrument. To form a hemispherical liquid drop on a transparent quartz surface, the plate is rendered hydrophobic by a methylation process<sup>32</sup>. The hydrophobized plate exhibits a water contact angle of 100°. A liquid droplet is placed on the hydrophobized quartz surface using a glass syringe with a stainless-steel needle. The quartz plate sits on a piezo stage, which moves the water droplet with a maximum traveling distance of 15  $\mu\text{m}$ . A multi-axis translational stage is used to control the position of the coal surface. An infinity-corrected 20 $\times$  long-working distance objective (Mitutoyo) is used to observe optical fringes. The magnification of the objective is calibrated using a standard microscope calibration slide (Thorlabs). Three synchronized cameras record images simultaneously at a rate of 150-250 frames per second. In another set of experiments, a high-speed camera is used to replace one camera to record fast-evolving interference fringes. Under the current setting, this high-speed camera is capable of recording 1000 frames of interference fringes per second. A side-view camera is installed and used to monitor the spreading of the water droplets on the flat coal surface when the air film is ruptured. Both the contact angles and the radii of the three-phase contact line are determined from the side-view images.

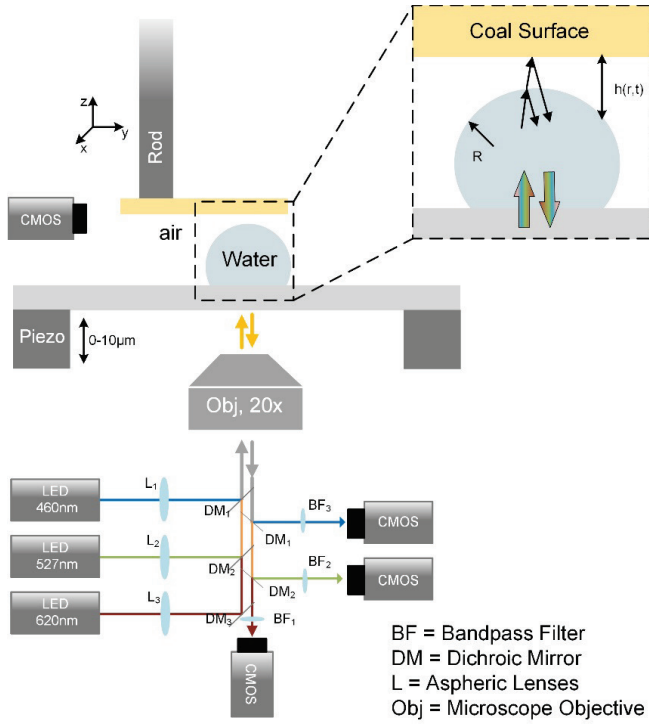


**Figure 7.2** A schematics of the synchronized tri-wavelength reflection interferometry microscope (STRIM) used for studying interactions between water droplets and coal surfaces.

The interference fringes are processed to determine spatiotemporal thickness profiles of the air films using Eq. (1),

$$\frac{2I - (I_{\max} + I_{\min})}{I_{\max} - I_{\min}} = \cos\left(\frac{4\pi nh}{\lambda} + \delta\right) \quad (1)$$

where  $I_{\max}$  and  $I_{\min}$  are the maximum and minimum intensity values in each pattern when phase differences  $(4\pi nh/\lambda + \delta)$  are even and odd multiples of  $\pi$ , respectively. In Eq. (1), the optical path length  $(2nh)$  is a product of twice the thickness  $(h)$  of the thin air film and the reflective index  $(n)$  of the medium in which the light propagates;  $\lambda$  is the light wavelength;  $\delta$  is the phase shift of the light reflected from the interfaces. The  $\delta$  value is determined from the reflective indexes  $(n, k)$  of the interference layers using a matrix of a multilayer system<sup>36</sup>. The values of  $\delta$  are  $0.044\pi$ ,  $0.028\pi$  and  $0.019\pi$  at  $\lambda = 460$ ,  $526$ , and  $620$  nm, respectively<sup>37</sup>. The order of fringes is determined using a trial-and-error method, in which the film thickness at a fixed radial position  $(r)$  is iteratively determined using arbitrarily chosen fringe orders until the experimental data obtained at three different wavelengths overlap with each other.

Spatiotemporal thickness profiles of the air films are obtained using the method described previously<sup>38,39</sup>. In using this method, the temporal change in film thickness ( $h$  vs.  $t$ ) at a given radial position is determined by analyzing the pixel intensity value as a function of the elapsed time ( $I$  vs.  $t$ ) using Eq. (1). By determining  $h$  vs.  $t$  profiles along with radial positions ( $r$ ) from the symmetry axis of the interference fringe, the spatiotemporal thickness profile,  $h(r,t)$ , can be reconstructed<sup>39</sup>. The image processing is carried out using a custom-written Matlab program. In this study, the film thickness is determined at a maximum radial position of 25  $\mu\text{m}$ , where the inclination angle is below  $1.5^\circ$ . Therefore, the correction due to the curvature of water droplets can be neglected.

#### 7.2.4 Force Calculation

The interaction force between a water droplet and a flat surface across an air film is determined from the pressure distribution in the thin gap formed between the two surfaces. The pressure distribution within the gap is governed by the Reynolds lubrication equation<sup>40,41</sup>,

$$\frac{\partial p}{\partial r} = \frac{6\mu}{h^3} \frac{dh}{dt} r \quad (2)$$

where  $\mu$  is the viscosity of the air,  $h$  is separation distance,  $r$  is the radial position, and  $t$  is time. The water droplet remains spherical during the attachment, and therefore the separation distance can be represented as,

$$h(r,t) \approx h_0 + \frac{r^2}{2a} = h_0(1 + s^2) \quad (3)$$

where  $h_0$  is the closest separation distance,  $a$  is the radius of curvature, and  $s = r/(2ah_0)^{1/2}$ . The  $a$  value changes with  $t$  due to the presence of both hydrodynamic and electrostatic forces. By substituting Eq. (3) into Eq. (2) and integrating it under the boundary condition  $p = p_\infty$  at  $r = a$ , the pressure distribution can be determined as,

$$p(s,t) - p_\infty = -\frac{3\mu a}{h_0^2} \left( \frac{dh_0}{dt} - \frac{dh_e}{dt} \right) \frac{1}{(1 + s^2)^2} \quad (4)$$

where  $dh_e/dt$  is the approaching velocity at the outer region ( $r = a$ ), which is equivalent to external approaching velocity ( $V_e$ ). By integrating the pressure distribution over the total film area<sup>32</sup>, one obtains,

$$F = \int_0^{s=\sqrt{a/2h_0}} (p - p_\infty) 2\pi(2ah_0) s ds = -\frac{6\pi\mu a^2}{h_0} \left( \frac{dh_0}{dt} - \frac{dh_e}{dt} \right) \quad (5)$$

where both  $h_0$  and  $dh_0/dt$  can be determined from the spatiotemporal profiles experimentally. The  $a(t)$  value can be determined using Eq. (3). The force data are presented as a function of  $h_0$ . In this study,  $\mu = 1.825 \times 10^{-5} \text{ kg/m}\cdot\text{s}$  and  $dh_0/dt = 1.2 \text{ }\mu\text{m/s}$ .

## 7.3 Results

### 7.3.1 Instability of Air Films

Fig. 3a) shows a bottom view of the attachment process between a DI water droplet and a polished coal surface across an air film. The bottom view is shown as a series of interference fringes. The measurement was conducted by bringing a water droplet towards a polished coal surface at a velocity of approximately  $1.2 \text{ }\mu\text{m/s}$ . The initial  $h_0$  was approximately  $5\text{--}8 \text{ }\mu\text{m}$ , at which the interference fringes became visible. Interference fringe images were taken by three synchronized cameras at central wavelengths of  $460 \text{ nm}$ ,  $527 \text{ nm}$ , and  $620 \text{ nm}$ , respectively. Fig. 3b) shows spatiotemporal thickness profiles of air films. The data points in blue, green, and red represent the spatiotemporal profiles obtained at  $\lambda = 460 \text{ nm}$ ,  $527 \text{ nm}$ , and  $620 \text{ nm}$ , respectively. As shown, the profiles obtained at three distinct wavelengths overlap with each other, validating the methodology used in determining spatiotemporal thickness profiles of air films.

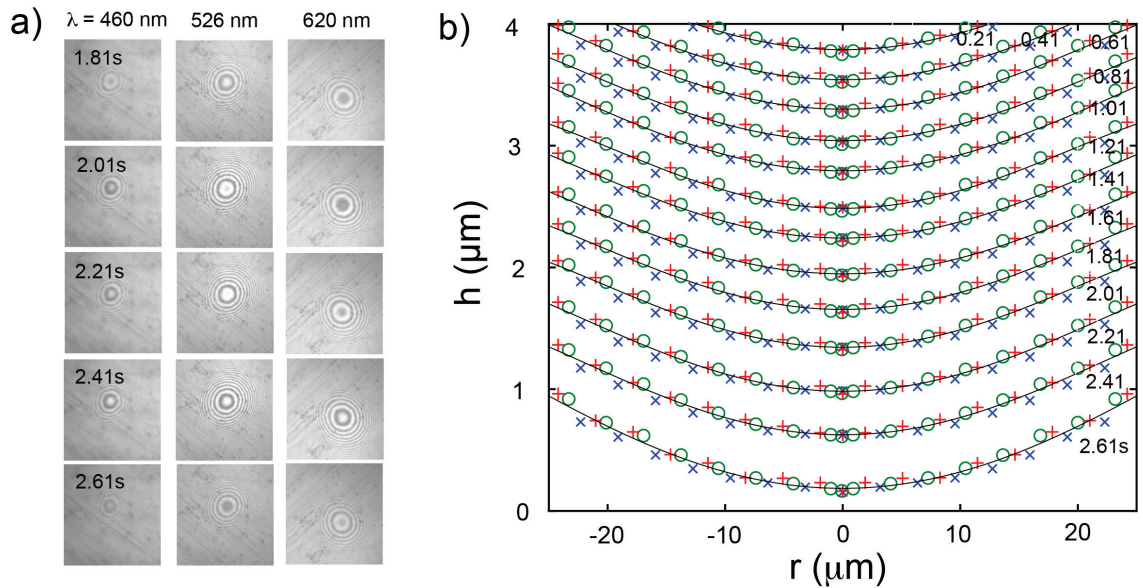


**Figure 7.3** a) Temporal changes in interference fringes of an air film between a DI water droplet and a polished bituminous coal surface at  $\lambda = 460 \text{ nm}$ ,  $526 \text{ nm}$ , and  $620 \text{ nm}$ ; b) spatiotemporal thickness profiles of the air films.

The spatiotemporal profiles (Fig. 3) show that the water droplet maintains its hemispherical shape during the approach. As shown, the fitted curves using Eq. (2) match well with the experimental data. The initial radius of the water droplet ( $R$ ) without the external influences is 0.441 mm.

One of the key characteristics of the spatiotemporal profiles is the thinning kinetics of air films. At the initial approach stage, *i.e.*, when  $h_0$  is above 1  $\mu\text{m}$ , the thinning of air films is dominantly governed by the external drive. This is manifested by equally sized gaps between two neighboring spatial profiles at an interval of 0.2 s. As the water droplet gets closer to the coal surface at a distance of below 1  $\mu\text{m}$ , the thinning of the air films is accelerated. For instance, at  $t = 2.41$  s and beyond, the gap between two spatial profiles at an interval of 0.2 seconds is increased from 240 nm to 420 nm. The acceleration in the thinning of air films is ascribed to the presence of an attractive force. The lowest spatial profile represents the last profile of the air film before the film ruptures. At this moment, the closest separation distance is defined as the critical rupture thickness ( $h_c$ ). The  $h_c$  of the air film was determined to be 104 nm for water droplets approaching bituminous coal surfaces.

The rapid spreading of liquids on coal surfaces initializes upon the rupture of the air films<sup>42,43</sup>. Fig. 4 shows both the bottom view and side view of a water droplet spreading on a coal surface. As shown, a three-phase contact line spread radially at a velocity of approximately 583  $\mu\text{m/s}$ . An equilibrium three-phase contact line was established within 3 milliseconds, and a contact angle of  $105^\circ$  was formed. This value is significantly larger than that ( $\approx 69^\circ$ ) determined using the sessile drop technique. This discrepancy is attributed to a fixture of the water droplet at the bottom of the hydrophobic quartz plate, resulting in a different boundary condition compared to a free liquid droplet on one solid surface.

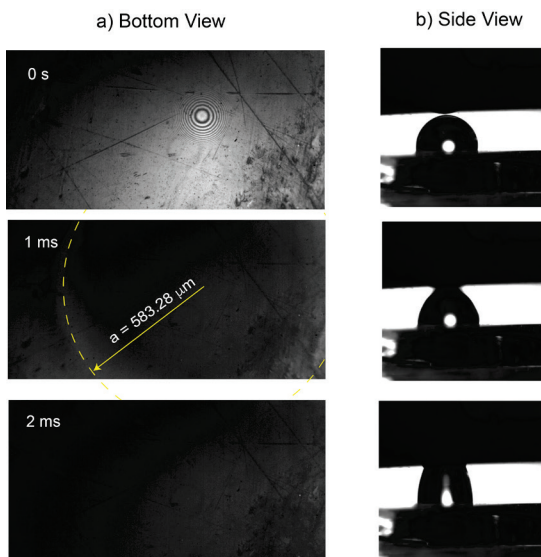


**Figure 7.4** a) Bottom-view and side-view images of a water droplet spreading on a bituminous coal surface.



### 7.3.2 Effect of the non-ionic surfactant

Triton X-100 is a non-ionic surfactant, which is commonly used as a dust suppressant chemical<sup>44,45</sup>. Table 1 shows both the surface tensions of Triton X-100 aqueous solutions<sup>46</sup> and the equilibrium contact angles ( $\theta$ ) on bituminous coal surfaces. The  $\theta$  was determined using the sessile drop technique, as described in the experimental section. Without any surfactants, the water contact angle is 69° on bituminous coal surfaces, which agrees well with literature data<sup>18,47</sup>. At 0.05 mM, 0.1 mM and 0.2 mM Triton X-100, the  $\theta$  is decreased to 54°, 42°, and 20°, respectively. The decrease in contact angles with increasing surfactant concentrations is due to a decrease in surface tensions of aqueous solutions<sup>23</sup>.

**Table 7.1** Effect of Triton X-100 concentration on surface tensions of the liquid droplet and the contact angles of polished bituminous coal surfaces.

Concentration (mM)	$\gamma^*$ (mN/m)	$\theta$ (°)
0	72.2	69
0.001	69.9	68
0.01	53.8	60
0.05	44.2	54
0.1	37.8	42
0.2	35.4	20

\*Source: Gobel et al.<sup>48</sup>, Chander et al.<sup>18</sup>

The effect of Triton X-100 concentration on the attachment process is investigated using STRIM. Fig. 5 shows the spatiotemporal thickness profiles of the air films between liquid droplets and bituminous coal surfaces at a) 0.001 mM, b) 0.01 mM, and c) 0.1 mM Triton X-100, respectively. For comparison, we define the  $t = 0$  s is when  $h_0$  is 4  $\mu\text{m}$ . As shown, the kinetics of thinning of the air films accelerates with increasing concentrations of Triton X-100. This is manifested by widening gaps between two spatial profiles at an interval of 0.1 s with increasing surfactant concentrations. Note that in this set of experiments, at least 10 independent experiments were conducted. The results shown in Figure 5 are reproducible.

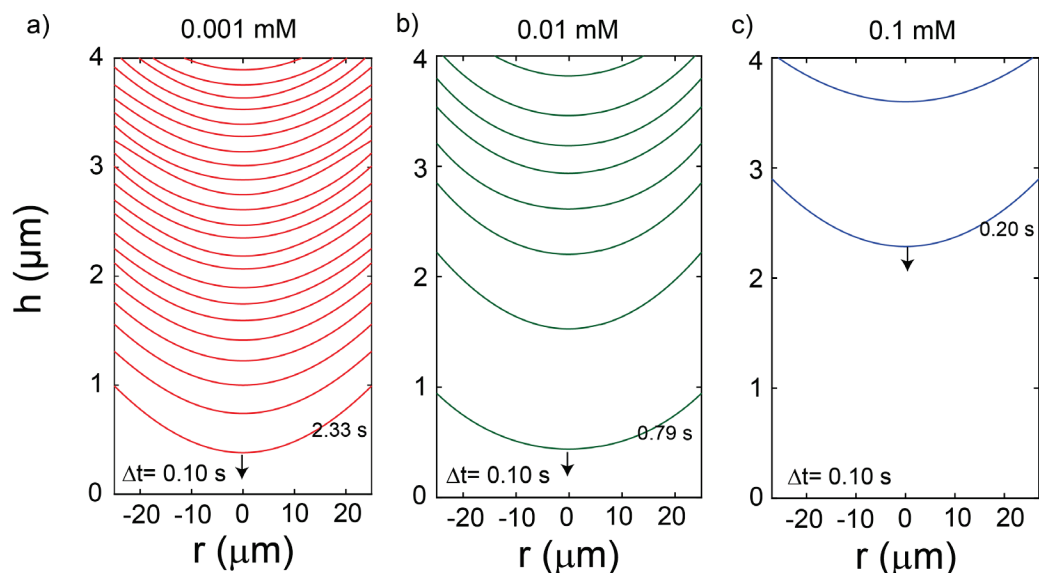


**Figure 7.5** Spatiotemporal thickness profiles,  $h(r,t)$ , of air films between aqueous Triton X-100 droplets and polished bituminous coal surfaces at a) 0.001 mM, b) 0.01 mM, and c) 0.1 mM Triton X-100.

Fig. 6 shows the kinetics of the thinning of the air films at different concentrations of Triton X-100. The result is shown as  $h_0$  vs.  $t$ . As shown, the approach velocity remains constant at  $1.2 \mu\text{m/s}$  when the closest separation distance ( $h_0$ ) is above  $1 \mu\text{m}$ . When  $h_0$  is decreased to below  $1 \mu\text{m}$ , the kinetics of thinning is accelerated. It has also been shown that the kinetics of thinning increases with increasing Triton X-100 concentrations. At  $0.1 \text{ mM}$  Triton X-100, the thinning velocity exceeds  $8.8 \mu\text{m/s}$ , which is 6 times larger than those obtained with DI water.

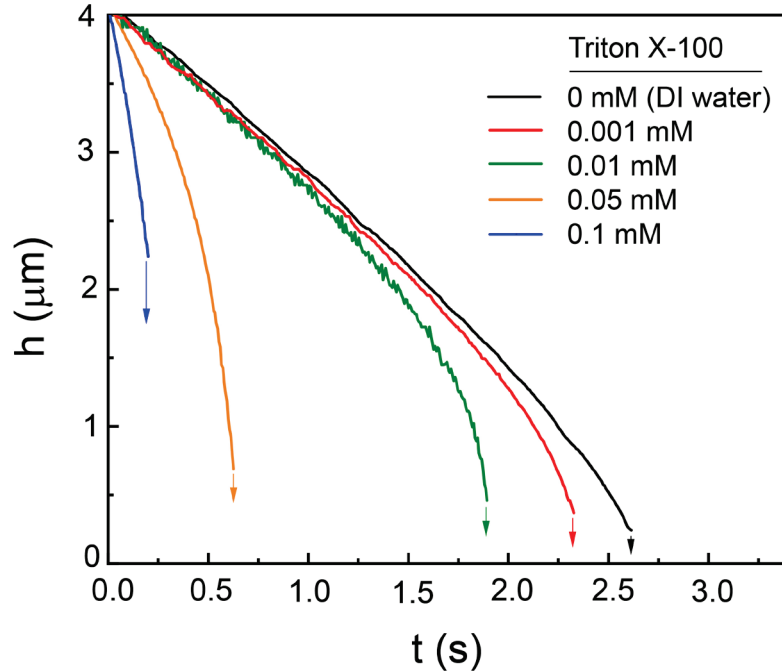


**Figure 7.6** Effect of Triton X-100 concentration on the kinetics of thinning of air films between aqueous Triton -100 droplets and polished bituminous coal surfaces.

Another characteristic of the attachment process is critical rupture thickness ( $h_c$ ) which signifies air film instability. It has been shown that the  $h_c$  is 369 nm at 0.001 mM Triton X-100, which is larger than that obtained with DI water ( $h_c = 104$  nm). At 0.01 mM and 0.1 mM Triton X-100, the air film becomes less stable, with  $h_c$  of 460 nm and 2239 nm, respectively.

Table 2 summarizes three characteristics of the attachment process, including critical rupture thickness ( $h_c$ ), critical rupture velocity ( $\Delta V_c$ ), and critical rupture time ( $t_c$ ). The  $\Delta V_c$  is defined as the difference between the thinning velocity right before the film rupture and the external driving velocity ( $V_e$ ), as  $\Delta V_c = V_c - V_e$  and  $V_e = 1.2 \mu\text{m/s}$ . A positive value signifies an accelerated thinning, while a negative value signifies a deaccelerated thinning. As shown in Table 2, the  $\Delta V_c$  increases from 0.27  $\mu\text{m/s}$  with DI water to 11.68  $\mu\text{m/s}$  with 0.2 mM Triton X-100 solution. The  $t_c$  is defined as the time spent from an initial closest separation distance of 4  $\mu\text{m}$  to a critical rupture thickness. As shown, the  $t_c$  is shortened from 2.33 s at 0.001 mM Triton X-100 solution to 0.20 s at 0.1 mM and 0.13 s at 0.2 mM Triton X-100.

**Table 7.2** Characteristics of the instability of air films between aqueous droplets and bituminous coal surfaces at different concentrations of Triton X-100.

Concentration (mM)	$\Delta V_c$ ( $\mu\text{m/s}$ )	$h_c$ (nm)	$t_c$ (s)
0	0.27	104	2.61
0.001	0.36	369	2.33
0.01	0.67	460	1.89
0.05	4.05	690	0.63
0.1	7.61	2239	0.20
0.2	11.68	2326	0.13

Fig. 7 shows interaction forces between liquid droplets and polished bituminous coal surfaces across air films at different concentrations of Triton X-100. Note that a negative value signifies the presence of an attractive force. As shown, the interaction force becomes more attractive and longer-ranged, with increasing concentrations of Triton X-100. For instance, the effective range of the attractive force with DI water is 300-400 nm, whereas the effective range with 0.1 mM Triton X-100 is increased to above 3  $\mu\text{m}$ .

To better understand the origin of the interaction force across the air film, the force data is fitted with an  $F = c/h$  equation, where  $c$  is a constant and  $h$  is the separation distance. The solid lines in Fig. 7 shows the best fitting result. As shown, the use of the  $c/h$  function fits the data very well. Since the measured forces follow coulomb's law, the force is believed to be the electrostatic force. Due to the attractive nature of the measured force, the surfaces of the water droplets and the bituminous coals carry opposite charges. Table 3 lists  $c$  as well as  $R$  values obtained at different Triton X-100 concentrations. The results show that  $c$  value becomes more negative with increasing Triton X-100 concentration, suggesting the attractive force increases with increasing surfactant concentrations.

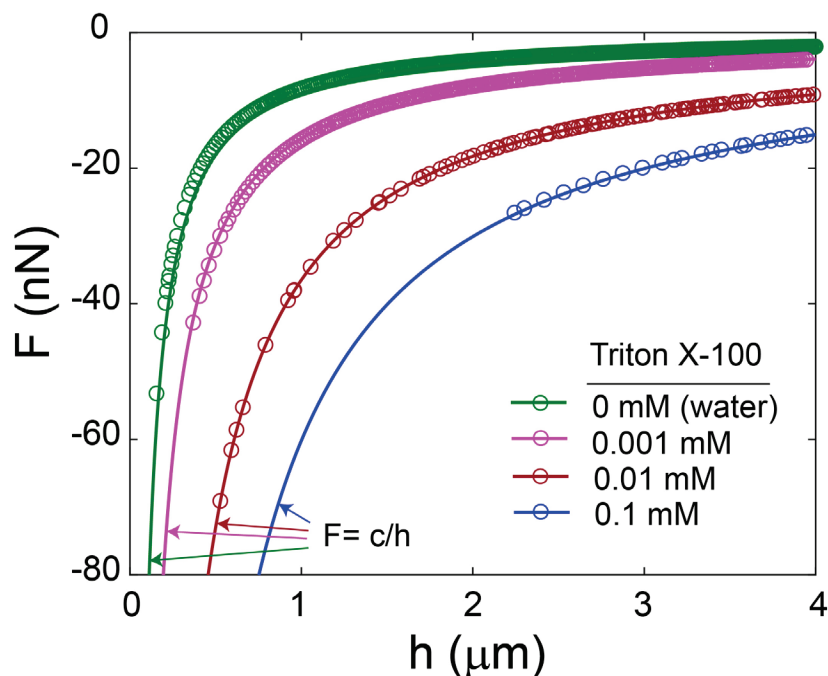


**Figure 7.7** Interaction forces between aqueous Triton X-100 droplets and bituminous coal surfaces across air films at different concentrations of Triton X-100. Solid lines show the fitted force curves with an  $F = c/h$  function.

**Table 7.3** A list of  $R$ ,  $c$ , and  $dF_{\max}/dh$  values at different concentrations of Triton X-100.

Concentration (mM)	$R$ (mm)	$c$ (nN·m)	$dF_{\max}/dh$ (mN/m)
0	0.468	$-0.9 \times 10^{-5}$	257.2
0.001	0.596	$-1.56 \times 10^{-5}$	100.1
0.01	0.554	$-3.65 \times 10^{-5}$	111.2
0.1	0.892	$-6.02 \times 10^{-4}$	11.0

### 7.3.3 Effect of anionic surfactants

We hypothesize that both the kinetics of film thinning and the instability of air films are independent of the types of surfactants. To validate this hypothesis, film instability measurements were conducted with two anionic surfactants, namely AOT and SDS. Table 4 shows both the surface tensions ( $\gamma$ ) and the contact angles ( $\theta$ ) of aqueous solutions on bituminous coal surfaces at different AOT and SDS concentrations. Both surfactants lower the surface tensions of the aqueous solutions, but the AOT solution

exhibits a much lower surface tension than the SDS solution at the same surfactant concentration. As expected, the contact angle of aqueous solutions on bituminous coal surfaces decreases with decreasing the surface tensions of wetting liquids.

Fig. 8 shows the kinetics of thinning of the air films obtained at different concentrations of a) AOT and b) SDS. It has been shown that for both AOT and SDS, the kinetics of thinning of the air films increases with increasing surfactant concentrations.

Correspondingly,  $t_c$  decreases with increasing surfactant concentrations. For instance,  $t_c$  is 2.61 s with DI water; however,  $t_c$  is reduced significantly to 0.25 s at 5 mM AOT.

Likewise,  $t_c$  is decreased from 1.03 s at 2.5 mM SDS to 0.08 s at 10 mM SDS.

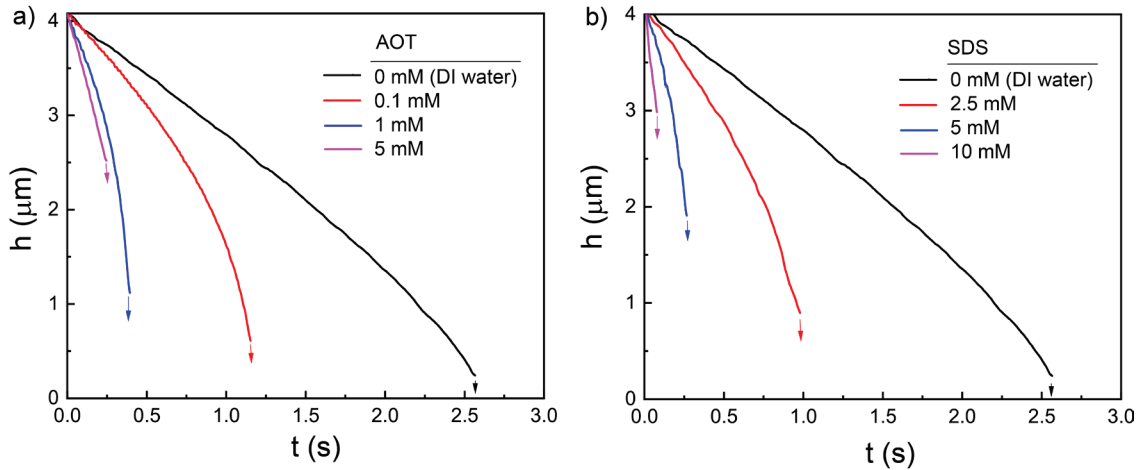


**Figure 7.8** Effects of AOT (a) and SDS (b) on the air film kinetics of approaching.

Also shown in Table 4 is a list of characteristics of the attachment process, including  $h_c$ ,  $\Delta V_c$ , and  $t_c$ . All three characteristics signify accelerated kinetics of thinning and an increase in film instability with increasing surfactant concentrations. For instance,  $h_c$  increases from 600 nm at 0.1 mM AOT to 2460 nm at 5 mM AOT, and it increases from 750 nm at 2.5 mM SDS to 2250 nm at 5 mM SDS. Besides,  $\Delta V_c$  increases from 1.76  $\mu\text{m/s}$  at 0.1 mM AOT to 5.47  $\mu\text{m/s}$  at 1 mM AOT. Likewise, the  $\Delta V_c$  increases from 1.96  $\mu\text{m/s}$  at 0.1 mM of SDS to 11.30  $\mu\text{m/s}$  at 10 mM SDS.

One noticeable difference between AOT and SDS is the effectiveness of destabilizing air films. For instance, at 0.1 mM AOT,  $h_c$  is increased 600 nm, while  $t_c$  is decreased to 1.15 s. Similar performance is achieved at 2.5 mM SDS, with  $h_c = 750$  nm and  $t_c = 1.03$  s. Evidently, all three surfactants surveyed in this study show positive impacts on the kinetics of attachment.

**Table 7.4** Characteristics of attachments between bituminous coal surfaces and aqueous droplets of AOT and SDS.

Surfactant	Conc. (mM)	Wetting		Attachment		
		$\gamma$ (mN/m)	$\theta$ ( $^\circ$ )	$h_c$ (nm)	$\Delta V_c$ ( $\mu\text{m/s}$ )	$t_c$ (s)
AOT	0	72.2	69	104	0.27	2.61
	0.1	56.9	56.9	600	1.76	1.15
	1	36	43.8	1265	5.47	0.41
	5	32	20	2460	5.90	0.25
SDS	0	72.2	69	104	0.27	2.61
	2.5	62	58.9	750	1.96	1.03
	5	50	31.5	2250	5.28	0.27
	10	44	18	>3000	11.30	0.08

Sources: Mysels et al.<sup>49</sup>, Dharmawardana et al.<sup>50</sup>, Yuan et al.<sup>51</sup>

## 7.4 Discussion

The capture of dust particles by water/surfactant droplets involves three sub-processes including 1) collision<sup>19,52</sup>, 2) attachment<sup>53</sup>, and 3) engulfment<sup>9,54</sup>. Conventional wisdom on the role of surfactants is that the adsorption of surfactant molecules effectively lowers the surface tension ( $\gamma$ ) of wetting liquids and increases the wettability of coal surfaces, and therefore enhances the engulfment process<sup>55</sup>. It has been previously shown a complete wetting occurs when  $\gamma$  of the wetting liquid is close to the critical surface tension of solids ( $\gamma_c$ ). The  $\gamma_c$  of the bituminous coal is reported to be  $30 \text{ mN}\cdot\text{m}^{-1}$ <sup>28,56</sup>, and it increases with decreasing the ranks of coals<sup>57</sup>. We have shown that the contact angles are reduced to below  $20^\circ$  at 5 mM AOT, at which  $\gamma$  is equal to 32 mN/m. A similar result is observed with Triton X-100. For SDS, the  $\gamma$  of the wetting liquids at which the contact angle is below  $20^\circ$  is 44 mN/m. At this condition, the interfacial force between coal surfaces and wetting liquids might contribute to a complete wetting of the coal surfaces by SDS solutions<sup>58</sup>. Clearly, the present result agrees well with the literature data.

As concluded in the result section, the use of wetting agents impacts not only the engulfment of dust particles in liquid droplets but also the attachment process. One of the

key metrics of the attachment process is air film instability, which has been signified by  $h_c$ . It has been shown that the  $h_c$  increases with increasing surfactant concentrations. Fig. 9 shows a)  $h_c$  vs.  $\gamma$  and b)  $h_c$  vs.  $\theta$ . The result shows that  $h_c$  increases with decreasing the  $\gamma$  of aqueous solutions as well as the  $\theta$  of aqueous solutions on coal surfaces. The relations can be fitted by a linear model, with coefficients of determination ( $R^2$ ) of 0.5461 and 0.9141, respectively. The present result suggests that  $h_c$  is more relevant to the contact angles than the surface tension of aqueous liquids.

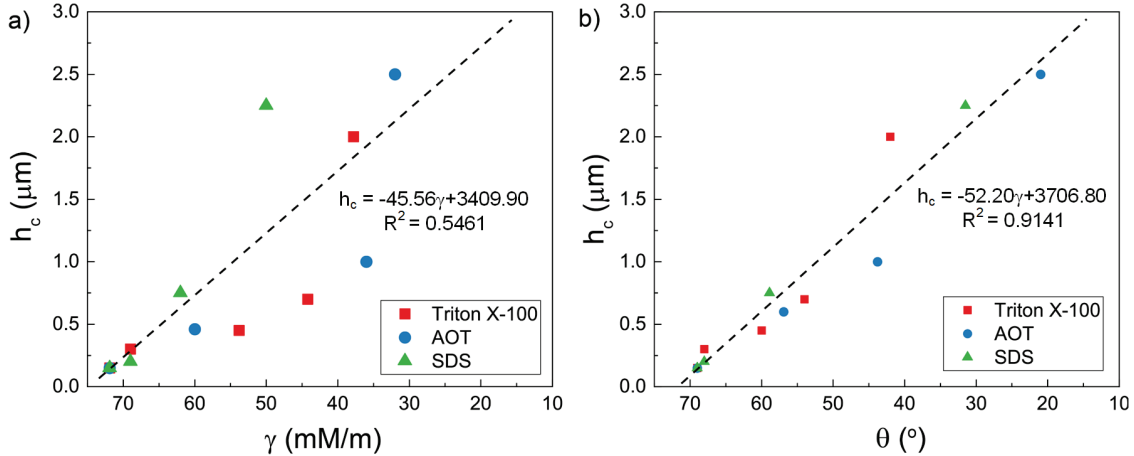


**Figure 7.9** a) critical rupture thickness as a function of surface tension of wetting liquids, b) critical rupture thickness of air films as a function of contact angles of wetting liquids on coal surfaces.

The film rupture might occur when the gradient of interaction force exceeds the spring constant of a free liquid surface<sup>59</sup>. For liquid droplets, the spring constant is proportional to the surface tension of the liquid<sup>60</sup>. Table 3 also lists the maximum gradient of the interaction force at different surfactant concentrations ( $dF_{\text{max}}/dh$ ). The value is decreased from 257  $\text{mN/m}$  with DI water to 11.0  $\text{mN/m}$  with 0.1  $\text{mM}$  Triton X-100. The decrease in the critical gradient of the interaction force is anticipated because the spring constant of the free liquid surface decreases with decreasing the liquid's surface tension. The stronger the attraction force, the larger the critical rupture thickness.

Figure 10 shows a schematic representation of a possible mechanism for the attractive electric force observed between aqueous droplets and bituminous coal surfaces. We hypothesize that the liquid droplet might carry positive charges, while the coal surface might carry negative charges.



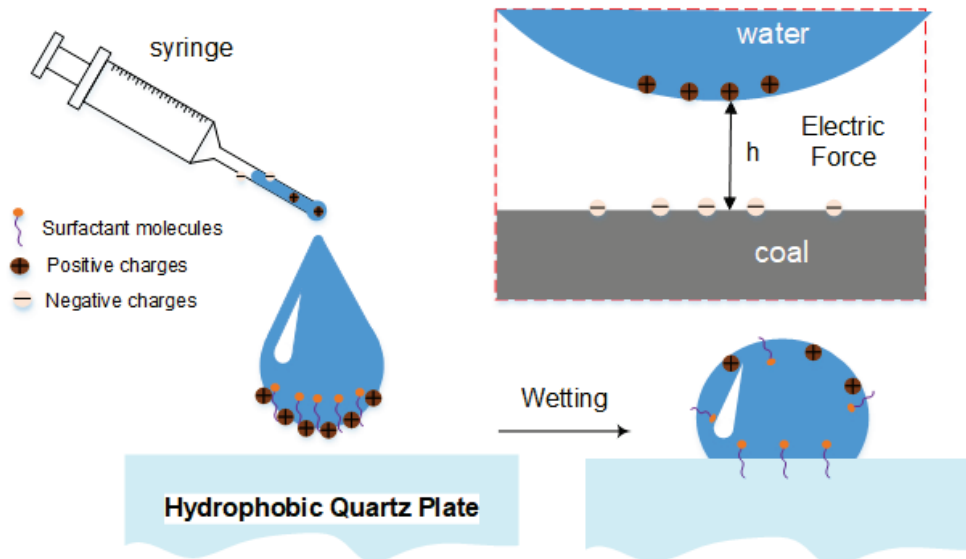


**Figure 7.10** A schematic representation of the mechanism for the attractive electric force between water droplets and coal surfaces.

The positive charges carried by liquid droplets on quartz surfaces are attributed to a charge separation process. Electric double layers are formed when the liquid flows through a metal needle. That the inner walls of the stainless-steel needle are negatively charged at a natural pH. When the liquid droplet is released from the tip of the needle, the droplet carries positive charges on its surface<sup>61</sup>. In the presence of wetting agents in water, surfactant molecules might adsorb at the liquid surface and cause a change in surface charges. For non-ionic surfactants, surface charges remain constant<sup>62</sup>. For anionic surfactants, surfactant adsorption may decrease positive electric charges carried by liquid droplets.

The negative charges carried on coal surfaces might be associated with the adsorption of water molecules on solid surfaces<sup>63,64</sup>. Bituminous coal is hydrophobic with a water contact angle of 69°. Under the reasonable laboratory condition with humidity of 35-50%, water molecules might have been adsorbed on coal surfaces forming patches of water islands, resulting in negative charges carried on the surface. The amount of negative charges increases with increasing the concentrations of water molecules on solid surfaces<sup>32,65</sup>. This conclusion seems to be consistent with the early finding reported by McCoy et al. that charged water droplets increase dust removal<sup>66</sup>. However, the mechanism associated with the increase in positive charges with increasing surfactant concentration is still not precise, requiring more investigations, including spectroscopy studies.

Given the results obtained from this work, it is clear that the use of surfactants not only impacts the engulfment of dust particles but also the attachment between water droplets and coal surfaces. The use of surfactant sprays not only accelerates the kinetics of thinning of air films but also shortens the time spent for the attachment to occur due to the presence of an attractive electrostatic force. The present work sheds new light into the microscopic mechanism involved in the dust capture by water and surfactant sprays. In

addition, the present work provides a fundamental basis for the future development of a new water spray system for dust control and new wetting agents for dust control.

## 7.5 Conclusion

Microscopic processes involved in the capture of coal dust particles by liquid droplets have been revealed by investigating the microscopic attachment process between aqueous droplets and polished coal surfaces. The Synchronized Tri-wavelength Reflection Interferometry Microscope (STRIM) was developed and used to determine spatiotemporal thickness profiles of the air films during the attachment process. The profiles were used to determine thinning kinetics as well as critical rupture thicknesses of the air films. From the thinning kinetics data, interaction forces have been identified by solving pressure distribution across air films using the numerical method.

We have shown that the thinning kinetics of air films increases with increasing surfactant concentrations. The accelerated film thinning is attributed to the presence of an attractive electrostatic force between the two oppositely charged surfaces. It has been found that this phenomenon is applicable to not only non-ionic surfactants but also anionic surfactants. In addition, the critical rupture thicknesses increase with increasing surfactant concentrations. The critical rupture thickness ( $h_c$ ) of the air films between water droplets and bituminous coal surfaces is 104 nm. The  $h_c$  value was increased to over 1000 nm at 0.1 mM Triton X-100 as well as at 1 mM AOT solutions. A linear relationship between  $h_c$  and  $\theta$  has been found. This result suggests that the critical rupture thickness is more relevant to the wettability of coal surfaces than the surface tension of wetting solutions. In this regard, surfactants with a strong capability to increase the wettability of coal surfaces might be a better wetting agent candidate.

## 7.6 Reference

- 1 Petavratzi, E., Kingman, S. & Lowndes, I. Particulates from mining operations: A review of sources, effects and regulations. *Minerals Engineering* **18**, 1183-1199 (2005).
- 2 Colinet, J., Listak, J. M., Organiscak, J. A., Rider, J. P. & Wolfe, A. L. *Best practices for dust control in coal mining*. (2010).
- 3 Wang, Q., Wang, D., Wang, H., Shen, Y. & Zhu, X. Experimental Investigations of a New Surfactant Adding Device Used for Mine Dust Control. *Powder Technology* **327**, 303-309 (2018).
- 4 Zhou, Q., Qin, B., Wang, J., Wang, H. & Wang, F. Effects of preparation parameters on the wetting features of surfactant-magnetized water for dust control in Luwa mine, China. *Powder Technology* **326**, 7-15 (2018).
- 5 Zhang, G., Zhang, L., Fan, H. & Hu, E. Concentration, enrichment, and partitioning behavior of heavy metals in ash from a down-fired furnace burning anthracite coal. *Energy & Fuels* **31**, 9381-9392 (2017).
- 6 Beck, T., Seaman, C., Shahan, M. & Mischler, S. Open-air sprays for capturing and controlling airborne float coal dust on longwall faces. *Mining engineering* **70**, 42 (2018).
- 7 Colinet, J. & Jankowski, R. Dust control considerations for deep-cut faces when using exhaust ventilation and a flooded-bed scrubber. *TRANSACTIONS-SOCIETY FOR MINING METALLURGY AND EXPLORATION INCORPORATED* **302**, 104-111 (1997).
- 8 Organiscak, J. Examination of water spray airborne coal dust capture with three wetting agents. *Transactions of Society for Mining, Metallurgy, and Exploration, Inc* **334**, 427 (2013).
- 9 Cheng, L. Collection of airborne dust by water sprays. *Industrial & Engineering Chemistry Process Design and Development* **12**, 221-225 (1973).
- 10 Srinivasa Rao, B. Design and development of a multi-scrubber dust control system for longwall faces: Experimental and modelling studies. (1993).
- 11 Arya, S. *et al.* Design and experimental evaluation of a flooded-bed dust scrubber integrated into a longwall shearer. *Powder technology* **339**, 487-496 (2018).
- 12 Xia, T. *et al.* Controlling factors of symbiotic disaster between coal gas and spontaneous combustion in longwall mining gobs. *Fuel* **182**, 886-896 (2016).
- 13 Colinet, J. Laboratory evaluation of quartz dust capture of irrigated-filter collection systems for continuous miners. (1990).
- 14 Li, Q., Lin, B., Zhao, S. & Dai, H. Surface physical properties and its effects on the wetting behaviors of respirable coal mine dust. *Powder Technology* **233**, 137-145 (2013).
- 15 Kilau, H. The wettability of coal and its relevance to the control of dust during coal mining. *Journal of adhesion science and technology* **7**, 649-667 (1993).
- 16 Fan, T., Zhou, G. & Wang, J. Preparation and characterization of a wetting-agglomeration-based hybrid coal dust suppressant. *Process Safety and Environmental Protection* **113**, 282-291 (2018).

- 17 Ofori, P., Firth, B., O'Brien, G., McNally, C. & Nguyen, A. V. Assessing the hydrophobicity of petrographically heterogeneous coal surfaces. *Energy & Fuels* **24**, 5965-5971 (2010).
- 18 Chander, S., Mohal, B. & Aplan, F. Wetting behavior of coal in the presence of some nonionic surfactants. *Colloids and surfaces* **26**, 205-216 (1987).
- 19 Chander, S., Alaboyun, A. & Aplan, F. in *Proceedings of the Third Symposium on Respirable Dust in the Mineral Industries*. 193-202 (Society for Mining, Metallurgy & Exploration Littleton, CO).
- 20 Zhou, G. *et al.* Experimental investigation of coal dust wettability based on surface contact angle. *Journal of Chemistry* **2016** (2016).
- 21 Xu, G., Chen, Y., Eksteen, J. & Xu, J. Surfactant-aided coal dust suppression: A review of evaluation methods and influencing factors. *Science of The Total Environment* **639**, 1060-1076 (2018).
- 22 Chen, R., Lee, I. & Zhang, L. Biopolymer stabilization of mine tailings for dust control. *Journal of Geotechnical and Geoenvironmental Engineering* **141**, 04014100 (2014).
- 23 Young, T. III. An essay on the cohesion of fluids. *Philosophical transactions of the royal society of London* **95**, 65-87 (1805).
- 24 Chow, T. Wetting of rough surfaces. *Journal of Physics: Condensed Matter* **10**, L445 (1998).
- 25 Glanville, J. O. & Wightman, J. P. Actions of wetting agents on coal dust. *Fuel* **58**, 819-822 (1979).
- 26 Schmidt-Ott, A. New approaches to in situ characterization of ultrafine agglomerates. *Journal of Aerosol Science* **19**, 553-563 (1988).
- 27 Walker, P., Petersen, E. & Wright, C. Surface active agent phenomena in dust abatement. *Industrial & Engineering Chemistry* **44**, 2389-2393 (1952).
- 28 Glanville, J. O. & Wightman, J. P. Wetting of powdered coals by alkanol-water solutions and other liquids. *Fuel* **59**, 557-562 (1980).
- 29 Chen, Y., Xu, G. & Albijanic, B. Evaluation of SDBS surfactant on coal wetting performance with static methods: Preliminary laboratory tests. *Energy Sources, Part A: Recovery, Utilization, and Environmental Effects* **39**, 2140-2150 (2017).
- 30 van der Veen, R. C., Tran, T., Lohse, D. & Sun, C. Direct measurements of air layer profiles under impacting droplets using high-speed color interferometry. *Physical Review E* **85**, 026315 (2012).
- 31 Tran, T., de Maleprade, H., Sun, C. & Lohse, D. Air entrainment during impact of droplets on liquid surfaces. *Journal of Fluid Mechanics* **726**, R3 (2013).
- 32 Gao, Y., Jung, S. & Pan, L. Interaction Forces between Water Droplets and Solid Surfaces across Air Films. *ACS Omega* **4**, 16674-16682 (2019).
- 33 Testing, A. S. f., Coal, M. C. D. o. & Coke. *Standard test method for ash in the analysis sample of coal and coke from coal*. (ASTM International, 2004).
- 34 Atluri, V., Gao, Y., Wang, X., Pan, L. & Miller, J. D. The influence of polysaccharides on film stability and bubble attachment at the talc surface. *Mining, Metallurgy & Exploration* **36**, 71-80 (2019).

- 35 Gao, Y. & Pan, L. Measurement of Instability of Thin Liquid Films by Synchronized Tri-wavelength Reflection Interferometry Microscope. *Langmuir* (2018).
- 36 Macleod, H. A. & Macleod, H. A. *Thin-film optical filters*. (CRC press, 2010).
- 37 Suhr, N. & Gong, H. A Data Base for the Analysis of Compositional Characteristics of Coal Seams and Macerals. *Some Procedures for the Chemical and Mineralogical Analysis of Coals*. University Park, PA: Penn. State Univ (1983).
- 38 Pan, L., Jung, S. & Yoon, R.-H. Effect of hydrophobicity on the stability of the wetting films of water formed on gold surfaces. *Journal of colloid and interface science* **361**, 321-330 (2011).
- 39 Pan, L. & Yoon, R.-H. Hydrophobic forces in the wetting films of water formed on xanthate-coated gold surfaces. *Faraday Discuss.* **146**, 325-340, doi:10.1039/b926937a (2010).
- 40 Pan, L., Jung, S. & Yoon, R. H. Effect of hydrophobicity on the stability of the wetting films of water formed on gold surfaces. *J. Colloid Interface Sci.* **361**, 321-330, doi:10.1016/j.jcis.2011.05.057 (2011).
- 41 Carnie, S. L., Chan, D. Y. C., Lewis, C., Manica, R. & Dagastine, R. R. Measurement of Dynamical Forces between Deformable Drops Using the Atomic Force Microscope. I. Theory. *Langmuir* **21**, 2912-2922, doi:10.1021/la0475371 (2005).
- 42 Xu, C. *et al.* Experimental investigation of coal dust wetting ability of anionic surfactants with different structures. *Process Safety and Environmental Protection* **121**, 69-76 (2019).
- 43 Dev, A. A., Dey, R. & Mugele, F. Behaviour of flexible superhydrophobic striped surfaces during (electro-) wetting of a sessile drop. *Soft matter* **15**, 9840-9848 (2019).
- 44 Glanville, J. O. & Haley, L. H. Studies of coal dust wetting by surfactant solutions. *Colloids and Surfaces* **4**, 209-212 (1982).
- 45 Lyu, X. *et al.* Adsorption and molecular dynamics simulations of nonionic surfactant on the low rank coal surface. *Fuel* **211**, 529-534 (2018).
- 46 Wiegand, G., Jaworek, T., Wegner, G. & Sackmann, E. Studies of structure and local wetting properties on heterogeneous, micropatterned solid surfaces by microinterferometry. *Journal of colloid and interface science* **196**, 299-312 (1997).
- 47 Crawford, R. & Mainwaring, D. The influence of surfactant adsorption on the surface characterisation of Australian coals. *Fuel* **80**, 313-320 (2001).
- 48 Göbel, J. & Joppien, G. Dynamic Interfacial Tensions of Aqueous Triton X-100 Solutions in Contact with Air, Cyclohexane, n-Heptane, and n-Hexadecane. *Journal of colloid and interface science* **191**, 30-37 (1997).
- 49 Mysels, K. J. Surface tension of solutions of pure sodium dodecyl sulfate. *Langmuir* **2**, 423-428 (1986).
- 50 Dharmawardana, U. R., Christian, S. D., Tucker, E. E., Taylor, R. W. & Scamehorn, J. F. A surface tension method for determining binding constants for

- cyclodextrin inclusion complexes of ionic surfactants. *Langmuir* **9**, 2258-2263 (1993).
- 51 Yuan, S., Xu, G., Luan, Y. & Liu, C. The interaction between polymer and AOT or NaDEHP in aqueous solution: mesoscopic simulation study and surface tension measurement. *Colloids and Surfaces A: Physicochemical and Engineering Aspects* **256**, 43-50 (2005).
- 52 Duchemin, L. & Josserand, C. Curvature singularity and film-skating during drop impact. *Physics of Fluids* **23**, 091701 (2011).
- 53 Pack, M. *et al.* Failure mechanisms of air entrainment in drop impact on lubricated surfaces. *Soft matter* **13**, 2402-2409 (2017).
- 54 Chander, S., Alaboyun, A. & Aplan, F. in *3rd Symposium on Respirable Dust in the Mineral Industries*, Eds. RL Franz and RV Ramani, SME, Littleton, CO.
- 55 Chen, Y. *et al.* Characterization of coal particles wettability in surfactant solution by using four laboratory static tests. *Colloids and Surfaces A: Physicochemical and Engineering Aspects* **567**, 304-312 (2019).
- 56 Fuerstenau, D., Diao, J. & Hanson, J. Estimation of the distribution of surface sites and contact angles on coal particles from film flotation data. *Energy & Fuels* **4**, 34-37 (1990).
- 57 Speight, J. G. *Handbook of coal analysis*. (John Wiley & Sons, 2015).
- 58 Xia, Y., Yang, Z., Zhang, R., Xing, Y. & Gui, X. Enhancement of the surface hydrophobicity of low-rank coal by adsorbing DTAB: An experimental and molecular dynamics simulation study. *Fuel* **239**, 145-152 (2019).
- 59 Butt, H.-J. Measuring electrostatic, van der Waals, and hydration forces in electrolyte solutions with an atomic force microscope. *Biophysical journal* **60**, 1438-1444 (1991).
- 60 Attard, P. & Miklavcic, S. J. Effective spring constant of bubbles and droplets. *Langmuir* **17**, 8217-8223 (2001).
- 61 Lee, V., James, N. M., Waitukaitis, S. R. & Jaeger, H. M. Collisional charging of individual submillimeter particles: Using ultrasonic levitation to initiate and track charge transfer. *Physical Review Materials* **2**, 035602, doi:10.1103/PhysRevMaterials.2.035602 (2018).
- 62 Karraker, K. & Radke, C. Disjoining pressures, zeta potentials and surface tensions of aqueous non-ionic surfactant/electrolyte solutions: theory and comparison to experiment. *Advances in colloid and interface science* **96**, 231-264 (2002).
- 63 Ciunel, K., Armélin, M., Findenegg, G. H. & Von Klitzing, R. Evidence of surface charge at the air/water interface from thin-film studies on polyelectrolyte-coated substrates. *Langmuir* **21**, 4790-4793 (2005).
- 64 Chen, L., He, X., Liu, H., Qian, L. & Kim, S. H. Water Adsorption on Hydrophilic and Hydrophobic Surfaces of Silicon. *The Journal of Physical Chemistry C* **122**, 11385-11391 (2018).
- 65 Sendner, C., Horinek, D., Bocquet, L. & Netz, R. R. Interfacial water at hydrophobic and hydrophilic surfaces: Slip, viscosity, and diffusion. *Langmuir* **25**, 10768-10781 (2009).

- 66 McCoy, J., Schroeder, W., Rajan, S., Ruggieri, S. & Kissell, F. New laboratory measurement method for water spray dust control effectiveness. *American Industrial Hygiene Association Journal* **46**, 735-740 (1985).

## 8 Summary and Future Work

### 8.1 Summary

In this work, a newly developed Synchronized Tri-wavelength Reflection Interferometry Microscope (STRIM) technique was developed to study the instability of liquid films and air films for the first time. The STRIM technique uses three synchronized high-speed cameras that simultaneously record monochromatic interference fringes at three different wavelengths (i.e., 460nm, 527nm, and 620nm). These three sets of monochromatic interference fringes can be used to obtain spatiotemporal profiles without any assumptions. The accuracy of the film thickness measurements was found to be within 1 nm over a range of 0- 200 nm and within 3 nm over the range of 200 – 1000 nm.

**On the liquid film side**, results obtained between air bubbles and hydrophobic silicon surfaces showed that the critical rupture thicknesses scattered over a range of 57 – 335 nm, with a median rupture thickness of 122 nm, at bubble sizes of 0.71-0.88 mm. When the bubble sizes were reduced to 0.13-0.26 mm, the range of the critical rupture thicknesses was reduced to 17-156 nm, with a median rupture thickness of 27 nm. The result indicates that the rupture of wetting films formed on hydrophobic surfaces might be associated with a formation of gas channels that effectively bridges hydrophobic solid plates and air bubbles in the water. Compared to wetting films formed on hydrophobic surfaces, the rupture thickness for foam films between two air bubbles in a  $10^{-2}$  M NaCl solution was much more consistent in the range of 22-45 nm. The critical rupture thicknesses were found to increase with increasing bubble sizes, which is attributed to the increased fluctuation waves at the air/water interface. This result was compared with those obtained between one air bubble and one droplet of dodecane. It was found that the critical rupture thickness obtained between the air bubble and the droplet of dodecane was smaller than those obtained between two air bubbles, indicating that the critical rupture thickness of TLFs is correlated to the hydrophobicities of the interacting surfaces.

Besides, in the study of the molybdenite flotation by oily collectors, we found that both kerosene and dodecane oils are present as micron-sized oil droplets in DI water. The results obtained from the film stability measurements indicate that the TLFs formed between air bubbles and freshly peeled molybdenite surfaces are stable due to the presence of a repulsive electrostatic double-layer force. Hydrocarbon oils in oil emulsions adsorb on hydrophobic molybdenite face surfaces spontaneously in the forms of isolated oil patches, resulting in an increase in surface hydrophobicity. The result obtained from the film stability measurement shows that the TLFs between air bubbles and collector-treated molybdenite surfaces become unstable and rupture despite that the kinetics of thinning of TLFs are nearly the same with and without oil collector treatment. When the molybdenite surfaces are covered with a large number of hydrocarbon oils, the kinetics of thinning is decelerated due to the presence of oil droplets for the liquid in the TLF to drain. The film rupture may be in various forms. When nano-sized oil droplets were attached to molybdenite surfaces, the rupture occurs when the closest separation distance



between the two reaches a real critical rupture thickness of 30-50 nm. For large oil droplets adsorbed on molybdenite face surfaces, which happened in high collector dosage, the observational rupture thicknesses significantly vary, but the real critical rupture thicknesses maintain the same. In this regard, film stability depends on oil drop sizes as well as the surface chemistry of TLFs. It has also been shown that the occurrence of the film rupture largely depends on the density of oil drops adsorbed on molybdenite face surfaces. Kerosene exhibits a better dispersibility than dodecane, leading to higher coverage of oils on molybdenite surfaces at the same oil dosage.

In addition, the follow-up research on the adsorption of oil drops on hydrophobic surfaces showed that before the adsorption of dodecane drops on a hydrophobic surface, the liquid films should drain and rupture first. During the drainage of the liquid film, two pressures can be adjusted: capillary pressure and disjoining pressure. The former is modified by changing the oil drop sizes, while the latter can be adjusted by altering the electrolyte concentrations. Experimental results showed smaller drop sizes and higher electrolyte concentrations benefit the adsorption of oil on hydrophobic surfaces. And for more hydrophobic surfaces, the required drop size for film rupture is more extensive, and the concentration of electrolyte needed is smaller. The stability of liquid film is crucial to the control of many industrial processes, especially oil recovery and froth flotation.

**On the air film side**, we have studied the kinetics of thinning and rupture of air films formed between liquid droplets of DI water and mineral surfaces. Results showed that water droplets spread on solid surfaces spontaneously, regardless of the surface hydrophobicity. The critical rupture thickness of the air films increases exponentially with decreasing the surface hydrophobicity of solid surfaces. The critical rupture thickness was found to be above 2  $\mu\text{m}$  on a very hydrophilic quartz surface having a water contact angle of below  $20^\circ$ . An acceleration of approaching was found between water droplets and hydrophilic solid surfaces. The acceleration in the film thinning was attributed to the presence of attractive surface forces. These interactions were strongly attractive on hydrophilic surfaces and became less attractive with increased hydrophobicity of the surfaces. These attractive forces might be electric forces. The charging status was found to be more relevant to the hydrophobicity of surfaces, indicating that the charges on solid surfaces might be associated with the adsorption of water molecules on surfaces.

In the meantime, the microscopic processes involved in the capture of coal dust particles by liquid droplets have been revealed by investigating the microscopic attachment process between aqueous droplets and polished coal surfaces. The thinning kinetics of air films increases with increasing surfactant concentrations. The accelerated film thinning is attributed to the presence of an attractive electrostatic force between the two oppositely charged surfaces. It has been found that this phenomenon is applicable to not only non-ionic surfactants but also anionic surfactants. In addition, the critical rupture thicknesses increase with increasing surfactant concentrations. The critical rupture thickness ( $h_c$ ) of the air films between water droplets and bituminous coal surfaces is 104 nm. The  $h_c$  value was increased to over 1000 nm at 0.1 mM Triton X-100 as well as at 1 mM AOT

solutions. A linear relationship between  $h_c$  and  $\theta$  has been found. This result suggests that the critical rupture thickness is more relevant to the wettability of coal surfaces than the surface tension of wetting solutions. In this regard, surfactants with a strong capability to increase the wettability of coal surfaces might be a better wetting agent candidate.

## 8.2 Future work

The instability of liquid and air films will still be the critical point that should be addressed in future work. There are three aspects of great importance and urgency:

1. The rupture processes still maintain a mystery. Although in the present work, the involved interactions can be resolved, the specific rupture process is not well-described. One primary reason for that is the limitation of the processing speed of the employed cameras, which can only record the images at a rate of 150 frames per second. The rupture is occurring in an extremely short moment, which requires high-speed cameras to completely collect the rupture information of liquid/air films.
2. Another meaningful topic is the spreading of the three-phase contact (TPC) line, which involves both thermodynamics and kinetics. Using the STRIM system, the initial spreading process can be observed simultaneously from both the side-view and bottom-view images. However, similar to the rupture process, sometimes the spreading of TPC can reach a rate that is too high for the current cameras to capture. Thus updated cameras can help to better investigate the TPC movement after the film rupture process. In addition, appropriate models associated with simulations are desired to fit the experimental data obtained by STRIM.
3. STRIM system should be extensively used in other areas since it is such a powerful tool to characterize the small distance between two surfaces. For example, the bubble collapse is vital for foam stability, which can be widely used in personal-care supplies and fire extinction equipment. And STRIM is flexible to control the experimental conditions, making the systematic studies possible. However, it requires the light beams to go through. Thus at least one material should be transparent, which may limit a part of its applications. Inspired by the RICM-AFM system, the combination of STRIM and AFM may be a promising solution that should be attempted in the next project to enlarge the ranges of applicable materials.

## A. Copyright permission documentation

### A.1 Figure 2.2 permission

This Agreement between Yuesheng Gao ("You") and Elsevier ("Elsevier") consists of your license details and the terms and conditions provided by Elsevier and Copyright Clearance Center.

License Number	4943810985940
License date	Nov 07, 2020
Licensed Content Publisher	Elsevier
Licensed Content Publication	Minerals Engineering
Licensed Content Title	Experimental observations of bubble–particle collisional interaction relevant to froth flotation, and calculation of the associated forces
Licensed Content Author	Shuofu Li,M. Philip Schwarz,William Yang,Yuqing Feng,Peter Witt,Chunbao Sun
Licensed Content Date	Jun 1, 2020
Licensed Content Volume	151
Licensed Content Issue	n/a
Licensed Content Pages	1
Start Page	106335

End Page	0
Type of Use	reuse in a thesis/dissertation
Portion	figures/tables/illustrations
Number of figures/tables/illustrations	5
Format	both print and electronic
Are you the author of this Elsevier article?	No
Will you be translating?	No
Title	INVESTIGATION OF LIQUID/AIR FILM STABILITY BY SYNCHRONIZED TRI-WAVELENGTH REFLECTION INTERFEROMETRY MICROSCOPE (STRIM)
Institution name	Michigan Technological University
Expected presentation date	Dec 2020
Order reference number	13
Portions	Figure 2.2
Requestor Location	Yuesheng Gao 238 Quincy St Apt 9 HANCOCK, MI 49930 United States Attn: Michigan Tech
Publisher Tax ID	98-0397604
Total	0.00 USD

## A.2 Figure 2.3 permission

This Agreement between Yueheng Gao ("You") and Elsevier ("Elsevier") consists of your license details and the terms and conditions provided by Elsevier and Copyright Clearance Center.

License Number	4943810086605
License date	Nov 07, 2020
Licensed Content Publisher	Elsevier
Licensed Content Publication	International Journal of Mineral Processing
Licensed Content Title	Collision processes involving a single rising bubble and a larger stationary spherical particle
Licensed Content Author	P. Basařová, V. Machoň, M. Hubička, D. Horn
Licensed Content Date	Feb 19, 2010
Licensed Content Volume	94
Licensed Content Issue	1-2
Licensed Content Pages	9
Start Page	58
End Page	66

Number of figures/tables/illustrations	1
Format	both print and electronic
Are you the author of this Elsevier article?	No
Will you be translating?	No
Title	INVESTIGATION OF LIQUID/AIR FILM STABILITY BY SYNCHRONIZED TRI-WAVELENGTH REFLECTION INTERFEROMETRY MICROSCOPE (STRIM)
Institution name	Michigan Technological University
Expected presentation date	Dec 2020
Order reference number	6
Portions	Figure 2.3
Requestor Location	Yuesheng Gao 238 Quincy St Apt 9 HANCOCK, MI 49930 United States Attn: Michigan Tech
Publisher Tax ID	98-0397604
Total	0.00 USD

### A.3 Figure 2.4 permission

This Agreement between Yuesheng Gao ("You") and AIP Publishing ("AIP Publishing") consists of your license details and the terms and conditions provided by AIP Publishing and Copyright Clearance Center.

License Number 4943820337221

License date Nov 07, 2020

Licensed Content Publisher AIP Publishing

Licensed Content Publication Journal of Chemical Physics

Licensed Content Title The drainage of thin liquid films between solid surfaces

Licensed Content Author D. Y. C. Chan, R. G. Horn

Licensed Content Date Nov 15, 1985

Licensed Content Volume 83

Licensed Content Issue 10

Type of Use Thesis/Dissertation

Requestor type Student

Format Print and electronic

Portion Figure/Table

Number of figures/tables 1

Title INVESTIGATION OF LIQUID/AIR FILM STABILITY BY SYNCHRONIZED TRI-WAVELENGTH REFLECTION INTERFEROMETRY MICROSCOPE (STRIM)

Institution name Michigan Technological University

Expected presentation date Dec 2020

Order reference number 14

Portions Figure 2.4

Requestor Location Yuesheng Gao  
238 Quincy St  
Apt 9  
HANCOCK, MI 49930  
United States  
Attn: Michigan Tech

Total 0.00 USD

Terms and Conditions



## A.4 Figure 2.5 permission

This Agreement between Yuesheng Gao ("You") and Elsevier ("Elsevier") consists of your license details and the terms and conditions provided by Elsevier and Copyright Clearance Center.

License Number	4943820767483
License date	Nov 07, 2020
Licensed Content Publisher	Elsevier
Licensed Content Publication	Colloids and Surfaces A: Physicochemical and Engineering Aspects
Licensed Content Title	Application of compound reagent H511 in the flotation removal of unburned carbon from fly ash
Licensed Content Author	Yijiang Li,Zhiwei Hu,Wencheng Xia,Huaizhi Shao,Kanghao Zheng,Long Liang,Yaoli Peng,Guangyuan Xie
Licensed Content Date	Jun 20, 2020
Licensed Content Volume	595
Licensed Content Issue	n/a
Licensed Content Pages	1
Start Page	124699
End Page	0

Type of Use	reuse in a thesis/dissertation
Portion	figures/tables/illustrations
Number of figures/tables/illustrations	1
Format	both print and electronic
Are you the author of this Elsevier article?	No
Will you be translating?	No
Title	INVESTIGATION OF LIQUID/AIR FILM STABILITY BY SYNCHRONIZED TRI-WAVELENGTH REFLECTION INTERFEROMETRY MICROSCOPE (STRIM)
Institution name	Michigan Technological University
Expected presentation date	Dec 2020
Order reference number	44
Portions	Figure 2.5
Requestor Location	Yuesheng Gao 238 Quincy St Apt 9 HANCOCK, MI 49930 United States Attn: Michigan Tech
Publisher Tax ID	98-0397604
Total	0.00 USD

## A.5 Figure 2.6 permission

This Agreement between Yuesheng Gao ("You") and Elsevier ("Elsevier") consists of your license details and the terms and conditions provided by Elsevier and Copyright Clearance Center.

License Number	4943821427811
License date	Nov 07, 2020
Licensed Content Publisher	Elsevier
Licensed Content Publication	International Journal of Mineral Processing
Licensed Content Title	Kinetics of bubble collision and attachment to hydrophobic solids: I. Effect of surface roughness
Licensed Content Author	M. Krasowska,K. Malysa
Licensed Content Date	Jan 1, 2007
Licensed Content Volume	81
Licensed Content Issue	4
Licensed Content Pages	12
Start Page	205
End Page	216

Type of Use	reuse in a thesis/dissertation
Portion	figures/tables/illustrations
Number of figures/tables/illustrations	1
Format	both print and electronic
Are you the author of this Elsevier article?	No
Will you be translating?	No
Title	INVESTIGATION OF LIQUID/AIR FILM STABILITY BY SYNCHRONIZED TRI-WAVELENGTH REFLECTION INTERFEROMETRY MICROSCOPE (STRIM)
Institution name	Michigan Technological University
Expected presentation date	Dec 2020
Order reference number	45
Portions	Figure 2.6
Requestor Location	Yuesheng Gao 238 Quincy St Apt 9 HANCOCK, MI 49930 United States Attn: Michigan Tech
Publisher Tax ID	98-0397604
Total	0.00 USD
Terms and Conditions	

## A.6 Figure 2.7 permission

This Agreement between Yuesheng Gao ("You") and Elsevier ("Elsevier") consists of your license details and the terms and conditions provided by Elsevier and Copyright Clearance Center.

License Number	4943830184221
License date	Nov 07, 2020
Licensed Content Publisher	Elsevier
Licensed Content Publication	Journal of Colloid and Interface Science
Licensed Content Title	Bubble rubbing on solid surface: Experimental study
Licensed Content Author	Stoyan I. Karakashev, Klaus W. Stöckelhuber, Roumen Tsekov, Gert Heinrich
Licensed Content Date	Dec 15, 2013
Licensed Content Volume	412
Licensed Content Issue	n/a
Licensed Content Pages	6
Start Page	89
End Page	94

Type of Use	reuse in a thesis/dissertation
Portion	figures/tables/illustrations
Number of figures/tables/illustrations	1
Format	both print and electronic
Are you the author of this Elsevier article?	No
Will you be translating?	No
Title	INVESTIGATION OF LIQUID/AIR FILM STABILITY BY SYNCHRONIZED TRI-WAVELENGTH REFLECTION INTERFEROMETRY MICROSCOPE (STRIM)
Institution name	Michigan Technological University
Expected presentation date	Dec 2020
Order reference number	46
Portions	Figure 2.7
Requestor Location	Yuesheng Gao 238 Quincy St Apt 9 HANCOCK, MI 49930 United States Attn: Michigan Tech
Publisher Tax ID	98-0397604
Total	0.00 USD

## A.7 Figure 2.8 permission

This is an open access article published under an ACS AuthorChoice License, which permits copying and redistribution of the article or any adaptations for non-commercial purposes.



# LANGMUIR

Invited Feature Article

pubs.acs.org/Langmuir

## Surface Forces and Interaction Mechanisms of Emulsion Drops and Gas Bubbles in Complex Fluids

Lei Xie, Chen Shi, Xin Cui, and Hongbo Zeng\*

Department of Chemical and Materials Engineering, University of Alberta, Edmonton, Alberta T6G 1H9, Canada

### Standard ACS AuthorChoice/Editors' Choice Usage Agreement

This ACS article is provided to You under the terms of this Standard ACS AuthorChoice/Editors' Choice usage agreement between You and the American Chemical Society ("ACS"), a federally-chartered nonprofit located at 1155 16th Street NW, Washington DC 20036. Your access and use of this ACS article means that you have accepted and agreed to the Terms and Conditions of this Agreement. ACS and You are collectively referred to in this Agreement as "the Parties").



#### 1. SCOPE OF GRANT

ACS grants You non-exclusive and nontransferable permission to access and use this ACS article subject to the terms and conditions set forth in this Agreement.

#### 2. PERMITTED USES

a. For non-commercial research and education purposes only, You may access, download, copy, display and redistribute articles as well as adapt, translate, text and data mine content contained in articles, subject to the following conditions:

i. The authors' moral right to the integrity of their work under the Berne Convention (Article 6bis) is not compromised.

ii. Where content in the article is identified as belonging to a third party, it is your responsibility to ensure that any reuse complies with copyright policies of the owner.

iii. Copyright notices or the display of unique Digital Object Identifiers (DOIs), ACS or journal logos, bibliographic (e.g. authors, journal, article title, volume, issue, page numbers) or other references to ACS journal titles, web links, and any other journal-specific "branding" or notices that are included in the article or that are provided by the ACS with instructions that such should accompany its display, should not be removed or tampered with in any way. The display of ACS AuthorChoice or ACS Editors' Choice articles on non-ACS websites must be accompanied by prominently displayed links to the definitive published versions of those articles on the ACS website.

iv. Any adaptations for non-commercial purposes must prominently link to the definitive published version on the ACS website and prominently display the statement: "This is an unofficial adaptation of an article that appeared in an ACS publication. ACS has not endorsed the content of this adaptation or the context of its use."

v. Any translations for non-commercial purposes, for which a prior translation agreement with ACS has not been established, must prominently link to the definitive published version on the ACS website and prominently display the statement: "This is an unofficial translation of an article that appeared in an ACS publication. ACS has not endorsed the content of this translation or the context of its use."

b. Each time You distribute this ACS article or an adaptation, ACS offers to the recipient a license to this ACS article on the same terms and conditions as the license granted to You under this License.

c. For permission to use ACS copyrighted articles beyond that permitted here, visit: <http://pubs.acs.org/copyright/permissions.html>

#### 3. PROHIBITED USES

a. Use of this ACS article for commercial purposes is prohibited. Examples of such prohibited commercial purposes include but are not limited to:

i. Copying or downloading of articles, or linking to such postings, for further distribution, sale or licensing, for a fee;

ii. Copying, downloading or posting by a site or service that incorporates advertising with such content;

iii. The inclusion or incorporation of article content in other works or services (other than normal quotations with an appropriate citation) that is then available for sale or licensing, for a fee;

iv. Use of articles or article content (other than normal quotations with appropriate citation) by a for-profit organizations for promotional purposes, whether for a fee or otherwise;

v. Sale of translated versions of the article that have not been authorized by license or other permission from the ACS

#### 4. TERMINATION

ACS reserves the right to limit, suspend, or terminate your access to and use of the ACS Publications Division website and/or all ACS articles immediately upon detecting a breach of this License.

## 5. COPYRIGHTS; OTHER INTELLECTUAL PROPERTY RIGHTS

Except as otherwise specifically noted, ACS is the owner of all right, title and interest in the content of this ACS article, including, without limitations, graphs, charts, tables illustrations, and copyrightable supporting information. This ACS article is protected under the Copyright Laws of the United States Codified in Title 17 of the U.S. Code and subject to the Universal Copyright Convention and the Berne Copyright Convention. You agree not to remove or obscure copyright notices. You acknowledge that You have no claim to ownership of any part of this ACS article or other proprietary information accessed under this Agreement.

The names "American Chemical Society," "ACS" and the titles of the journals and other ACS products are trademarks of ACS.

## 6. DISCLAIMER OF WARRANTIES; LIMITATION OF LIABILITY

ACS warrants that it is entitled to grant this Agreement.

EXCEPT AS SET FORTH IN THE PRECEDING SENTENCE, ACS MAKES NO WARRANTY OR REPRESENTATION OF ANY KIND, EXPRESS OR IMPLIED, WITH RESPECT TO THIS ACS ARTICLE INCLUDING, BUT NOT LIMITED TO WARRANTIES AS TO THE ACCURACY OR COMPLETENESS OF THE ACS ARTICLE, ITS QUALITY, ORIGINALITY, SUITABILITY, SEARCHABILITY, OPERATION, PERFORMANCE, COMPLIANCE WITH ANY COMPUTATIONAL PROCESS, MERCHANTABILITY OR FITNESS FOR A PARTICULAR PURPOSE.

ACS SHALL NOT BE LIABLE FOR: EXEMPLARY, SPECIAL, INDIRECT, INCIDENTAL, CONSEQUENTIAL OR OTHER DAMAGES ARISING OUT OF OR IN CONNECTION WITH THE AGREEMENT GRANTED HEREUNDER, THE USE OR INABILITY TO USE ANY ACS PRODUCT, ACS'S PERFORMANCE UNDER THIS AGREEMENT, TERMINATION OF THIS AGREEMENT BY ACS OR THE LOSS OF DATA, BUSINESS OR GOODWILL EVEN IF ACS IS ADVISED OR AWARE OF THE POSSIBILITY OF SUCH DAMAGES. IN NO EVENT SHALL THE TOTAL AGGREGATE LIABILITY OF ACS OUT OF ANY BREACH OR TERMINATION OF THIS AGREEMENT EXCEED THE TOTAL AMOUNT PAID BY YOU TO ACS FOR ACCESS TO THIS ACS ARTICLE FOR THE CURRENT YEAR IN WHICH SUCH CLAIM, LOSS OR DAMAGE OCCURRED, WHETHER IN CONTRACT, TORT OR OTHERWISE, INCLUDING, WITHOUT LIMITATION, DUE TO NEGLIGENCE.

The foregoing limitations and exclusions of certain damages shall apply regardless of the success or effectiveness of other remedies. No claim may be made against ACS unless suit is filed within one (1) year after the event giving rise to the claim.

## 7. GENERAL

This Agreement sets forth the entire understanding of the Parties. The validity, construction and performance of this Agreement shall be governed by and construed in accordance with the laws of the District of Columbia, USA without reference to its conflicts of laws principles. You acknowledge that the delivery of the ACS article will occur in the District of Columbia, USA. You shall pay any taxes lawfully due from it, other than taxes on ACS's net income, arising out of your use of this ACS article and/or other rights granted under this Agreement. You may not assign or transfer its rights under this Agreement without the express written consent of ACS.

## 8. ACCEPTANCE

You warrant that You have read, understand, and accept the terms and conditions of this Agreement. ACS reserves the right to modify this Agreement at any time by posting the modified terms and conditions on the ACS Publications Web site. Any use of this ACS article after such posting shall constitute acceptance of the terms and conditions as modified.



## A.8 Figure 2.9 permission

Copyright Clearance Center | RightsLink®

Home | ? Help | Email Support | Yuesheng Gao

**Probing the Interaction Mechanism between Air Bubbles and Bitumen Surfaces in Aqueous Media Using Bubble Probe Atomic Force Microscopy**

Author: Lei Xie, Chen Shi, Xin Cui, et al  
Publication: Langmuir  
Publisher: American Chemical Society  
Date: Jan 1, 2018  
Copyright © 2018, American Chemical Society

**PERMISSION/LICENSE IS GRANTED FOR YOUR ORDER AT NO CHARGE**

This type of permission/license, instead of the standard Terms & Conditions, is sent to you because no fee is being charged for your order. Please note the following:

- Permission is granted for your request in both print and electronic formats, and translations.
- If figures and/or tables were requested, they may be adapted or used in part.
- Please print this page for your records and send a copy of it to your publisher/graduate school.
- Appropriate credit for the requested material should be given as follows: "Reprinted (adapted) with permission from (COMPLETE REFERENCE CITATION). Copyright (YEAR) American Chemical Society." Insert appropriate information in place of the capitalized words.
- One-time permission is granted only for the use specified in your request. No additional uses are granted (such as derivative works or other editions). For any other uses, please submit a new request. If credit is given to another source for the material you requested, permission must be obtained from that source.

## A.9 Figure 2.10 permission

Copyright Clearance Center | RightsLink®

Home | ? Help | Email Support | Yuesheng Gao

**On the measurement of weak repulsive and frictional colloidal forces by reflection interference contrast microscopy**


Author: Joachim Raedler, Erich Sackmann  
Publication: Langmuir  
Publisher: American Chemical Society  
Date: Mar 1, 1992  
Copyright © 1992, American Chemical Society

**PERMISSION/LICENSE IS GRANTED FOR YOUR ORDER AT NO CHARGE**

This type of permission/license, instead of the standard Terms & Conditions, is sent to you because no fee is being charged for your order. Please note the following:

- Permission is granted for your request in both print and electronic formats, and translations.
- If figures and/or tables were requested, they may be adapted or used in part.
- Please print this page for your records and send a copy of it to your publisher/graduate school.
- Appropriate credit for the requested material should be given as follows: "Reprinted (adapted) with permission from (COMPLETE REFERENCE CITATION). Copyright (YEAR) American Chemical Society." Insert appropriate information in place of the capitalized words.
- One-time permission is granted only for the use specified in your request. No additional uses are granted (such as derivative works or other editions). For any other uses, please submit a new request. If credit is given to another source for the material you requested, permission must be obtained from that source.

## A.10 Figure 2.11 permission



**RightsLink®**

[Home](#)
[?](#)
[Help](#)
[Email Support](#)
[Yuesheng Gao](#)

**Measuring Forces and Spatiotemporal Evolution of Thin Water Films between an Air Bubble and Solid Surfaces of Different Hydrophobicity**


**Author:** Chen Shi, Xin Cui, Lei Xie, et al  
**Publication:** ACS Nano  
**Publisher:** American Chemical Society  
**Date:** Jan 1, 2015  
Copyright © 2015, American Chemical Society

**PERMISSION/LICENSE IS GRANTED FOR YOUR ORDER AT NO CHARGE**

This type of permission/license, instead of the standard Terms & Conditions, is sent to you because no fee is being charged for your order. Please note the following:

- Permission is granted for your request in both print and electronic formats, and translations.
- If figures and/or tables were requested, they may be adapted or used in part.
- Please print this page for your records and send a copy of it to your publisher/graduate school.
- Appropriate credit for the requested material should be given as follows: "Reprinted (adapted) with permission from (COMPLETE REFERENCE CITATION). Copyright (YEAR) American Chemical Society." Insert appropriate information in place of the capitalized words.
- One-time permission is granted only for the use specified in your request. No additional uses are granted (such as derivative works or other editions). For any other uses, please submit a new request.
- If credit is given to another source for the material you requested, permission must be obtained from that source.

## A.11 Figure 2.12 permission



**Marketplace™**

**Royal Society of Chemistry - License Terms and Conditions**

This is a License Agreement between Yuesheng Gao ("You") and Royal Society of Chemistry ("Publisher") provided by Copyright Clearance Center ("CCC"). The license consists of your order details, the terms and conditions provided by Royal Society of Chemistry, and the CCC terms and conditions.

All payments must be made in full to CCC.

<b>Order Date</b>	07-Nov-2020	<b>Type of Use</b>	Republish in a thesis/dissertation
<b>Order license ID</b>	1075944-1	<b>Publisher</b>	ROYAL SOCIETY OF CHEMISTRY
<b>ISSN</b>	1744-6848	<b>Portion</b>	Chart/graph/table/figure

**LICENSED CONTENT**

<b>Publication Title</b>	Soft matter	<b>Country</b>	United Kingdom of Great Britain and Northern Ireland
<b>Author/Editor</b>	Royal Society of Chemistry (Great Britain)	<b>Rightsholder</b>	Royal Society of Chemistry
<b>Date</b>	06/01/2005	<b>Publication Type</b>	e-Journal
<b>Language</b>	English	<b>URL</b>	<a href="http://www.rsc.org/Publishing/Journals/s...">http://www.rsc.org/Publishing/Journals/s...</a>

**REQUEST DETAILS**

<b>Portion Type</b>	Chart/graph/table/figure	<b>Distribution</b>	Worldwide
<b>Number of charts / graphs / tables / figures requested</b>	1	<b>Translation</b>	Original language of publication
<b>Format (select all that apply)</b>	Print, Electronic	<b>Copies for the disabled?</b>	No
<b>Who will republish the content?</b>	Not-for-profit entity	<b>Minor editing privileges?</b>	No
<b>Duration of Use</b>	Life of current edition	<b>Incidental promotional use?</b>	No
<b>Lifetime Unit Quantity</b>	Up to 499	<b>Currency</b>	USD
<b>Rights Requested</b>	Main product		

## NEW WORK DETAILS

<b>Title</b>	INVESTIGATION OF LIQUID/AIR FILM STABILITY BY SYNCHRONIZED TRI-WAVELENGTH REFLECTION INTERFEROMETRY MICROSCOPE (STRIM)	<b>Institution name</b>	MICHIGAN TECHNOLOGICAL UNIVERSITY
<b>Instructor name</b>	Lei Pan	<b>Expected presentation date</b>	2020-11-30

## ADDITIONAL DETAILS

<b>Order reference number</b>	N/A	<b>The requesting person / organization to appear on the license</b>	Yuesheng Gao
-------------------------------	-----	--	--------------

## REUSE CONTENT DETAILS

<b>Title, description or numeric reference of the portion(s)</b>	Fig. 1 (a) Schematic illustration of the ITLFFA and (b) enlarged image of the stainless steel chamber filled with liquid.	<b>Title of the article/chapter the portion is from</b>	N/A
<b>Editor of portion(s)</b>	N/A	<b>Author of portion(s)</b>	Xurui Zhang, Plamen Tchoukov, Rogerio Manica, Louxiang Wang, Qingxia Liu and Zhenghe Xu
<b>Volume of serial or monograph</b>	N/A	<b>Issue, if republishing an article from a serial</b>	44
<b>Page or page range of portion</b>	9105-9114	<b>Publication date of portion</b>	2016-10-19

## A.12 Figure 2.13 permission

[Home](#)
[Help](#)
[Email Support](#)

Yuesheng Gao

**A Study on Picobubble Enhanced Coarse Phosphate Froth Flotation**

**Author:** Maoming Fan, Daniel Tao

**Publication:** Separation Science and Technology

**Publisher:** Taylor & Francis

**Date:** Jan 1, 2008

*Rights managed by Taylor & Francis*

**Thesis/Dissertation Reuse Request**

Taylor & Francis is pleased to offer reuses of its content for a thesis or dissertation free of charge contingent on resubmission of permission request if work is published.

BACK
CLOSE

## A.13 Figure 2.14 permission

[Home](#)
[Help](#)
[Email Support](#)
[Sign In](#)
[Create Account](#)

**Detachment Force of Particles from Air-Liquid Interfaces of Films and Bubbles**

**Author:** Javed Ali, Michael Kapp, Hans-Jürgen Butt, et al

**Publication:** Langmuir

**Publisher:** American Chemical Society

**Date:** Dec 1, 2010



Copyright © 2010, American Chemical Society

**PERMISSION/LICENSE IS GRANTED FOR YOUR ORDER AT NO CHARGE**

This type of permission/license, instead of the standard Terms & Conditions, is sent to you because no fee is being charged for your order. Please note the following:

- Permission is granted for your request in both print and electronic formats, and translations.
- If figures and/or tables were requested, they may be adapted or used in part.
- Please print this page for your records and send a copy of it to your publisher/graduate school.
- Appropriate credit for the requested material should be given as follows: "Reprinted (adapted) with permission from (COMPLETE REFERENCE CITATION). Copyright (REAB) American Chemical Society." Insert appropriate information in place of the capitalized words.
- One-time permission is granted only for the use specified in your request. No additional uses are granted (such as derivative works or other editors). For any other uses, please submit a new request. If credit is given to another source for the material you requested, permission must be obtained from that source.

## A.14 Figure 2.15 permission

Home ? Email Support Sign in Create Account

**Contact Line and Adhesion Force of Droplets on Concentric Ring-Textured Hydrophobic Surfaces**

Author: Donghui Wang, Youhua Jiang, Zhanlei Zhu, et al.  
Publication: Langmuir  
Publisher: American Chemical Society  
Date: Mar 1, 2020  
Copyright © 2020, American Chemical Society

**PERMISSION/LICENSE IS GRANTED FOR YOUR ORDER AT NO CHARGE**

This type of permission/license, instead of the standard Terms & Conditions, is sent to you because no fee is being charged for your order. Please note the following:

- Permission is granted for your request in both print and electronic formats, and translations.
- If figures and/or tables were requested, they may be adapted or used in part.
- Please print this page for your records and send a copy of it to your publisher/graduate school.
- Appropriate credit for the requested material should be given as follows: "Reprinted (adapted) with permission from (COMPLETE REFERENCE CITATION). Copyright (YEAR) American Chemical Society." Invert appropriate information in place of the capitalized words.
- One-time permission is granted only for the use specified in your request. No additional uses are granted (such as derivative works or other editions). For any other uses, please submit a new request.

If credit is given to another source for the material you requested, permission must be obtained from that source.

## A.15 Figure 2.16 permission

This Agreement between Yuesheng Gao ("You") and Elsevier ("Elsevier") consists of your license details and the terms and conditions provided by Elsevier and Copyright Clearance Center.

License Number	4944010300266
License date	Nov 07, 2020
Licensed Content Publisher	Elsevier
Licensed Content Publication	Powder Technology
Licensed Content Title	Effect of vibration mode on detachment of low-rank coal particle from oscillating bubble
Licensed Content Author	Youfei Zhang, Yaowen Xing, Shihao Ding, Yijun Cao, Xiahui Gui
Licensed Content Date	Nov 1, 2019
Licensed Content Volume	356
Licensed Content Issue	n/a
Licensed Content Pages	4
Start Page	880
End Page	883
Type of Use	reuse in a thesis/dissertation

Portion	figures/tables/illustrations
Number of figures/tables/illustrations	1
Format	both print and electronic
Are you the author of this Elsevier article?	No
Will you be translating?	No
Title	INVESTIGATION OF LIQUID/AIR FILM STABILITY BY SYNCHRONIZED TRI-WAVELENGTH REFLECTION INTERFEROMETRY MICROSCOPE (STRIM)
Institution name	Michigan Technological University
Expected presentation date	Dec 2020
Order reference number	113
Portions	Figure 2.15
Requestor Location	Yuesheng Gao 238 Quincy St Apt 9 HANCOCK, MI 49930 United States Attn: Michigan Tech
Publisher Tax ID	98-0397604
Total	0.00 USD

## A.16 Figure 2.17 permission



Marketplace™

### Annual Reviews, Inc. - License Terms and Conditions

This is a License Agreement between Yuesheng Gao ("You") and Annual Reviews, Inc. ("Publisher") provided by Copyright Clearance Center ("CCC"). The license consists of your order details, the terms and conditions provided by Annual Reviews, Inc., and the CCC terms and conditions.

All payments must be made in full to CCC.

Order Date	08-Nov-2020	Type of Use	Republish in a thesis/dissertation
Order license ID	1076060-1	Publisher	ANNUAL REVIEWS
ISSN	1545-4479	Portion	Abstract

#### LICENSED CONTENT

Publication Title	Annual review of fluid mechanics	Rightsholder	Annual Reviews, Inc.
Date	01/01/1969	Publication Type	e-Journal
Language	English	URL	<a href="http://arjournals.annualreviews.org/loi/fl...">http://arjournals.annualreviews.org/loi/fl...</a>
Country	United States of America		

#### REQUEST DETAILS

Portion Type	Abstract	Distribution	Worldwide
Format (select all that apply)	Print, Electronic	Translation	Original language of publication
Who will republish the content?	Not-for-profit entity	Copies for the disabled?	No
Duration of Use	Life of current edition	Minor editing privileges?	No
Lifetime Unit Quantity	Up to 499	Incidental promotional use?	No
Rights Requested	Main product	Currency	USD

#### NEW WORK DETAILS

Title	INVESTIGATION OF LIQUID/AIR FILM STABILITY BY SYNCHRONIZED TRI-WAVELENGTH REFLECTION INTERFEROMETRY MICROSCOPE (STRIM)	Institution name	MICHIGAN TECHNOLOGICAL UNIVERSITY
Instructor name	Lel Pan	Expected presentation date	2020-11-30

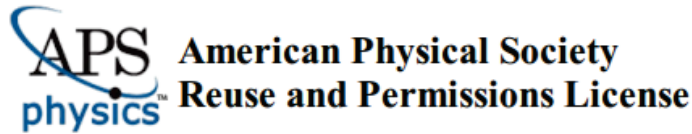
#### ADDITIONAL DETAILS

Order reference number	N/A	The requesting person / organization to appear on the license	Yuesheng Gao
------------------------	-----	---	--------------

#### REUSE CONTENT DETAILS

Title, description or numeric reference of the portion(s)	Figure 12	Title of the article/chapter the portion is from	DROP IMPACT DYNAMICS: Splashing, Spreading, Receding, Bouncing...
Editor of portion(s)	N/A	Author of portion(s)	A.L. Yarin
Volume of serial or monograph	38	Issue, if republishing an article from a serial	N/A
Page or page range of portion	159-192	Publication date of portion	2006-01-21

## A.17 Figure 2.18 permission



08-Nov-2020

This license agreement between the American Physical Society ("APS") and Yuesheng Gao ("You") consists of your license details and the terms and conditions provided by the American Physical Society and SciPris.

### Licensed Content Information

**License Number:** RNP/20/NOV/032856  
**License date:** 08-Nov-2020  
**DOI:** 10.1103/PhysRevLett.109.204501  
**Title:** How Does an Air Film Evolve into a Bubble During Drop Impact?  
**Author:** Ji San Lee et al.  
**Publication:** Physical Review Letters  
**Publisher:** American Physical Society  
**Cost:** USD \$ 0.00

### Request Details

**Does your reuse require significant modifications:** No  
**Specify intended distribution locations:** Worldwide  
**Reuse Category:** Reuse in a thesis/dissertation  
**Requestor Type:** Student  
**Items for Reuse:** Figures/Tables  
**Number of Figure/Tables:** 1  
**Figure/Tables Details:** Figure 1  
**Format for Reuse:** Print and Electronic  
**Total number of print copies:** Up to 1000

### Information about New Publication:

**University/Publisher:** Michigan Technological University  
**Title of dissertation/thesis:** INVESTIGATION OF LIQUID/AIR FILM STABILITY BY SYNCHRONIZED TRI-WAVELENGTH REFLECTION INTERFEROMETRY MICROSCOPE (STRIM)  
**Author(s):** Yuesheng Gao  
**Expected completion date:** Nov. 2020

### License Requestor Information

**Name:** Yuesheng Gao  
**Affiliation:** Individual  
**Email Id:** ygao4@mtu.edu  
**Country:** United States



## A.18 Figure 2.19 permission

This is a License Agreement between Yuesheng Gao ("You") and Annual Reviews, Inc. ("Publisher") provided by Copyright Clearance Center ("CCC"). The license consists of your order details, the terms and conditions provided by Annual Reviews, Inc., and the CCC terms and conditions.

All payments must be made in full to CCC.

Order Date	08-Nov-2020	Type of Use	Republish in a thesis/dissertation
Order license ID	1076074-1	Publisher	ANNUAL REVIEWS
ISSN	1545-4479	Portion	Image/photo/illustration

### LICENSED CONTENT

Publication Title	Annual review of fluid mechanics	Rightsholder	Annual Reviews, Inc.
Date	01/01/1969	Publication Type	e-Journal
Language	English	URL	<a href="http://arjournals.annualreviews.org/loi/fl...">http://arjournals.annualreviews.org/loi/fl...</a>
Country	United States of America		

### REQUEST DETAILS

Portion Type	Image/photo/illustration	Distribution	Worldwide
Number of images / photos / illustrations	1	Translation	Original language of publication
Format (select all that apply)	Print, Electronic	Copies for the disabled?	No
Who will republish the content?	Not-for-profit entity	Minor editing privileges?	No
Duration of Use	Life of current edition	Incidental promotional use?	No
Lifetime Unit Quantity	Up to 499	Currency	USD
Rights Requested	Main product		

### NEW WORK DETAILS

Title	INVESTIGATION OF LIQUID/AIR FILM STABILITY BY SYNCHRONIZED TRI-WAVELENGTH REFLECTION INTERFEROMETRY MICROSCOPE (STRIM)	Institution name	MICHIGAN TECHNOLOGICAL UNIVERSITY
Instructor name	Lei Pan	Expected presentation date	2020-11-30

### ADDITIONAL DETAILS

Order reference number	N/A	The requesting person / organization to appear on the license	Yuesheng Gao
------------------------	-----	---	--------------

### REUSE CONTENT DETAILS

Title, description or numeric reference of the portion(s)	Figure 2	Title of the article/chapter the portion is from	Drop Impact on a Solid Surface
Editor of portion(s)	N/A	Author of portion(s)	C. Jossierand and S.T. Thoroddsen
Volume of serial or monograph	48	Issue, if republishing an article from a serial	N/A
Page or page range of portion	365-391	Publication date of portion	2015-09-21

## A.19 Figure 2.20 permission

This Agreement between Yuesheng Gao ("You") and AIP Publishing ("AIP Publishing") consists of your license details and the terms and conditions provided by AIP Publishing and Copyright Clearance Center.

License Number 4944480847488

License date Nov 08, 2020

Licensed Content Publisher AIP Publishing

Licensed Content Publication Physics of Fluids

Licensed Content Title Air cushioning in droplet impact. I. Dynamics of thin films studied by dual wavelength reflection interference microscopy

Licensed Content Author Jolet de Ruiter, Frieder Mugele, Dirk van den Ende

Licensed Content Date Jan 1, 2015

Licensed Content Volume 27

Licensed Content Issue 1

Type of Use Thesis/Dissertation

Requestor type	Student
Format	Print and electronic
Portion	Figure/Table
Number of figures/tables	1
Title	INVESTIGATION OF LIQUID/AIR FILM STABILITY BY SYNCHRONIZED TRI-WAVELENGTH REFLECTION INTERFEROMETRY MICROSCOPE (STRIM)
Institution name	Michigan Technological University
Expected presentation date	Dec 2020
Order reference number	157
Portions	Figure2.20
Requestor Location	Yuesheng Gao 238 Quincy St Apt 9 HANCOCK, MI 49930 United States Attn: Michigan Tech
Total	0.00 USD

## A.20 Chapter 3 permission

Copyright Science Center | RightsLink®

Home | Help | Email Support | Yueheng Gao

Measurement of Instability of Thin Liquid Films by Synchronized Tri-wavelength Reflection Interferometry Microscope

Author: Yueheng Gao, Lei Pan  
Publication: Langmuir  
Publisher: American Chemical Society  
Date: Nov 1, 2018  
Copyright © 2018, American Chemical Society

ACS Publications  
Web Portal, Next-Chat, Next Read

PERMISSION/LICENSE IS GRANTED FOR YOUR ORDER AT NO CHARGE

This type of permission/license, instead of the standard Terms & Conditions, is sent to you because no fee is being charged for your order. Please note the following:

- Permission is granted for your request in both print and electronic formats, and translations.
- If figures and/or tables were requested, they may be adapted or used in part.
- Please print this page for your records and send a copy of it to your publisher/graduate school.
- Appropriate credit for the requested material should be given as follows: "Reprinted (adapted) with permission from (COMPLETE REFERENCE CITATION), Copyright (YEAR) American Chemical Society." Insert appropriate information in place of the capitalized words.
- One-time permission is granted only for the use specified in your request. No additional uses are granted (such as derivative works or other editors). For any other uses, please submit a new request.

## A.21 Chapter 6 permission

### Standard ACS AuthorChoice/Editors' Choice Usage Agreement

This ACS article is provided to You under the terms of this Standard *ACS AuthorChoice/Editors' Choice* usage agreement between You and the American Chemical Society ("ACS"), a federally-chartered nonprofit located at 1155 16th Street NW, Washington DC 20036. Your access and use of this ACS article means that you have accepted and agreed to the Terms and Conditions of this Agreement. ACS and You are collectively referred to in this Agreement as "the Parties").



#### 1. SCOPE OF GRANT

ACS grants You non-exclusive and nontransferable permission to access and use this ACS article subject to the terms and conditions set forth in this Agreement.

#### 2. PERMITTED USES

a. For non-commercial research and education purposes only, You may access, download, copy, display and redistribute articles as well as adapt, translate, text and data mine content contained in articles, subject to the following conditions:

i. The authors' moral right to the integrity of their work under the Berne Convention (Article 6bis) is not compromised.

ii. Where content in the article is identified as belonging to a third party, it is your responsibility to ensure that any reuse complies with copyright policies of the owner.

iii. Copyright notices or the display of unique Digital Object Identifiers (DOI's), ACS or journal logos, bibliographic (e.g. authors, journal, article title, volume, issue, page numbers) or other references to ACS journal titles, web links, and any other journal-specific "branding" or notices that are included in the article or that are provided by the ACS with instructions that such should accompany its display, should not be removed or tampered with in any way. The display of *ACS AuthorChoice* or *ACS Editors' Choice* articles on non-ACS websites must be accompanied by prominently displayed links to the definitive published versions of those articles on the ACS website.

iv. Any adaptations for non-commercial purposes must prominently link to the definitive published version on the ACS website and prominently display the statement: "This is an unofficial adaptation of an article that appeared in an ACS publication. ACS has not endorsed the content of this adaptation or the context of its use."

v. Any translations for non-commercial purposes, for which a prior translation agreement with ACS has not been established, must prominently link to the definitive published version on the ACS website and prominently display the statement: "This is an unofficial translation of an article that appeared in an ACS publication. ACS has not endorsed the content of this translation or the context of its use."

b. Each time You distribute this ACS article or an adaptation, ACS offers to the recipient a license to this ACS article on the same terms and conditions as the license granted to You under this License.

c. For permission to use ACS copyrighted articles beyond that permitted here, visit: <http://pubs.acs.org/copyright/permissions.html>

### 3. PROHIBITED USES

a. Use of this ACS article for commercial purposes is prohibited. Examples of such prohibited commercial purposes include but are not limited to:

- i. Copying or downloading of articles, or linking to such postings, for further distribution, sale or licensing, for a fee;
- ii. Copying, downloading or posting by a site or service that incorporates advertising with such content;
- iii. The inclusion or incorporation of article content in other works or services (other than normal quotations with an appropriate citation) that is then available for sale or licensing, for a fee;
- iv. Use of articles or article content (other than normal quotations with appropriate citation) by a for-profit organizations for promotional purposes, whether for a fee or otherwise;
- v. Sale of translated versions of the article that have not been authorized by license or other permission from the ACS

### 4. TERMINATION

ACS reserves the right to limit, suspend, or terminate your access to and use of the ACS Publications Division website and/or all ACS articles immediately upon detecting a breach of this License.

### 5. COPYRIGHTS; OTHER INTELLECTUAL PROPERTY RIGHTS

Except as otherwise specifically noted, ACS is the owner of all right, title and interest in the content of this ACS article, including, without limitations, graphs, charts, tables illustrations, and copyrightable supporting information. This ACS article is protected under the Copyright Laws of the United States Codified in Title 17 of the U.S. Code and subject to the Universal Copyright Convention and the Berne Copyright Convention. You agree not to remove or obscure copyright notices. You acknowledge that You have no claim to ownership of any part of this ACS article or other proprietary information accessed under this Agreement.

The names "American Chemical Society," "ACS" and the titles of the journals and other ACS products are trademarks of ACS.

### 6. DISCLAIMER OF WARRANTIES; LIMITATION OF LIABILITY

ACS warrants that it is entitled to grant this Agreement.

EXCEPT AS SET FORTH IN THE PRECEDING SENTENCE, ACS MAKES NO WARRANTY OR REPRESENTATION OF ANY KIND, EXPRESS OR IMPLIED, WITH RESPECT TO THIS ACS ARTICLE INCLUDING, BUT NOT LIMITED TO WARRANTIES AS TO THE ACCURACY OR COMPLETENESS OF THE ACS ARTICLE, ITS QUALITY, ORIGINALITY, SUITABILITY, SEARCHABILITY, OPERATION, PERFORMANCE, COMPLIANCE WITH ANY COMPUTATIONAL PROCESS, MERCHANTABILITY OR FITNESS FOR A PARTICULAR PURPOSE.

ACS SHALL NOT BE LIABLE FOR: EXEMPLARY, SPECIAL, INDIRECT, INCIDENTAL, CONSEQUENTIAL OR OTHER DAMAGES ARISING OUT OF OR IN CONNECTION WITH THE AGREEMENT GRANTED HEREUNDER, THE USE OR INABILITY TO USE ANY ACS PRODUCT, ACS'S PERFORMANCE UNDER THIS AGREEMENT, TERMINATION OF THIS AGREEMENT BY ACS OR THE LOSS OF DATA, BUSINESS OR GOODWILL EVEN IF ACS IS ADVISED OR AWARE OF THE POSSIBILITY OF SUCH DAMAGES. IN NO EVENT SHALL THE TOTAL AGGREGATE LIABILITY OF ACS OUT OF ANY BREACH OR TERMINATION OF THIS AGREEMENT EXCEED THE TOTAL AMOUNT PAID BY YOU TO ACS FOR ACCESS TO THIS ACS ARTICLE FOR THE CURRENT YEAR IN WHICH SUCH CLAIM, LOSS OR DAMAGE OCCURRED, WHETHER IN CONTRACT, TORT OR OTHERWISE, INCLUDING, WITHOUT LIMITATION, DUE TO NEGLIGENCE.

The foregoing limitations and exclusions of certain damages shall apply regardless of the success or effectiveness of other remedies. No claim may be made against ACS unless suit is filed within one (1) year after the event giving rise to the claim.

### 7. GENERAL

This Agreement sets forth the entire understanding of the Parties. The validity, construction and performance of this Agreement shall be governed by and construed in accordance with the laws of the District of Columbia, USA without reference to its conflicts of laws principles. You acknowledge that the delivery of the ACS article will occur in the District of Columbia, USA. You shall pay any taxes lawfully due from it, other than taxes on ACS's net income, arising out of your use of this ACS article and/or other rights granted under this Agreement. You may not assign or transfer its rights under this Agreement without the express written consent of ACS.

### 8. ACCEPTANCE

You warrant that You have read, understand, and accept the terms and conditions of this Agreement. ACS reserves the right to modify this Agreement at any time by posting the modified terms and conditions on the ACS Publications Web site. Any use of this ACS article after such posting shall constitute acceptance of the terms and conditions as modified.

## A.22 Chapter 7 permission



RightsLink®



Home



Help



Email Support



Yuesheng Gao



Interaction and instability of air films between bituminous coal surfaces and surfactant droplets

Author: Yuesheng Gao, Sunghwan Jung, Lei Pan

Publication: Fuel

Publisher: Elsevier

Date: 15 August 2020

© 2020 Elsevier Ltd. All rights reserved.

Please note that, as the author of this Elsevier article, you retain the right to include it in a thesis or dissertation, provided it is not published commercially. Permission is not required, but please ensure that you reference the journal as the original source. For more information on this and on your other retained rights, please visit: <https://www.elsevier.com/about/our-business/policies/copyright/author-rights>